Geochemical evolution in defunct gold mine tailings and modelling of seepage water quality: an investigation of a typical tailings storage facility in the East Rand, Johannesburg, South Africa

by

Petrus Johannes Fourie

Thesis

Submitted in fulfilment of the requirements in respect of the Doctor of Philosophy degree in the Department of Geology, Faculty of Natural and Agricultural Sciences, University of the Free State.

UNIVERSITY OF THE
FREE STATE
UNIVERSITEIT VAN DIE
VRYSTAAT
YUNIVESITHI YA
FREISTATA

NATURAL AND
AGRICULTURAL SCIENCES
NATUUR- EN
LANDBOUWETENSKAPPE
UFS·UV

In the first place, there can be no living science unless there is a widespread instinctive conviction in the existence of an Order of Things and, in particular, of an Order of Nature.

Alfred North Whitehead

ACKNOWLEDGEMENTS

I would like to express my gratitude to the following people/entities:

- Metron Laboratory, especially Dr Anneline Fourie, for assisting with all analyses in this thesis (except where otherwise indicated).
- Dr Brent Usher (my supervisor at KCB Australia) proofread some parts of the thesis and approved my leave to finish the final sections.
- Prof Marian Tredoux, my initial study supervisor at UFS and, sadly passed away in 2019, with whom I had several fruitful discussions.
- Dr Robert Hansen, my study supervisor, for his patience and encouragement over the past three years.
- Special thanks to my wife, Anneline; my kids, Pieter, Idalise and Hanné; my parents, Johan and Alet, for their love and support during this study.
- Thanks to the Lord, Creator of all things, for giving me loved ones and the ability to complete this study.

DISCLAIMER

I declare that this thesis, submitted for PhD to the faculty of Natural and Agricultural Sciences, University of Free State, is my own work and has not been previously submitted to any other university or institution of higher education for a degree.

Signature: ________________

Date: 18/01/2022

Place: UFS, Bloemfontein, South Africa.

ABSTRACT

The geochemical evolution in a defunct tailings dam was investigated in the East Rand Basin of the Witwatersrand. The research aimed to geochemically characterise the tailings, quantify oxygen infiltration into the tailings dam and develop a numerical geochemical model to simulate the geochemical evolution within the dam over the past 60 years.

Two holes (3.4 and 6 m deep, respectively) were hand-augured into the tailings dam to geochemically characterize the tailings. Tailings samples were collected at roughly 15 cm intervals. On selected samples from the 6 m hole, the whole-rock elemental composition (using X-ray Fluorescence and a Leco Element Analyser) was performed, as well as acid-base testing, X-ray diffraction and Scanning Electron Microscope. Field measurements of pH, Electrical Conductivity (EC) and Oxidation-reduction Potential (ORP) were performed on drilled-out samples of the 3.4 m hole.

The oxygen concentration in the tailings gas phase was measured to correlate the oxygen ingress with the other measured geochemical parameters and for later use in the geochemical model. Air chambers were installed in the 6 m hand-augered hole. Each air chamber comprised a perforated 7 cm high plastic container wrapped in a geotextile that is then connected with an 8 mm silicon pipe. Air collection chambers were installed at depths of 0.5 m, 1 m, 1.5 m, 2 m, 2.5 m, 3 m, 4 m, 5 m, and 6 m. Based on the oxygen concentration in the gas phase, the top of the tailings dam was subdivided into three geochemical environments, namely the Oxic Zone (0-2 m), the Transition Zone (2-4 m), and the Anoxic Zone (>4 m). The data shows that oxygen penetrates slightly deeper during the winter than in the summer months. The seasonal effect could be attributed to the higher rainfall in the summer than in winter.

A conceptual model of the geochemical evolution within the tailings dam was developed. The aim was to outline the major mechanisms that influence the geochemical evolution in the dam to include them in the numerical model.

Batch reactor testing was performed at three different pH's (pH ~3, pH ~5 and pH ~7) to back-calculate the effective surface area of the pyrite in a tailings sample based upon its reaction during the experiment. The experiments were performed over about 14 days. Except for the last few days, samples were collected twice a day. The sulphate production was the lowest in the pH ~3 experiment and the highest in the pH ~7 experiment. This is because pyrite oxidation by oxygen is inversely proportional to hydrogen activity. The modelled pyrite reaction rate fitted the results for all three experiments. The optimal surface area was determined at 1046.26 g/cm^2.

A numerical geochemical model was performed to simulate the geochemical evolution within the dam over the past 60 years. The primary objective of the modelling was to improve the understanding of the mechanisms that control the geochemical reactions and dispersion of chemicals. A secondary objective of the model was to match the model results with the observations 60 years after closure.

Measured and Modelled Parameters

The field paste pH ranged between pH 3.5 – 4 in the Oxic and Transition Zone and is only slightly higher at 4 – 4.2 in the Anoxic Zone. The Eh ranged between 600 – 675 mV, averaging at ~650 mV, in the Oxic Zone and between 430 – 520 mV, averaging at ~475 mV, in the underlying Transition Zone. The EC is the lowest (<5 mS/cm) at the top (0-25 cm), where the tailings are leached by infiltrating water. The EC reaches a maximum of ~35 mS/cm at 0.5 m in the Oxic Zone, whereafter, it decreases close to 13 mS/cm.

The acid-base test results indicated that the tailings have no potential to buffer significant acid generation. Iron-hydroxides do, however, provide some buffering at pH 3 and gibbsite from aluminosilicate weathering at around pH 4. This buffering was also observed for the pH ~3 batch reactor experiment, where the pH was always slightly above pH 3 when samples were taken (and had to be corrected with HCl).

From the numerical model results, it was shown that the pH is significantly lowered in the Oxic and Transition Zone because of sulphide oxidation and the subsequent acid generation that took place over the years. The pH is more elevated at the top of the Oxic Zone because of infiltrating circum-neutral water. The pH in the Oxic Zone matched the observed data well for the model with high and medium recharge (12% and 8% of annual precipitation).

The sulphide sulphur is significantly lower in the first two meters of the tailings, where oxygen ingress occurs throughout the year, and the sulphide minerals have been converted through oxidation reactions. The sulphate and sulphide sulphur are slightly elevated in the Transition Zone at 2 – 4 m, where oxygen is only present during the drier months. This corresponds to the model results that indicated precipitation of gypsum in the Transition Zone.

Uranium abundance in the tailings is lower in both the oxic and Transition Zone, indicating the uranium's high mobility under acidic, oxidising conditions. This corresponds to the modelling results that indicated that uraninite would oxidise in the Oxic Zone with some precipitation of hydrous uranyl sulphates in the Transition Zone and upper Anoxic Zone.

The major oxides do not show detectable enrichment or depletion throughout the profile. Although some are typically more resistant to weathering (e.g. SiO_2, Al_2O_3, Fe_2O_3 that can be present in resistant minerals like quartz, gibbsite, hematite etc.), the Oxic Zone is probably not weathered (“mature”) enough for the more resistant oxides to be enriched. CaO and Na_2O were relatively low in abundance in comparison to K_2O and MgO. The latter are major constituents of muscovite and chlorite. Muscovite was found not to be very reactive in the model, whereas chlorite was faster reacting and was the major contributor of Mg in the interstitial water.

More mobile trace elements like Cu, Ni, and Zn show lower abundance in the Oxic Zone, whereas the less mobile elements like Cr, Mn, Pb, Th, and Ti show no relative decrease in the Oxic Zone. Arsenic shows a minimal decrease in the Oxic Zone as it can form relatively stable secondary minerals in their higher oxidation state. This corresponds to the model results that indicated that Cu and Zn would leach from the Oxic Zone. Although not included in the model, Ni will show similar behaviour. This is because these metals are fairly mobile under acidic conditions and will not precipitate as secondary minerals. In the model, Pb and As precipitates as anglesite and secondary arsenate sulphate, bukovskýite, respectively. Although not included in the model Cr, Mn, Th, and Ti will form fairly inert oxides, which will not be significantly leached from the Oxic Zone.

Recommendations for Future Studies

The following recommendations relate to the measurement of oxygen in the tailings dam:

- The oxygen directly after drilling overestimates the oxygen depth. Oxygen should be measured in follow-up measurements at least two months after drilling, as was performed in this study.
- The measured oxygen showed some seasonal effects. Measurements could be improved by monthly (manual) measurements or by using permanently installed oxygen probes at different depths. The latter will, however, be significantly more expensive and could, however, easily be vandalised.
- Monthly oxygen measurements should be accompanied by a measurement of moisture content in the tailings dam. This could be achieved by monthly drilling or by installing water content probes (like Watermark) at different depths.

The following recommendations relate to the geochemical characterization of the tailings:

- Ideally, characterisation of the tailings should be performed over the whole vertical profile of the tailings dam. The sampling frequency of 15 cm was adequate for the Oxic and Transition Zone. A smaller frequency (e.g. 0.5 m) might be adequate for the Anoxic Zone.
- More samples from the Oxic and Anoxic Zone should be tested by Scanning Electron Microscopy to assess the mineralisation in the tailings, especially the sulphides present. Most sulphides are not detected by X-ray Diffraction. It could also be useful to determine the composition of major minerals, although Laser Ablation might be more useful in this regard.
- X-ray Fluorescence is only semi-quantitative but could be useful to determine the major oxides. To determine the whole-rock elemental composition for trace elements more accurately, acid digestion with an ICP-MS finish would improve the test results significantly.
- Interstitial water sampling could be performed by directly sampling the wet tailings after drilling and extracting the pore water through a vacuum.
- The methodology for the batch reactor testing should be refined so that the reaction of more minerals can be determined. This test could also be performed along with kinetic column leach leaching.

The following recommendations relate to the geochemical numerical modelling:

- The modelling of geochemical scenarios with multiple variables is a challenge, especially when trying to manually match the simulation results with observed data. For this purpose, automatic parameter estimation software like PEST could be used in further modelling. PEST automates calibration by estimating or adjusting model parameters within certain ranges by running it many times (PEST, 2022).

TABLE OF CONTENTS

TABLE OF CONTENTS

(continued)

TABLE OF CONTENTS

(continued)

TABLE OF CONTENTS

(continued)

List of Tables

TABLE OF CONTENTS

(continued)

List of Figures

TABLE OF CONTENTS

(continued)

TABLE OF CONTENTS

(continued)

TABLE OF CONTENTS

(continued)

TABLE OF CONTENTS

(continued)

1 INTRODUCTION

1.1 Background

The Witwatersrand gold deposit is a quartz-pebble conglomerate ore deposit of the Archaean and Early Proterozoic age. It presents the earliest known sedimentary concentration of gold and uranium (Smits, 1990). Acid Mine Drainage (AMD) forms part of the gold mining legacy of the Witwatersrand of nearly 130 years. As far back as 1905, farmers in the Witwatersrand area complained about changing water quantity and quality (Adler et al., 2007)[1]. Today, the impact on the Vaal River catchment is evidence of the scale of the AMD problem, as more than 50% of the salt load in the Vaal River between the Vaal Dam and the barrage (Vaal Triangle area) could be attributed to gold mining activities in the Witwatersrand (McCarthy, 2011).

In the Witwatersrand Basin, nearly 270 tailings dams are present (Rösner, 1999), which are often poorly rehabilitated, constructed with no underlying barrier system, and frequently situated near-surface water features. It seems that historically, not much thought was given to the placement of some of these dams, or rather, there was limited understanding of their potential environmental impact at the time of construction or operation. For example, on the 30 km stretch between Brakpan, Springs and Nigel, there are 12 tailings dams adjacent to the Blesbokspruit and

---

[1] According to A. R. Turton (personal communication, 2017) the original source of this comment was from an archive of the Far West Rand Dolomitic Water Association that was established in 1964 and existed until the transition to democracy in South Africa in 1994. It is uncertain what happened to the bulk of the archive although some part of it probably found its way to private collections.

its tributaries. Run-off and seepage from these tailings dams contribute to the salt load towards the Blesbokspruit.[2]

According to Rösner (1999), it is improbable that most tailings dams will be rehabilitated, and more active management measures will likely only be employed at dams, posing a significant risk to the downgradient environment. However, several tailings dams in the Witwatersrand Basin are earmarked for reclamation. *Ergo Mining Proprietary Limited* (Ergo) has mining rights to about 100 sand dumps[3] and tailings dams (about 750 Mt to 900 Mt material, respectively) across the western, central and eastern Witwatersrand Basin, making Ergo one of the world's largest gold surface tailings retreatment companies (Ergo, 2021).

Because they form more or less permanent features in the Witwatersrand landscape (either as individual dams or mega-dams emanating from reclamation), it is critical to understand the long-term AMD generation potential from the tailings dams. The seepage water quality from the dams is controlled by the geochemical reactions in the tailings material; therefore, changes in the long-term seepage quality from the dams are only possible to predict if the evolution of geochemical properties within the dam is well understood. This research aims to develop and implement a systematic approach for predicting AMD from tailings dams that could also be employed in future studies.

---

[2] The most significant recent impact on the Blesbokspruit were related to the pumping of mine water from Grootvlei gold mine (since 1995) as well as effluent from the Sappi paper mill; since the cessation of these impacts in 2011, the water quality in the Blesbokspruit has improved significantly (Ambani & Annegarn, 2015).

[3] Sand dumps are the result of the less efficient 'stamp-milling' process employed in the early gold mining years (Ergo, 2021).

1.2 Research Objectives

The geochemistry of tailings facilities was considered through an appreciation of the fundamental hydrogeochemical processes, bolstered by empirical evidence from a defunct facility and expanded by the development of suitable numerical methods to model the hydrogeochemical behaviour of tailings dams.

The geochemical evolution in a defunct tailings dam was investigated in the East Rand Basin of the Witwatersrand, which provided the bulk of the firsthand data for this research. The tailings dam investigated is situated in Springs and is also referred to as 5L27. The dam is further discussed in Chapter 3. This dam was also previously investigated by Yibas et al. (2010), which study is briefly discussed in the literature review.

The aims of the research were: 1) to geochemically characterise the tailings; 2) to quantify oxygen infiltration into the tailings dam; and 3) to develop a numerical geochemical model to simulate the geochemical evolution that took place within the dam over the past 60 years.

The most challenging part of such predictive modelling is to quantify both the oxygen migration into the dams as well as the kinetic reactions of the pyrite and then to include the interaction of all relevant processes and reactions into a numerical geochemical model. The more specific research questions of the research included:

- Could the migration of oxygen and the subsequent geochemical changes in a defunct tailings dam be quantified, and how will it seasonally change? Oxygen migration into tailings dams is an important rate-limiting step for acid-mine drainage generation (Davis & Ritchie, 1986), and studies involved in the prediction of acid-mine drainage should carefully evaluate this mechanism for a specific site. As part of this study, oxygen chambers were installed in the study site in order to monitor the oxygen over several months.

- Is it possible to quantify pyrite's kinetic reaction and effective surface area in a typical tailings dam subjected to weathering? Kinetic leach tests (e.g. humidity leach cells) are generally performed as part of a geochemical assessment to determine the leachate rate of mine waste. However, secondary minerals may precipitate when saturated in humidity cells, complicating the interpretation of the results. As part of this study, batch reactor testing was performed to calculate the effective surface area of the pyrite in the tailings based on its reaction rate in a batch reactor.
- Is it possible to generate a model that could simulate geochemical evolution (and subsequent acid mine drainage generation) within the tailings that could match field observations? A numerical geochemical model was developed that considers both vertical and horizontal flow. The model also considered various flow and pyrite oxidation scenarios. Several model scenarios were run to determine which scenarios best match the observed field data.

1.3 Project Outline

A literature review was performed In Chapter 2 to discuss general and specific issues related to acid mine drainage generation at tailings dams with emphasis on the Witwatersrand where possible.

In Chapter 3, some background to the investigated site and a description of the fieldwork performed is provided. The field and laboratory test results from a vertical tailings profile are presented in Chapter 4. The migration of oxygen, and subsequent pyrite oxidation, commences at the top of the dam profile; therefore, the variation of geochemical properties was investigated at the top of the dam down to the Anoxic Zone.

In Chapter 5, a conceptual model was generated to provide a framework for the numerical modelling. The conceptual model outlined the major mechanisms that influence the geochemical evolution in the dam.

A batch reactor experiment was performed on a tailings sample from the Anoxic Zone, and the results of the experiment are discussed in Chapter 6. The experiment was performed to determine the pyrite's kinetic reaction rate and effective surface area in the tailings.

A numerical geochemical model was generated in Chapter 7 to model the evolution of the geochemical parameters within the tailings. The interaction between the air, water and mineral phases was then modelled in a reactive transport model. Several scenarios were performed to evaluate the model's sensitivity in terms of variation in pyrite surface area, oxygen fugacity and flow rate. Therefore, the model's objective was not to make any future predictions but rather to model the geochemical processes that already took place.

A final discussion is provided in Chapter 8, with conclusions and recommendations for further study in Chapter 9.

2 LITERATURE REVIEW

2.1 Introduction

This chapter provides relevant background information and summaries of pertinent research on tailings dams in the Witwatersrand Basin. Several aspects of mine drainage were reviewed as background to the project. Some general aspects of mine drainage are discussed in Section 2.2. The Witwatersrand Basin’s mineralogy, gold processing and tailings dam construction methods are outlined in Sections 2.3 to 2.5. Oxygen and water migration processes in post-closure tailings dams are discussed in Section 2.6. Previous studies on the depth of oxidation in Witwatersrand tailings dams are discussed in Section 2.8. Previous geochemical modelling of mine drainage from the Witwatersrand tailings dams was reviewed in Section 2.9.

2.2 Mine Drainage Water Quality

2.2.1 Classification of Mine Drainage in Terms of Salinity and pH

The impact on drainage at a mine depends on the interaction of the solid, water and air phases. The drainage water quality is a function of the mine waste mineralogy, gas (especially oxygen) migration, as well as water flow.

Drainage from disturbed pyrite-bearing rock material at mines could be classified into three types, namely: Acid-mine Drainage (AMD), Saline Mine Drainage (SMD) and Neutral Mine Drainage (NMD) (GARDGuide, 2021). Based upon the USGS classification of water salinity (Krieger et al., 1957), the USDA classification of acidic soils (USDA, 2021), and the GARDGuide classification of mine drainage (GARDGuide, 2021), a simplified classification for mine drainage as a function of pH and Total Dissolved Solids (TDS) was constructed and is depicted in Figure 1 below.

AMD occurs when pyrite-bearing rock material is exposed to weathering and oxidation and produces acidity, metals and sulphate. Acidic drainage (< pH 6) will arise with inadequate neutralisation from carbonate minerals. Carbonic acid is an essential buffer of AMD and has a pKa of about 6.52 – 6.35 (5°C to 40°C) when in equilibrium with bicarbonate (Stumm & Morgan, 1995). Below this pH range, carbonic acid becomes the dominant carbonate species. At a pH of 6, carbonic acid already comprises 70-75% of the total carbonate of the solution and below pH 4.5, >99% (Stumm & Morgan, 1995). Therefore, acid drainage below pH 6 has a low bicarbonate content and often high saline drainage (with a high metal load) due to sulphate production and metals from sulphide mineral oxidation.

Mine drainage will often evolve from NMD to SMD before AMD is reached (GARDGuide, 2021). Drainage may initially be neutral (NMD), but if the exposed rock material has a high pyrite content, the sulphate concentration will typically increase until a slightly to moderate salinity is reached (SMD) (GARDGuide, 2021). If all inherent neutralisation potential from the rock material is consumed or inadequately available, the pH will decrease (often with a consistent increase in salinity), and AMD will be reached over the long term. For NMD to be maintained, pyrite should be absent or not exposed to weathering and oxidation. For SMD not to evolve to AMD over the long term, the rock material should have a larger neutralisation than acidification potential. In this case, most neutralisation should also come from highly reactive minerals (like calcite) that can maintain a pH above 6. In NMD and SMD, the metal load is often lower than in AMD; however, a few amphoteric metals (that form soluble complexes) can still be present under neutral-alkaline conditions (GARDGuide, 2021).

In Figure 1, the different fields for mine drainage are plotted on a TDS vs. pH diagram. AMD is present below pH 6 (GARDGuide, 2021) and saline and neutral mine drainage is above that. The United States Geological Survey (USGS) reported the boundary between fresh and saline to be at a TDS concentration of 1 000 mg/l (Krieger et al., 1957). Above this boundary, slightly-, moderately- and highly saline water ranges are 1 000 – 3 000 mg/l, 3 000 – 10 000 mg/l, and 10 000 to 35 000 mg/l, respectively.

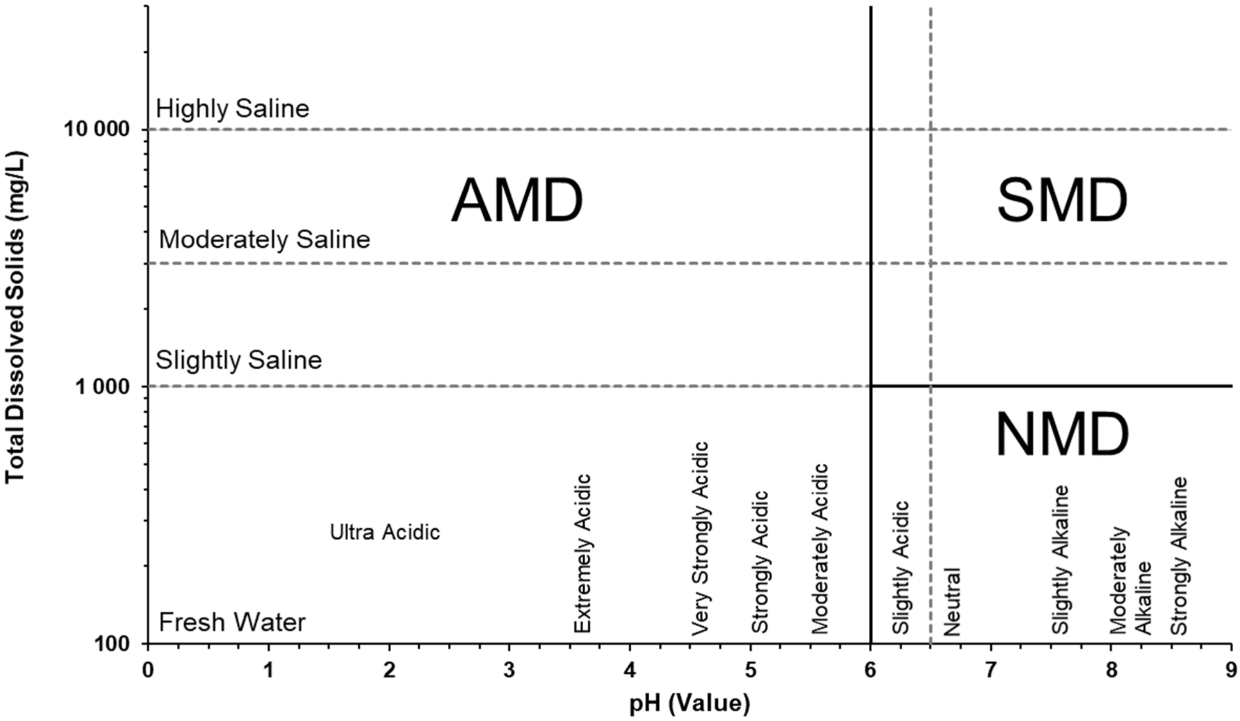

Figure 1: Simplified classification of mine drainage from exposed pyrite-bearing rock material as a function of pH and TDS. PH and TDS classes were adopted from Krieger et al. (1957) and USDA (2021).

2.2.2 Assessment of Redox Processes

As discussed before, oxygen migration into tailings dams is an important rate-limiting step for acid-mine drainage generation (Davis & Ritchie, 1986). Under oxic conditions, sulphides will be oxidised, and the produced ferrous iron will be oxidised to ferric iron oxide or hydroxide because of the loss of an electron to oxygen.

The United States Geological Survey (USGS) considers a dissolved oxygen concentration of <0.5 mg/L to be indicative of sub-oxic conditions in the groundwater, e.g. McMahon and Chapelle (2008). The next most energetically favourable electron acceptor under anoxic conditions is NO_3^{2-}, followed by Mn(IV), Fe(III), sulphate, and carbon dioxide (CO_2). Segregation of redox processes results in that different zones forms, which are dominated by a single electron-accepting process

(Berner, 1980). This tendency, as well as the distinctive end products of redox processes (dinitrogen gas (N_2), ammonium (NH_4^+), ferrous iron (Fe(II)), Hydrogen sulphide (H_2S), and methane (CH_4)), make it possible to use water quality to assess ambient redox processes in ground water systems as shown in Table 1 (McMahon & Chapelle, 2008).

Table 1: Threshold Concentrations for Identifying Redox Processes in Groundwater (McMahon & Chapelle, 2008)

Redox Process	**Water Quality Criteria**				
	O_2	**NO_3^{2-}-N**	**Mn^{2+}**	**Fe^{2+}**	**SO_4^{2+}**
Oxic					
O_2 Reduction	≥0.5	-	<0.5	<0.1	-
Suboxic [a]					
-	<0.5	<0.5	<0.5	<0.1	-
Anoxic					
NO_3^{2-} reduction	<0.5	≥0.5	<0.5	<0.1	-
Mn(IV) reduction	<0.5	<0.5	≥0.5	<0.1	-
Fe(III)/SO_4^{2-} reduction	<0.5	<0.5	-	≥0.1	≥0.5
Methanogenesis	<0.5	<0.5	-	≥0.1	<0.5
Mixed [b]	-	-	-	-	-

[a] Further definition of redox processes is not possible.

[b] Criteria for more than one redox process are met.

2.3 Regional Geology and Mineralogy

2.3.1 Introduction

The setting and stratigraphy of the Witwatersrand Supergroup are depicted in Figure 2 below. The tailings dam investigated in this study is situated in the East Rand Goldfield. The tailings were sourced from the conglomerate reefs of the Central Rand Group (CRG) and can be expected to have a similar primary mineral composition. A brief overview of the mineralogy of the Witwatersrand Group, with specific reference to the Central Rand Group, is provided in this section.

The Witwatersrand Au-bearing conglomerate has a typical mineralogical composition comprised of quartz (70–90%), muscovite and other phyllosilicates (10–30%), and; accessory and minor minerals (1–5%) (Feather & Koen, 1975). More than 70 minor minerals have been identified in the reefs, including base metal sulphides and U-bearing minerals, but the most common is pyrite (FeS_2), with an abundance of 3– 5% (Feather & Koen, 1975).

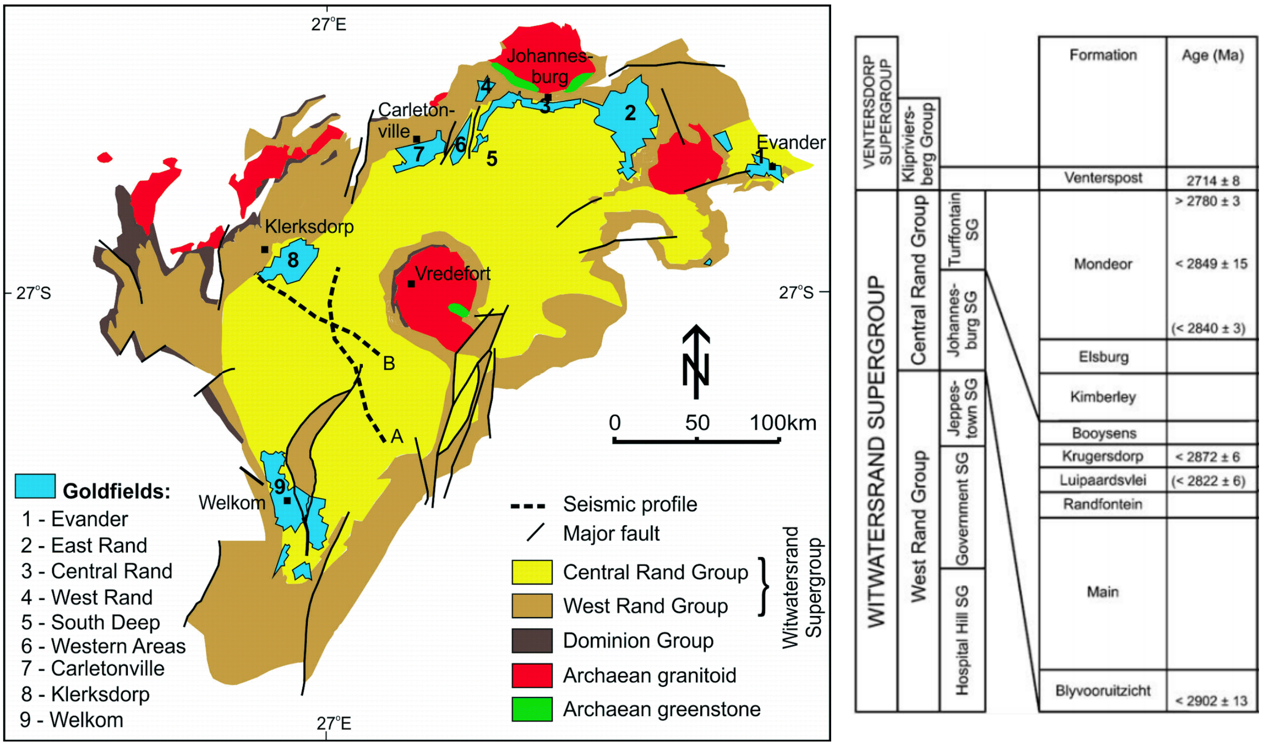

Figure 2: Setting and stratigraphy of the Witwatersrand Supergroup (Frimmel, 2019)

2.3.2 Paragenetic Sequence of Mineralisation

The Witwatersrand deposit is comprised mainly of arenites, with lesser rudits, which were deposited on an alluvial fan and alluvial braid plain environments (Robb & Meyer, 1995). The CRG is a dominantly arenaceous sequence comprised of quartz-pebble conglomerates, quartzites, quartzwackes and minor shales. The quartzite to shale ratio is 12.6:1 (Pretorius, 1974), as opposed to a ratio of only 1:1 for the West Rand Group (WRG). Gold-bearing ore bodies occur mainly in the form of very mature pebble and gravel bar deposits (Robb & Meyer, 1995). The CRG was deposited mainly as alluvial braid-plain sediments with lesser alluvial fan conditions (Els, 1998). During deposition, the geochemical environment played an important role in the initial preservation of the detrital minerals, especially pyrite, arsenopyrite, and uraninite, which would not be stable under today's atmospheric conditions. The amount of oxygen available at the earth's surface during the Archaean was limited (Smits, 1990). The atmosphere is comprised mostly of nitrogen and carbon dioxide with minor hydrogen sulphide (Krupp et al., 1994). The surface conditions in the provenance area and *en route* to the depositional environment must have been acidic partly due to the higher carbon dioxide in the atmosphere (5 – 30 times higher than present) (Smits, 1990).

The sediments were subjected to diagenesis and metamorphism, with the silicate assemblage indicating the lower stage of low-grade metamorphism at a temperature of below 400°C and a pressure of about 3 kbar (Smits, 1990). The low-grade metamorphism also resulted in some mineralisation that had a hydrothermal character.

In an attempt to explain the mineralisation's detrital and hydrothermal character, Mellor (1916) proposed the modified placer theory that suggested that detrital gold and some pyrite were reconstituted during the low-grade metamorphic alteration. The modified placer theory is the most widely accepted model in recent years (da Costa et al., 2020).[4] Robb & Meyer (1995) proposed a detailed multistage paragenetic sequence for mineralisation. The initial stage of mineralisation involved placer development with the deposition of detrital minerals (including gold, uraninite and pyrite) originating from the erosion of greenstones and hydrothermally altered granites. During the second to fourth stages of mineralisation (2550, 2300 and 2000 Ma, respectively, correlating with the two Transvaal depositional stages and the intrusion of the Bushveld Complex), hydrothermal alteration resulted in the remobilisation of gold as well as the

---

[4] Only the modified placer theory is briefly discussed here. The modified placer and hydrothermal models are reviewed in more detail by McCarthy et al. (2006). A hydrothermal model for gold mineralisation in the Witwatersrand is discussed by Barnicoat et al. (1997).

authentic growth of various sulphides like pyrite, pyrrhotite, galena, chalcopyrite and pentlandite (Robb & Meyer, 1995).

2.3.3 Silicate Mineralogy

In all the major Witwatersrand goldfields, the silicate mineral assemblages suggest near-uniform peak metamorphic conditions of greenschist facies (equivalent to the "chlorite zone"). The silicate mineralogy of the deposited sediments is dominated by quartz with some minor to major phyllosilicates, namely, chlorite, muscovite, sericite, pyrophyllite and chloritoid. Most phyllosilicates were formed during metamorphism (fine-grained interstitial fillings), although some (larger-grained) rounded chlorite, and rarely some muscovite is of detrital origin (Smits, 1990). Possible precursor minerals for the post-burial phyllosilicates are shown in Table 2 below.

Biotite is rare in the Witwatersrand Group as it was either weathered to clay minerals before diagenesis or altered to other phyllosilicates during late diagnesis and the very early stage of metamorphism (Smits, 1990). Smits (1990) notes that muscovite is often a constituent of the pseudomorphs after biotite; she also describes an example of an intergrowth of chlorite and muscovite that replaced biotite.

Table 2: Possible precursor minerals of metamorphic phyllosilicate assemblages (Smits, 1990).

Metamorphic Mineral	Precursor: Immediate	Precursor: Earlier
Chloritoid	Pyrophyllite, Chlorite IIb	See Pyrophyllite See Chlorite IIb
Pyrophyllite	Kaolinite, Chlorite Ib	Kaolinite Multilayered Chlorite/Smectite
Chlorite IIb	Chlorite Ib	Multilayered Chlorite/Smectite
Muscovite 2M	Phengite or Illite of High Crystallinity	Multilayered Illite/Smectite

2.3.4 Pyrite

Modes of Occurrence in the Witwatersrand

The three modes of occurrence for pyrite in the Witwatersrand are 1) allogenic, detrital, well-rounded compact grains; 2) synsedimentary, rounded or concretionary pyrite; and 3) authigenic, post-sedimentary pyrite (Hallbauer & Gehlen (1983), Hallbauer (1986), Smits (1990), Koglin et al. (2010)). Da Costa et al. (2020) proposed a revised classification scheme for Witwatersrand pyrite and classified all pyrite grains either as detrital or authigenic.

Hallbauer & Gehlen (1983) estimated that about 90% of pyrite in the Witwatersrand is abraded pebbles of detrital origin; however, Hallbauer (1986) gives a more realistic estimate of 30-70%. The detrital pyrite is referred to as well-rounded, compact grains by Smits (1990). The detrital pyrite often contains fluid and (often rounded) mineral inclusions, including pyrrhotite, pentlandite, chalcopyrite, galena, ilmenite, rutile and quartz (Hallbauer & Gehlen, 1983). According to Hallbauer & Gehlen (1983), detrital pyrite has many resemblances to pyrite from granites in terms of mineral and fluid inclusions as well as geochemistry; however, the detrital pyrite originates from various provenance sources as discussed further below.

Hallbauer (1986) estimates that syn-sedimentary pyrite makes up about 10-40% of pyrite in the Witwatersrand Goldfields. Concretionary pyrite is a framework of small granular or crystalline pyrite with other minerals filling the interstices and is angular or irregular-shaped (Smits, 1990). These are referred to by Hallbauer & Gehlen (1983) as mud-ball pyrite as they formed in pyrite muds on the floor of abandoned channels. Because of other mineral inclusions in the mud-balls, they appear dull and rounded, often referred to in older literature as “buckshot pyrite”, which was also an informal indicator of conglomerate with higher potential gold grade Hallbauer (1986). Da Costa et al. (2020) view these as detrital pyrite (although reworked) and somewhat cynically note that the term buckshot pyrite should be abandoned as it relates to a time when a rifle was part of the prospecting geologist's field kit. Smits (1990), however, notes that with concretionary pyrite, several generations of pyrite may be present in the same grain. Other forms of synsedimentary pyrite include radial (concentric), layered, aggregate and framboidal pyrite (Hallbauer, 1986).

Authigenic pyrite formed during metamorphism is anhedral to euhedral, cement heavy minerals, or forms encrustation on allogenic pyrite (Smits, 1990). The authigenic pyrite also has no inclusions (Hallbauer & Gehlen, 1983; Smits, 1990). Pseudomorphic pyrite represents primarily non-sulfidic detrital grains like ilmenite or titaniferous magnetite that have been replaced by pyrite (da Costa et al., 2020). These pyritized grains contain relict structures like rutile laths that allow them to be identified as pyrite pseudomorphs after these individual minerals (da Costa et al., 2020).

According to Smits (1990), the diameter of the rounded (detrital), synsedimentary and discrete authigenic pyrite in the several CRG reefs she investigated are typically at 0.15 - 0.35 mm, 0.15 - 5.00 mm and 0.01 - 0.30 mm, respectively. Some minute authigenic pyrite inclusions in phyllosilicates or chert are, however, smaller than 0.03 mm. Hallbauer (1986) gives an approximate diameter for the same three main groups of pyrite in the Witwatersrand Goldfields as 0.06 - 5 mm, 0.1 – 20 mm and 0.01 - 2 mm, respectively.

Chemical Composition of Allogenic Pyrite

As discussed above, Hallbauer & Gehlen (1983) notes that the detrital pyrite resembles pyrite from granites, implying that Archean granites may have been present in the provenance area. However, variations in mineral inclusions and trace element composition indicate heterogeneity in the provenance area (even for the same reef), and probably more than one source rock was present (Hallbauer, 1986). The trace-element content of single grains of detrital pyrite from two Witwatersrand Reefs is given in Table 3 below.

Hallbauer (1986) further reports some correlation between the trace elements in pyrite from the Basal Reef and the pyrite from the Archaean Greenstone Belts; however, this similarity does not extend to pyrites in other reefs.

Table 3: Trace-element content of single grains of detrital pyrite from two Witwatersrand Reefs (Hallbauer, 1986)

Locality	**Trace Element Content (ppm)**										
	Cu	**Co**	**Ni**	**Zn**	**Pb**	**Mg**	**Ca**	**Na**	**K**	**Na/K**	**Co/Ni**
Elsburg Reef EA 12 (Loraine Mine)	123	246	820	72	328	451	492	2200	500	4.40	0.30
	355	301	1740	33	676	870	268	680	318	2.14	0.17
	405	176	1745	44	1163	485	432	1200	264	4.55	0.10
	255	579	2086	58	927	719	695	2400	522	4.60	0.28
	300	376	1955	75	1128	564	921	3500	1034	3.38	0.19
	136	5	954	273	5	750	920	4100	1022	4.01	0.01
	442	442	2212	221	1106	1051	1493	7900	1272	6.21	0.20
Average	288	304	1645	111	762	699	746	3140	705	4.46	0.18
St. dev	125	187	546	95	449	217	411	2414	398	6.07	0.34
Geomean	260	181	1549	83	395	670	652	2422	604	4.01	0.12
VCR (East Driefontein Mine)	106	62	86	22	120	408	134	400	168	2.38	0.72
	86	70	135	16	172	201	110	300	256	1.17	0.52
	2989	322	2115	69	2299	632	540	2000	540	3.70	0.15
	78	93	98	93	249	85	295	1500	78	19.23	0.95
	5	186	186	62	309	192	743	1600	155	10.32	1.00
	40	92	94	26	172	22	112	400	40	10.00	0.98
	5	5	5	58	5	156	347	3800	159	23.90	1.00
Average	473	119	388	49	475	242	326	1429	199	7.16	0.31
St. dev	1110	105	763	29	810	210	242	1250	165	7.56	0.14
Geomean	58	73	111	41	164	162	254	981	151	6.50	0.66

2.3.5 Other Sulphides

Except for small inclusions in detrital pyrite grains, pyrrhotite, galena, chalcopyrite, and sphalerite are of post-burial origin and are usually associated with quartz or enclosed by chlorite (Smits, 1990). Smits (1990) notes that pentlandite has rarely been observed as inclusion in detrital pyrite and is mainly in the authigenic form.

Textural studies indicate that arsenopyrite (FeAsS) and cobaltite (CoAsS) are of detrital origin, and gersdorffite (NiAsS) formed post-burial (Smits, 1990). According to Robb & Meyer

(1990), the mineral association of cobaltite-arsenopyrite-gersdorffite span over syn- and epigenetic processes. Gold is frequently associated with all three sulphurarsenides, according to Smits (1990).

2.3.6 Uranium Bearing Minerals

Detrital uraninite $(U, Th)O_2$ and authigenic uranous titanates $(U,Th)_{1-x}Ti_{2+x}O_6$ are the major uranium minerals and are about equally distributed in reefs exploited for uranium (Smits, 1990). The latter is subdivided by uraniferous leucoxene (UO_2/TiO_2 <1) or brannerite (UO_2/TiO_2 >1). Other minerals include anhydrous $(U, Th)SiO_4$ (with end-members anhydrous coffinite-thorite) and hydrated $(U, Th)SiO_4.4H_2O$ (with end-members coffinite-thorogummite).

Minute particles of galena, formed in the course of geological time, are present in all uranium-bearing minerals investigated by Smits (1990).

2.4 Overview of Gold Processing and its Influence on Tailings Mineralogy

The tailings dam being investigated in this study was constructed before the 1970s. Before the 1970s, gold extraction from non-refractory ore (where gold is not in solid-solution in minerals) was mostly performed by the cyanidation technique[5] (Marsden & House, 2006).

The conventional cyanidation method involved grinding the ore where after it is leached with an alkaline[6], aerated cyanide solution. After decantation or filtering, the gold was precipitated from the solution using zinc dust or was electrochemically deposited (Prasad et al., 1991).

---

[5] In 1972 there was a boom in the gold extraction metallurgy with the addition of the carbon-in-leach (CIL) and the carbon-in-pulp (CIP) methods (Marsden & House, 2006). The activated carbon adsorbs the gold out of the cyanide solution as it has a very high affinity for the aurocyanide complex. With CIL, the carbon is added to the cyanide leach, whereas in CIP, concentration takes places place through a series of tanks.

[6] A high alkalinity is obtained through the addition of lime in order to prevent the formation of HCN gas.

HCN is a weak acid and dissociates in solution to form H^+ and CN^-. More than 90% of cyanide is speciated as the free ion CN- in solution at pH ~10.2. At a pH of ~8.4, more than 90% of cyanide speciates as HCN, which has a high vapour pressure and volatilizes easily, leading to a loss of cyanide in the system (Marsden & House, 2006)

The overall dissolution of gold through the cyanide leaching process is described by the following two simultaneous reactions (Marsden & House, 2006):

$$2Au + 4CN^- + O_2 + 2H_2O \rightarrow 2Au(CN)_2^- + 2H_2O_2 + 2OH^-$$

Equation 1

$$2Au + 4CN^- + 2H_2O_2 \rightarrow 2Au(CN)_2^- + 2OH^-$$

Equation 2

Some sulphide minerals will partially oxidise during leaching with resultant oxygen consumption and generation of acid. This would require additional aeration and the addition of lime to the system.

The most significant effect of the gold processing on the deposited tailings is the reduction of the grain size to fine sand and silt size fractions. Smits (1990) notes that the average diameter of detrital pyrite in the ores ranges between 0.15 mm and 0.30 mm. Reducing the grain size to silt fraction (0.002 – 0.063 mm) will significantly increase the surface area, and therefore, the reaction rate of the pyrite in the tailings will increase when in contact with oxygen. A proportion of the sulphide mineral content will also undergo minor oxidation during processing. The tailings are deposited as an alkaline slurry; however, the pH will rapidly drop to neutral pH due to exposure to the atmosphere. Exposed tailings will eventually become even more acidic, especially when the tailings dam is slowly built up, allowing amble reaction time for pyrite oxidation.

2.5 Tailings Dam Construction

Tailings Storage Facilities (TSF) are designed as dams to retain tailings slurry and enable the reclamation of water during the operational phase. The TSF comprises an embankment with tailings slurry stored in the centre. Three methods are used for the raising of the TSF perimeter embankments, as discussed by Vick (1990) and depicted in Figure 3 below:

- Downstream Method: The embankment moves progressively downstream or outwards from the stored tailings with the downstream embankment raise. The downstream method is considered the safest but the most expensive means of constructing a TSF embankment. This is due to the large volume of material required and the greater expansion of the footprint of the TSF during operation.
- Centreline Method: With the centreline construction raise, the embankment crest remains in the same position, which is a compromise between the upstream and downstream techniques.
- Upstream Method: The embankment is progressively raised upstream or partially over previously deposited tailings with the upstream construction method. This is usually the least expensive option but is less inherently safe (from a geotechnical stability perspective) than the other methods.
- These methods can be used in combination to minimize costs while achieving an acceptable level of risk.

According to Vermeulen (2001), upstream lifting of the embankment is commonly (and safely) employed in arid environments with low seismic activity. Historically, construction through upstream embankment lifts has been the most common construction method of Witwatersrand TSFs. Typical TSF (or slimes dams as these are commonly referred to) construction by Anglo American in South Africa was reported by Ruhmer (1974), who discussed the upstream method, e.g. the typical inner and outer wall construction is depicted in Figure 4. For terraced walls, the slope varies between 31 ° and 36° (with the average slope of the dam wall, including terraces, varying between 23 ° and 30 °), while for dam walls without terraces, the slope varies between 27 ° and 36° (Ruhmer, 1974).

Tailings can be placed through several methods, including the paddock system, the cyclone system, the spigot system, and open-end discharge behind a mechanically formed containment wall (McPhail & Wagner, 1987). Only the paddock system will be discussed further as this was employed at most, if not all, of the (now defunct) tailings dams in South Africa, including the tailings dam investigated in this study. The upstream paddock system was historically used almost exclusively in South Africa with its prevailing semi-arid climate (McPhail & Wagner, 1987). On the Witwatersrand, evaporation generally exceeds precipitation, and dams up to 60 m high have been built successfully (Penman, 1994, cited in Vermeulen, 2001). The paddock system used in South Africa is described by McPhail & Wagner (1987) as follows:

- After the initial construction of the earth starter walls and underdrainage, the tailings are deposited with a rising rate of not more than 2.5 m/yr.
- The outer wall ("day wall") is subdivided into paddocks by ploughing up dykes as shown in Figure 5c. During the day shift, slurry (or pulp as it is also called) is led from the delivery points into each paddock and deposited to a depth of about 150 mm. Excess water from the pulp is decanted into the inner part of the dam. The remaining tailings are left to dry for up to 3 weeks before the next deposition (in this period, cracks are often formed in these surficial portions of the drying tailings).
- At night, tailings are discharged directly into the interior of the dam ("night area" or "night pan") behind the walls formed during the day.
- Supernatant water in the centre of the dam is collected through a penstock. In South Africa, evaporation generally exceeds rainfall with the result that the surface

(except the pool area) becomes desiccated and large shrinkage cracks develop. The successive tailings' deposition fills these cracks. This desiccation is fundamental to the paddocked dam construction as drying results in densification and strengthening of the tailings. The cracks also tend to become filled with slightly coarser tailings which improve the vertical drainage of the dam.

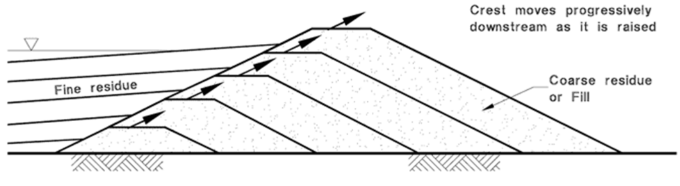

(a) Downstream Method

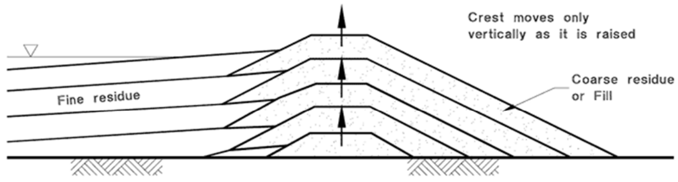

(b) Centreline Method

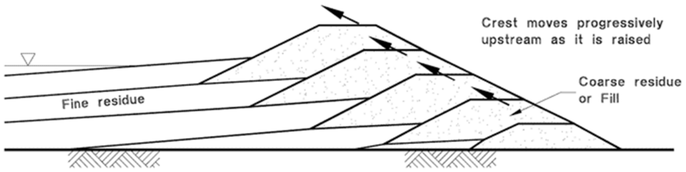

(c) Upstream Method

Figure 3: Three methods of lifting TSF perimeter embankments (Vick, 1990)

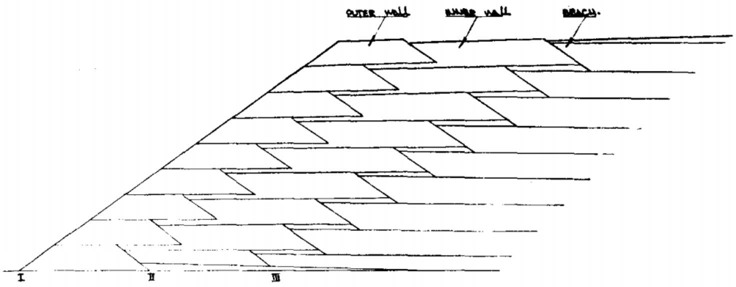

a) Stepwise repositioning of inner and outer walls without terraces

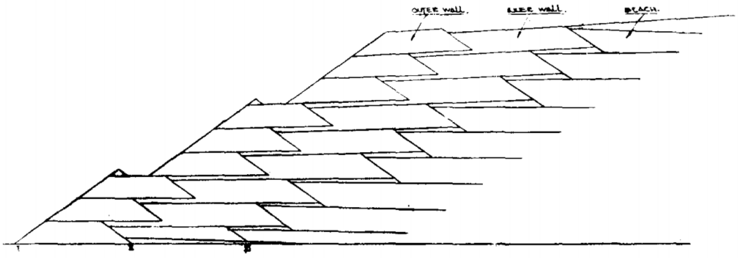

b) Stepwise repositioning of inner and outer walls with terraces

Figure 4: Inner and outer wall construction with and without terraces (Ruhmer, 1974)

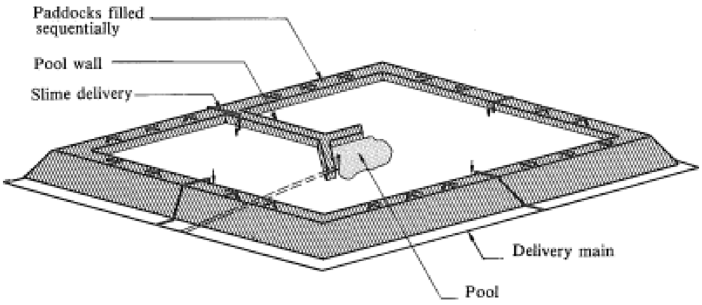

(a) Perspective view

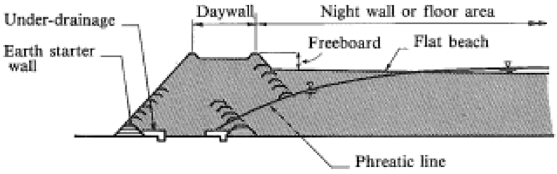

(b) Typical section

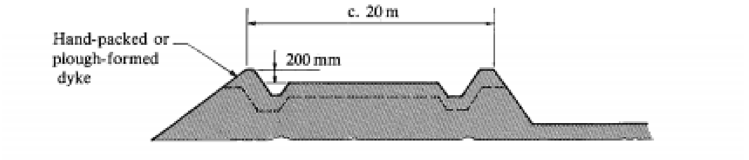

(c) Typical daywall section

Figure 5: Paddock system of tailings dam construction (McPhail & Wagner, 1987)

2.6 Water and Oxygen Migration in Post-Closure Tailings Dams

2.6.1 Oxygen Diffusion

Diffusion is the most dominant process of oxygen migration through partially air-filled pores within a tailings dam (Nicholson, 1994; Ritchie, 1994)[7]. Oxygen diffusion results from a concentration gradient between the atmospheric oxygen and the tailings due to oxygen consumption from the oxidation of pyrite contained in the tailings. Both the abiotic and biotic oxidation mechanisms of pyrite require oxygen. Acidophilic bacteria that mediate pyrite oxidation (below ~pH 3.5) can also only survive if oxygen is available (Jaynes et al., 1984). Oxygen is, therefore, a requirement for the AMD generation process.

According to Fick's Law, the mass flux of oxygen is proportional to the effective diffusion coefficient D_e (m.s^{-1}) and the oxygen concentration gradient (mol.m^{-3}m^{-1}) (Appelo & Postma, 2005). Fick's First and Second Laws (for steady-state and transient state) for diffusional solute transport in one dimension, x (m), is given by:

$$F_x = D_e \frac{\partial C}{\partial x}$$

Equation 3

$$F(x,t) = D_e(x,t)\,\frac{\partial^2 C(x,t)}{\partial x^2}$$

Equation 4

where F is the diffusive flux (mol.m^{-2}s^{-1}), D_e (m.s^{-1}) is the effective diffusion coefficient, and C is the oxygen concentration in air (mol.m^{-3}). The change of the concentration of oxygen over time during the diffusion process in both the air and water phase of pyrite containing porous medium is described by the following form of Fick's Law (Molson et al., 2005):

---

[7] Other oxygen transport processes include advection due to temperature convection or barometric pumping. The driving forces for these processes are thermal gradient and atmospheric pressure changes respectively (GARDGuide, 2021).

$$\left(\theta_a(x,t) + H\,\theta_w(x,t)\right)\frac{\partial C(x,t)}{\partial t} = D_e(x,t)\,\frac{\partial^2 C(x,t)}{\partial x^2} - \frac{\partial q(x,t)}{\partial t}$$

Equation 5

Where q is the pyrite consumption rate (mol.m^{-3}.s^{-1}), ϑ_a and ϑ_w are the air and water content of the pores, respectively (m^3.m^{-3}), H is the dimensionless Henry's Law coefficient for equilibrium oxygen partitioning between air and water. In Equation 5, the left side represents the oxygen storage, the first term on the right-hand side is the diffusive oxygen flux, and the last term is the oxygen consumption rate by pyrite.

The effective diffusion coefficient, D_e, expresses the resistance to diffusion but is lower than the molecular diffusion coefficient of oxygen in a free fluid (gas, liquid). This resistance is due to the presence of solids hindering diffusion by increasing the tortuosity of the transport pathways (Wels et al., 2003). At STP (Standard Temperature and Pressure, T = 0˚C and P = 1 atm), the diffusion coefficient of oxygen in the air and in water are approximately $1.8x10^{-5}$ m.s^{-1} and $2.1x10^{-7}$ m.s^{-1} respectively (Elberling & Nicholson, 1996). The degree of saturation within the pore space dramatically affects the value of the oxygen diffusion coefficient. Various semi-empirical and theoretical equations for effective diffusion are found in the literature, for instance, the Reardon & Moddle (1985) equation:

$$D_e = 3.98x10^{-9}\ x\left(\frac{\theta_a - 0.05}{0.95}\right)^{1.7}\ x\ (T + 273.15)^{1.5}$$

Equation 6

Mbonimpa et al. (2003) state that diffusion in porous media occurs predominantly in the air phase or at least when the degree of saturation is below 85 – 90%, where the air-filled porosity is discontinuous. Therefore, the oxygen will only infiltrate significantly into a tailings dam where unsaturated conditions are present.

2.6.2 Post-closure Tailings Dam Water Balance

All water on top of a decommissioned tailings dam originates from precipitation (*P*). Run-off (*R*) from the walls will be relatively high, with some smaller run-off from the beach area towards the pre-pool area that will decant through the penstock. If the penstock is closed, this water will form part of the evaporation from the tailings dam (Yibas et al., 2011). Run-off from paddocks will be zero as these are not free draining and are constrained by the paddock walls. Evaporation (E_v) is the vaporization of surface- or soil water in contact with the atmosphere and will depend on the temperature, humidity, wind and solar radiation (Ward & Trimble, 2003). Transpiration (E_t) is the water loss from the vascular system of plants into the atmosphere and depends on the vegetation cover thickness, plant species and root depth (Ward & Trimble, 2003). The total evapotranspiration (E_{vt}) comprises evaporation from surface water (E_s) as well as evapotranspiration from the top of the unsaturated zone (E_u). The water balance at the top of the tailings dam could be expressed as follows:

$$P = I + R + E_s$$

Equation 7

The actual rate of infiltration (*I*) is a function of the soil water content, texture, density, hydraulic conductivity and porosity (Ward & Trimble, 2003). The infiltration into the tailings dam will vary between the dry winter months and the summer rainfall season in the South African interior (as well as between wet and dry years), resulting in a slight change of water storage (ΔS) within the unsaturated tailings. Rainfall infiltration into the tailings dam will be lost to seepage to drains (S_d), seepage through the base (S_b), evapotranspiration from the unsaturated zone and a change in storage in the unsaturated zone:

$$I = S_d + S_b + E_u + \Delta S$$

Equation 8

Yibas et al. (2011) measured the rainfall deep infiltration at two decommissioned tailings dams to vary between 15 - 17% of the MAP using lysimeters. However, the monitoring by Yibas et al. (2011) was only performed over a short (4-month) period. Yibas et al. (2011) calculated the run-off from the beach towards the pre-pool area at 17% of the MAP, with the evaporation at a minimum of 69% of MAP (with an open penstock) and a maximum of 83% (with a closed penstock).

Substituting Equation 7 into Equation 8 yields:

$$P = S_d + S_b + R + E_{vt} + \Delta S$$

Equation 9

The seepage through the base and drains of the facility and towards the underlying aquifer could be expressed as follows:

$$S_b + \ S_d = P - R - E_{vt} - S_d + \Delta S$$

Equation 10

Deep percolation (D_p) into the tailings dam is defined in this study as the remainder of the infiltration after evapotranspiration losses:

$$D_p = I - E_u = \ S_d + S_b + \Delta S$$

Equation 11

Suppose the long-term change in storage is zero (which signifies steady-state conditions). In that case, the seepage through the base and drains could be expressed in terms of the precipitation, recharge and total evapotranspiration as follows:

$$S_b + \ S_d = D_p = \ P - R - E_{vt} \ , \ S = 0 \, , \qquad \textit{(steady state)}$$

Equation 12

Long-term seepage from tailings dams (to aquifer) was found at 1 - 6% of the MAP (after the phreatic surface subsides) in modelling studies (Bezuidenhout & Rousseau, 2005). Naudé (2016) also calibrated a 2D unsaturated-saturated flow model for a mega tailings dam in South Africa using a recharge of 6%. These latter seepage rates are substantially lower than the fourmonth rainfall deep infiltration (15 - 17% MAP) measured by Yibas et al. (2011), which was referred to above.

2.6.3 Saturated Water Flow

Darcy's law for saturated flow states that the rate of flow through a porous medium is proportional to the change in head and inversely proportional to the length of the flow path:

$$v_{dx} = \frac{Q_x}{A_{tx}} = K_x \frac{dh}{dx}$$

Equation 13

where v_{dx} is the Darcy flux of the water (m/yr) in the x-direction, Q is the volumetric flow rate (m^3/a), A_{tx} is the flow-through area (m^2), K_x is the saturated hydraulic conductivity (m/yr), and dh/dx the gradient of the hydraulic head, h (m), in the x-direction (m).

The effective flow-through area (A_{ex}) will be smaller than the total flow-through area (A_{tx}) for a porous medium, as flow is essentially limited to the pores. The actual water flow velocity (v_w) could be expressed in terms of porosity, n (m^3/m^3), as follows:

$$v_w = \frac{Q_x}{A_{tx} n} = \frac{v_{dx}}{n}$$

Equation 14

The total porosity in Witwatersrand tailings varies between 0.46 and 0.51 (Bezuidenhout & Rousseau, 2005). The saturated hydraulic conductivities of the Witwatersrand tailings dams have been found in selected studies to range between 1×10^{-6} and 1×10^{-8} m/s (Bezuidenhout & Rousseau, 2005).

The saturated flow in the tailings dam will be in the vertical and horizontal directions towards the base and the toe of the tailings dam, respectively. In most sedimentary deposits, horizontal hydraulic conductivity (K_h) is higher than in the vertical plane (K_v) because of the differential settlement of sediments during deposition. The quotient between K_h/K_v is called the anisotropy factor and, in general, varies between 2 and 10 for alluvium but may be up to 100 where clay layers are present (Todd & Mays, 2004). The hydraulic conductivity in Witwatersrand tailings dams is highly anisotropic, and anisotropic values of up to 200 have been reported (Rösner, 1999).

The rate of retreat of the phreatic surface depends on the hydraulic properties of the tailings, the under-drainage system and the size of the tailings dam (Yibas et al., 2011). Rösner & van Schalkwyk (2000) state that most South Africa tailings dams were historically constructed without seepage collection systems. The hydraulic properties of the tailings depend on the grain size (which typically determine the hydraulic conductivity and water retention) and the depositional history (differential settling by hydraulic deposition vs. thickened slurry deposition) (Yibas et al., 2011). The piezometric surface of a tailings dam retreats at approximately 0.3 m/a to 0.5 m/a after decommissioning (Bezuidenhout & Rousseau, 2005). Monitoring of piezometers by Yibas et al. (2011) at the Old North Complex (ONC) No. 3 tailings dam showed that the retreat rate of the phreatic surface (during operational phase) was initially 4.03, 2.81 and 2.87 m/y for the wall, beach and ex-pool part of the dam, eventually dropping to 0.97 and 0.25 m/y for the beach and ex-pool parts of the dam (after decommissioning). Monitoring by Yibas et al. (2011) at the Driefontein No. 3 dam showed that the retreat rate of the phreatic surface at the dam's edge has dropped from 8.82 m/y to 0.88 m/y.

Therefore, the hydraulic head, and the seepage of a tailings dam, will be the highest during the operational phase. After decommissioning, the piezometric surface will retreat with a subsequent decline in hydraulic head and seepage rate. Over the long term, seepage from the dam will approach the deep percolation of rainfall into the dam.

2.6.4 Unsaturated Water Flow

In the unsaturated zone, the (soil moisture) pressure is determined by the radius of curvature of pore water menisci which in turn depends on the pore (grain) size and the pore water content (ϑ) (Dingman, 2015). Unsaturated flow (v_u) in the z-direction (vertical) will be along the maximum gradient of the pressure head (ψ) according to Darcy's Law for unsaturated flow (Dingman, 2015):

$$v_{uz} = K(\theta) - K(\theta)\frac{d\psi(\theta)}{dz}$$

Equation 15

where z is the vertically downward direction (m) and K(ϑ) is the hydraulic conductivity as a function of the moisture content.

Over the long term, there will only be a seasonal variation in the moisture content at the top of the unsaturated zone. In the deeper portion of the tailings dam, the moisture content will approach a steady state with negligible water storage changes. Seepage from the dam will approach the deep percolation of rainfall infiltration into the tailings facility through the unsaturated zone, as shown in Equation 12.

When infiltrating water pushes the old water ahead (called piston flow), the deep percolation into the dam will equal the seepage from the dam. The unsaturated water flow velocity could then be derived by mass balance (Appelo & Postma, 2005) as follows:

$$v_p = \frac{D_p}{n_w}$$

Equation 16

where v_p is the (piston flow) velocity of the water (m/yr), D_p is the deep rainfall percolation (m/yr), and n_w is the water-filled porosity (m^3/m^3). Piston flow is based on the water balance of the tailings dam and could only be employed if no significant preferential flow zones (e.g. desiccation cracks or micro-fissures in the root zone etc.) are present (Appelo & Postma, 2005) and flow in the tailings dam has reached a near steady-state.

2.7 Equilibrium and Kinetic Mineral Reactions

The mineral reactions in the tailings dam investigated could be described by either equilibrium reactions for fast-reacting minerals or kinetic rate laws for slower-reacting minerals. Primary and secondary minerals considered in the model are discussed in the Conceptual Model in Section 5.3.

Equilibrium Mineral Reactions

Nordstrom & Munoz (1994) state: “Thermodynamics is the study of energy and its transformations. Kinetics is the study of the rates and mechanisms of reactions. Thermodynamics tells us which geochemical processes are possible, whereas kinetics tells us which processes are the fastest.”

Various authors describe chemical equilibrium in detail (e.g. Appelo & Postma, 2005, Bethke, 2007, Nordstrom & Munoz, 1994). Differences in chemical potential are the driving force behind chemical reactions (Appelo & Postma, 2005). The chemical potential of a species is the energy that can be absorbed or released due to a change in the given species' particle number. The chemical potential indicates the change in the Gibbs free energy at a constant temperature and pressure if the amount of a constituent *i* vary while all the other constituents remain constant ($dT = 0$ and $dP = 0$) (Appelo & Postma, 2005):

$$\mu_i = \left(\frac{\partial \Delta G}{\partial n_i}\right)_{T,P,n_{j \neq i}}$$

Equation 17

Using the gas law, the non-ideal state can be written as:

$$\mu^0 = \mu_i^0 + RT \ln a_i$$

Equation 18

where a_i is the activity of substance *i,* and μ_i^0 is defined as the standard state of a hypothetical one-molal solution in which activity and molality are equal, and the species' properties have been extrapolated to infinite dilution (Appelo & Postma, 2005).

The change in the free energy of the reaction *aA + bB ↔ cC + dD* can be written as (Appelo & Postma, 2005):

$$\Delta G_R = \Delta G_A + \Delta G_A + \Delta G_A + \Delta G_A$$

Equation 19

and Equation 18 and Equation 19 can be combined as:

$$\Delta\mu_R^0 = -\mathrm{RTln}\frac{a_C^c a_D^d}{a_A^a a_B^b}$$

$$= -\mathrm{RTlnQ}$$

Equation 20

At the equilibrium point, the change in the free energy of the reaction is zero $\Delta G_R = 0$, and *Q* is replaced with *K*. The relation *Q/K* indicates in which direction a reversible chemical reaction will proceed to minimize the change in free energy of the reaction. If *Q* is smaller than K, the products will be favoured, and if larger, the reactants; if *Q = K,* then equilibrium is reached. To indicate the precipitation or dissolution of a mineral, the term saturation index *SI* is introduced and is expressed as *SI = log Q/K*. Therefore, if *SI* is negative, the mineral will dissolve; if positive, it will precipitate and if *SI = 0*, it is at equilibrium.

Kinetic Reactions

The kinetic rate law r_a for mineral *a* is expressed as follows (Bethke, 2007):

$$r_a = -A_s k_+ \prod^i (a_i)^n \ [1-\Omega]$$

Equation 21

where, A_s is the mineral surface area (cm^2), k_+ is the forward rate constant ($mol.cm^{-2}.s^{-1}$);

a is the activity of basis species *i* to the power of *n*, and Ω is the ratio between the reaction quotient (*Q*) and the equilibrium constant (*K*).

The reactive surface area of a mineral is a considerable uncertainty when using kinetic data. According to Appelo & Postma (2005), estimation of the surface area for field situations has hardly passed the stage of reasonable guessing. The rate constant k can be related to temperature by the Arrhenius equation (Bethke, 2007):

$$k = Ae^{-E_a/RT_k}$$

Equation 22

where *A* is the pre-exponential or frequency factor ($mol.cm^{-2}.s^{-1}$), E_a is the activation energy (J.mol-1), *R* is the gas constant ($8.314\ J.\ K^{-1}mol^{-1}$), and *Tk* is the absolute temperature (K).

The activation energy E_a is the minimum collision energy required for the molecules to react. Reactions with large activation energies have small rate constants, and reactions with small activation energies have large rate constants.

2.8 Oxidation depth in Witwatersrand Tailings

Yibas et al. (2010) undertook research for the Water Research Commission of South Africa (WRC) on the development of oxidation zones in Witwatersrand tailings dams. The study was first summarized by Nengovhela et al. (2006).

Six tailings dams were investigated, with their relative location depicted in Figure 6 below. These dams were referred to as Site A – F by Nengovhela et al. (2006). As discussed in the introduction (Section 1.2), the tailings dam investigated in this thesis is situated in Springs and is referred to as 5L27. This is the same Site A that was also investigated in the research study of Yibas et al. (2010).

The depth of oxidation at the top of the tailings dams, as measured after the installation of oxygen chambers by Yibas et al. (2010), is depicted in Figure 7 below. Because the oxygen was measured just after installation, some low levels of oxygen were still present in some of the deeper measurement compartments.

This research concluded that oxygen depletion occurs rapidly within the first few meters in the Witwatersrand tailings dams. The measurements suggested that oxygen drops to <1% atm O_2 by ~5 m depth for all the investigated facilities. At the oldest dam (Site A), oxygen depletion was measured to occur closer to the surface, ~1% atm O_2 at 3 m deep. The study concluded that because the oxygen flux is strongly controlled by diffusion, the oxidation depth will generally be limited to the top ~3 - 5 m because the tailings are relatively fine-grained (sandy silt or silty sand). The study also found that because of this limitation on the oxidation depth, the relative age of the dump does not have a significant bearing on the depth of the oxidation zone.

With the installation of the oxygen chambers, tailings samples were retrieved that were also subjected to geochemical testing. Results of the 1:10 solid-to-water extraction of the Site A tailings samples are summarised in Table 4 below, with paste pH in Table 5. X-ray diffraction (XRD) results per depth interval are listed in Table 6. These results will be referred to later in this thesis.

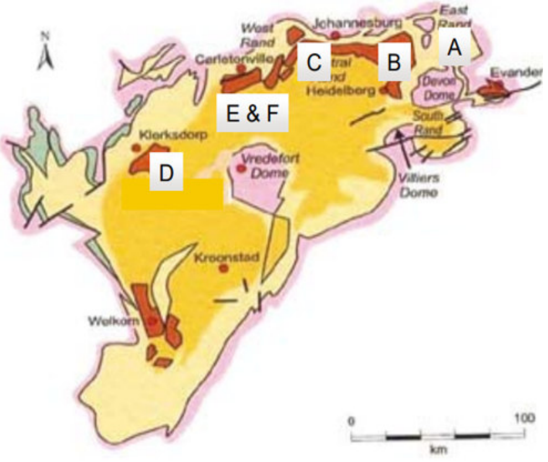

Site Name	Area (ha)	Height (m)	Volume (m³)	Date of decommission-ing
Site A	#	10.5 -22.5	#	1950s?
Site B	38	25	7 828 000	1976
Site C	44.2	32	7 576 000	1975
Site D	#	34	#	1973
Site E	#	#	31 422 569	1997
Site F	#	#	#	1999

#Unavailable information.

Figure 6: Information of and location of tailings dams investigated (Nengovhela et al., 2006)

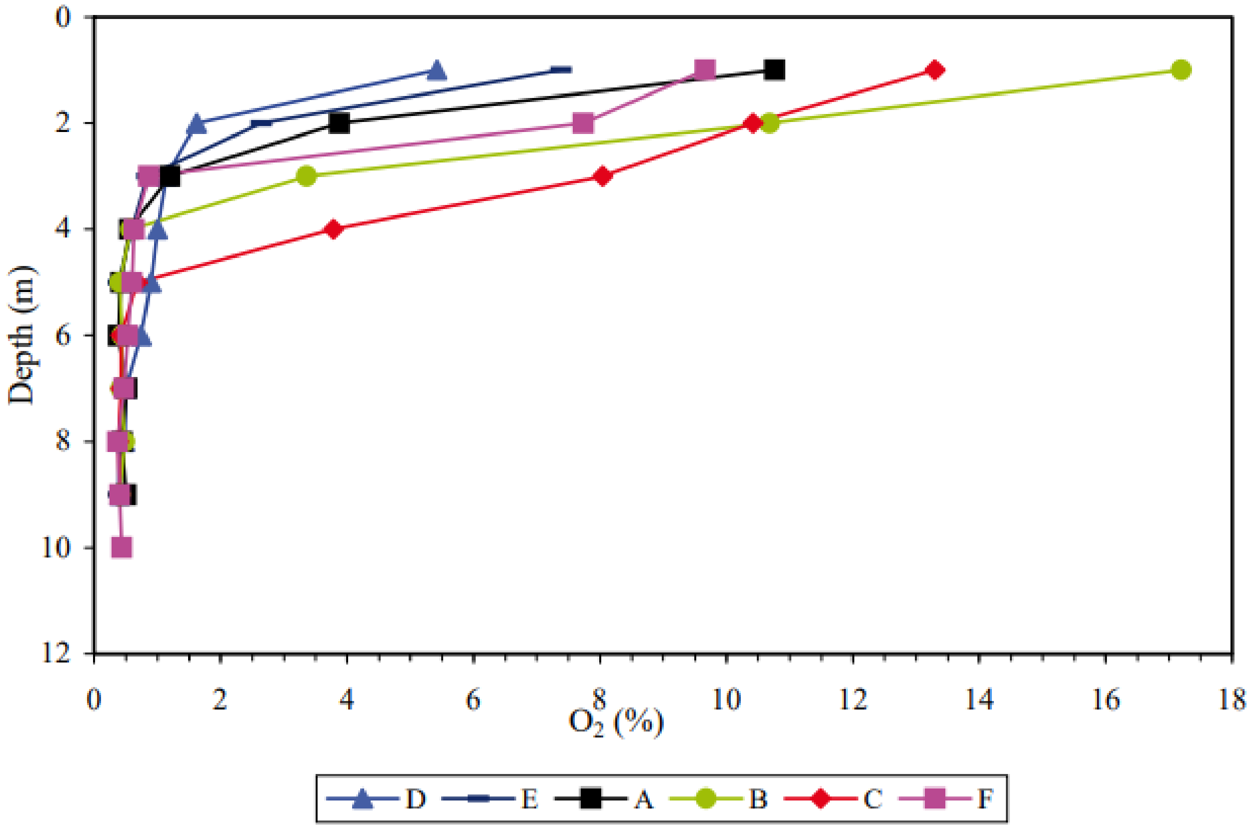

Figure 7: Oxygen concentration as measured at the top of six tailings dams (Nengovhela et al., 2006)

Table 4: Results of 1:10 water extraction tests of Site A Tailings Samples (Nengovhela et al., 2006). Where OZ = Oxidised Zone, TZ = Transition Zone, UZ = Unoxidised Zone.

Zone	**OZ**	**TZ**	**UZ1**	**UZ2**
Depth (cm)	**400**	**600**	**900**	**1000**
pH (value)	3	4	4	4
Alkalinity (mg/L $CaCO_3$)	0	0	0	0
Conductivity (mS/m)	314	185	223	115
Redox Potential (mV)	218	215	255	217
Sulphate (mg/L)	2934	1158	1273	584
Aluminium as Al (mg/L)	233	66	26	2
Calcium as Ca (mg/L)	265	212	263	193
Cobalt as Co (mg/L)	5	4	4	2
Copper as Cu (mg/L)	2	1	0	<0.1
Iron as Fe (mg/L)	157	69	300	30
Lead as Pb (mg/L)	<0.5	<0.5	<0.5	<0.5
Magnesium as Mg (mg/L)	101	25	96	24
Manganese as Mn (mg/L)	4	4	8	5
Nickel as Ni (mg/L)	10	8	12	5
Potassium as K (mg/L)	0	5	3	7
Sodium as Na (mg/L)	2	15	6	6
Zinc as Zn (mg/L)	5	4	6	2

Table 5: paste pH (Yibas et al., 2010)

Zone	**OZ**	**TZ**	**UZ**
pH (value)	3.62	4.1	6.4

Table 6: XRD results per depth interval (wt%) (Yibas et al., 2010)

Zone	**Pyrite**	**Jarosite**	**K-feldspar**	**Quartz**	**Mica**	**Chlorite**	**Gypsum**
Site A OZ	0	2	0	80	8	8	1
Site A TZ	1	1	1	82	9	7	0
Site A UZ1	1	1	1	80	10	7	0
Site A UZ2	0	0	1	80	11	7	0

2.9 Geochemical Numerical Modelling of Witwatersrand Tailings Storage Facilities

Different approaches have been followed to model the seepage water quality emanating from Witwatersrand tailings dams. Most of these studies have been performed as part of unpublished projects in the mining industry. Indeed, Hansen (2015) states that not one peer-reviewed geochemical model of Witwatersrand tailings impoundments could be sourced at the time. Most studies focused on predicting the pH, sulphate, total dissolved solids, and, very seldom, the metal concentrations in seepage from the tailings dam. Modelling the metal concentrations in tailings dam seepage is challenging as it is difficult to quantify the mineral sources of the metals since, except for forming their own minerals (e.g. nickel as pentlandite), the metals may also occur in solid solution (e.g. nickel as a trace in pyrite) or as mineral inclusions in the various mineral phases (Hansen, 2015).

Hansen (2015) and Hansen (2018)

Hansen (2015) generated a 25-year generic model for the typical seepage water quality from a Witwatersrand tailings dam by developing separate geochemical models for the Oxidation zone (OZ), the Transition Zone (TZ) and the Reduction Zone (RD) using the React application of the Geochemist Workbench Standard (GWB, 2020). The output of one model was used as input to the next in spatial order. Time series data could not be generated for the tailings dam as a whole, although it could be generated for each of the distinct geochemical zones (Hansen, 2015). Metals (Ni, Co, Cu, Cr, Mn and Zn) were included in the model in the solution based on the mass balance data from whole-rock analyses. The model of Hansen (2015) predicted that for a generic tailings dam with a pyrite content of about 3% and with little or no neutralization capacity, the resultant seepage would be acidic within the 25 years of the model time.

Hansen (2018) used a similar approach where the OZ, TZ and RD were modelled, and the output for one model was used as input for the next. Two model iterations were run. The trace elements arsenic, cobalt, nickel, lead and zinc present in the pyrite and uraninite were added to the model as fluxes based on the dissolution rate of these two minerals. Therefore, all trace elements were assumed to be associated with either pyrite or uraninite.

Harck (2016)

Harck (2016) performed a geochemical model for the ERGO Brakpan tailings dam. He modelled the oxygen ingress using a spreadsheet model and the vertical geochemical reaction path using a 1D PHREEQCi model. The modelled oxygen ingress reaches about 40 meters below the surface after 50 years in a tailings dam with a low pyrite content (max S% 0.34 wt%). The tailings dam was acidic at the top 2 m with a pH of about 3 – 4. The sulphate only increased from about 1 600 mg/l to about 2 800 mg/l over the 50 model years because of the low pyrite content of the tailings. The deep oxygen migration used in this study was not validated with field measurements from similar studies.

Fourie (2013) and Fourie (2018)

Fourie (2013) performed a 1D numerical oxygen diffusion model and a 1D geochemical reaction path model using the 1xt application of the Geochemist Workbench (GWB, 2020). Under oxidation conditions, the pyrite oxidation rate was calibrated by simulating kinetic leach test results. The final model comprised a 1D transport model through 40 m thick tailings dams that also incorporated the temporal oxygen concentration. The model of Fourie (2013) indicated that the tailings with relatively low pyrite (pyrite S% = 0.5) and low neutralization capacity produce an oxidized, acidic rim at the top of the tailings dam of fewer than 8 m below the surface within 60 years. The outer rim of the tailings dam will have a sulphate concentration that will range between 1 500 - 5 000 mg/l over time. Below the outer rim, the tailings dam will remain neutral with sulphate close to gypsum saturation at 1 500 - 2 500 mg/l. According to Fourie (2013), this deeper part of the tailings dam will not be acidic, although it will slightly decrease in size over time with the advance of the acidic front. Fourie (2013) did not specifically include the prediction of metal concentrations in the numerical model.

In Fourie (2018), a similar model approach was followed as in Fourie (2013); however, the actual depth of oxidation was also measured in the field by installing oxygen chambers, similar to those performed in this study reported in Section 4.2. Field measurements indicated that oxygen had migrated about 1.5 m into the tailings profile during the operational phase of the mine. However, the sulphide %S was relatively high at 2.5%, and measurements indicated that the tailings interstitial water was already acidic (pH 2-3) soon after deposition. The geochemical model showed that the outer (oxic) rim of the tailings dam (>5 m) would have the poorest interstitial water quality from acidity and increased sulphate and metals perspective. Although the inner part of the tailings dam will also be acidic (deeper than 5 – 10 m), the water quality will not deteriorate further for several decades because of the absence of pyrite oxidation. Over time, transport from the outer rim takes place deeper into the tailings dam; the inner tailings dam will worsen in quality after about 50 - 100 years. The outer rim of the tailings dam is subjected to oxidation and will have a sulphate of roughly 6 000 – 8 000 mg/l in its drainage. Interstitial water in the inner part of the tailings dam will have a sulphate of 2 500 – 3 500 mg/l for about 50 years, sulphate concentrations gradually increasing. Because of the absence of carbonate minerals, dissolved concentrations of metals such as aluminium, iron, and manganese will become major cations in the acidic tailings dam seepage.

3 SITE BACKGROUND AND FIELDWORK PERFORMED

3.1 Introduction

This section provides a background to the investigated site and describes the fieldwork performed. Some field observations regarding the physical and hydrological aspects of the site are included in this section.

The objective of the fieldwork was to collect data that could be used to observe the geochemical change in the tailings dam over the past 60 - 70 years. Tailings, water, and some efflorescence samples were collected for further testing in the laboratory.

Field measurements were performed on drilled-out tailings samples, and in-situ oxygen measurements were routinely performed; the results are described elsewhere (Section 4.2. and 4.3).

3.2 Site Background

The tailings dam investigated is situated in Springs in the East Rand Goldfield of South Africa (see Figure 2 for a layout of the Witwatersrand goldfields). A Google Earth image of the dam is depicted in Figure 18 below. The tailings dam is currently being reworked by DRD Gold and is referred to as 5L27; it is the same Site A that was investigated by Yibas et al. (2010) discussed in Section 2.8. The tailings dam was completed about 60 - 70 years ago, in the 1950s to early 1960s. The dam is relatively small (125 ha) and has tailings from the processing of one of the Central Rand Group reefs. At the time of construction, only the cyanide method was used for gold processing in South Africa, as discussed in Section 2.4.

The tailings dam was constructed using the upstream paddock system historically used almost exclusively in South Africa with its prevailing semi-arid climate (McPhail & Wagner, 1987). With the paddock system, a tailings dam is slowly built up (2.5 m/yr), with tailings typically deposited in layers of 0.15 m (McPhail & Wagner, 1987), as discussed in Section 2.5. The horizontal layering is visually evident in parts of the Oxic Zone that have now become visible due to the reworking, as discussed further below.

Figure 8: Google image (June 2015) of tailings dam 5L27 and location of oxygen monitoring hole constructed as part of this study. Reclamation of the dam by DRD Gold started in the second half of 2016.

3.3 Site Characterisation

The fieldwork was performed over several months in different phases, as summarized below:

- In July 2015, the Council of Geoscience drilled a 10 m deep hole using a reverse circulation drill rig. The tailings sample recovery from the drilling was poor, and sampling could not be performed at regular intervals. A water sample was bailed from this borehole at 8 - 9 m deep before the hole collapsed. Water quality results are presented in Section 4.8.
- A 6 m deep hole was drilled using a hand auger next to the reverse circulation rig hole by the author for the research reported in this study. This auger hole allowed tailings samples to be collected at roughly 15 cm intervals.
- Air collection chambers were installed at depths of 0.5 m, 1 m, 1.5 m, 2 m, 2.5 m, 3 m, 4 m, 5 m, and 6 m below the tailings surface. The oxygen was measured 11 times over 22 months (July 2015 – April 2017). In-situ measurements of the oxygen are presented in Section 4.2. Whole-rock geochemical analyses, acid-base testing, and Scanning Electron Microscopy were performed on tailings samples from this hole; these results are presented in Sections 4.4 - 4.7.
- In August 2015, another hole (3.4 m in depth) was hand-augered by the author next to the oxygen monitoring hole to perform the in-field collection of paste pH, Electrical Conductivity (EC), and Oxidation-Reduction Potential (ORP). The procedure, as well as the results, are discussed in Section 4.3.
- Water samples from surface drains (water collected as part of the reclamation process) and toe seepage in drains were also collected in April 2017. Water quality results are presented in Section 4.8.

3.4 Field Observations

During the fieldwork performed in 2015 - 2017, field observations were logged, and photos were collected.

The tailings dam is 10 - 22 m high (Nengovhela et al., 2006) and is currently partly reworked by DRD Gold. In Figure 9, a newly exposed part of the tailings dam is depicted, which has a distinct oxidised zone in the first 2 - 3 meters underlain by tailings that visually appear to be unoxidised.

Paddocks on the upper surface of the tailings dam are overgrown with vegetation with poor surface water drainage (see Figure 10). After rainfall events, considerable water pooling occurs at the top of the dam. This pooling may contribute to the deep infiltration of water into the dam.

Iron-oxyhydroxide enriched laminae observed at the bottom of the lamination/bedding are shown in Figure 11 and Figure 12. During operation, the heavier minerals were fractionated to the bottom of each newly deposited slurry layer.

The deposition layers are also observable deeper in the tailings dam; however, the laminae of ferric-oxyhydroxides are not observed because of the more (iron) reducing conditions present in the Anoxic Zone. In Figure 13, a tailings sample from the Transition Zone is shown with blue-green and orange precipitates (likely to be hydrated ferrous and ferric minerals, respectively). The blue-green precipitates are typically ferrous sulphate (e.g. like melanterite $FeSO_4 \cdot 7H_2O$), with the orange precipitates typically ferric hydroxides or sulphates (e.g. ferrihydrite $Fe(OH)_3$ or schwertmannite $Fe_8O_8(OH)_{4.8}(SO_4)_{1.6}$). The presence of these minerals indicates that conditions in the Transition Zone are close to the Fe(II)/Fe(III) boundary.

Secondary minerals that precipitate from a surface drain next to the dam is shown in Figure 14 and Figure 15. The sample was taken in April 2017 when excess water was present in the surface drains originating from the dam reclamation. The precipitation of secondary minerals in the drain was promoted by exposure of the drainage to oxygen and evaporation. XRD analyses show that white precipitates are mostly hydrated, magnesium-, sodium/aluminium-ammonium/aluminium-, and calcium sulphates, with yellow precipitates hydrated ferric sulphates. The presence of natro-jarosite indicates that seepage from the dam is acidic. The XRD results are discussed in more detail in Section 4.6.3.

Figure 9: A newly exposed part of the tailings dam showing a distinct oxidised zone in the first 2-3 meters (October 2016).

Figure 10: The surface of the tailings dam with overgrown paddocks and minimal water drainage (July 2015).

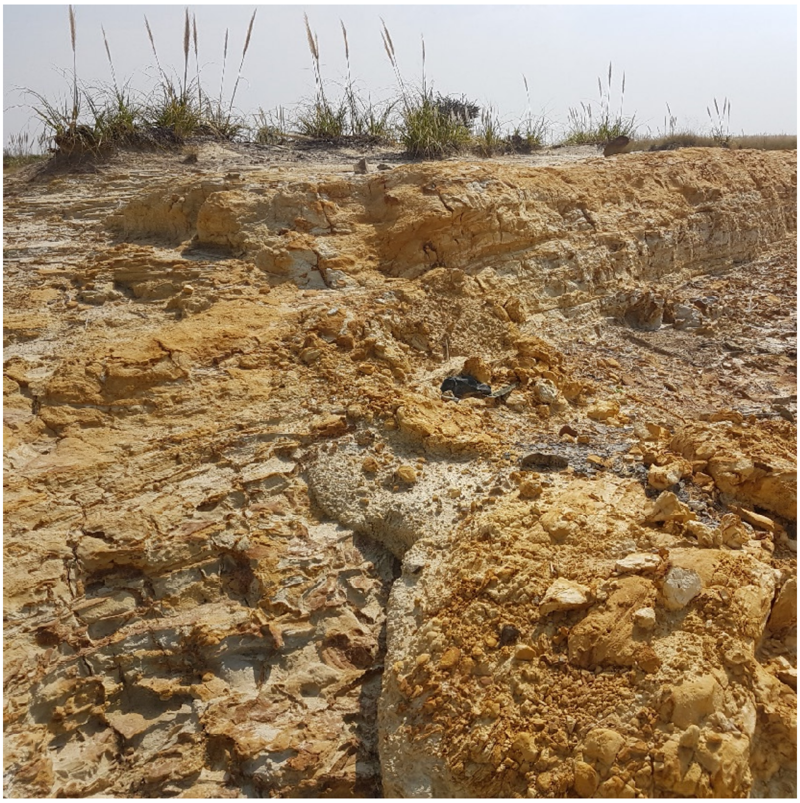

Figure 11: Exposed top 2 m of tailings dam showing parallel lamination/bedding (July 2015).

Figure 12: Exposed top 2 m of tailings dam showing parallel lamination/bedding as well as heavy mineral fractionation that resulted in iron-oxyhydroxide enriched laminae (July 2015).

Figure 13: A tailings sample from the Transition Zone showing green and yellow precipitates of hydrated Fe(II)- and Fe(III)-minerals, respectively (August 2015).

Figure 14: Secondary mineral precipitates from toe seepage. The photo was taken at the northeastern corner of the tailings dam (April 2017).

Figure 15: Secondary mineral precipitates from toe seepage. The photo was taken at the location above.

4 GEOCHEMICAL CHARACTERISATION OF THE TAILINGS

4.1 Introduction

Geochemical characterisation of the tailings forms the starting point for conceptualising its geochemical evolution. Selected geochemical data will also be used as input for the geochemical model in Section 7. The following characteristics of the tailings were investigated through field and laboratory testing:

- In-situ oxygen gas measurements
- Field pH, EC and ORP measurements
- Whole-rock elemental composition
- Mineralogy through X-ray diffraction
- Scanning Electron Microscopy
- Water quality

4.2 In-situ Oxygen Gas Measurements

4.2.1 Introduction

The oxygen concentration was measured to correlate the oxygen ingress with the other measured geochemical parameters and for later use in the geochemical model. Direct measurement of oxygen in the tailings would also indicate the depth range of the Oxic, Transition and Anoxic Zones.

Oxygen is expected to occur in the top few meters of the tailings dam, analogous to the observed depth of oxidation (e.g., see Figure 9). The oxygen should decrease from a P_{O2} of about 0.2 at the surface to close to zero over this extent. The oxygen is expected to vary slightly over dry and wet seasons due to differences in the soil moisture content at the top of the tailings dam.

4.2.2 Instruments and methods

Air chambers were installed within the top 6 m of the tailings profile from which gas samples could be retrieved. A schematic diagram of the installed air chambers for the measurement of oxygen at the top of the tailings dam is depicted in Figure 16 below. The following methodology was followed for the installation:

A 6 m hole was hand-augered through the oxidised (yellowish) and into the unoxidized (greyish) tailings. Each air chamber comprises a perforated 7 cm high plastic container wrapped in a geotextile that is then connected with an 8 mm silicon pipe. Air collection chambers were installed at 0.5 m, 1 m, 1.5 m, 2 m, 2.5 m, 3 m, 4 m, 5 m, and 6 m.

The air chambers were individually installed from the bottom-up by first lowering the lowest (6 m) chamber to the appropriate depth, backfilling it with tailings around the chamber (lowering and lightly pressing the loose tailings down with a PVC pipe) and about 2 cm above it. A measuring tape was used to measure the progress of the backfilling. A layer of bentonite pellets was then placed to block the vertical preferential flow of air and water in the backfilled hole.

The hole was further backfilled with tailings, another bentonite seal was installed, and the procedure above was repeated. The distance between the seal above and below the chambers was about 10 cm.

A C-16 PortaSens II Gas Detector, depicted in Figure 17, was used for gas monitoring. The gas sensor was within its 1-year laboratory calibration and had a measurement resolution of 0.1%. The oxygen measurement was performed by attaching the “Sensing Wand” to the 8 mm silicon pipe connected to each air chamber. Air was then pumped for about 1 - 2 min until a steady reading was obtained. The oxygen was measured 11 times over 22 months (July 2015 – April 2017).

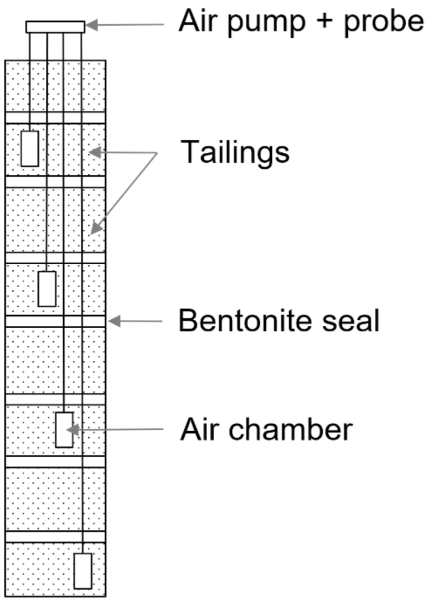

Figure 16: Schematic diagram of the installed air chambers for measuring oxygen at the top of the tailings dam (air chambers were installed at depths of 0.5 m, 1 m, 1.5 m, 2 m, 3 m, 4 m, 5 m, 6 m).

Figure 17: C-16 PortaSens II Gas Detector equipped with an internal pump used to take oxygen gas measurements.

4.2.3 Results

The results from in-situ oxygen gas measurements are depicted in Figure 18 below. Based on the oxygen abundance, the top of the tailings dam was subdivided into three geochemical environments: 1) the Oxic Zone (0-2 m), 2) the Transition Zone (2-4 m), and 3) Anoxic Zone (>4 m). The nomenclature of Oxic/Anoxic (instead of Oxidised/Reduced as used by Yibas et al., 2010) was used to reference the presence or absence of oxygen (similar to that used by USGS for groundwater described in Section 2.2.2).

The criteria used for the spatial division were based on the presence or absence of oxygen. In the Oxic Zone, oxygen was present throughout the year. In the Transition Zone, oxygen was only present during the drier months, with the zone also showing a distinct decrease in oxygen concentration relative to the overlying Oxic Zone. In the Anoxic Zone, oxygen was absent except just after drilling.

The volumetric water content was measured from the samples collected during drilling in the laboratory. The bounds of the Anoxic Zone correlate with the maximum volumetric water volume. Drilled-out samples from the Anoxic Zone were also water-saturated.

The oxygen measurements are comparable to previous oxygen measurements in Witwatersrand tailings dams performed by Yibas et al. (2010). However, a significant controlling factor on the oxygen infiltration is the extent of water-saturated conditions that are still present in the 60 - 70-year-old dam.

The geometric mean of the measured oxygen concentration per interval as a percentage of atmospheric oxygen is given in Table 7 below. In Figure 19, the oxygen concentration in the top 2 meters of the tailings dam is presented against the average maximum temperature of the previous 30 days. The data shows that the oxygen penetrates slightly deeper during the winter months than in the summer months. This could be attributed to higher rainfall in the summer than in winter.

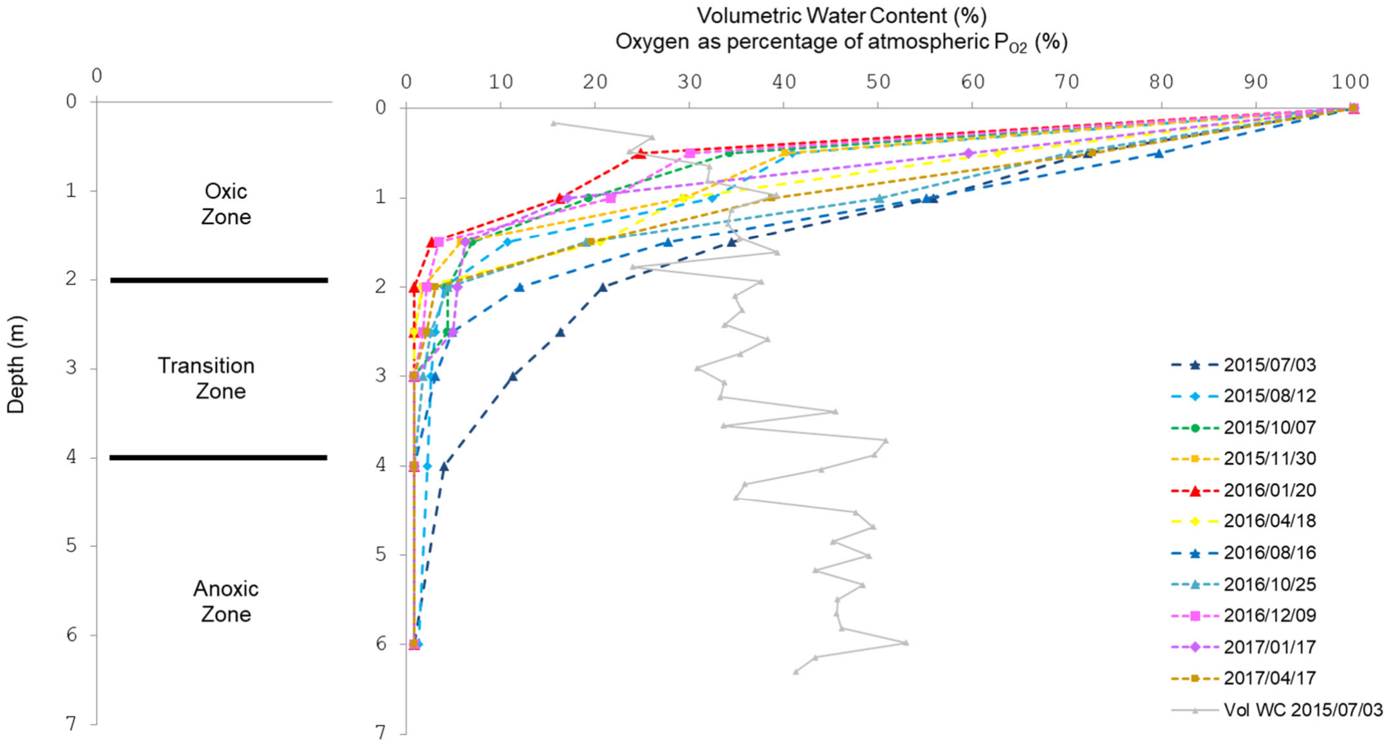

Figure 18: Measured oxygen concentration (as a percentage of atmospheric oxygen) at the top 6 m of the tailings dam. Also shown is the volumetric water content of tailings samples.

Table 7: Geometric mean of the measured oxygen concentration per interval as a percentage of atmospheric oxygen.

Date	Time Elapsed (days)	Oxic Zone		Transition Zone		Anoxic Zone	Avg Max Temperature (°C)*
		0 - 1 m	1 - 2 m	2 - 3 m	3 - 4 m	4 - 6 m	
3/07/2015	0.00	73.6	33.8	15.3	6.3	1.3	17.7
12/08/2015	40.00	50.6	10.6	2.8	2.0	1.3	23.0
7/10/2015	96.00	40.1	7.9	1.9	<1	<1	28.4
30/11/2015	150.00	48.7	5.9	<1	<1	<1	27.3
20/01/2016	201.00	33.8	2.5	<1	<1	<1	27.0
18/04/2016	290.00	56.5	9.2	<1	<1	<1	24.3
16/08/2016	410.00	75.7	25.9	5.2	1.1	<1	21.2

Date	**Time Elapsed (days)**	**Oxic Zone**		**Transition Zone**		**Anoxic Zone**	**Avg Max Temperature (°C)***
		0 - 1 m	**1 - 2 m**	**2 - 3 m**	**3 - 4 m**	**4 - 6 m**	
25/10/2016	480.00	70.3	15.5	2.3	<1	<1	26.5
9/12/2016	525.00	39.8	4.9	1.0	<1	<1	26.1
17/01/2017	564.00	46.2	7.9	2.1	<1	<1	24.9
17/04/2017	654.00	65.2	12.5	1.3	<1	<1	22.3

* Average maximum ambient temperature of the previous 30 days for Jan Smuts Weather Station (SA Weather, personal communication, 2021)

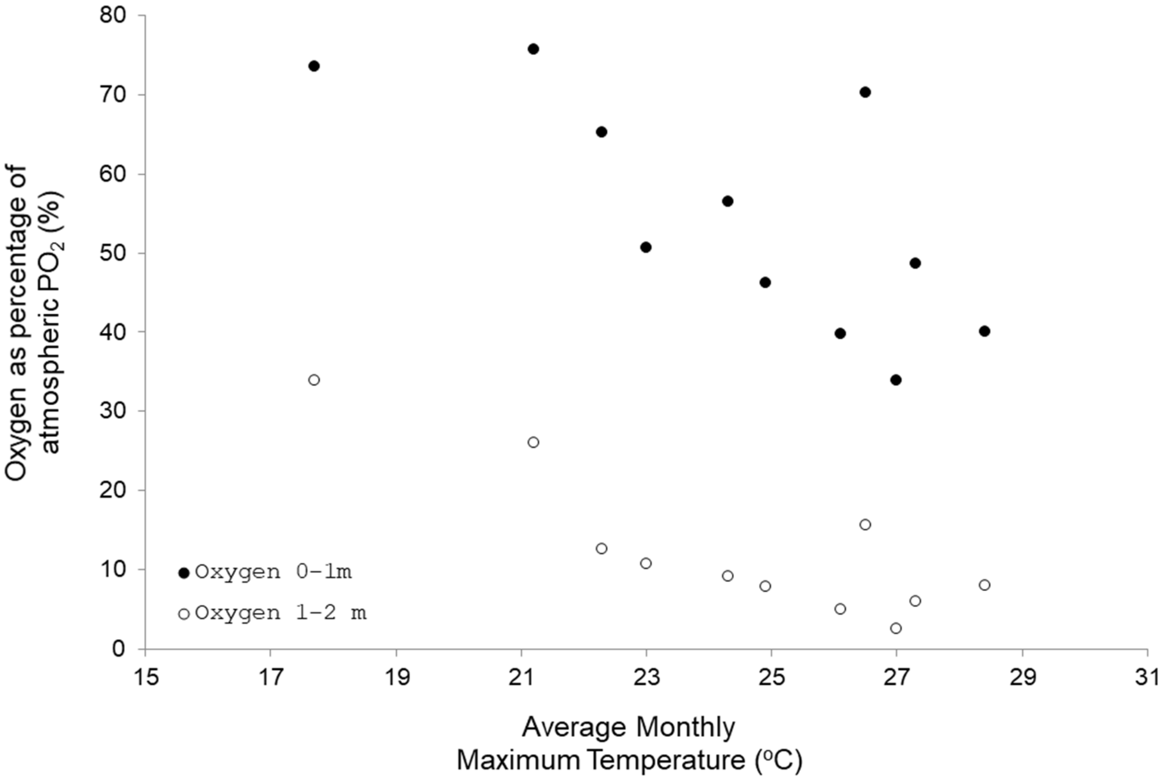

Figure 19: Oxygen concentration in the top 2 meters of the tailings dam against the average maximum temperature of the previous 30 days.

4.3 Field paste pH, EC and ORP measurements

4.3.1 Introduction

Field measurements of pH, Electrical Conductivity (EC) and Oxidation-reduction Potential (ORP) were performed on drilled-out samples from a hand auger hole drilled next to the oxygen monitoring hole. In the field, drilled-out unoxidized tailings often show a discolouring from grey to rust-brown when exposed to the atmosphere due to the oxidation of ferrous iron compounds. Field measurements, especially ORP measurements, need to be performed in the field before oxidation (of ferrous to ferric iron) of the drilled-out samples can occur.

4.3.2 Instruments and methods

Measurements were completed using the Forston LabNavigator 2 multi-parameter meter. A photo of field measurement on the tailings dam is shown in Figure 20 below.

The field measurements were performed by inserting the probe into a wet tailings sample. About 10 ml of distilled water was added to the tailings sample in a 100 ml container to ensure that it was wet enough to have good contact between the probe and the sample. The calibration of the probes used for the pH, EC and ORP measurements is discussed below.

The pH sensor is an Ag/AgCl single-junction electrode and is stored in a pH-4 buffer/KCl storage solution. 2-point calibration has been performed at pH 4 and 7, respectively. After each measurement, the probe was rinsed in distilled water. According to the manufacturer, the accuracy of measurements is 0.1 pH units within a pH 0-14 range, and the probe has a resolution of 0.005 pH units.

The EC probe is automatically temperature compensated between temperatures of 5 and 35°C. The temperature of the solution is read by a thermistor that extends into the space between the graphite electrodes. 2-point calibration has been performed at 0 uS/cm and 12 880 uS/cm, respectively. After each measurement, the probe was rinsed in distilled water. According to the manufacturer, the accuracy is 1%, with the probe having a resolution of 10 uS/cm in the high-range mode.

The ORP electrode is a combination-style electrode comprised of a pure platinum metal measuring half-cell and a reference half-cell (sealed gel-filled Ag/AgCl) to which the platinum half-cell is referenced. The Forston Labs ORP can measure redox potential in the range of –450 to +1100 mV. A two-point calibration has been performed at 100 mV and 300 mV. After each measurement, the probe was rinsed in distilled water. The ORP measurements were converted to Eh using the conversion table in USEPA (2017).

Figure 20: In-field pH and ORP measurements.

4.3.3 Results

The field pH, EC and Eh results are depicted in Figure 21 below. The laboratory paste pH is also shown for comparison. From the results, the following observations could be made:

- The field paste pH ranges between pH 3.5 – 4 in the Oxic and Transition Zone and is only slightly higher at 4 – 4.2 in the Anoxic Zone. This corresponds with the laboratory-measured paste pH depicted in Figure 21. This also corresponds with the pH of 3 and 4 reported by Nengovhela et al. (2009), measured at 4 m, 6 m, 9 m, and 10 m) for the same tailings dam. The lower pH in the Oxic Zone could be attributed to the oxidation of pyrite and the absence of neutralisation minerals. The low pH in the Anoxic Zone may indicate that the tailings became acidic because of, 1), transport of acidic water from the Oxic Zone, or, 2), it became acidic just after deposition, which was also observed at an operational tailings dam in the East Rand by Fourie (2018) in Section 2.9.
- The Eh ranges between 600 – 675 mV, averaging at ~650 mV, in the Oxic Zone and between 430 – 520 mV, averaging at ~475 mV, in the underlying Transition Zone. This also corresponds with the ORP reported by Nengovhela et al. (2009), which, when converted to Eh, ranges between ~440 – 475 mV (for the 4 m, 6 m, 9 m and 10 m depths) for the same tailings dam.
- The pH and Eh of the samples from the Oxic and Transition Zones are plotted on two Fe-S-H_2O Eh-pH stability diagrams at relatively lower and higher iron activities in Figure 32 and Figure 33 in the Conceptual Model in Section 5.3.2. The stability fields are indicative of specific iron and sulphate activities. The samples of the Oxic Zone fall on the boundary of two ferric sulphate minerals and aqueous ferrous sulphate, and the position more closely corresponds with the lower dissolved iron (Activity = $10^{-4.2}$) activity diagram (Figure 32). The samples of the Transition Zone fall on the boundary of schwertmannite and aqueous ferrous sulphate (Figure 32).

- The EC is the lowest (<5 mS/cm) at the top (0-25 cm), where the tailings are leached by infiltrating water. The EC reaches a maximum of ~35 mS/cm at 0.5 m in the Oxic Zone, whereafter, it decreases close to 13 mS/cm. It gradually increases in the Transition Zone, where it reaches a maximum of ~28 mS/cm before decreasing towards the bottom of the Transition Zone to ~13 mS/cm. The spike of the EC in the Transition Zone is most likely related to the spike of sulphate, also observed as discussed in the section below.

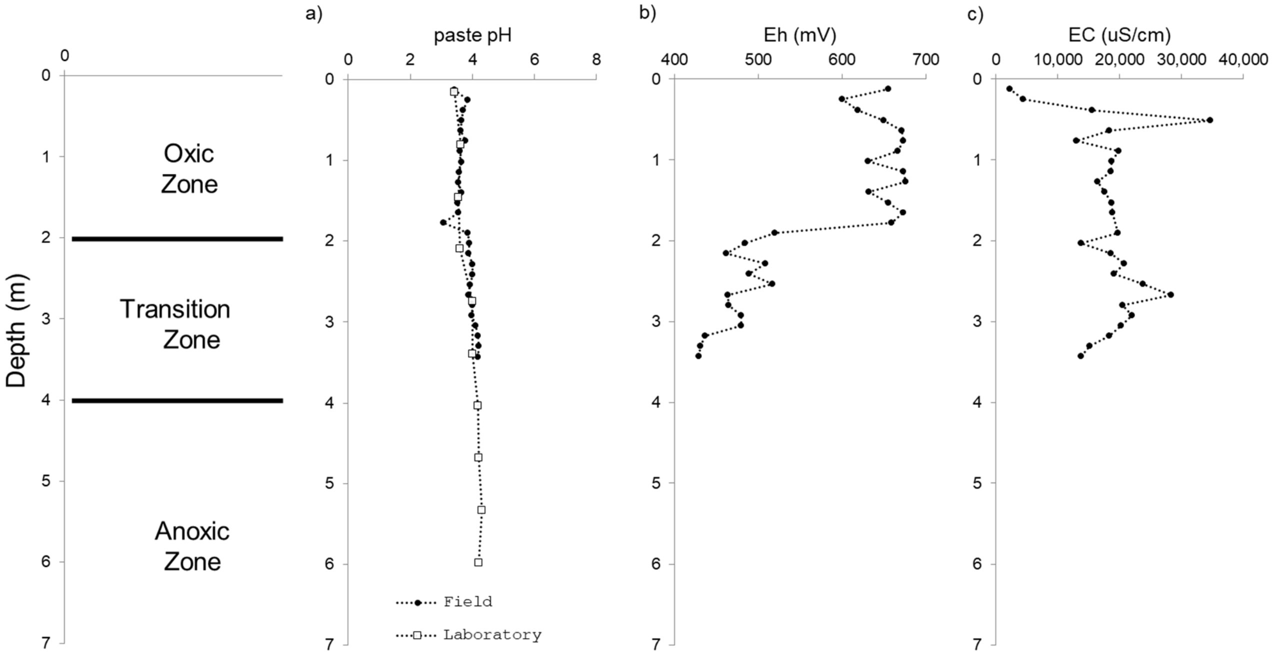

Figure 21: Paste pH, Eh, and EC field measurements of tailings. The laboratory paste pH is also shown for comparison. The ORP measurement has been converted to Eh.

4.4 Whole Rock Elemental Composition

4.4.1 Introduction

An Eltra elemental analyser and X-ray Fluorescence (XRF) were used to determine the elemental composition of the tailings. The objective was to identify any fractionation of the elements between the Oxic vs Anoxic Zones in the 60 -70-year-old tailings dam.

4.4.2 Instruments and methods

The Total %S was determined at 15 cm intervals after heating the sample together with fluxes at ±2 200°C in an Eltra Furnace. The resulting SO_2 was measured using an infrared (IR) detector. These high temperatures and fluxes are required to combust both sulphides and hexavalent (-6) sulphate. The latter is in an already oxidized state and very stable, e.g. $BaSO_4$, $CaSO_4.2H_2O$, Al-Fe-sulphates. The %S of the samples were also determined at 1 000°C in the same furnace but without the use of fluxes, which, according to the instrument manual, comprises the more easily combustible Sulphide %S.

Samples collected at 30 cm intervals were submitted for total element analyses using XRF. Samples were analysed using pressed powder pellets. XRF is the fluorescent X-rays from a material that has been excited with high-energy X-rays. Analyses were performed with a Rigaku Supermini 200 with SC and F-PC detectors and fixed receiving slits with Zr of Al filtered Pd-K radiation. The elements were identified using ZSX software.

Loss of ignition (LOI) was determined by measuring the weight loss of samples after heating to 750ºC overnight to remove water, organic matter and carbonates. After heating, the firebrick holding crucibles is allowed to cool completely in the oven or furnace before weighing.

4.4.3 Results

The average Elemental Composition and measured radiation in the Oxic, Transition and Anoxic Zones are summarized in Table 8 below.

Sulphur speciation over depth is depicted in Figure 22 below. The Total S% includes the total sulphur from sulphur-bearing minerals, whereas the sulphide S% presents the total sulphur from sulphide minerals, including pyrite. The sulphate %S presents the sulphur from all sulphate-bearing minerals, including the more difficult heat decomposable sulphates like jarosite. The sulphur speciation shows a good correlation with the depth of oxygen ingress discussed in Section

4.2. The sulphide sulphur is significantly lowered in the first two meters, where oxygen ingress occurs throughout the year, and the sulphide minerals have been converted through oxidation reactions. The sulphate and sulphide sulphur are slightly elevated in the Transition Zone at 2 – 4 m, where oxygen is only present during drier months (which is a result of sulphate mineral precipitation as indicated by the modelling in Section 7.6.4).

The radiation and uranium abundance at the top of the tailings dam is depicted in Figure 23. The radiation measurements are only semi-quantitatively performed using a scintillation counter. Uranium abundance in the tailings is lower in both the Oxic and Transition Zone, indicating the uranium's high mobility under acidic, oxidising conditions. The uranium abundance is higher at the top of the Anoxic Zone due to secondary uranium precipitation, as shown in the model in Section 7.6.6.

Selected major oxide abundance, namely SiO_2, Al_2O_3, Fe_2O_3, CaO, K_2O, MgO and Na_2O, are depicted in Figure 24. The major oxides do not show detectable enrichment or depletion throughout the profile. Although some are typically more resistant to weathering (e.g. SiO_2, Al_2O_3, Fe_2O_3 that can be present in resistant minerals like quartz, gibbsite, hematite etc., as discussed by Perkins, 2021), the Oxic Zone is probably not weathered enough (not “mature” enough) for the more resistant oxides to get enriched. The trace element abundance, including As, Cu, Cr, Mn, Ni, Pb, and Zn, is depicted in Figure 25. More mobile trace elements like Cu, Ni, and Zn show lower abundance in the Oxic Zone, whereas the less mobile elements like Cr, Pb and Th show no relative decrease in the Oxic Zone. Arsenic shows a minimal decrease in the Oxic Zone as it can form relatively stable secondary minerals in their higher oxidation state.

Table 8: Average Elemental Composition and Measured Radiation of the Oxic, Transition and Anoxic Zones.

Parameter	**Oxic Zone**	**Transition Zone**	**Anoxic Zone**
XRF Major Oxides (wt%)			
SiO_2	78.3	78.5	77.4
Al_2O_3	11.5	11.9	11.9
Fe_2O_3	3.61	3.16	3.69
CaO	0.196	0.183	0.172
MgO	0.902	0.796	0.851
K_2O	2.06	2.25	2.35
Na_2O	0.123	0.153	0.161
TiO_2	0.440	0.463	0.451
XRF Trace Elements (ppm)			
As	245	353	364
Co	<2	19.3	40.0
Cu	18.5	62.8	64.5
Ni	48.0	236	338
Pb	98.8	113	114
Th	48.0	48.8	47.9
U	4.67	34.0	116
Zn	57.8	110	150
Cr	503	472	473
Mn	115	79.8	116
Elemental Analyser (%)			
Sulphide S%	0.067	0.865	0.842
Sulphate S%	0.132	0.256	0.203
Total S%	0.20	1.12	1.04
Scintillation Counter (uR/hr)			
Radiation	32.9	36.6	63.3

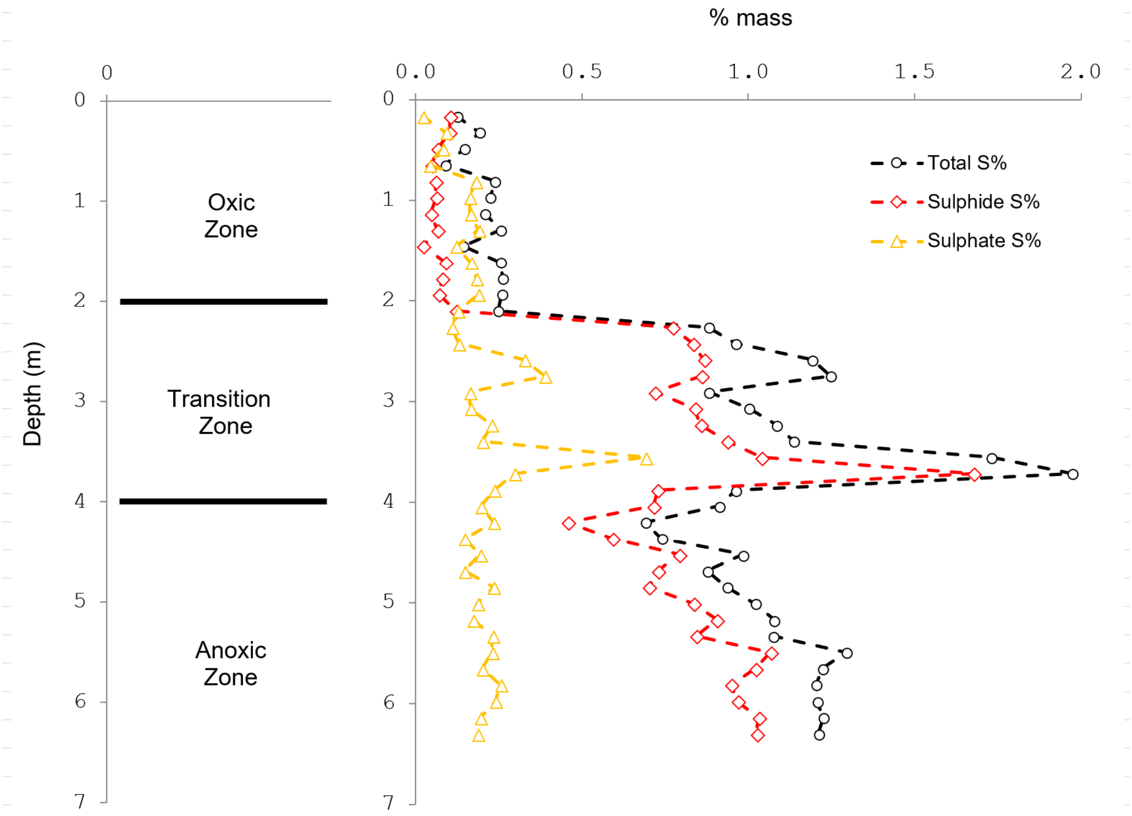

Figure 22: Sulphur speciation in tailings at 15 cm intervals.

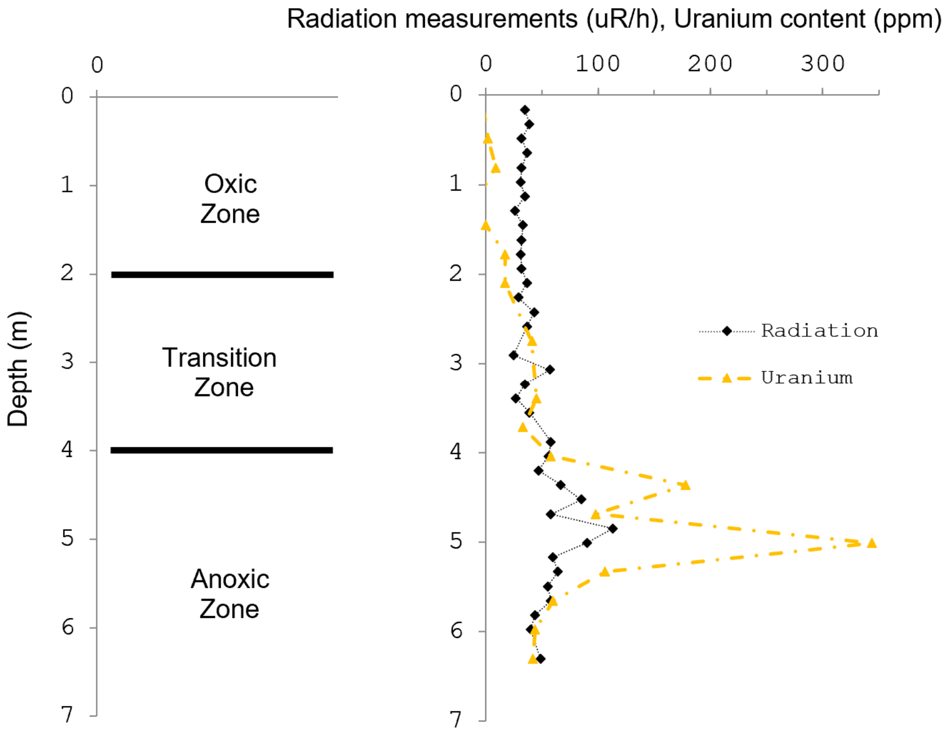

Figure 23: Radiation and uranium content of tailings at 15 cm and 30 cm intervals, respectively. The background radiation is at about 20-30 uR/h.

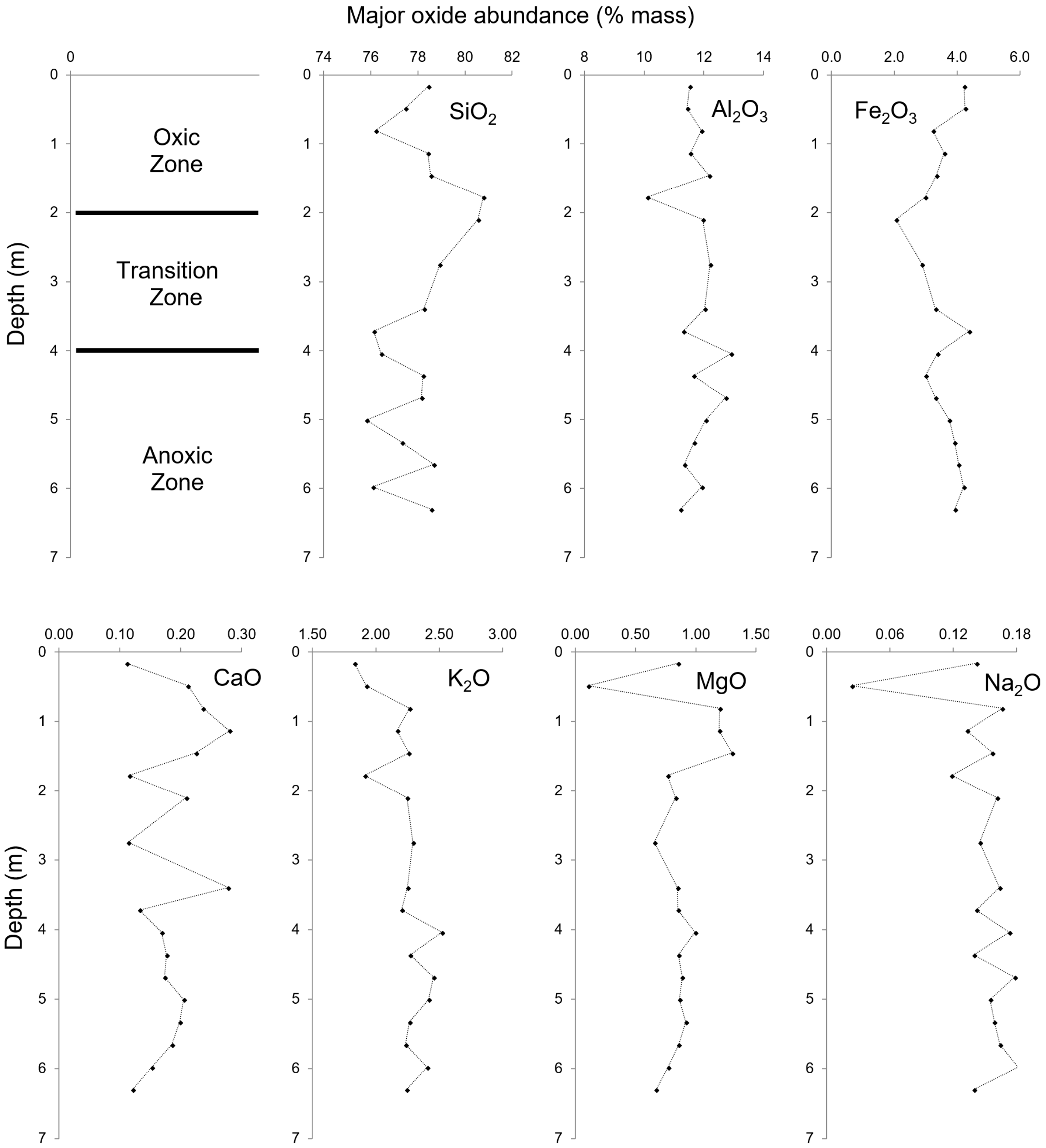

Figure 24: Major oxide abundance of tailings at 30 cm intervals.

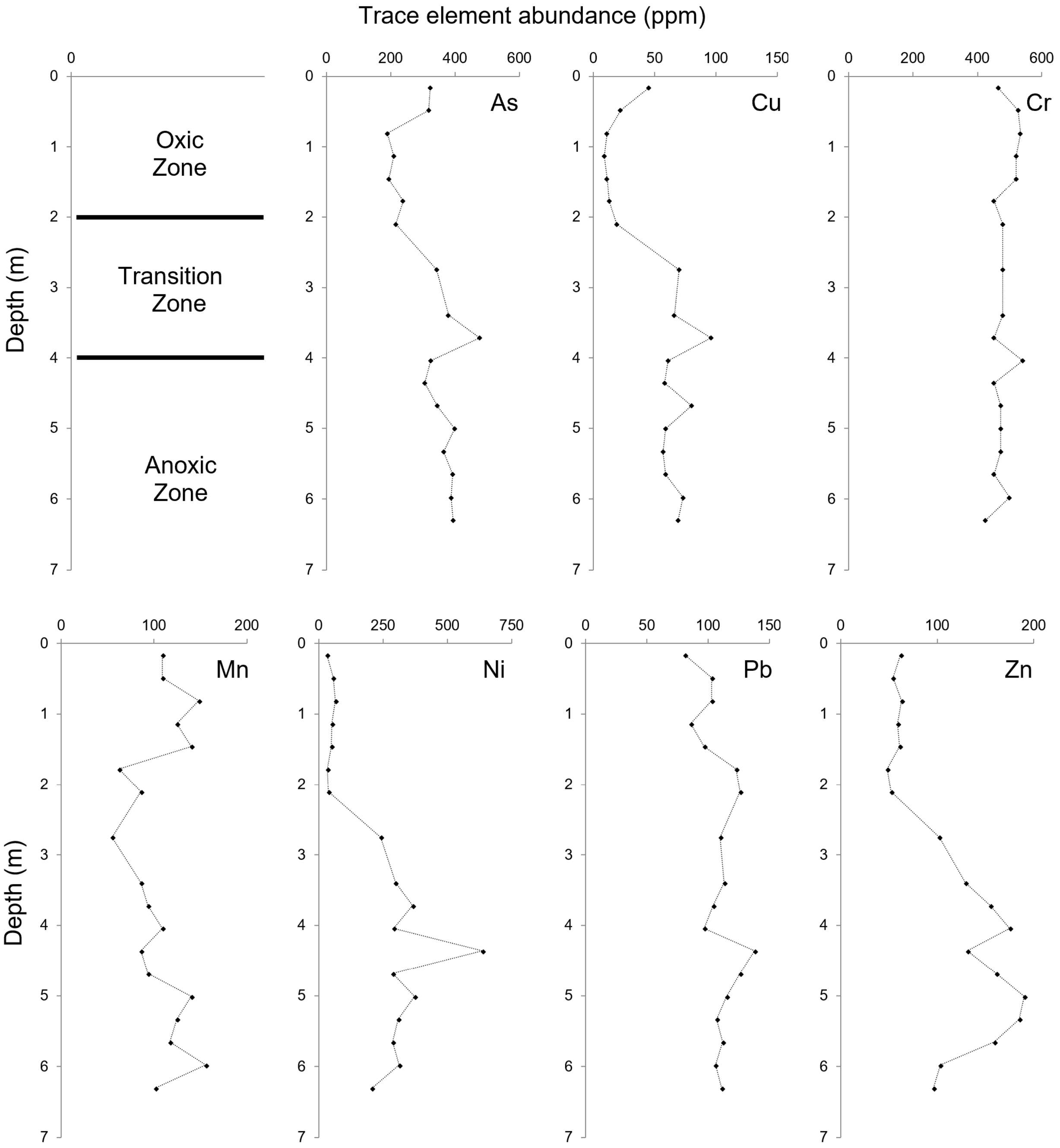

Figure 25: Trace element abundance of tailings at every 30 cm.

4.5 Acid-base Testing

4.5.1 Introduction

The acid generation potential of rock is usually related to its sulphide, specifically its pyrite content. However, the tailings samples are already acidic, and no carbonate minerals are present in the tailings that would potentially neutralise the acid to a circumneutral pH. The NAG (Net-acid Generation) test directly measures the balance between the acid-producing and the acid-consuming components in mine waste material upon oxidation with peroxide.

4.5.2 Instruments and methods

The paste pH was performed by measuring the pH in tailings and water paste. The paste is prepared by adding 10 ml of distilled water to 10 g of tailings sample. The probe used was discussed in Section 4.3.2 above.

The Maximum Potential Acidity (MPA) is the maximum theoretical acid that the oxidation of pyrite could produce and is calculated as MPA = wt% Sulfur (S) multiplied by 30.6, which is based on the stoichiometric conversion factor for wt% S to kg H_2SO_4/tonne, where all S is assumed to be pyrite. The sulphur analyses are discussed in Section 4.4. The Acid Neutralisation Capacity (ANC) represents the mass of sulfuric acid, which acid-consuming minerals can neutralize. The ANC is determined by treating a sample with a known excess of standardized acid, whereafter, it is back titrated to pH 7 with standardized sodium hydroxide to determine the amount of unconsumed acid. The Net Acid Production Potential (NAPP) is the MPA minus the ANC. The tailings samples were already acidic and had no capacity to produce any neutralisation. The NAPP was, therefore, equal to the MPA.

The NAG test directly assesses the potential for a material to produce acid after oxidation of the sulphides (using peroxide). The test involves adding 25 ml of 15% H_2O_2 (the pH of the H_2O_2 stock were corrected to pH 4.5 beforehand) to 0.25 g of sample in a 250 ml flask. The sample is placed in a fume hood and a well-ventilated area for about two hours. Once effervescing ceases, the solution is allowed to cool to room temperature, and the final pH (NAG pH) is measured. If the NAG pH is below pH 4.5, the sample is potentially acid-forming, and the solution is back titrated (with sodium hydroxide) to a pH 4.5 to determine the net amount of acid that was generated (NAG value). If the NAG Value is above 10 kg H_2SO_4/t, the sample is considered to have a high capacity to be acid-forming, and when positive but below 10 kg H_2SO_4/t, the sample has a lower capacity to be acid-forming (Miller et al., 1997).

4.5.3 Results

The paste pH and NAG pH values of the samples over depth are depicted in Figure 26 below. The paste pH ranges between pH 3.4 – 4 in the Oxic and Transition Zone and is only slightly higher at 4 – 4.3 in the Anoxic Zone. This corresponds with the field pH measurements as discussed in Section 4.3.3. The NAG pH was between pH 3 - 4 in the Oxic Zone and below pH 2.3 in the Transition and Anoxic Zone. All samples have a paste pH in the acidic range, and the tailings will potentially remain acidic as the NAG pH is below 4.5.

The MPA and the NAG Value are depicted over the depth profile in Figure 26. The MPA was calculated using the Total Sulphur (TS) as well as the Sulphide Sulphur (SS). The samples in the Oxic Zone have a lower MPA (and NAG Value) because the sulphides in the Oxic Zone are significantly oxidised. Because the samples have no neutralisation potential, the MPA should theoretically be close to the NAG Value (SS). Figure 27 depicts the MPA plotted against the NAG Value, also showing the 1:1 line between these two parameters. The MPA(SS) are much closer to the 1:1 line than MPA(TS), indicating that the maximum potential acidity of the samples is a function of the pyrite content. In the Transition Zone and Anoxic Zone, where the correlation should be the closest (because of no or limited oxidation), the MPA(TS) overestimate the NAG Value by about 28%. In contrast, the MPA(SS) overestimate the NAG Value by only 2%. This 2%

difference could be attributed to sulphides that produce no or less acidity than pyrite, and /or the acid produced during the NAG test (from the sulphide oxidation with peroxide) is sightly consumed by the matrix.

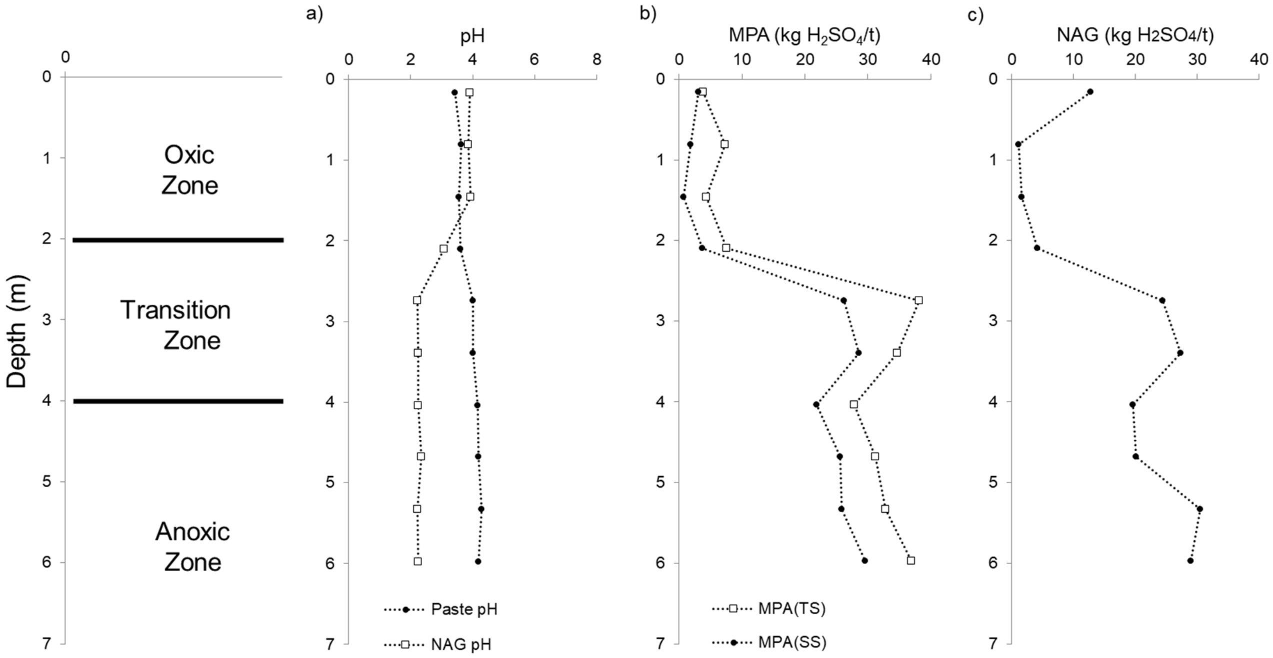

Figure 26: Laboratory paste pH, NAG pH, MPA and NAG Value of tailings.

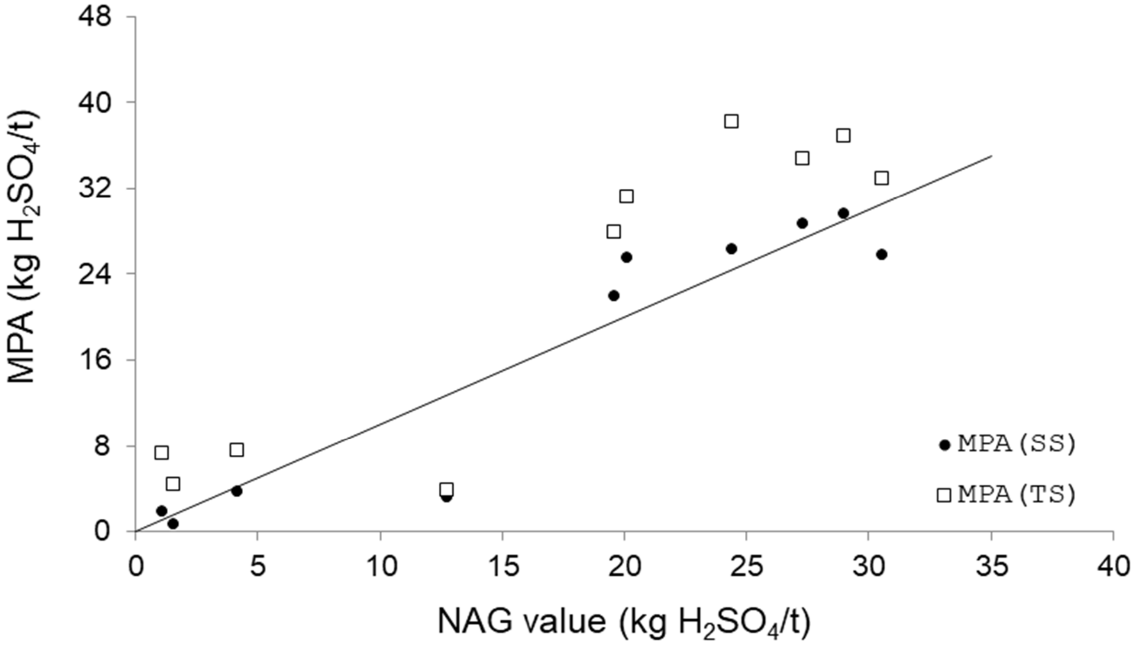

Figure 27: Maximum Potential Acidity (MPA) calculated from Sulphide Sulphur against the Net Acid Generation (NAG) Value.

4.6 X-ray Diffraction

4.6.1 Introduction

X-ray diffraction (XRD) was used to identify the major mineral phases in the tailings samples. The XRD on all samples was performed by Sabine Verryn (XRD Analytical and Consulting) except for two samples submitted for Scanning Electron Microscopy (SEM) analyses which were also tested by XRD by Mintek's Mineralogy Division.

4.6.2 Instruments and Methods

The mineral phases present were semi-quantified through means of XRD. Crystalline atoms cause diffraction of incident X-rays, with each mineral unit cell having a unique diffraction pattern. Milled samples were prepared using a back-loading preparation method.

XRD Analytical used a PANalytical Empyrean diffractometer with a PIXcel detector and fixed receiving slits with Fe-filtered Co-K radiation. The phases were identified using X'PertHighscore plus software. The weight percentages of the minerals were determined using the Rietveld method (Autoquan Program).

Mintek used a Bruker D8 diffractometer. The instrument is equipped with a Linxeye detector and variable divergence- and fixed receiving slits with Fe-filtered Co-K radiation. The phases were identified with the aid of DIFFRAC.EVA© software. For these two samples, the Rietveld method was not used.

Amorphous phases were not considered in the quantification, and trace minerals at concentrations below ±2% (JCU, 2021) are also often not detected in whole-rock samples in XRD.

4.6.3 Results

XRD testing has been performed on efflorescence sampled at the toe of the dam, on selected drilled tailings samples, and on different grain sizes of a tailings sample.

X-ray Diffraction of Efflorescence Sample

The major mineral composition of a seepage efflorescence sample (which was split into a whitish and a white-yellowish fraction) is summarised in Table 9 below. A photo of the efflorescence is shown in Figure 15 in Section 3.4. These effloresce minerals result from the evaporation of seepage drainage from the dam. A detailed evaluation of all efflorescence over the site was not performed and was only sampled once off. The drainage quality from the tailings dam was very much influenced by the reworking of the dam that was in progress when this sample was collected in April 2017.

All secondary minerals identified were hydrated sulphates. Cations include sodium, aluminium, magnesium, iron, calcium and ammonium. Potassium minerals were surprisingly not identified, but some potassium may be contained in the sodium minerals. Tamarugite, a sodium-aluminium-sulphate, is abundant, especially in the white efflorescence (61 wt% and 19 wt% in the split samples). The sodium was not elevated in the interstitial water sample analysed in this study or in water extractions of the tailings previously performed (see Table 4; Nengovhela et al., 2006). The sodium probably originates from the water used in the reprocessing of the tailings dam, which was also identified in some more recent water samples from the drains (see Section 4.8.3). Hexahydrite was the only magnesium mineral identified and was relatively abundant at about 31 – 33 wt% in the samples. Magnesium (originating from the muscovite) was fairly elevated in the interstitial water sample. Two ferric sulphates were identified in the white-yellowish efflorescence, namely natrojarosite and sideronatrite. It is, however, possible that some poorly crystalline minerals (especially iron-oxyhydroxides) that could be present under these acidic conditions were not identified by the XRD. Gypsum was the most abundant calcium mineral identified in the tailings (see XRD in Section 4.6 and SEM in Section 4.7), and some traces of gypsum were also present in the efflorescence (<5 wt%). Tschermigite is an ammonium sulphate that was identified. Ammonium was present in all water samples from the tailings dam and probably originated from the muscovite, as discussed in Section 4.8.3.

Table 9: Major mineral composition of seepage efflorescence sample (wt%)

Mineral	**Ideal Formula**	**White Efflorescence**	**White-Yellow Efflorescence**
Silicates			
Quartz	SiO_2	5.55	18.15
Pyrophyllite	$Al_2Si_4O_{10}(OH)_2$	0.16	2.83
Sulphates			
Tamarugite	$NaAl(SO_4)2.6H_2O$	60.93	18.75
Hexahydrite	$MgSO_4.6H_2O$	31.01	33.41
Sideronatrite	$Na_2Fe^{3+}(SO_4)_2(OH).3H_2O$	0	13.07
Tschermigite	$NH_4Al(SO_4)_2{\cdot}12(H_2O)$	1.4	7.22
Gypsum	$CaSO_4.2H_2O$	0.96	4.15
Natrojarosite	$NaFe^{3+}{}_3(SO_4)_2(OH)_6$	0	2.42
Total		100	100

X-ray Diffraction over Depth Profile

XRD results of tailings per depth interval (wt%) analysed by *XRD Analytical and Consulting* and *Mintek* are listed in Table 10 and Table 11 below, respectively.

Quartz was present as a dominant mineral at between 75 – 87 wt% over the profile, which corresponds to the SiO_2 in the whole rock elemental composition (see Figure 24). The CRG is mostly arenaceous with quartz-pebble conglomerate reefs, as discussed in Section 2.3.2.

Muscovite is a minor to intermediate mineral between 11 – 21 wt%. Muscovite is a metamorphic mineral formed after clays (e.g. illite and smectite), as discussed in Section 2.3.2.

Chlorite is present as a trace to a minor mineral at between 1 – 4 wt%. Chlorite is a metamorphic mineral that formed after previously formed chlorite and/or biotite as well as clays (e.g., smectite), as discussed in Section 2.3.2.

Pyrophyllite is present as a trace mineral at below 2 wt%. Pyrophyllite is a metamorphic mineral formed after previously formed chlorite and clays (e.g., kaolinite, smectite), as discussed in Section 2.3.2.

XRD is not the ideal method to detect trace minerals. Other trace minerals identified include plagioclase, pyrite, pyrrhotite, chromite, rutile and zircon. These minerals, except chromite, were also identified in the SEM analyses in Section 4.7. However, chromite and chrome spinel are common trace minerals in the Witwatersrand (e.g. Marakushev et al., 2012). Yibas et al. (2010) also identified traces of jarosite, K-feldspar and gypsum, as presented in Table 6 in Section 2.8.

Table 10: XRD results per depth interval (wt%) analysed by XRD Analytical and Consulting (OZ = Oxic Zone; TZ = Transition Zone; AZ = Anoxic Zone)

Mineral	**Ideal Formula**	**OZ** 0 – 16 cm	**OZ** 16 – 32 cm	**OZ** 65 – 81 cm	**TZ** 355 – 372 cm	**AZ** 485 – 501 cm	**AZ** 630 – 646 cm
Silicates							
Quartz	SiO_2	87.0	74.4	81.9	81.3	76.7	81.8
Muscovite	$KAl_2(Si_3Al)O_{10}(OH,F)_2$	11.0	20.7	15.6	17.0	20.5	15.6
Chlorite	$(FeMg)_2Al_2SiO_5(OH)_4$	0.780	3.63	1.66	0.610	1.77	0.95
Pyrophyllite	$Al_2Si_4O_{10}(OH)_2$	1.28	1.31	0.880	0.770	0.720	0.790
Sulphides							
Pyrite	FeS_2	0	0	0	0.32	0.24	0.82
Total		100.1	100.0	100.0	100.0	99.9	100.0

Table 11: XRD results of Scanning Electron Microscope samples (wt%) analysed by Mintek (TZ = Transition Zone; AZ = Anoxic Zone)

Mineral	**Ideal Formula**	**TZ** 275 – 291 cm	**AZ** 614 – 630 cm
Silicates			
Quartz	SiO_2	Dominant	Dominant
Mica	$KAl_2(Si_3Al)O_{10}(OH, F)_2$	Major	Major
Chlorite	$(FeMg)_2Al_2SiO_5(OH)_4$	Minor	Minor
Clay Mineral	$Al_2Si_2O_5(OH)_4$	Minor	Minor
Plagioclase	$NaAlSi_3O_8$	Trace	Trace
Zircon	$ZrSiO_4$	Trace	Trace
Sulfides			
Pyrite	FeS_2	Trace	Trace
Pyrrhotite	$Fe_{x-1}S$	N/D	Trace
Oxides			
Rutile	TiO_2	Trace	N/D
Corundum	Al_2O_3	Trace	Trace

* N/D Not Detected; Trace <5; Minor 5-15; Intermediate 15-25; Major 25-50; Predominant >50 wt%

X-ray Diffraction per Grain Size

XRD has also been performed on different grain fractions on a sample from the Anoxic Zone. This sample was also submitted for SEM analyses (Section 4.7) and batch reaction testing (Section 5).

The majority of the sample (66 wt%) falls within the 50 – 125 um size fraction, which would classify it as *unsorted fine sand with coarse silt*. Quartz, muscovite, and chlorite abundance per grain size fraction are depicted in Figure 28 below. The proportion of minerals seems to be evenly distributed between the grain fractions. However, quartz reaches its maximum proportion in the 75 – 125 um fraction, whereas the sheet silicates reach their maximum in the 50 – 63 um fraction.

Quantitative sulphur analyses (Eltra Furnace with infrared detection) per grain size fraction for this sample are presented in Section 6.2.2. As discussed in this section, almost all sulphate sulphur is associated with the sample's coarser (>180 um; medium to coarse sand) fraction. This is because gypsum was not subjected to the milling process (as the other minerals) but precipitated in the tailings dam, as observed in the SEM analyses. Sulphide sulphur is fairly distributed over grain fractions. However, the highest proportion of sulphide sulphur was present in the finest -50 um and the coarsest +425 um fractions. However, some of the pyrite in the coarse fraction could be particles on quartz or replacements in the phyllosilicates, as observed in the SEM analyses.

Table 12: Semi-quantitative mineral composition per grain size fraction of 6.14 – 6.30 m (wt%) analysed by XRD Analytical and Consulting

Grain size (um)	Weight of fraction (%)	Quartz	Musco-vite	Chlo-rite	Pyro-phyllite	Pyrite	Hema-tite	Gyp-sum	Total
+425	10.66	73.8	21.2	3.29	0.110	0.430	0.010	1.27	100.0
+355	1.14	70.3	24.6	3.49	0.280	0.380	0.110	0.790	100.0
+300	1.52	70.9	22.2	6.45	0.060	0.240	0.110	0	100.0
+250	1.96	71.7	22.5	3.8	0.080	0.420	0.150	1.29	100.0
+212	0.75	73.7	21.7	3.11	0.120	0.300	0.050	0.980	100.0
+180	1.42	74.0	21.2	3.58	0.040	0.200	0.130	0.880	100.0
+125	5.32	80.8	16.1	2.25	0.080	0.130	0.010	0.630	100.0
+75	19.79	86.2	11.3	2.20	0.040	0.050	0.120	0	100.0
+63	32.45	76.8	19.0	3.32	0.100	0.250	0.050	0.460	100.0
+50	13.82	66.0	26.8	5.61	0.350	0.420	0.130	0.650	100.0
-50	11.17	73.6	22.9	2.37	0.080	0.480	0	0.520	100.0
Weighted average	100.00	76.4	19.3	3.31	0.120	0.280	0.070	0.520	100.0

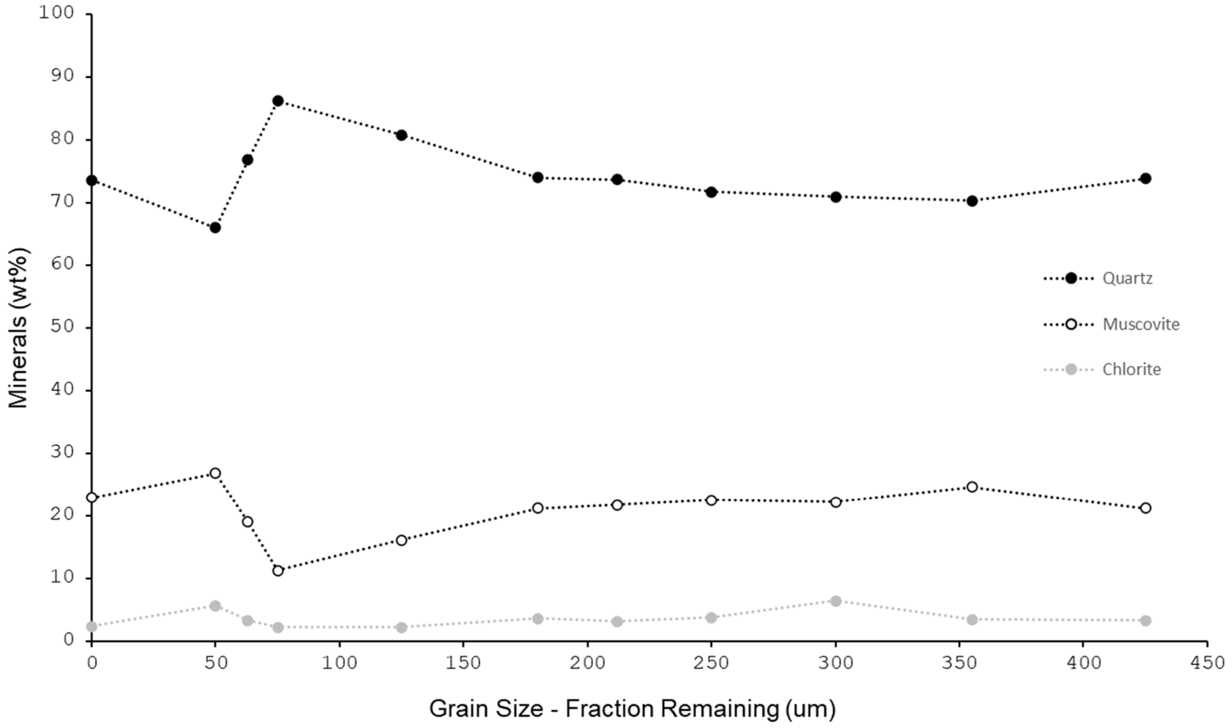

Figure 28: Quartz, muscovite and chlorite abundance per grain size fraction (the -50 um passing fraction is presented as 0 um in the graph)

4.7 Scanning Electron Microscopy

4.7.1 Introduction

Scanning Electron Microscopy (SEM) was completed to inspect the interrelation between minerals and to identify the major sulphide and secondary minerals present. SEM images and ED XRF (Energy Dispersive X-Ray Fluorescence) were generated by Mintek.

4.7.2 Instruments and methods

Mintek utilised a Zeiss Evo MA15 equipped with a Bruker Quantax EDS system. In general, the SEM uses high-energy electrons to target a sample. Detectors collect X-rays, backscattered electrons, and secondary electrons and convert them into a signal to produce the final image.

The sampled tailings were dried, placed into 2.5 cm moulds, and embedded in epoxy. After the epoxy had been set, the sample was polished with increasingly finer diamond grit to obtain a flat surface. After the final polish, the sample was cleaned ultrasonically with deionized water, and the sample surface wiped with ether. The sample was given a carbon coating of ~20 nm using a vacuum evaporator.

4.7.3 Scanning Electron Microscopy Results: Sample from 275 – 291 cm

The results for a sample from the Transition Zone from the 275 – 291 cm horizon are presented in Table 13 below. A brief description of the identified minerals is given below.

Table 13(a): Pyrite with surrounding quartz and muscovite matrix. The muscovite, especially the muscovite/chlorite intergrowth, is potentially a pseudomorph after biotite, as was also described by Smits (1990) on a CRG sample.

Table 13(b): Small remnants of detrital pyrite with a significant iridium content on quartz. Iridium di-sulphide adopts the pyrite crystal structure at high pressure (Munson, 1968) and much higher temperatures than was present in the Witwatersrand; therefore, the pyrite originates from the original source rock (i.e. detrital pyrite).

Table 13(c): Pyrite with no inclusions in fine surrounding quartz and muscovite matrix.

Table 13(d): Cobaltite (Co ~26-31 molar %) with a high lead content (~12 molar %) in fine surrounding quartz and muscovite matrix. The cobaltite also contains impurities of nickel (~7 - 11 molar %) and iron (~3-6 molar %).

Table 13(e): The image shows a dominant quartz matrix when zoomed out (300 um). The pyrrhotite and chalcopyrite are much larger than the pyrite in the sample and are individual autogenic grains.

Table 13(f): A small detrital pyrite on quartz with pentlandite inclusions. One pentlandite analysis included a significant tungsten impurity (1.8 molar %).

Table 13(g): Authigenic pentlandite in mostly quartz matrix, including pyrite on quartz.

Table 13(h): Muscovite with gersdorfite. Chlorite is also present together with TiO_2, which potentially replaced biotite.

Table 13: Scanning Electron Microscope images for tailings sampled at a depth of 275 – 291 cm.

	Borehole CC1 Sample #17 **Oxic Zone Depth 275 – 291 cm**	**Description**
a)	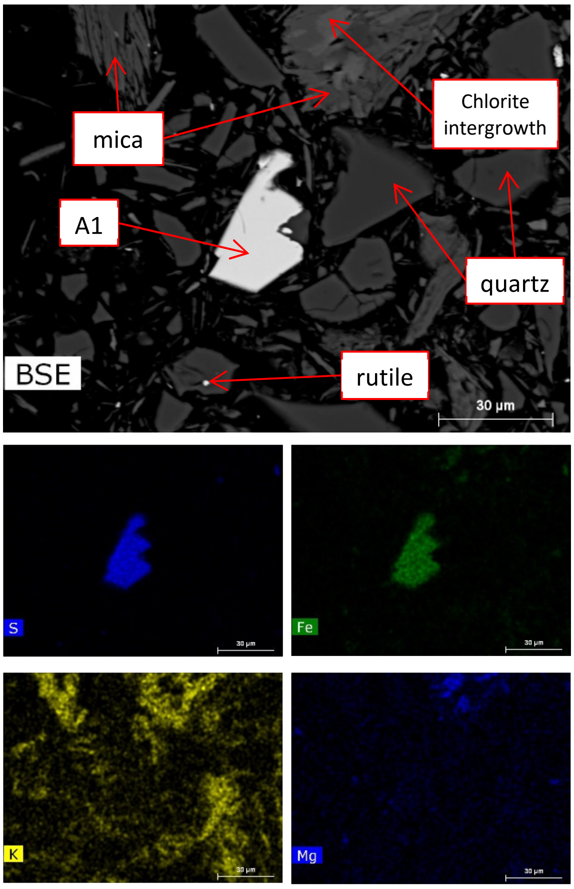	Pyrite (A1) with surrounding quartz and muscovite matrix. The pyrite has no inclusions. A1 ED XRF (wt%): sulfur = 49.5, iron = 46.6 oxygen = 3.9
b)	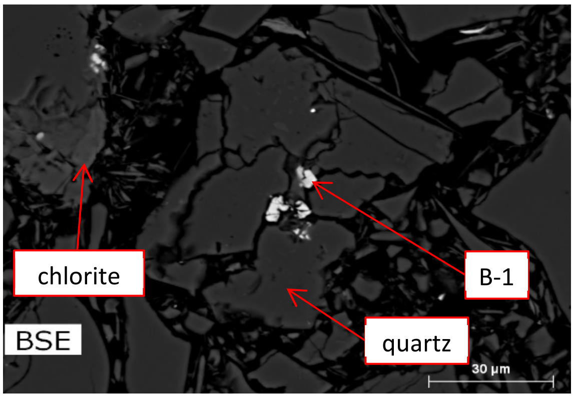	Pyrite (B1) with a significant iridium content situated on quartz. B1 ED XRF (wt%): sulfur = 43.8, iron = 38.0, iridium = 13.5, oxygen = 3.9
c)	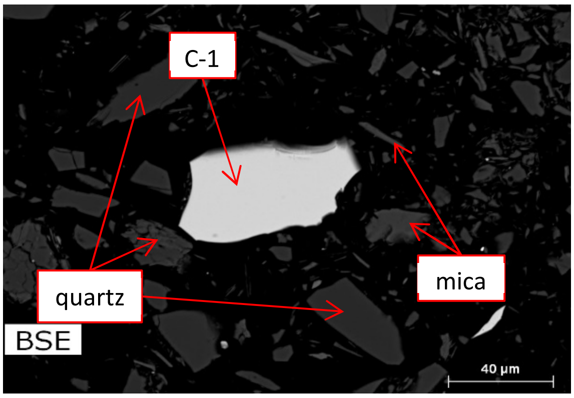	Pyrite (C1) in surrounding quartz and muscovite matrix. C1 ED XRF (wt%): sulfur = 52.7, iron = 43.7, oxygen = 2.9

	Borehole CC1 Sample #17 **Oxic Zone Depth 275 – 291 cm**	**Description**
d)	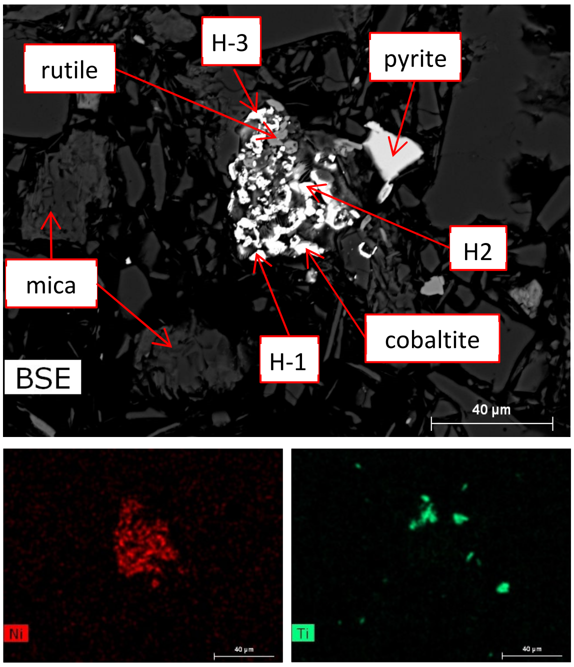	Cobaltite (H1, H2, H3) with a high lead content. H1 ED XRF (wt%): Arsenic = 23.4, cobalt = 15.0, sulfur = 10.4, nickel = 8.4, lead = 38.2, iron = 3.1, oxygen = 1.3 H2 ED XRF (wt%): Arsenic = 15.9, cobalt = 14.4, sulfur = 11.6, nickel = 10.3, lead = 40.6, iron = 5.4, oxygen = 1.8 H3 ED XRF (wt%): Arsenic = 21.3, cobalt = 17.5, sulfur = 9.7, nickel = 6.6, lead = 39.2, iron = 3.9, oxygen = 1.8
e)	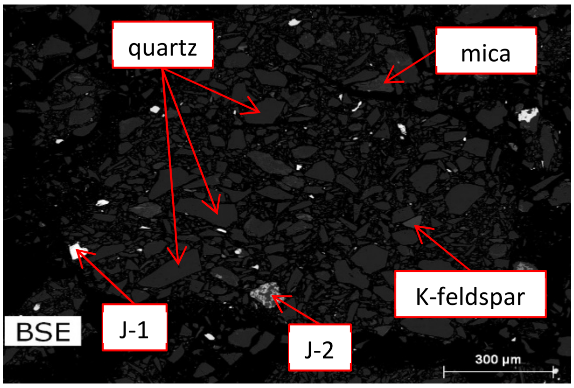	Quartz matrix with pyrite grains as well as a pyrrhotite (J-1) and a chalcopyrite grain (J-2). J1 ED XRF (wt%): sulfur = 37.1, iron = 59.7, oxygen = 3.3 J2 ED XRF (wt%): sulfur = 32.2, iron = 31.4, copper = 34.5, oxygen = 2
f)	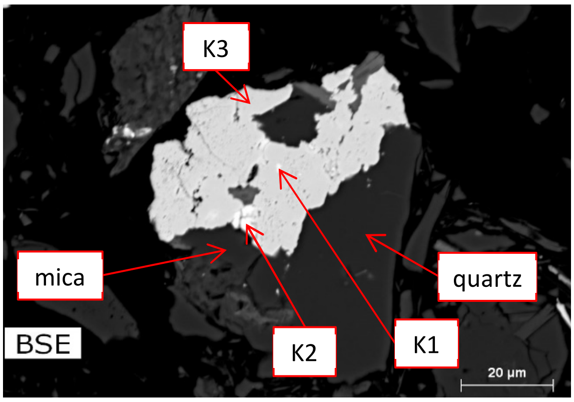	Pyrite (K3) with pentlandite (K1, K2) inclusion intergrown with quartz. K1 ED XRF (wt%): sulfur = 34.4, iron = 31.5, nickel = 30.9, oxygen = 3.2 K2 ED XRF (wt%): sulfur = 30.8, iron = 29.2, nickel = 28.4, tungsten = 9.3, oxygen = 2.3 K3 ED XRF (wt%): sulfur = 50.6, iron = 45.2, oxygen = 4.2

	Borehole CC1 Sample #17 Oxic Zone Depth 275 – 291 cm	Description
g)	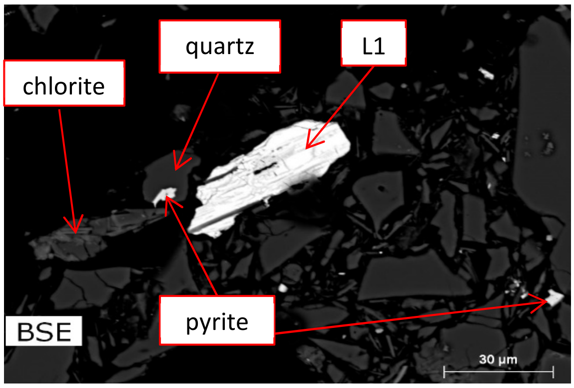	Pentlandite (L1) in mostly quartz matrix, including pyrite on quartz. L1 ED XRF (wt%): Sulfur = 30.5, Iron = 29.5, nickel = 37.7, oxygen = 2.3
h)	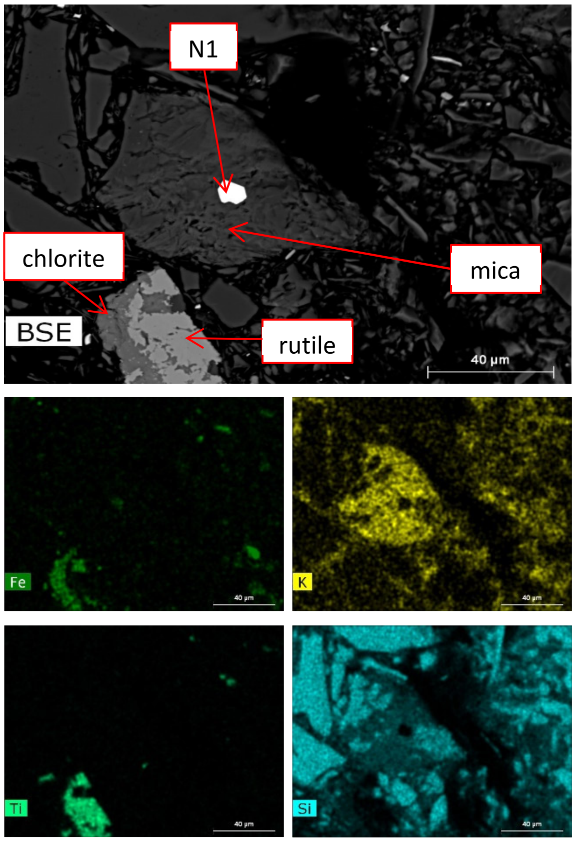	Muscovite with gersdorfite (N1). N1 ED XRF (wt%): Arsenic = 42.5, nickel = 25, sulfur = 19.6, iron = 12.9

4.7.4 Scanning Electron Microscopy Results: Sample from 372 – 388 cm

The results for a sample from the Transition Zone from the 372 – 388 cm horizon are presented in Table 14 below. A brief description of the identified minerals is given below.

Table 14(a): Pyrite and pentlandite with a surrounding quartz matrix. The pyrrhotite is an authigenic (post-burial) mineral.

Table 14(b): Autigenic pyrrhotite with a surrounding quartz matrix.

Table 14(c): Pyrite with quartz matrix including an apatite grain. Apatite is one of the few calcium minerals except gypsum that was identified in the SEM images.

Table 14(d): Detrital pyrite with a small inclusion of pentlandite with a surrounding quartz matrix, including a pyrrhotite grain. Smits (1990) found pentlandite seldom as inclusion in detrital pyrite.

Table 14(e): Quartz matrix with pyrite grains, including a pyrite grain in contact with pentlandite. The pentlandite potentially was an inclusion in the pyrite broken up by milling of the tailings.

Table 14(f): Post-sedimentary pseudomorphic pyrite enclosed in quartz adjacent to a pyrrhotite grain. This appears to be the pebble pyrite pseudomorph referred to by Hallbauer (1986).

Table 14(g): Quartz and pyrite aggregate (~40 um x ~85 um) in quartz and muscovite matrix, which include authigenic chalcopyrite and pentlandite overgrowth on a quartz crystal. The aggregate is syn-sedimentary but formed from reworked older (detrital) sediments, as described by Hallbauer (1986). Aggregate pyrite is also described briefly by da Costa et al. (2020), with a very similar example presented.

Table 14: Scanning Electron Microscope images for tailings sampled at a depth of 372 – 388 cm.

	Borehole CC1 Sample #23 **Transition Zone Depth 372 – 388 cm**	**Description**
a)	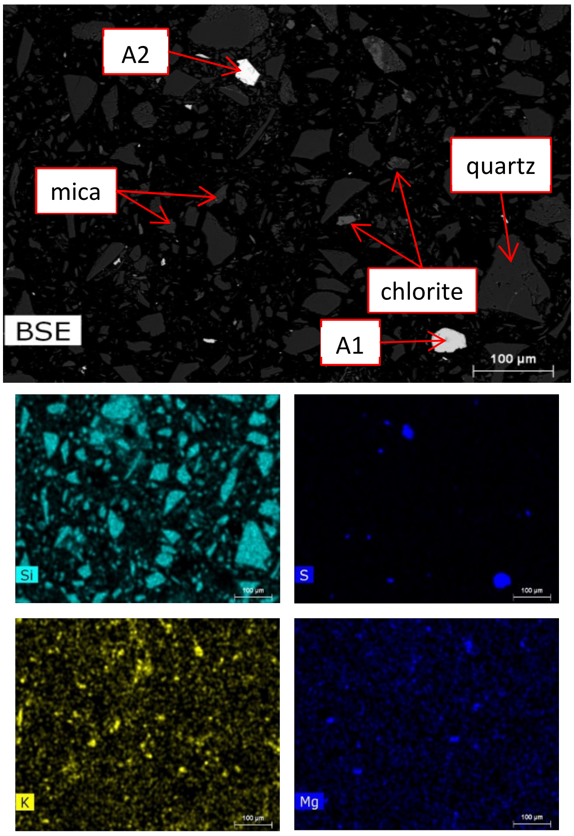	Pyrite (A1) and pentlandite (A2) with a surrounding quartz matrix. A1 ED XRF (wt%): sulfur = 46, iron = 46, oxygen = 7 A2 ED XRF (wt%): sulfur = 35, iron = 32, nickel = 34
b)	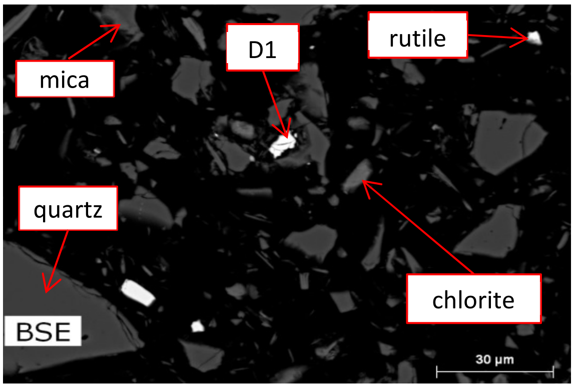	Pyrrhotite (D1) with quartz matrix. D1 ED XRF (wt%): sulfur = 35, iron = 64, oxygen = 1
c)	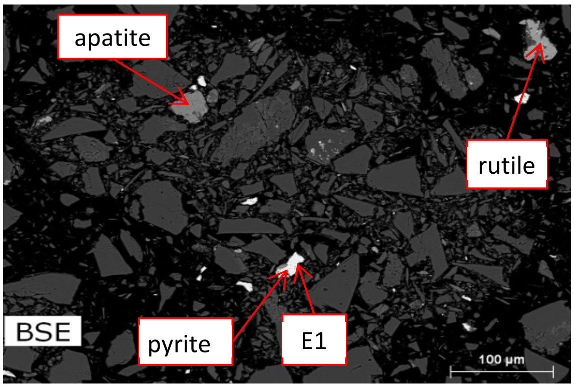	Pyrite (E1) with quartz matrix, including an apatite grain. E1 ED XRF (wt%): sulfur = 47, iron = 50, oxygen = 4

	Borehole CC1 Sample #23 **Transition Zone Depth 372 – 388 cm**	**Description**
d)	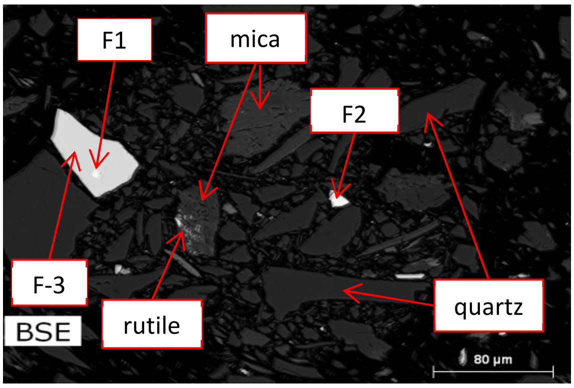	Pyrite (F1) with a small inclusion of pentlandite (F2) with a surrounding quartz matrix including a pyrrhotite (F2) grain. F1 ED XRF (wt%): sulfur = 34, iron = 47, nickel = 18, oxygen = 1 F2 ED XRF (wt%): sulfur = 37, iron = 60, oxygen = 3 F3 ED XRF (wt%): sulfur = 48, iron = 50, oxygen = 2
e)	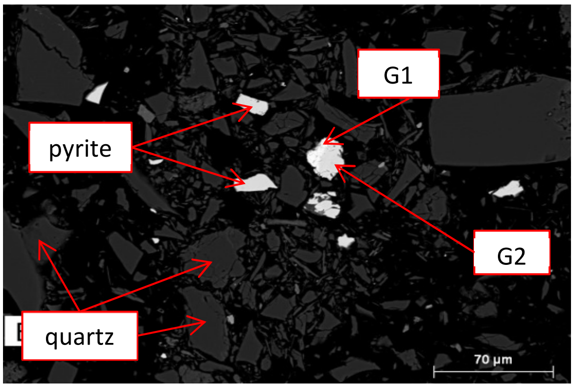	Quartz matrix with pyrite grains including a pyrite grain (G2) in contact with pentlandite (G1). G1 ED XRF (wt%): sulfur = 31, nickel = 34, iron = 32, oxygen = 3 G2 ED XRF (wt%): sulfur = 50, iron = 47, oxygen = 3
f)	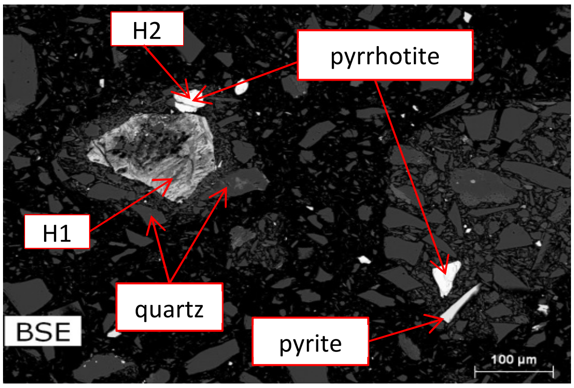	Pyrite (H1) enclosed in quartz adjacent to a pyrrhotite (H2) grain. H1 ED XRF (wt%): sulfur = 45, iron = 44, oxygen = 11 H2 ED XRF (wt%): sulfur = 36, iron = 62, oxygen = 1
g)	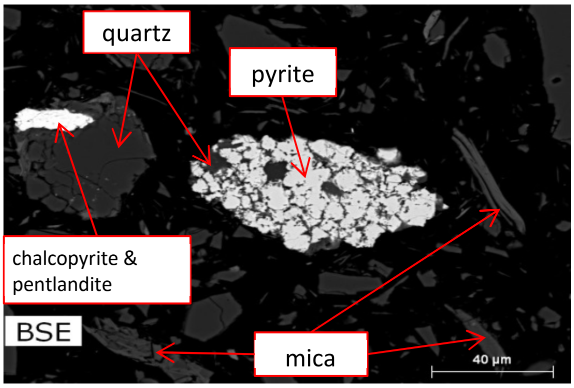	Quartz and pyrite aggregate in a quartz and muscovite matrix which includes chalcopyrite and pentlandite on a quartz crystal.

4.7.5 Scanning Electron Microscopy: Sample from 598 – 614 cm

The results for a sample from the Transition Zone from the 598 – 614 cm horizon are presented in Table 15 below. A brief description of the identified minerals is given below.

Table 15(a): Gypsum with a surrounding quartz matrix. The gypsum is a secondary mineral that formed in the tailings dam after deposition and precipitated between some pyrite grains.

Table 15(b): Autogenic pyrrhotite and rutile that formed potentially a pseudomorph after ilmenite or titaniferous magnetite.

Table 15(c): Pyrite with a galena inclusion within the surrounding quartz and muscovite matrix. Smits (1990) notes that galena occurs in detrital pyrite. The galena also contains some traces of arsenic.

Table 15(d): Autogenic pyrrhotite with chlorite forming a well-formed boundary. A quartz grain with TiO_2 exsolution that appears to be a detrital relic from the source rock (TiO_2 exsolution from quartz magma occurs at much higher temperatures, e.g. Zhang et al., 2020, that the Witwatersrand have been exposed to). Chlorite in the sample occurs as overgrowths on quartz grains.

Table 15(e): Pyrite and gersdorffite on quartz. Smits (1990) notes that gersdorffite is not a detrital but authigenic, which would imply that it formed during hydrothermal processes.

Table 15(f): A single, ellipsoidal gypsum crystal. The crystal was probably more elongated, but due to the reaction with the interstitial tailings dam water, the edges are smoothed.

Table 15(g): More large gypsum crystals (>200 um). As discussed before, the gypsum precipitated in the tailings dam. Most gypsum encloses matrix minerals, including quartz and pyrite grains. Where exposed, some of the gypsum has also been rounded due to weathering. Sulphate sulphur (mostly gypsum) is also the highest in the coarser fraction of the tailings, as discussed in Section 6.2.2.

Table 15: Scanning Electron Microscope images for tailings sampled at a depth of 598 – 614 cm.

	Borehole CC1 Sample #38 **Transition Zone Depth 5.98 – 6.14 m**	**Description**
a)	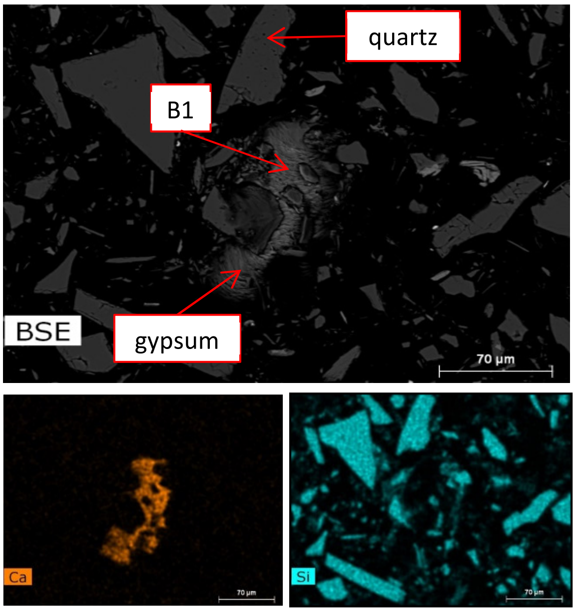	Gypsum with a surrounding quartz matrix. D1 ED XRF (wt%): calcium = 42, oxygen = 28, sulfur = 25, silicon = 5, aluminium = 1
b)	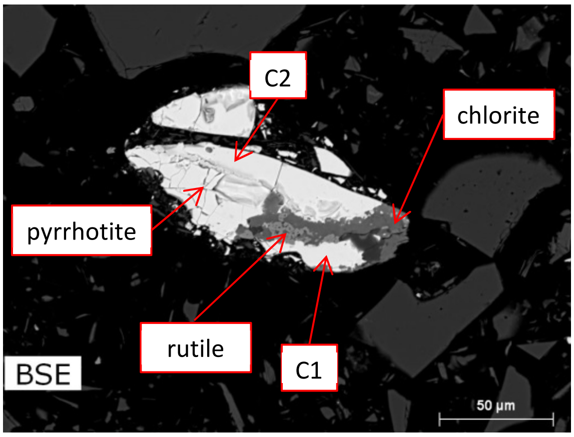	Pyrrhotite (C1,C2), rutile and chlorite with surrounding quartz matrix. C1 ED XRF (wt%): sulfur = 37, iron = 63 C2 ED XRF (wt%): sulfur = 38, iron = 60, oxygen = 2
c)	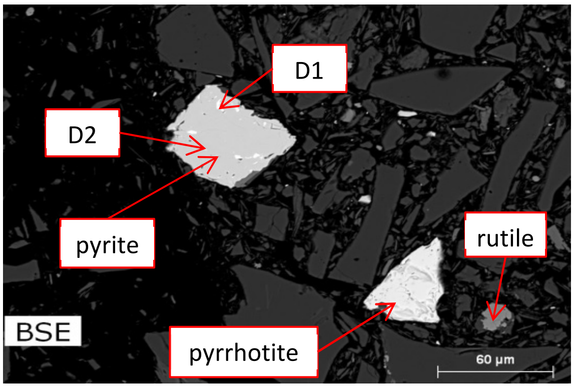	Pyrite (D2) with a galena inclusion (D1) within a surrounding quartz and muscovite matrix. D1 ED XRF (wt%): lead = 77, sulfur = 7, arsenic = 4, iron = 4, aluminium = 2, oxygen = 5 D2 ED XRF (wt%): sulfur = 51, iron = 49

	Borehole CC1 Sample #38 **Transition Zone Depth 5.98 – 6.14 m**	**Description**
d)	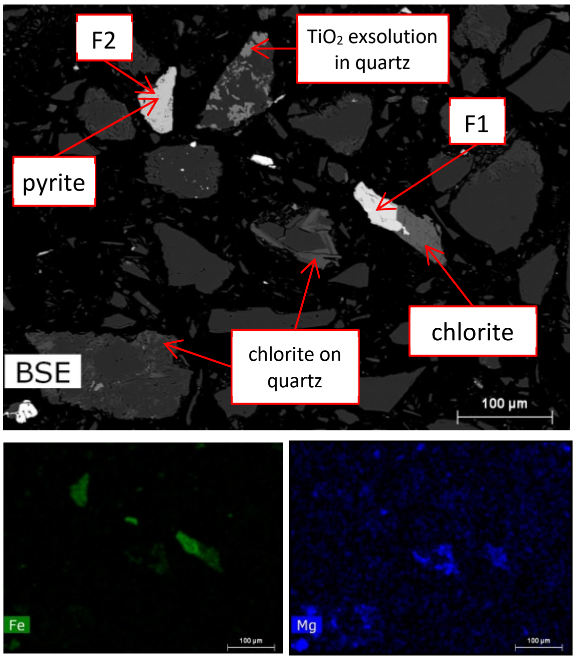	Pyrrhotite (F1) on chlorite, pyrite (F2), TiO_2 exsolution in quartz and chlorite on quartz. F1 ED XRF (wt%): sulfur = 36, iron = 62, oxygen = 2 F2 ED XRF (wt%): sulfur = 51, iron = 46, oxygen = 3
e)	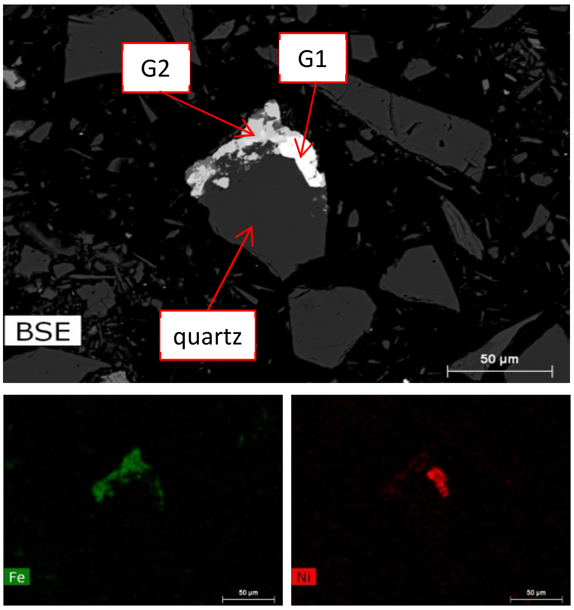	Pyrite (G2) and gersdorffite (G1) on quartz. G1 ED XRF (wt%): sulfur = 22, arsenic = 44, nickel = 30, iron = 3, oxygen = 1 G2 ED XRF (wt%): sulfur = 46, iron = 50, oxygen = 4
f)	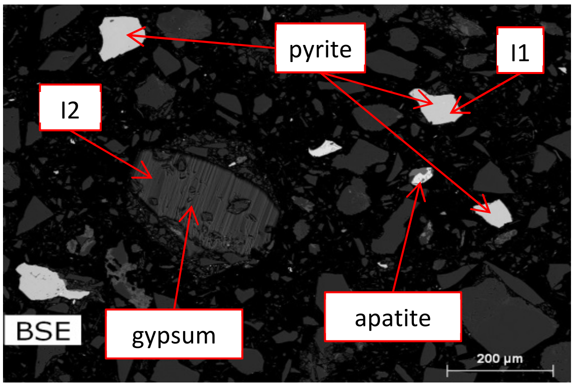	Pyrite (I1) and gypsum (I2) in quartz matrix that also includes an apatite grain. I1 ED XRF (wt%): sulfur = 48, iron = 46, oxygen = 6 I2 ED XRF (wt%): sulfur = 17, calcium = 27, oxygen = 56

	Borehole CC1 Sample #38 **Transition Zone Depth 5.98 – 6.14 m**	**Description**
g)	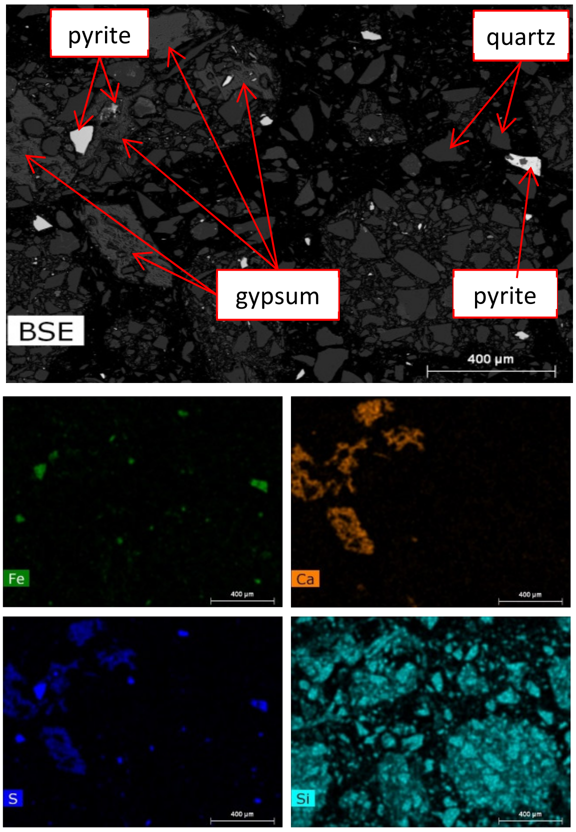	Gypsum in quartz matrix with some pyrite grains.

4.8 Water Quality

4.8.1 Introduction

Water samples were collected from a 10 m drilled hole, as well as from toe seepage and surface drains, as discussed in Section 3.3. The water quality measurements from the hole will be used to compare with the results of the geochemical model performed in Section 7. However, a once-off measurement of the interstitial water presents only a snapshot in time of a 60 - 70-year-old tailings dam.

4.8.2 Instruments and methods

A 10 m deep borehole was drilled by the Council of Geoscience in July 2015 adjacent to the oxygen monitoring hole. A slurry sample was collected 8.3 – 9.3 m deep from the borehole before the borehole collapsed. Water samples were also collected from toe seepage and drains on the northeastern side of the dam in April 2017.

The pH of the samples was first recorded before the samples were filtered through an 8-um filter paper. The filtrate was used for analyses of Total Alkalinity, chloride, orthophosphate, nitrate, ammonium and fluoride using an AQ2 Discrete Analyser. A 10 ml subsample of the -8 um filtrate was further filtered through a 0.45 um syringe filter before being preserved with 1 ml HNO3 for analysis. Sulphur and all the tested metals and metalloids were determined using an ICP-OES.

4.8.3 Results

The interstitial water composition is depicted in Table 1 below. The water quality was compared to the SANS 241:2015 Drinking Water Standard to indicate relatively elevated parameters.

Interstitial Water 8.3 – 9.3 m

It is uncertain whether the sample only presents interstitial water at this depth or, more likely, a mix of water from different saturated horizons which had flowed into the borehole during drilling.

The pH of the sample is 4.03, which is in a similar range to the paste pH measurements of the tailings below the Transition Zone described in Section 4.2.3.

The Total Sulphur (as SO_4) is at 5 347 mg/l. This may include all sulphur species; however, given the Eh range, sulphate will be the dominant aqueous sulphur species.

The Total Alkalinity of the sample is zero, while the chloride is at 7.48 mg/l. Orthophosphate, nitrate and fluoride are below the detection limit, and ammonium as N at 5.49 mg/l. The ammonium was present in all water samples and may originate from the weathering of the muscovite in the tailings dam. Ammonium in the Witwatersrand muscovite has been described before, and it was suggested that it originates from the hydrothermal fluid that circulated through the deposit where ammonium replaced the potassium in muscovite (Meyer & Ridgway, 1991).

The calcium, magnesium, sodium and potassium concentrations are at 487, 495, 18.3 and 75.3 mg/l, respectively. The potassium originates mostly from muscovite weathering, and the magnesium from the chlorite weathering. The only calcium minerals identified in the SEM analyses in Section 4.7 were gypsum and apatite. The sample is also close to gypsum saturation, as indicated in Table 16 below. As discussed in Section 4.7.5, gypsum precipitated in the tailings dam after deposition.

Toe Seepage Drain 1

Overall, this drain is very similar in composition to the interstitial water, apart from the following exceptions: the sample had a slightly lower pH (pH 3.63) and substantially lower dissolved iron (2.94 mg/L) than the interstitial water (pH 4.03 and dissolved iron 1 197 mg/L). This is because of ferrous iron oxidation (e.g. $Fe^{2+} + 2.5H_2O + 0.25O_2 \rightarrow Fe(OH)_3 + 2H^+$) that occurs as the seepage daylight and are exposed to atmospheric conditions.

The sample does not have the high sodium and chloride of the drains from the tailing’s reclamation. The sample has a lower Ca, Mg and K than the interstitial water (potentially because of precipitation of secondary minerals, e.g. gypsum, jarosite), but slightly higher trace metals like Co, Cu, Ni, and Zn (because of the lower pH).

Drain 2 and 3

Overall, the reclamation water sampled in the drains was very similar in composition to that of the interstitial water and Drain 1, apart from a few exceptions. The pH is, however, below pH 3, and the sodium and chloride concentrations are higher. A few trace metals (Co, Cu, Cr, Mn, Ni, and Zn) are also higher in the drains than in the interstitial water because of the lower pH.

Table 16: Interstitial and drain water quality compared to the SANS 241:2015 Drinking Water Standard (N/V = No Value)

Parameter (Unit *mg/L* or as indicated)	**Interstitial water at 8.3-9.3 m (July 2015)**	**Drain 1 (April 2017)**	**Drain 2 (April 2017)**	**Drain 3 (April 2017)**	**SANS 241:2015 Drinking Water Guideline**		
					<50% of Guide	**50-100% of Guide**	**>100% of Guide**
pH (Value)	4.03	3.63	2.92	2.79	6 - 8.4	5-6; 8.4-9.7	<5 ; >9.7
Electrical Conductivity (mS/m)	598	349	701	692	<85	85-170	>170
Sulphur as SO_4	5 347	2 683	4 356	4 011	<250	250-500	>500
Total Alkalinity as $CaCO_3$	<10	<10	<10	<10	N/V	N/V	N/V
Chloride as Cl	7.48	8.88	157	169	<150	150-300	>300
Orthophosphate as P	<0.2	0.04	1.60	0.89	N/V	N/V	N/V
Nitrate as N	<0.2	<0.2	<0.2	<0.2	<5.5	5.5-11	>11
Ammonia as N	5.49	2.27	36.1	39.0	<0.75	0.75 -1.5	>1.5
Fluoride as F	<0.1	<0.1	<0.1	<0.1	<0.75	0.75 -1.5	>1.5
Aluminium as Al	212	296	196	130	<0.15	0.15-0.3	>0.3
Arsenic as As	1.96	0.019	1.13	0.642	<0.005	0.005-0.01	>0.01
Boron as B	N/V	<0.01	0.115	0.118	<1.2	1.2-2.4	>2.4
Barium as Ba	<0.01	<0.01	<0.01	<0.01	<0.35	0.35-0.7	>0.7
Beryllium as Be	<0.01	0.011	0.017	<0.01	N/V	N/V	N/V
Calcium as Ca	487	61.0	386	410	N/V	N/V	N/V

Parameter (Unit *mg/L* or as indicated)	Interstitial water at 8.3-9.3 m (July 2015)	Drain 1 (April 2017)	Drain 2 (April 2017)	Drain 3 (April 2017)	SANS 241:2015 Drinking Water Guideline <50% of Guide	50-100% of Guide	>100% of Guide
Cadmium as Cd	<0.0015	0.023	0.035	0.017	<0.0015	0.0015-0.003	>0.003
Cobalt as Co	0.220	7.30	13.7	10.0	<0.25	0.25-0.5	>0.5
Chromium as Cr	<0.02	0.147	1.03	0.713	<0.025	0.025-0.05	>0.05
Copper as Cu	0.054	3.87	6.31	4.41	<1	1-2	>2
Iron as Fe	1 197	2.42	332	356	<1	1-2	>2
Potassium as K	75.3	2.02	19.9	36.0	N/V	N/V	N/V
Magnesium as Mg	495	267	199	182	N/V	N/V	N/V
Manganese as Mn	14.6	10.3	25.7	20.5	<0.25	0.25-0.5	>0.5
Molybdenum as Mb	<0.02	0.551	0.342	0.198	N/V	N/V	N/V
Sodium as Na	18.3	3.49	204	319	<100	100-200	>200
Nickel as Ni	0.900	22.2	34.1	28.8	<0.035	0.035-0.07	>0.07
Lead as Pb	0.354	<0.01	<0.005	0.029	<0.005	0.005-0.01	>0.01
Antimony as Sb	0.183	<0.02	<0.01	<0.01	N/V	N/V	N/V
Selenium as Se	0.304	<0.02	<0.02	<0.02	<0.02	0.02-0.04	>0.04
Strontium as Sr	0.271	0.035	0.384	0.537	N/V	N/V	N/V
Vanadium as V	<0.01	<0.01	<0.01	<0.01	N/V	N/V	N/V
Zinc as Zn	0.426	7.86	14.6	13.9	<2.5	2.5-5.0	>5

Parameter (Unit *mg/L* or as indicated)	Interstitial water at 8.3-9.3 m (July 2015)	Drain 1 (April 2017)	Drain 2 (April 2017)	Drain 3 (April 2017)	SANS 241:2015 Drinking Water Guideline		
					<50% of Guide	50-100% of Guide	>100% of Guide
Thorium as Th	0.011	N/V	N/V	N/V	N/V	N/V	N/V
Uranium as U	0.032	N/V	N/V	N/V	N/V	N/V	N/V
Gypsum Q/K	-0.0161	-1.0652	-0.1401	-0.1251	-	-	-

5 CONCEPTUAL GEOCHEMICAL MODEL

5.1 Introduction

A conceptual model was developed for the geochemical evolution within the tailings dam. The aim was to outline the major mechanisms that influence the geochemical evolution in the dam to include them in the numerical model in Chapter 7.

In Section 5.2, the water and oxygen infiltration within a tailings dam are deliberated. Oxygen is an important oxidation agent of sulphides in the shallow environment, while water serves as the medium for transport and chemical reactions in the tailings. In Section 5.3, an outline is given of the essential mineral reactions. Kinetically controlled dissolution of primary minerals releases chemicals into the solution (the interstitial water), which actual concentrations are controlled by secondary minerals' formation (or dissolution).

5.2 Water and Oxygen Flow

A conceptual model illustrating the development of the Oxic Zone in a tailings dam is depicted in Figure 29 and Figure 30 below. During the operational phase, the tailings dam is water-saturated at the pool area, and oxygen infiltration will be limited to some wall and dry beach areas. After closure, the piezometric surface in the dam will subside, resulting in more oxygen infiltration into the upper few meters of the dam. The outer part of the tailings dam will become unsaturated, and the deeper part will remain saturated for several decades after closure.

Water flow in the unsaturated zone will be vertical, whereas in the saturated zone, there will be both a horizontal and vertical flow component, as illustrated in Figure 30. As discussed in Section 2.6.2, the deep infiltration into the tailings dam is higher than the seepage through the base because of horizontal flow and subsequent losses at the toe. In Section 2.6.2, it has been stated that deep infiltration measured at two decommissioned tailings dams varied between 15 - 17% of the MAP using lysimeters (Yibas et al., 2011) calculated, whereas other authors found long-term seepage from tailings dams (recharge to aquifer) at 1 - 6% of the MAP. The 15-17% may be a bit high for a yearly average as it was measured only over 4 months and at the end of a wet season, as noted in Section 2.6.2. The horizontal hydraulic conductivity in the Witwatersrand tailings dams is also much higher than the vertical, and anisotropic values of up to 200 times higher have been reported for Wits tailings dams. This makes a 1D geochemical model with flow only in one direction challenging to reconcile with the 2D flow in a tailings dam. This study overcame this difficulty by allowing only vertical flow in the model nodes situated in the unsaturated zone but both vertical and horizontal flow in the saturated zone nodes.

Consumption of oxygen will lead to a gradient in oxygen fugacity in the material (see Figure 30) that initiates oxygen diffusion (flow from high concentration to low concentration). The oxygen concentration will be at its highest in material, directly in contact with the atmosphere. Due to its consumption, the oxygen concentration will gradually become depleted within only a few meters. Initially, only the upper part of the material will be situated in the Oxic Zone, and the oxidation front will shift deeper into the material as sulphide minerals are depleted. According to the shrinking core model of Davis & Ritchie (1986), oxygen diffusion takes place through the pore space of the wastes, followed by diffusion into a moving reaction front within the particles. In other words, the front of the oxidation zone is at the reaction front within the pyrite grains, and no sharp oxidation front is present in the tailings dam itself (which will result in the presence of a Transition Zone). Fully oxidized pyrite remnants will be present at the top of the Oxic Zone, partially oxidized pyrite deeper down, with unoxidized pyrite grains present only in the Anoxic Zone, as shown in Figure 30.

According to GARDGuide (2021), the oxidation front within a tailings dam frequently "stalls" at a relatively shallow depth, approaching steady-state conditions. This means that at some point in time, the diffusive oxygen flux will approach the pyrite consumption rate, with the storage of oxygen in the porous medium (left side of Equation 5) becoming smaller. Pseudo-steady-state conditions are often reached more rapidly in tailings with significant pyrite (GARDGuide, 2021) and water content (this study).

In this study, the oxygen ingress has been measured in the top 6 m of the tailings dam, as discussed in Section 4.2. In the Oxic Zone (0 – 2 m), oxygen is present throughout the year. In the Transition Zone (2 – 4 m), oxygen is erratically present and shows a distinct change in its oxygen decrease. In the Anoxic Zone (>4 m), oxygen is absent except just after drilling. The Anoxic Zone also correlates with the maximum volumetric water content. Drilled-out samples from the Anoxic Zones were also water-saturated. Because the stalled Oxic Zone is so shallow, the depth of the Oxic Zone was taken to be constant over the life of the tailings dam in the geochemical model.

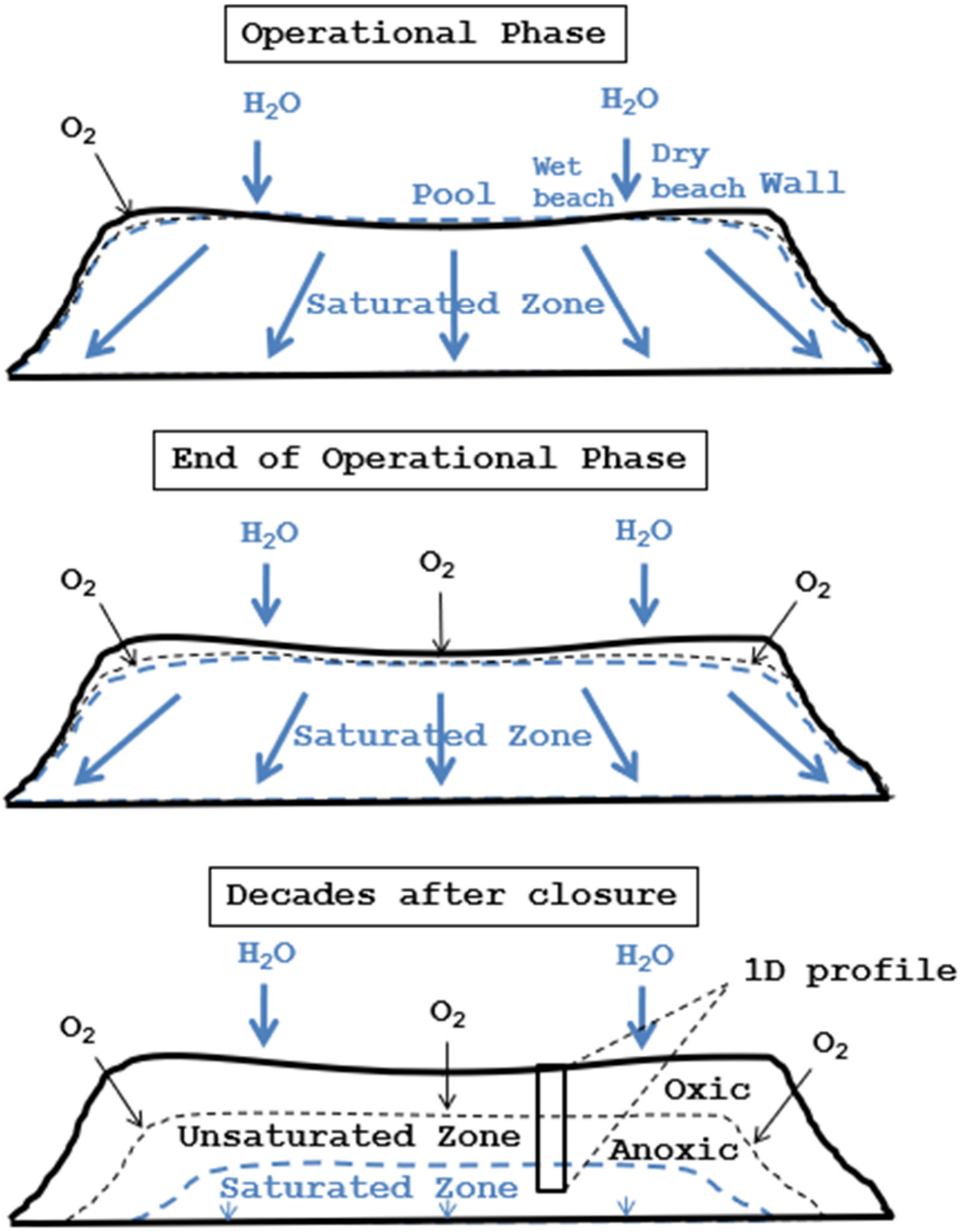

Figure 29: Conceptual model of the tailings dam illustrating the presence of the Oxic and Anoxic Zones. The position of the 1D profile is shown in the lower figure.

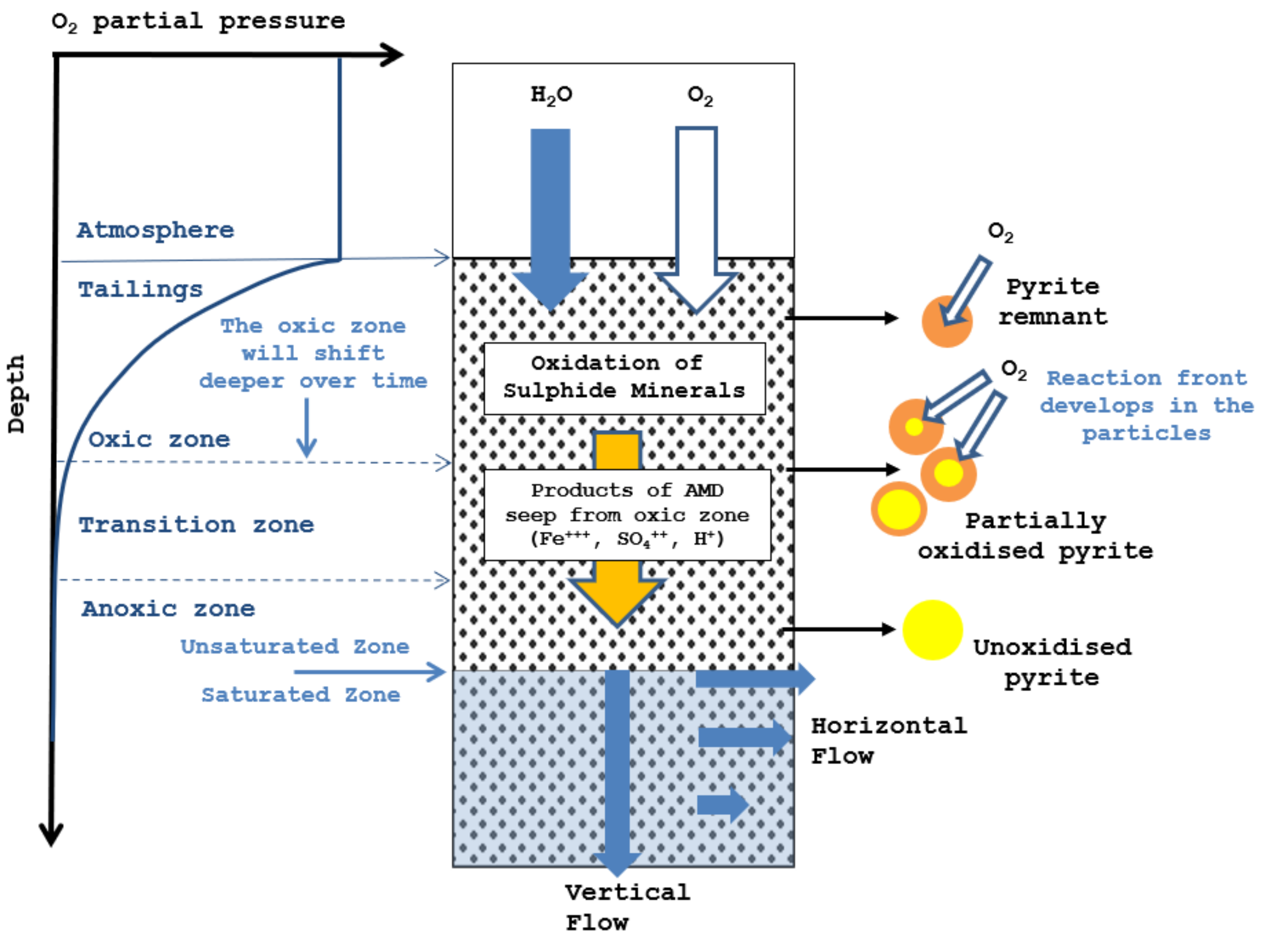

Figure 30: Conceptual model of the physicochemical process in the unsaturated zone.

5.3 Mineral Reactions

The mineral reactions in the tailings dam investigated could be described by either equilibrium reactions for fast-reacting minerals or kinetic rate laws for slower-reacting minerals. The theoretical basis for these was discussed in Section 2.7.

5.3.1 Pyrite

Pyrite has been identified as the dominant sulphide in the tailings dam investigated. The oxidation of pyrite is key to the geochemical evolution of the tailings dam. In mine waste, pyrite is oxidized by either oxygen or ferric iron, depending on the pH conditions. The following equations show the generally accepted sequence of pyrite reactions:

$$\text{Pyrite } FeS_2 + 3.5O_2 + H_2O \rightarrow Fe^{2+} + 2SO_4^{2-} + 2H^+$$

Equation 23

$$Fe^{2+} + 0.25O_2 + H^+ \rightarrow Fe^{3+} + 0.5H_2O$$

Equation 24

$$Fe^{3+} + 3H_2O \rightarrow Fe(OH)_3 + 3H+$$

Equation 25

$$\textit{Sum of Eq15 – 17:} \quad FeS_2 + 3.75O_{2(aq)} + 3.5H_2O \rightarrow Fe(OH)_3 + 2SO_4^{2-} + 4H^+$$

Equation 26

$$FeS_2 + 14Fe^{3+} + 8H_2O \rightarrow 15Fe^{2+} + 2SO_4^{2-} + 16\ H^+$$

Equation 27

In the initial step of pyrite oxidation by oxygen (Equation 23), 1 mole of pyrite reacts with oxygen and water to oxidise the pyrite sulphur producing 2 moles of sulphate, 1 mole of ferrous iron, and 2 moles of hydrogen ions. The second step (Equation 24) involves the conversion of ferrous iron to ferric iron, whereby 1 mole of hydrogen is consumed. The third step (Equation 25) involves the hydrolysis of ferric iron with water to form ferrihydrite (under circumneutral conditions) and the release of additional acidity. The overall reaction for pyrite oxidation is given in Equation 26. However, this equation presents an oversimplification of the oxidation process as well as the products formed. The reaction is often incongruent with several other intermediately products that may form, i.e. hydrated iron-sulphates like schwertmannite, as discussed in Section 5.3.2. Equation 27 involves the oxidation of pyrite by ferric iron. The ferric iron is generated by the oxidation reaction in Step 2 (Equation 24), where ferric iron is reduced to ferrous iron. This step is often bacterially catalysed under acidic conditions. Jaynes et al. (1984) state that *At. ferrooxidans* require oxygen molal fractions of at least 0.01 for their survival. The optimum pH levels for *At. ferrooxidans* are 2.0 - 3.5 (Ledin & Pedersen, 1996).

The dissolution rate of pyrite as a function of pH is depicted in Figure 31 below. Above pH ~3-3.25, oxidation by dissolved oxygen is dominant as the solubility of Fe^{+3} oxyhydroxides decreases. The reaction of pyrite with dissolved oxygen has a slight dependence on pH. Below this pH, oxidation by ferric iron becomes more dominant. The oxidation rate ($mol.m^{-2}.s^{-1}$) of pyrite by oxygen and ferric iron from Williamson & Rimstidt (1994) is given below in Equation 28 and Equation 29, respectively below.

$$r = 10^{-8.19}\frac{a_{DO}^{0.50}}{a_{H^+}^{0.11}}$$

Equation 28

$$r = 10^{-6.07}\frac{a_{Fe^{3+}}^{0.93}}{a_{Fe^{2+}}^{0.40}}$$

Equation 29

The oxidation rate of pyrite by oxygen is proportional to the dissolved oxygen but inversely proportional to the hydrogen activity. The oxidation rate by ferric iron is positively correlated to the ferric iron content but inversely proportional to the presence of ferrous iron.

In the geochemical model, only oxidation by oxygen was considered as the pH was above pH 3.5 in the interstitial water, and for this reason, bacterial catalysis was also ignored. In Section 6, it was found that the above oxidation rate of pyrite by oxygen (Equation 28) was applicable for kinetic tests on the tailings performed at different pHs.

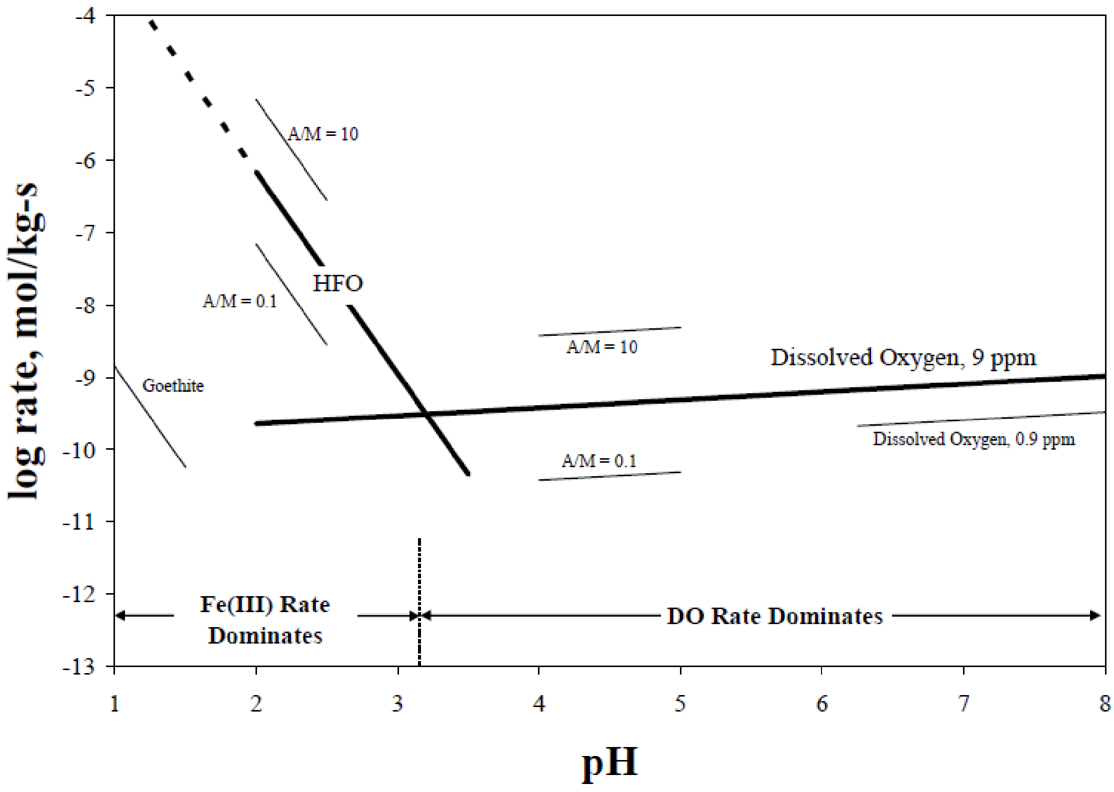

Figure 31: The oxidation rate of pyrite as a function of pH (A/M = Mineral Surface Area/Mass) (from Williamson et al., 2006).

5.3.2 Secondary Iron and Sulphate Minerals

Precipitation and dissolution of secondary minerals exert a major control on the concentration of chemical parameters in the interstitial and seepage water of tailings dams. Gypsum ($CaSO_4.2H_2O$) is a common secondary mineral in mine drainage, especially when appreciable calcium carbonate minerals are present that can maintain medium to high calcium concentrations in solution. Gypsum is fairly soluble, and the sulphate and calcium will be released into the solution as soon as gypsum becomes undersaturated again.

Under humic, acidic conditions, one could expect roughly the following sequence, following pyrite oxidation: 1) hydrated Fe(II)-sulphates like melanterite and rozenite; 2) mixed hydrous F(II) and Fe(III)-sulphates like römerite; 3) hydrous Fe(III)-sulphates like coquimbite; 4) more stable Fe(III)-sulphates like schwertmannite or jarosite and goethite upon dehydration (Bigham & Nordstrom, 2000). Under more neutral conditions, there will be fewer intermediates, and ferrihydrite $Fe(OH)_3$ and goethite will form quicker (Bigham & Nordstrom, 2000). The more stable hematite (Fe_2O_3) and goethite (FeOOH) are not formed directly at low temperatures (Bethke, 2007).

The pH and Eh of the samples from the Oxic and Transition Zones for the tailings dam investigated are plotted on two Fe-S-H_2O Eh-pH stability diagrams at relatively lower and higher iron activities in Figure 32 and Figure 33. The stability fields are indicative of specific iron and sulphate activities. The samples of the Oxic Zone fall on the boundary of two ferric minerals and aqueous ferrous sulphate and are fitted better with the lower iron (Activity = $10^{-4.2}$) activity diagram (Figure 32). Samples from the Transition Zone are close to the ferric-sulphate mineral and aqueous ferrous sulphate boundary and are fitted better with the higher iron activity (Activity = $10^{-2.3}$) diagram (Figure 33). Interstitial water will therefore contain both ferric and ferrous species in the Oxic Zone but mostly ferric iron in the Anoxic Zone. There are no other major redox couples in the tailings, and ferric and ferrous iron is therefore expected to control the system Eh.

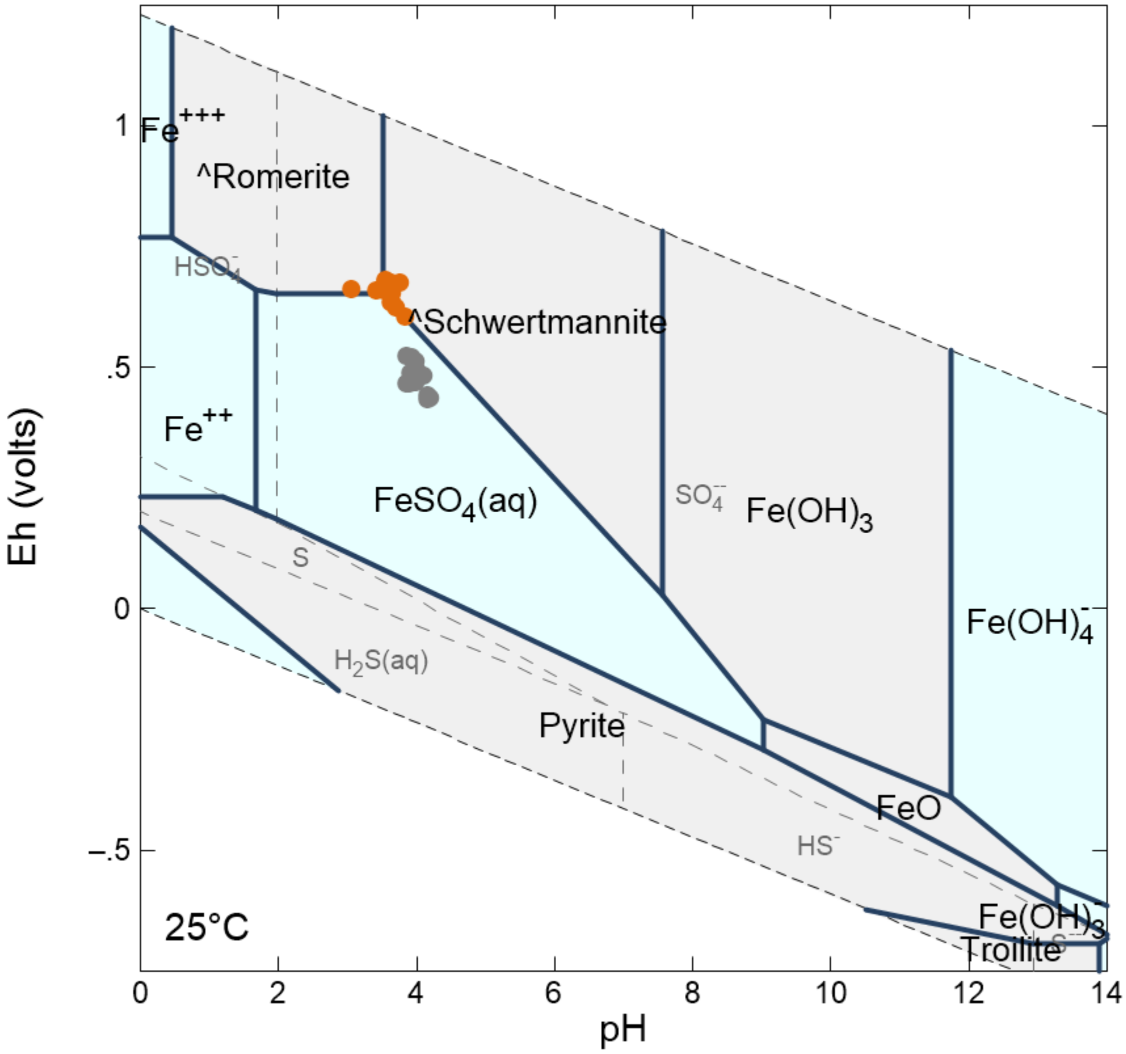

Figure 32: Stability diagram for the Fe-S-H_2O system with lower iron activity ($10^{-4.2}$) (20^oC, 1.013 bar pressure, activity sulphur = 10^{-2}). Orange = Samples from Oxic Zone, Grey = Samples from Transition Zone.

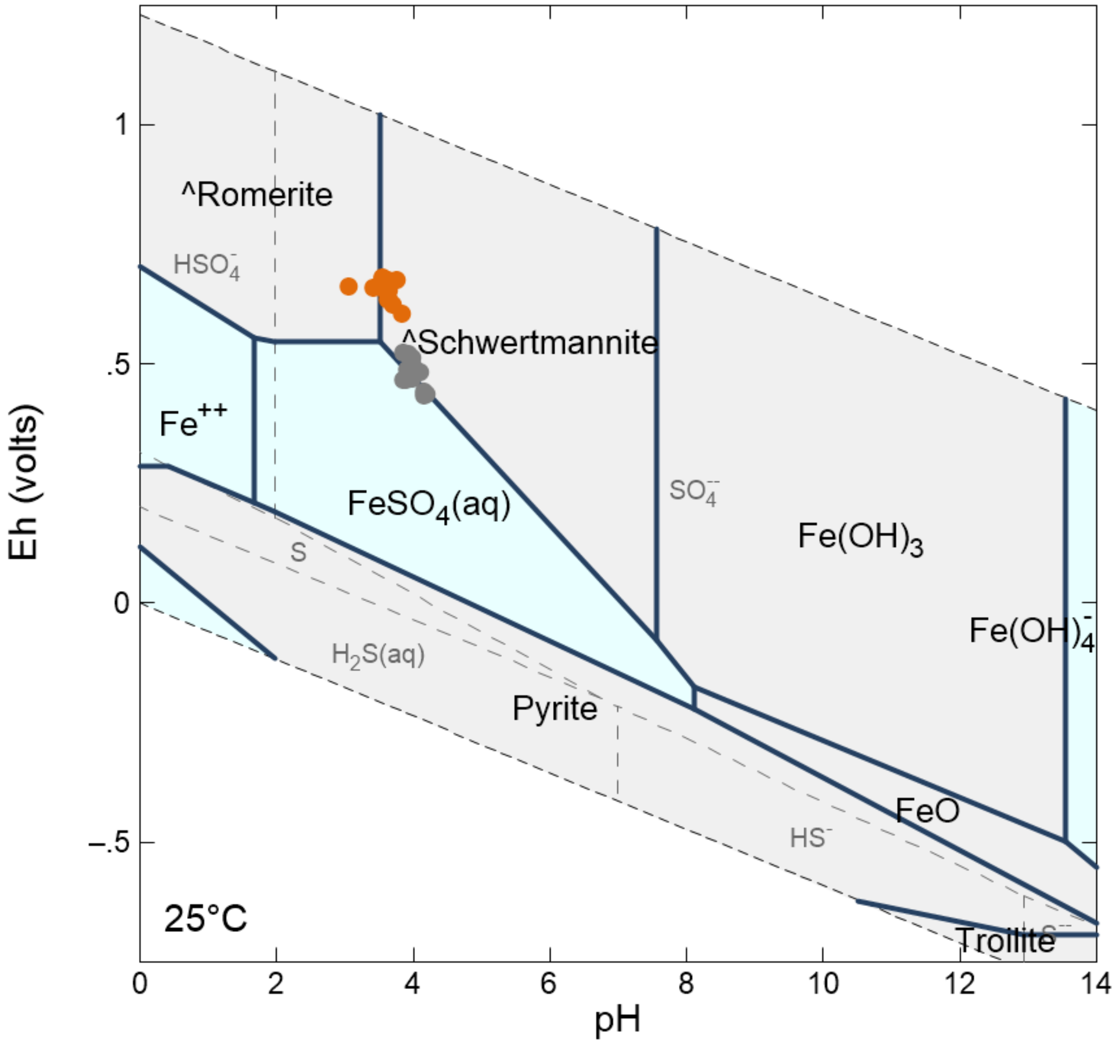

Figure 33: Stability diagram for the Fe-S-H_2O system with higher iron activity ($10^{-2.3}$) (20ºC, 1.013 bar pressure, activity sulphur = 10^{-2}). Orange = Samples from Oxic Zone, Grey = Samples from Transition Zone.

5.3.3 Arsenic Minerals and Stability

Arsenopyrite, cobaltite and gersdorfite have been identified as the dominant arsenic-bearing minerals in the tailings dam investigated. The oxidation of these minerals will be important to understand the distribution of arsenic in the tailings dam. The dissolution of these minerals to produce arsenate are as follows:

Arsenopyrite $FeAsS + 4H_2O + 3.5O_2(aq) \rightarrow 3H^+ + Fe(OH)_3 + H_2AsO_4^- + SO_4^{2-}$

Equation 30

Cobaltite $CoAsS + 1.5H_2O + 3.25O_2(aq) \rightarrow H^+ + Co^{2+} + H_2AsO_4^- + SO_4^{2-}$

Equation 31

Gersdorfite $NiAsS + 1.5H_2O + 3.25O_2(aq) \rightarrow H^+ + Ni^{2+} + H_2AsO_4^- + SO_4^{2-}$

Equation 32

The oxidation of arsenopyrite results in 3 mol of hydrogen, with the oxidation of cobaltite and gersdorfite producing 1 mole of hydrogen. The arsenate specie $H_2AsO_4^-$ is the most stable aqueous specie under slightly acidic to acidic solutions under oxidizing conditions, as will be discussed further below.

In the numerical geochemical only arsenopyrite was considered as both the mass, as well as the kinetic data of cobaltite and gersdorffite are unknown.

The oxidation rate of arsenopyrite ($mol.m^{-2}.s^{-1}$) by oxygen for the pH range 2 – 4.5, is given by McKibben et al. (2008) as follows:

$$r = 10^{-6.11} a_{DO}^{0.33} a_{H^+}^{0.27}$$

Equation 33

In comparison to pyrite, this rate is significantly (3-4 order) faster, and, according to McKibben et al. (2008), the oxidation of arsenopyrite by ferric iron (at pH 2) is at least 10 times faster than by dissolved oxygen.

The oxidation rate of arsenopyrite ($mol.m^{-2}.s^{-1}$) by oxygen given by Asta et al. (2010) (at pH <4) was found to match the observations in the model better:

$$r = 10^{-7.41} \frac{a_{DO}^{0.76}}{a_{H^+}^{0.12}}$$

Equation 34

Figure 34 shows the stability of aqueous arsenic species using the activity of the arsenic of the 8.3-9.3 m deep tailings water sample from Section 4.8. At pH 3-4, the boundary between the arsenite species ($HAsO_2(aq)$) and the arsenate species ($H_2AsO_4^-$) is at an Eh of about 300 to

350 mV. It is well documented that arsenic mobility in the aqueous environment depends significantly on the presence of iron activity and the presence of Fe-hydroxides sorption sites, e.g. Campbell & Nordstrom (2014) and Nordstrom et al. (2014). Arsenic can adsorb to hydrous ferric oxides in the aquifer, and according to Nordstrom et al. (2014), substances in the system Fe_2O_3-As_2O_5-H_2O are common at hazardous waste sites and mineral processing facilities. However, Nordstrom et al. (2014) state that complex mixtures of fine-grained poorly crystalline phases and hydrous ferric oxides containing sorbed As(V) are a considerable challenge to characterise mineralogically and thermodynamically. Because of its sheer predominance over other minerals in nature, the data for scorodite suffice for modelling most natural systems with abundant Fe(III) and As(V) (Nordstrom et al., 2014). Other common secondary minerals that formed after the weathering of arsenopyrite containing mine waste include bukovskýite, kaňkite, and zýkaite at both Kaňk, Czech Republic (Ondruš et al., 1999), and in the Southern Alps, New Zealand (Haffert et al., 2010). In the latter case, scorodite has replaced the arsenopyrite in the mine wastes; kaňkite (a more hydrated form) has formed instead of scorodite in moist areas; bukovskýite and zýkaite formed in acidic (pH 3-4), moist areas where higher dissolved sulphate concentrations were present; ferrihydrite with arsenate (up to 20 wt% As) occurred at all localities.

Following the suggestion from Nordstrom et al. (2014), a pH-Eh diagram was generated that included scorodite but excluded the thermodynamically more stable species listed by them (i.e. bukovskýite, Fe-amorphous, Fe-crystalline, kaňkite, parascorodite, pharmocolite, symplesite). Figure 35 shows the stability of aqueous arsenic species and minerals using the activity of the arsenic as well as those of other parameters of the 8.3-9.3 m deep tailings water sample from Section 4.8. Figure 35 shows the same diagram but with only pharmocolite and symplesite suppressed. These graphs show that ferric-arsenate minerals are stable in the Oxic Zone and to a lesser degree, also in the Anoxic Zone. This explains why, although arsenopyrite may be oxidised in the Oxic Zone, arsenate is not very mobile as it can precipitate as several (especially Fe- as well as some Ca-) minerals. Under low Eh conditions, arsenate (and some arsenite) will be more mobile in solution.

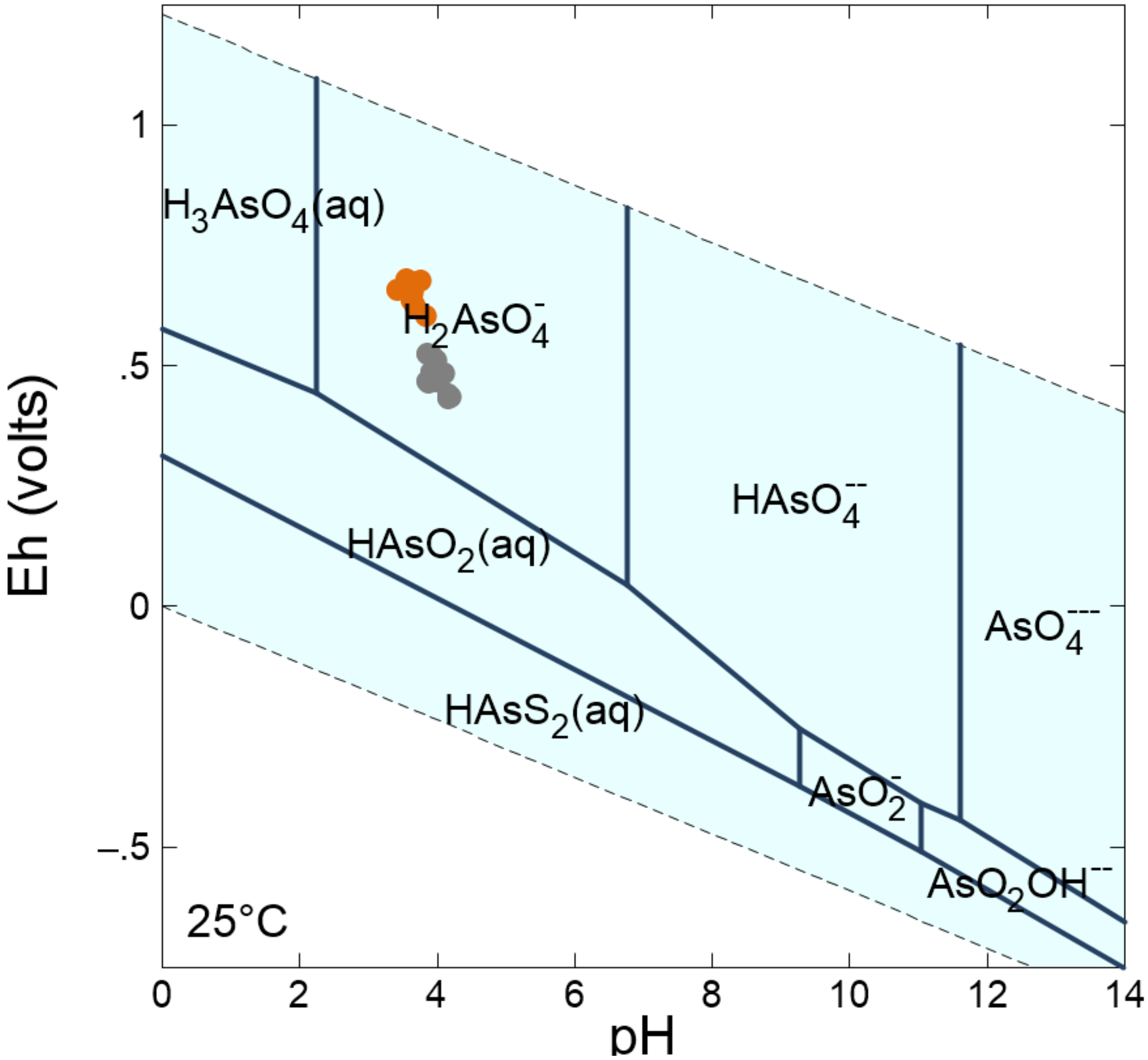

Figure 34: Eh vs pH diagram for aqueous arsenic species at standard conditions (25°C and 1 atm; log activity of As at -5). Orange = Samples from Oxic Zone, Grey = Samples from Transition Zone.

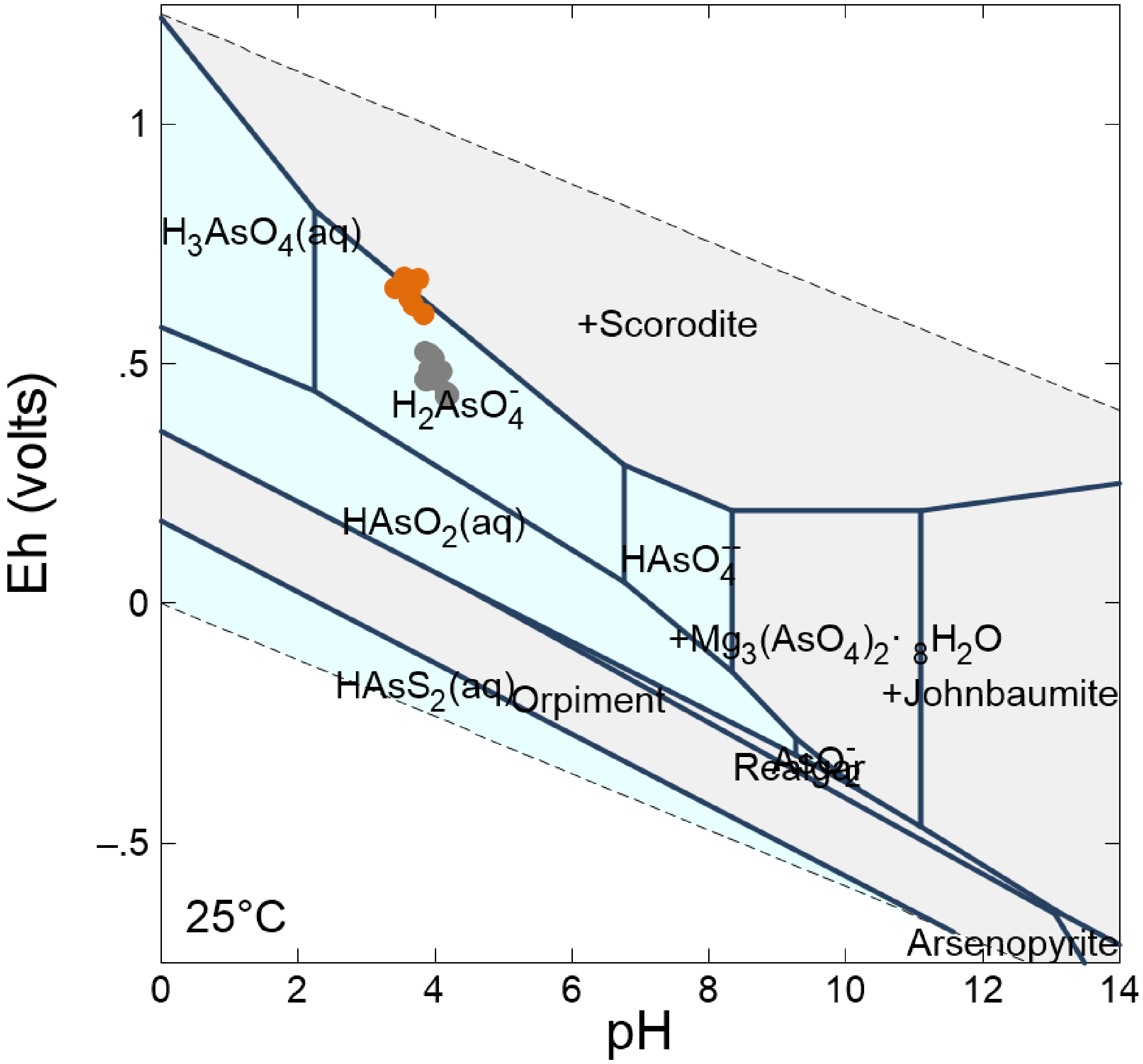

Figure 35: Eh vs pH diagram for different arsenic species at standard conditions (25°C and 1 atm; log activity of As at -5) (Minerals suppressed: bukovskyite, Fe-amorphous, Fe-crystalline, kankite, parascorodite, pharmocolite, symplesite). Orange = Samples from Oxic Zone, Grey = Samples from Transition Zone.

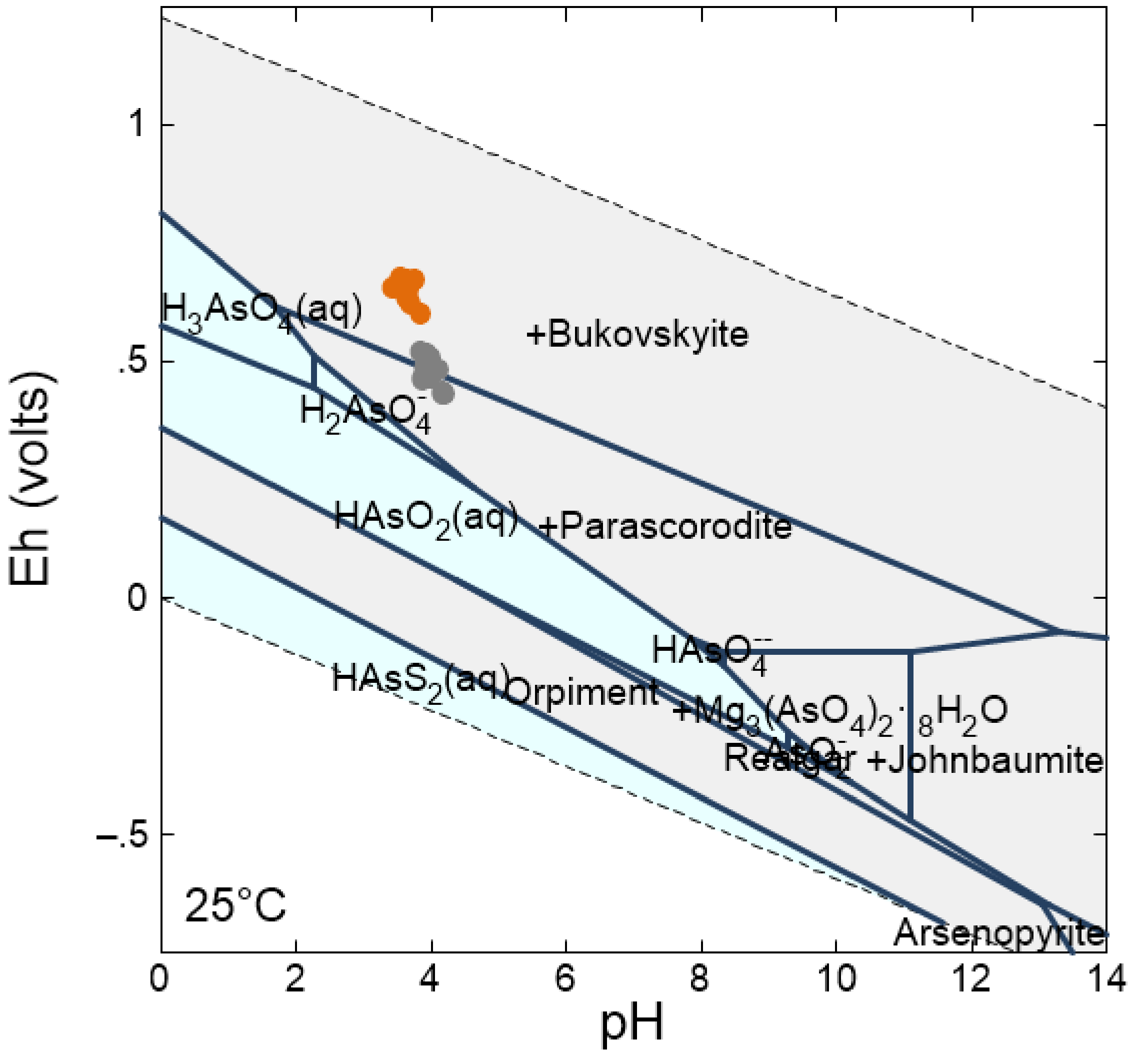

Figure 36: Eh vs pH diagram for different arsenic species at standard conditions (25°C and 1 atm; log activity of As at -5) (Minerals suppressed: pharmocolite, symplesite). Orange = Samples from Oxic Zone, Grey = Samples from Transition Zone.

5.3.4 Base Metal Sulphides and Stability

Pyrite is the dominant sulphide in the gold tailings, and only traces of other sulphides were identified through scanning electron microscopy. Together with arsenopyrite discussed above, these sulphides will, upon oxidation, exert a major control on the distribution of trace metal(loid)s (e.g. As, Co, Cu, Ni, Pb, and Zn) in the tailings. The simplified dissolution of these minerals in the presence of oxygen is as follows:

$$\text{Pyrrhotite } FeS + 2.25O_2(aq) + 2.5H_2O \rightarrow Fe(OH)_3 + SO_4^{2-} + 2H^+$$

Equation 35

Pentlandite $(Fe,Ni)_9S_8 + 17.63O_2(aq) + 10.25H_2O \rightarrow 4.5Ni^{2+} + 4.5Fe(OH)_3 + 8SO_4^{2-} + 7H^+$

Equation 36

Galena $PbS + 2O_2(aq) \rightarrow Pb^{2+} + SO_4^{2-}$

Equation 37

Chalcopyrite $CuFeS_2 + 4.25O_2(aq) + 2.5H_2O \rightarrow Cu^{2+} + Fe(OH)_3 + 2SO_4^{2-} + 2H^+$

Equation 38

Sphalerite $ZnS + 2O_2(aq) \rightarrow SO_4^{2-} + Zn^{2+}$

Equation 39

Kinetic rates for these sulphides are less common in literature than for pyrite. Cama et al. (2006) note that some sulphides like pyrite, galena, and arsenopyrite dissolve significantly slower in the absence of dissolved oxygen, but the dissolution rate of sphalerite and chalcopyrite are independent of the dissolved oxygen concentration. It is, however, not clear what pH range they are referring to, as pyrite oxidation is also not directly a function of oxygen below pH 3, although the reaction will still take place in the presence of oxygen. No kinetic rate for pentlandite could be found in the literature, and the dissolution rates ($mol.m^{-2}.s^{-1}$) of galena (pH 2 - 3), chalcopyrite (pH 1 - 3) and sphalerite (pH 1 - 4.2) were taken from Acero et al. (2007), Acero et al. (2009) and Acero et al. (2013) respectively, and are presented as Equation 40 to Equation 42 below:

$$r = 10^{-8.5}\frac{a_{DO}^{0.30}}{a_{H^+}^{0.78}}$$

Equation 40

$$r = 10^{-5.20}a_{H^+}^{0.16}$$

Equation 41

$$r = 10^{-6.49}a_{H^+}^{0.54}$$

Equation 42

Figure 37 to Figure 40 shows the stability of nickel, lead, copper and zinc (activities at 10^{-5}) aqueous species using the activity of parameters of the 8.3 - 9.3 m deep tailings water sample from Section 4.8.

Nickel, copper and zinc do not precipitate as secondary minerals at pH 3 - 5 and will be quite mobile in the interstitial water. This will result in these metals will be easily leached from the Oxic Zone, as was also observed in the whole rock elemental composition of the tailings, as shown in Section 4.4. In contrast, lead is less mobile, and lead released from the oxidation of galena, will also be prone to precipitate with sulphate as anglesite. The cerussite stability field is large, and above pH 4, the lead will precipitate with carbonate as cerussite.

These metals may also adsorb to some degree to iron-(hydr)oxides in the tailings dam. In the review of metal adsorption on mineral surfaces by Smith (1997), she notes that the sorption selection on most metal-oxide minerals follows the sequence Cr > Pb > Cu > Co > Zn, Ni > Cd. However, under the pH conditions of the Oxic Zone (pH 3 – 4), only lead will be prone to adsorption, and copper will only adsorb at a pH of about 4 – 5, with zinc and nickel only at pH values above this.

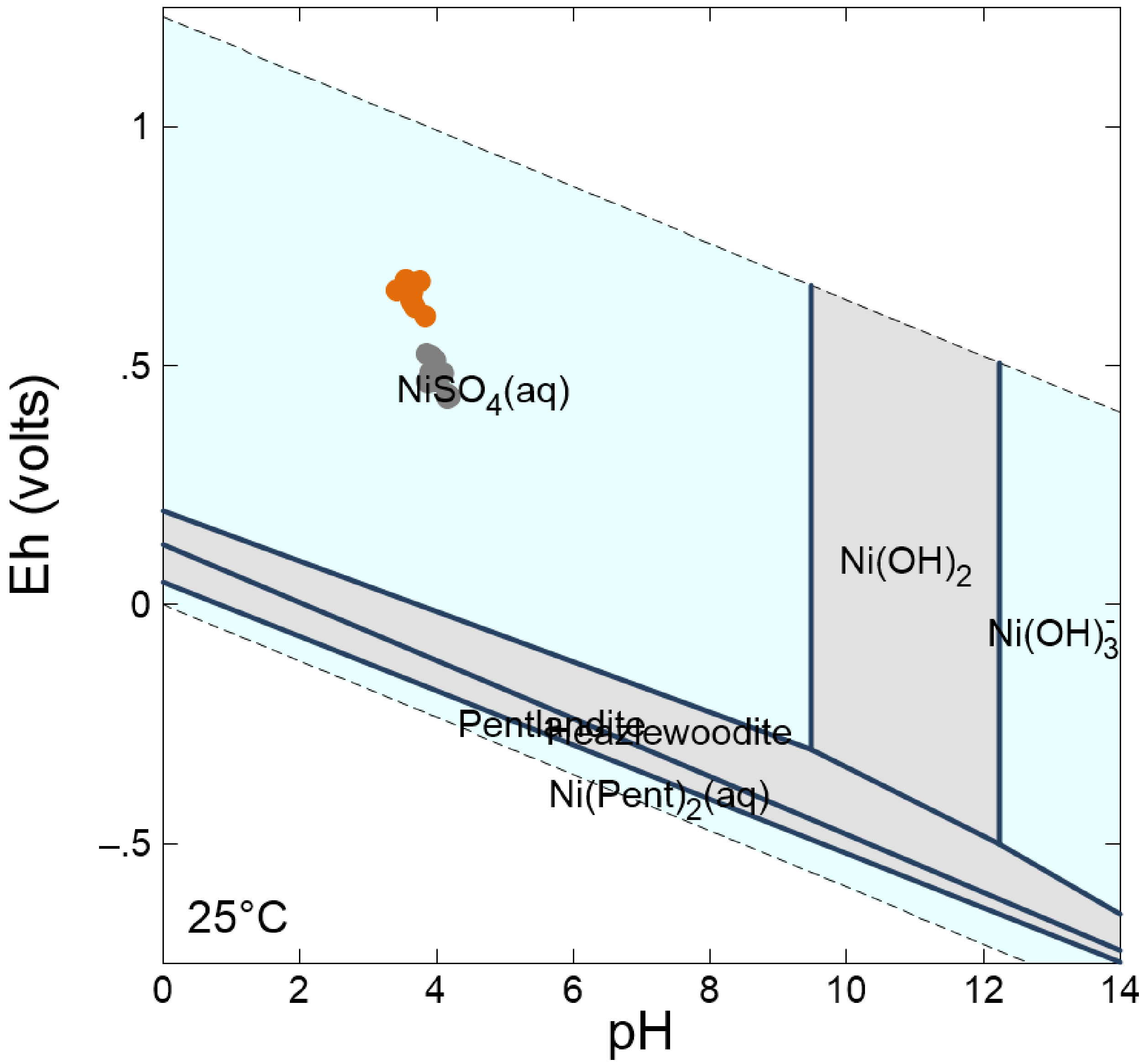

Figure 37: Eh vs pH diagram for different lead species at standard conditions (25°C and 1 atm; log activity of Ni at -5). Orange = Samples from Oxic Zone, Grey = Samples from Transition Zone.

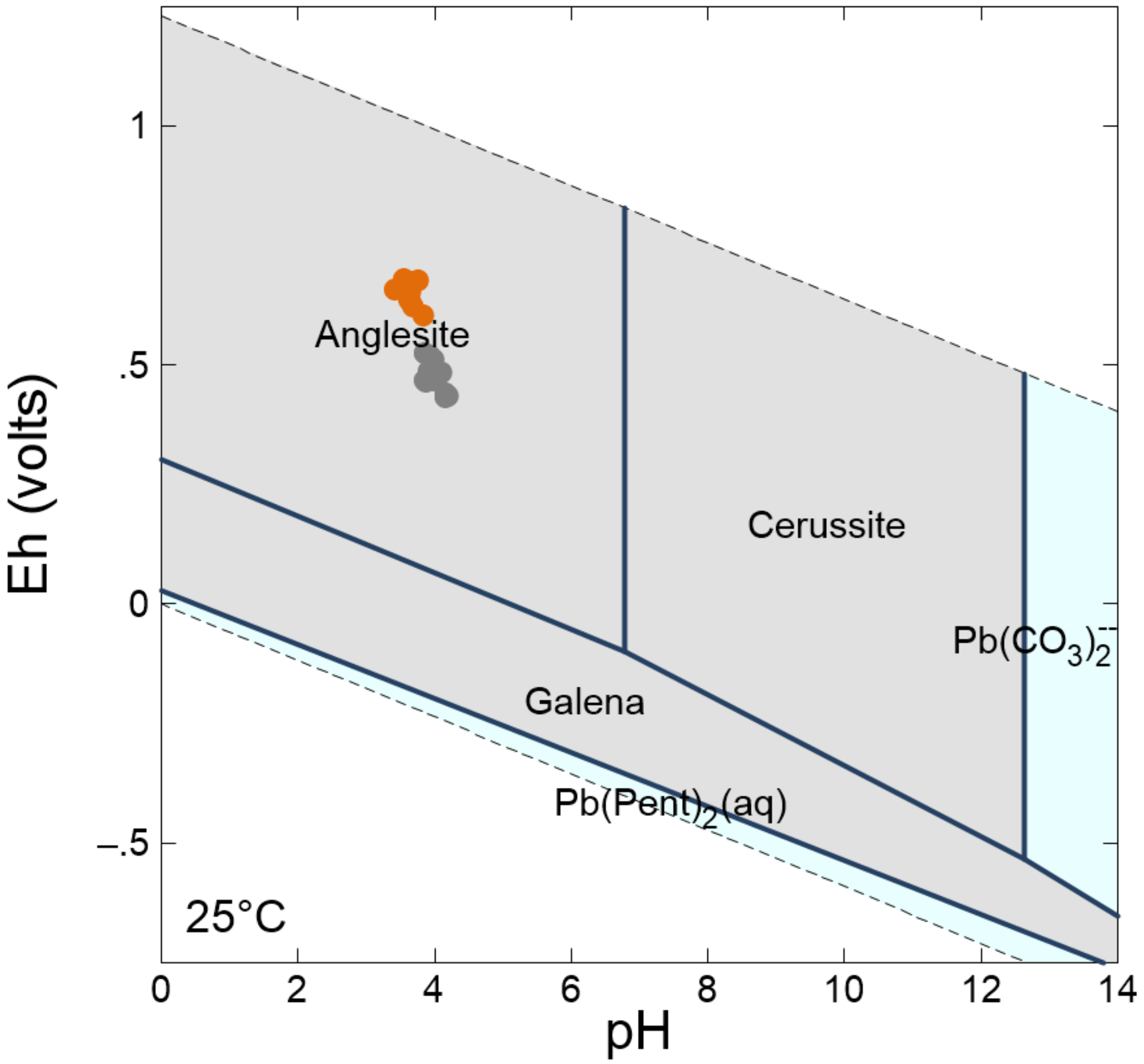

Figure 38: Eh vs pH diagram for different lead species at standard conditions (25°C and 1 atm; log activity of Pb at -5). Orange = Samples from Oxic Zone, Grey = Samples from Transition Zone.

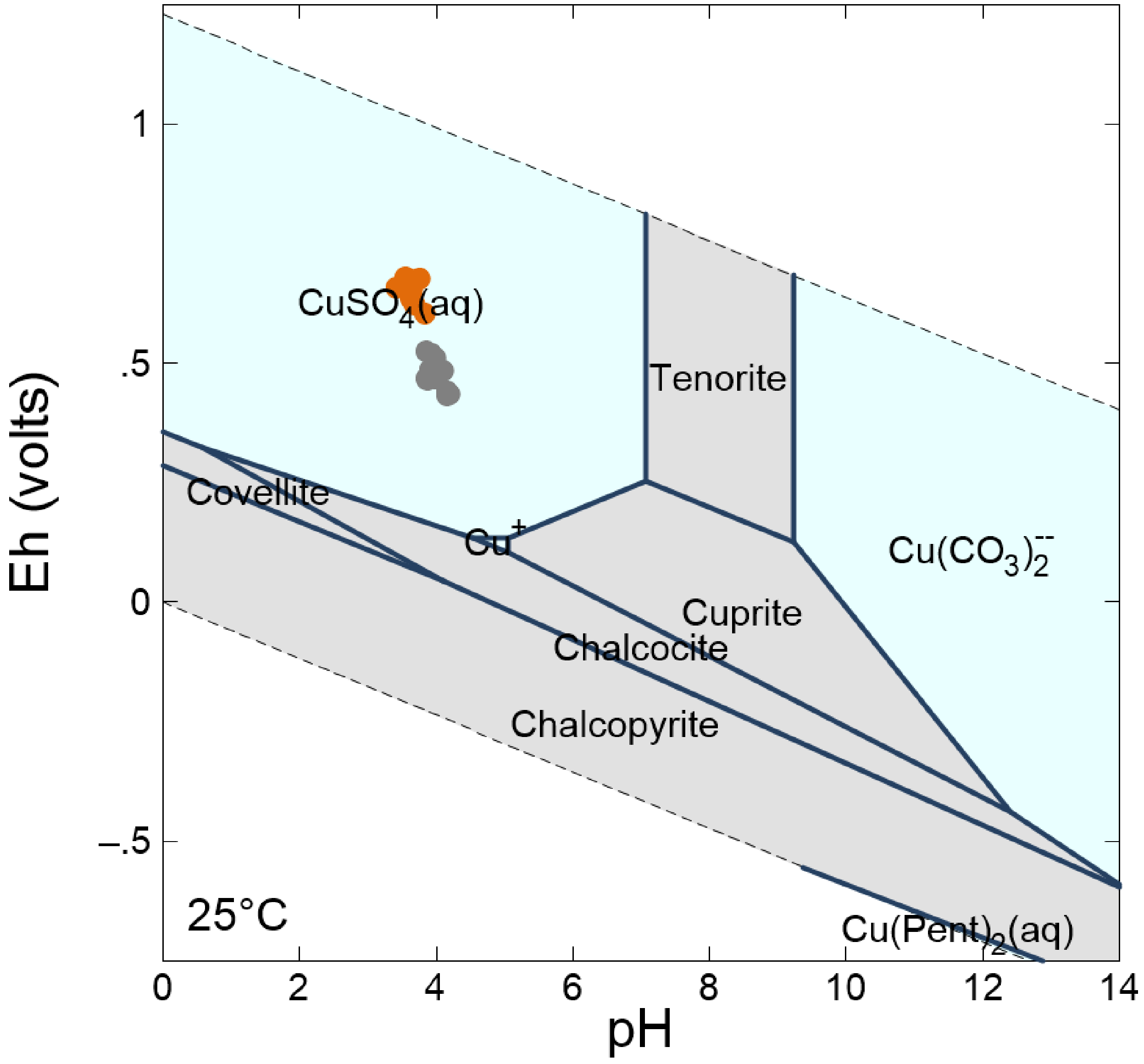

Figure 39: Eh vs pH diagram for different copper species at standard conditions (25°C and 1 atm; log activity of Cu at -5). Orange = Samples from Oxic Zone, Grey = Samples from Transition Zone.

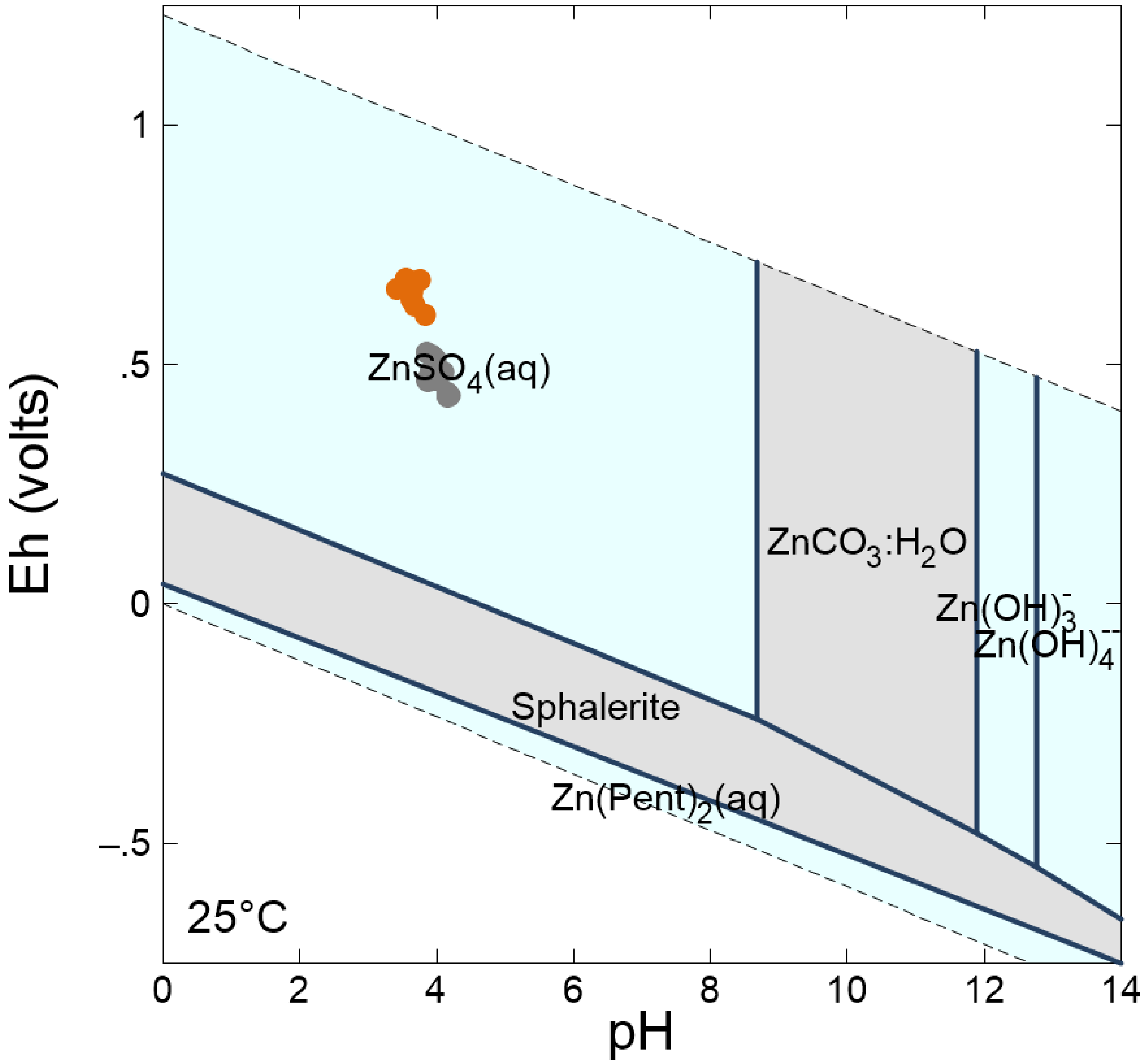

Figure 40: Eh vs pH diagram for different zinc species at standard conditions (25°C and 1 atm; log activity of Zn at -5). Orange = Samples from Oxic Zone, Grey = Samples from Transition Zone.

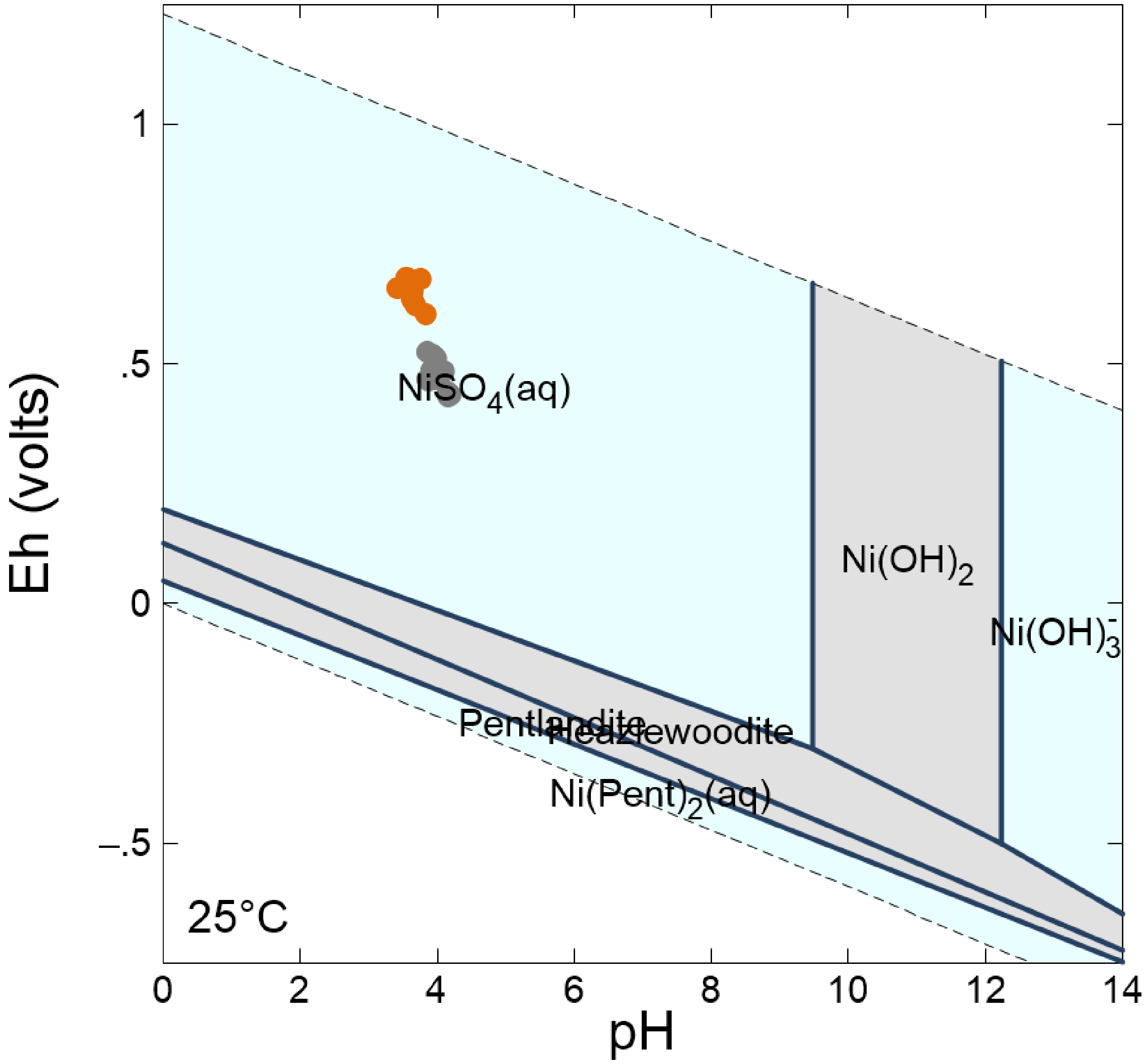

Figure 41: Eh vs pH diagram for different arsenic species at standard conditions (25°C and 1 atm; log activity of As at -5) (Minerals suppressed: pharmocolite, symplesite). Orange = Samples from Oxic Zone, Grey = Samples from Transition Zone.

5.3.5 Uranium Minerals and Stability

Detrital uraninite (U, Th)O_2 and authigenic uranous titanates $(U,Th)_{1-x}Ti_{2+x}O_6$ are the major uranium minerals and are about equally distributed in reefs exploited for uranium (Smits, 1990), as discussed in Section 2.3.6. Uraninite is unstable in an oxygen-rich environment and would oxidise by oxygen as follows:

$$\text{Uraninite } UO_2 + 0.5\ O_2(aq) + 2H^+ \rightarrow H_2O + UO_2^{++}$$

Equation 43

The oxidation rate of uraninite (mol.m^{-2}.s^{-1}) by oxygen (pH 3 – 6.7) is given by (Torrero et al., 1997) as follows:

$$r = 10^{-7.5} a_{DO}^{0.31} a_{H^+}^{0.37}$$

Equation 44

Uranyl (UO_2^{2+}) will mostly form soluble carbonate and sulphate complexes, as shown in Figure 42. Several secondary Ca-, Mg-, Na- and K-uranyl minerals can precipitate from the solution. The uranyl is stored in these secondary highly reactive phases for potential release. The store-and-release effect of uranyl in secondary uranyl phases is described by Gorman-Lewis et al., (2008). Uranyl (UO_2^{2+}) will be fairly mobile in the Oxic Zone. Uranyl will precipitate above pH 4 in the Anoxic Zone as hydrous uranyl sulphate (e.g. zippeite-Mg, $Mg_2(UO_2)_6(SO_4)_3(OH)_{10}$:$4H_2O$ or other Ca-, Mg-, Na- and K-uranyl sulphates), as illustrated in Figure 43.

Of the above radionuclides, uranium is the most soluble because of its complexation with carbonate and sulphate. Thorium will be fairly immobile and precipitate mostly as ThO_2. Elemental analyses showed no leaching of thorium from the Oxic Zone, as discussed in Section 4.4.3. Radium, like barium, forms the Ra^{2+} cation in an aqueous solution that does not readily form complexes. Insoluble radium compounds (e.g. sulphates) co-precipitate with all barium, most strontium, and most lead compounds.

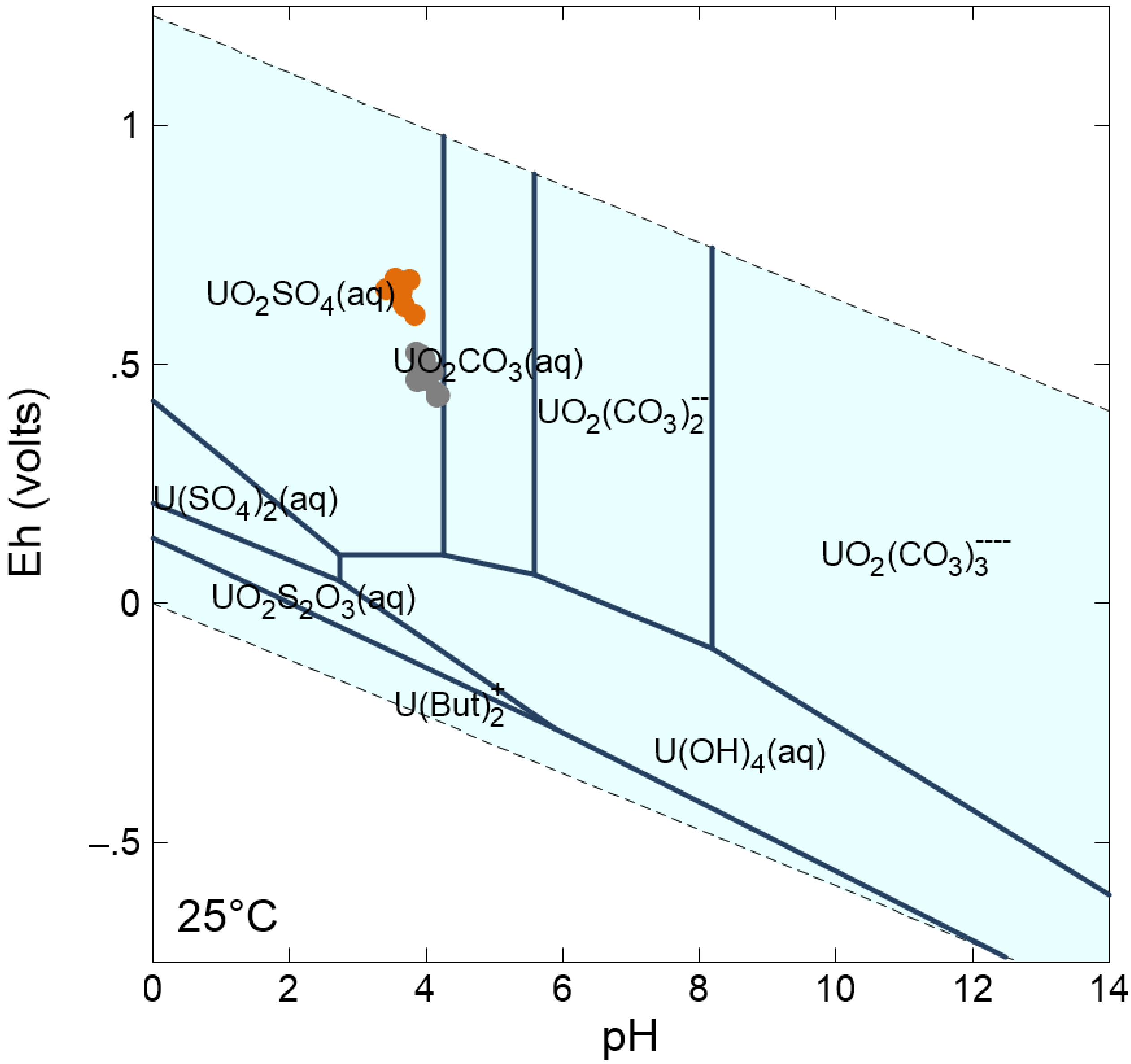

Figure 42: Eh vs pH diagram for aqueous species of the U-CO_3-SO_4-H_2O system at standard conditions (25°C and 1 atm; UO_2^{++} log activity at -5; HCO_3 log activity -3). Orange = Samples from Oxic Zone, Grey = Samples from Transition Zone.

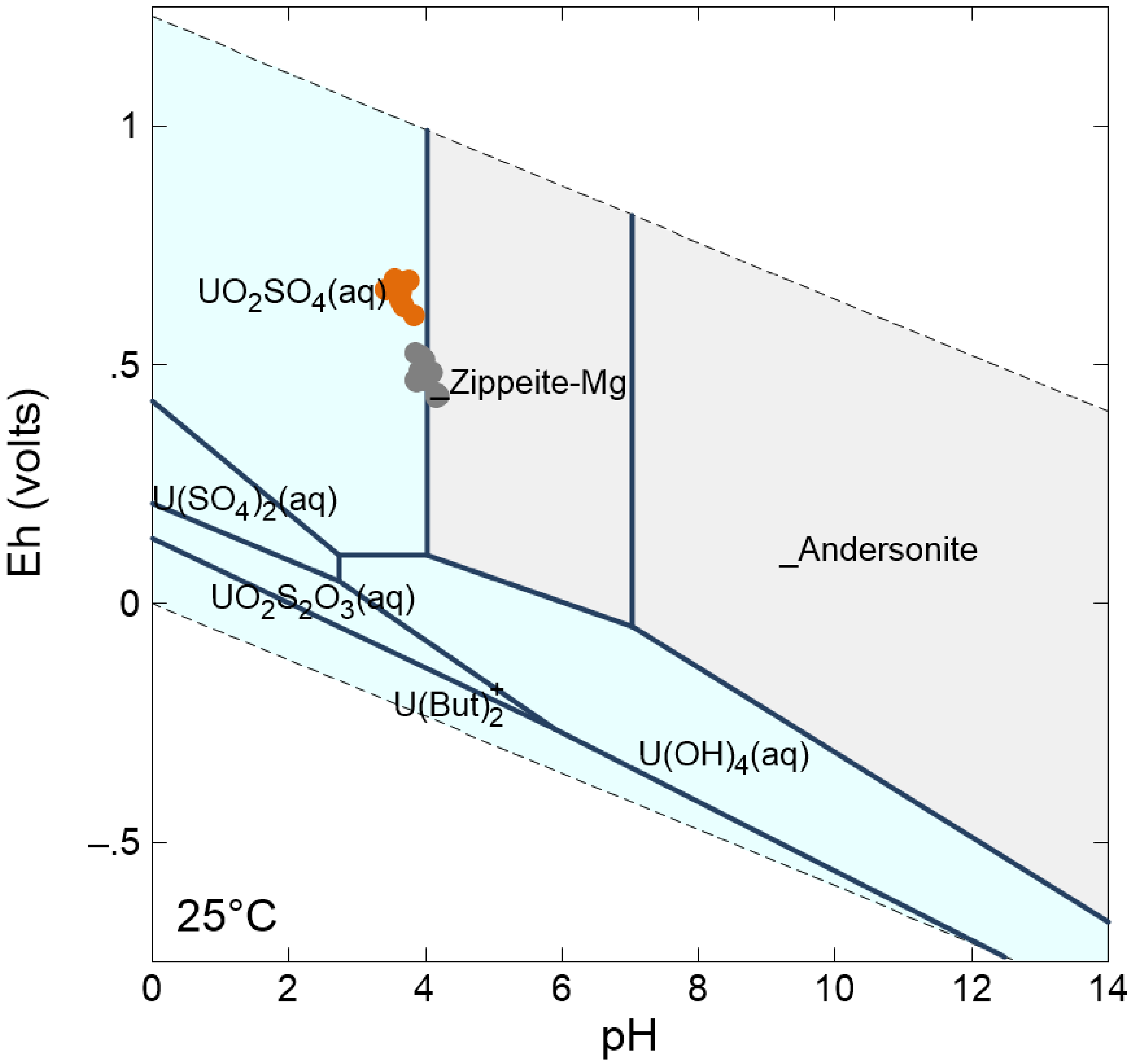

Figure 43: Eh vs pH diagram for the U-CO_3-SO_4-H_2O system at standard conditions (25°C and 1 atm; UO_2^{++} log activity at -5; HCO_3 log activity -3). Orange = Samples from Oxic Zone, Grey = Samples from Transition Zone.

5.3.6 Alumino-Silicate Minerals

Aluminium is present at about ~200 mg/l in the tailings water samples (See Section 4.8.3), which indicates significant weathering of alumino-silicates. Despite having no acid neutralisation potential, the tailings can still maintain a pH in the 3.5 – 4.2 range due to the reaction of alumino-silicates, i.e., muscovite and chlorite.

Muscovite is present as a minor to intermediate mineral at between 11 – 21 wt%. There is a fair amount of potassium present in water samples which could mostly be attributed to the dissolution of muscovite. As discussed in Section 4.8.3, the ammonium present in all water samples may also originate from the weathering of the muscovite in the tailings dam. Muscovite will consume 10 mol of hydrogen upon weathering:

Muscovite $KAl_3Si_3O_{10}(OH)_2 + 10H^+ \rightarrow 6H_2O + 3Al^{3+} + 3SiO_2(aq) + K^+$

Equation 45

The kinetic rate of muscovite ($mol.m^{-2}.s^{-1}$) from Nagy (1995) were used for muscovite:

$$r = 10^{-11.85} a_{H^+}^{0.37}$$

Chlorite is present as a trace to a minor mineral at between 1 – 4 wt% in the tailings. Magnesium is present in the tailings water, which could be attributed to the weathering of chlorite, although the chlorite is expected to be Fe-Mg-chlorites (e.g. Smits, 1990). Fe-Chlorite will consume 6 mol of hydrogen upon weathering:

Chamosite $Fe_2Al_2SiO_5(OH)_4 + 6H^+ + 0.5O_2(aq) \rightarrow 2H_2O + 2Al^{3+} + SiO_2(aq) + 2Fe(OH)_3$

Equation 46

For chlorite, the kinetic rate ($mol.m^{-2}.s^{-1}$) from Lowson et al. (2005) was used. The rate is proportional to the hydrogen activity and inversely proportional to the aluminium activity:

$$r = 10^{-10.46} \left(\frac{a_{H^+}^3}{a_{Al^{3+}}} \right)^{0.27}$$

Equation 47

5.3.7 Carbonate Minerals

Carbonate minerals would not endure the acidic conditions under which the Witwatersrand sediments were deposited (Smits, 1990). Smits (1990) also notes that carbonates would anyway be destroyed under post-burial conditions. Samples from the tailings dam investigated in this study had a paste pH of ~3.5 - 4 in the Oxic and Transition Zone. There are not ample samples from the Anoxic Zone. The water sample collected at 8.3 – 9.3 m deep (anoxic zone) had a pH of 4.03. Yibas et al. (2010) report that the paste pH of a sample from the Anoxic Zone on the same tailings dam had a paste pH of 6.4, which creates some inconsistency with the observation made in this study as well as with some other observations in their study. In the same study, they also reported water extracts of tailings from the Anoxic Zone to be at pH 4 (see Section 2.8). Despite having near-zero neutralisation potential, some Witwatersrand Tailings Dams still produce neutral seepage from some of the dams (e.g. Fourie, 2013). It is often argued that the addition of lime to the tailings may contribute to the increased calcium content in the tailings and the gypsum and (at least temporal) calcite precipitation in the tailings. This is because there is no major calcium-containing mineral that could have resulted in the observed calcium present in seepage.

In the numerical geochemical model, both acidic and more circum-neutral conditions deeper in the tailings dam will be considered.

The carbonate system is briefly discussed because the top of the tailings will be in contact with atmospheric CO_2. Alkalinity is the ability to consume or neutralize acidity. The sum of all the concentrations of acidity (H^+) consuming (inorganic) ions, namely hydroxide [OH^-], carbonate [CO_3^{2-}], and bicarbonate [HCO_3^-], is known as carbonate alkalinity:

$$\text{carbonate alkalinity} \text{ -> } [HCO_3^-] + 2[CO_3^{2-}] + [OH^-] - [H^+]$$

Equation 48

The carbonate mineral calcite ($CaCO_3$) can neutralize acid and provide alkalinity as follows:

$$CaCO_3 \text{ -> } Ca^{2+} + CO_3^{2-} \ (pH > 10.3)$$

Equation 49

$$CaCO_3 + H^+ \rightarrow Ca^{2+} + HCO_3^- \ (6.4 < pH < 10.3)$$

Equation 50

$$CaCO_3 + 2H^+ \text{ -> } Ca^{2+} + H_2CO_3 \ (pH < 6.4)$$

Equation 51

The H_2CO_3 largely decomposes to $CO_2(aq)$ ($pH < 6.4$):

$$H_2CO_3 \rightarrow CO_2(aq) + H_2O$$

Equation 52

Appelo & Postma (2005) state that at $pH < 6.4$ (at 25°C), $CO_2(aq)$ is about 250 times more abundant in solution than $H_2CO_3(aq)$. If a gas phase is present (i.e. open system), the $CO_2(aq)$ will equilibrate with $CO_2(g)$:

$$CO_2(aq) \rightarrow CO_2(g)$$

Equation 53

If the atmosphere is in full contact with the solution (open system), the $CO_2(g)$ will serve as a buffer and equilibrate with $CO_2(aq)$, where the average log fugacity of $CO_2(g)$ in the atmosphere is -3.5.

6 BATCH REACTOR EXPERIMENTS

6.1 Introduction

The objective of the batch reactor testing was to calculate the effective surface area of the pyrite in the tailings based on its reaction rate in a batch reactor. The batch reactor test does not have the limitations of secondary minerals that may precipitate (a typical problem in humidity cell tests that uses a much lower water-to-rock ratio) and complicates the interpretation of the results. The other advantage of the test is that it is performed over several days instead of months, like humidity cell testing. Batch reactor tests, however, require that excess soluble sulphate minerals (like gypsum) are removed from the solid sample so that the change in sulphate concentration in the solution could be designated to pyrite oxidation. The results will be used further for the numerical model of the tailings in Section 7.

6.2 Instruments and Methods

6.2.1 Experimental Setup

The test was performed on the sampled interval 598 – 614 cm, on which SEM analyses were also performed. This sample was selected as it is from the Anoxic Zone, and pyrite would not have been exposed to oxygen. The SEM images show that pyrite grains did not have any identifiable oxidation rim. The sample did, however, have gypsum minerals present, which could easily be removed. Other sulphates like jarosite or alunite were also not detected. Grain size analyses were performed on the sample, and XRD (Section 4.6.3) and sulphur analyses (Table 17, Section 6.2.2) were conducted on each grain size fraction.

To expose fresh surfaces on the pyrite for the dissolved oxygen to react with, any potential oxidation products, such as hydrous iron-sulphate coatings, were first removed. Secondary sulphates in the sample, like gypsum, should also be removed as pyrite oxidation should be the sole contributor to the sulphate in the solution during the experiment. This was performed by submerging the sample for 24 h in 1M HCl and rinsing it three times after that with a fresh solution of HCl, whereafter, the sample was rinsed three times with deionised water. This was lastly followed by drying the sample in a crucible at approximately 110^0C for 10 - 15 minutes. The clean, dry pyrite sample was weighed to the required mass and used immediately for the experimental run.

The experiment was performed at pH ~3, ~5, and ~7. Three 1 000 mL Erlenmeyer flasks were fitted with a sampling port as well as a pH probe fitted through the stopcock. The water-pyrite mixture was kept in equilibrium with atmospheric oxygen by continuously bubbling air through the solution through the sampling port. The flask was placed into a water bath preheated at 25^0C. The Erlenmeyer flask was filled with 400 mL of deionized water. A magnetic stirrer was used to continuously stir the solution.

The prepared tailings sample mass of 100 g was added to each flask. The pH of the solution in each flask was adjusted to pH 3, 5 and 7 by adding drops of either HCl or NaOH. The duration of the experiment was 340 hours, over which 10 ml aliquots of the solution were withdrawn from the reactor every 12 h and were subsequently analysed by means of ICP-OES. The first sample was collected after the first pH adjustment and was taken as the zero measurements. After every aliquot of sample was extracted, the same volume (10 ml) of deionised water was added to the reaction solution to maintain the volume of 400 mL.

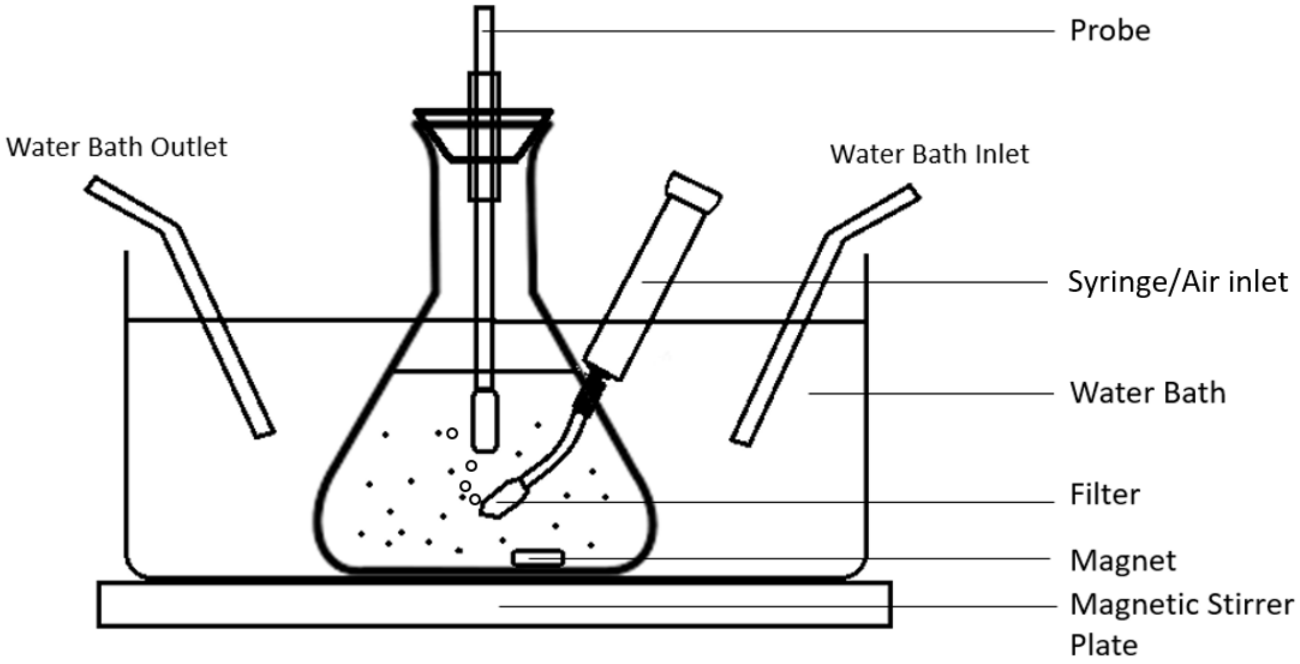

Figure 44: The batch reactor experimental setup for each flask.

6.2.2 Tailings Sulphur Analyses

The pyrite and gypsum mass were calculated from the sulphide sulphur and sulphate sulphur contents, respectively. Quantitative sulphur analyses per grain size fraction for this sample are summarised in Table 17 below. The sulphur was determined using an Eltra Furnace with infrared analyses as described before (Section 4.4).

Most of the calculated gypsum (~73%) is associated with the coarse (>250 um; medium to coarse sand) fraction of the sample. This is because gypsum was not subjected to the milling process (as the other minerals) but precipitated in the tailings dam, as observed in the SEM analyses. Sulphide sulphur is fairly distributed over all grain fractions. The highest proportion of the calculated pyrite fraction (~72 %) was, however, present in the -75 um fraction, although ~18 wt% was also present in the +425 um fraction. Some of the pyrite in the coarse fraction could, however, be particles on quartz or replacements of grains, as observed in the SEM analyses.

Table 17: Sulphur analyses per grain size fraction of 6.14 – 6.30 m (wt%)

Grain size (um)	Weight of fraction (%)	Total Sulphur %	Sulphide Sulphur %	Sulphate Sulphur %	Calculated Pyrite (g/100 g)	Pyrite distri-bution (%)	Calculated Gypsum (g/100 g)	Gypsum distri-bution (%)
+425	10.66	2.152	1.530	0.623	0.358	18.4	0.538	49.7
+355	1.14	1.655	0.916	0.739	0.023	1.18	0.063	5.81
+300	1.52	1.477	0.907	0.570	0.030	1.56	0.066	6.12
+250	1.96	1.732	0.876	0.855	0.038	1.95	0.124	11.4
+212	0.75	1.734	0.851	0.883	0.014	0.720	0.048	4.47
+180	1.42	1.509	0.804	0.706	0.025	1.29	0.074	6.86
+125	5.32	0.630	0.450	0.180	0.053	2.71	0.078	7.18
+75	19.79	0.232	0.231	0.001	0.101	5.18	0.025	2.33
+63	32.45	0.783	0.779	0.004	0.594	30.6	0.029	2.65
+50	13.82	0.996	0.980	0.016	0.318	16.4	0.027	2.47
-50	11.17	1.379	1.359	0.020	0.389	20.0	0.011	0.99
Total	100.00	-	-	-	1.943	100.00	1.082	100.00
Weighted Average	-	1.240	1.039	0.201	-	-	-	-

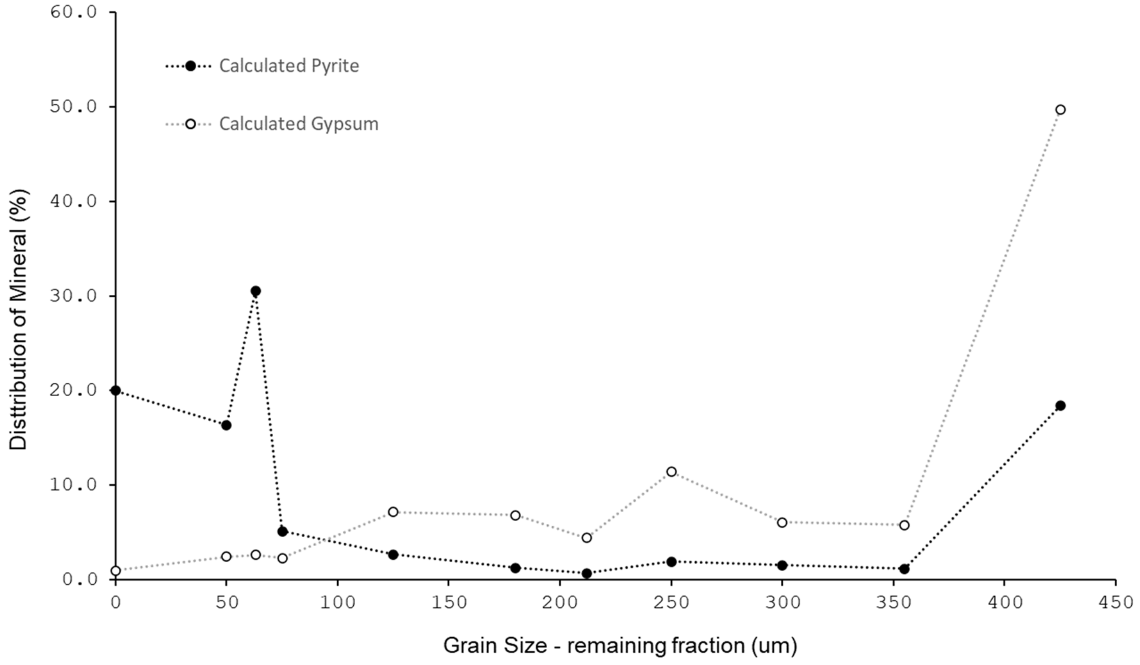

Figure 45: Calculated pyrite and gypsum per grain size fraction (the -50 um passing fraction is presented as 0 um in the graph)

6.2.3 Numerical Simulation

The interaction between the minerals, water, and gas phases was modelled using the *Geochemist's Workbench (GWB)*. GWB is a set of interactive software tools for solving problems in aqueous geochemistry, including *React*, for reactive transport and *X1t* and *X2t*, for one and two-dimensional modelling. The software solves the hydro-chemical and mineral reactions with the equilibrium model and the kinetic rate law for mineral dissolution.

ChemPlugin is a *GWB* software object that can be used to create reactive transport simulations in the required configuration. A subroutine was written in *Python 3.8* programming language, which used *ChemPlugin* to model the various scenarios, display their results, and perform statistical analyses.

6.2.4 Statistical Analyses

The test results were used to determine the effective surface area of the pyrite. The Error Sum of Squares (SSE) and the Total Sum of Squares (SSTO) were calculated for the data. SSE is the "error sum of squares" and quantifies how much the data points, y_i, vary from the estimated values, $\hat{y}_i$. SSTO is the "total sum of squares" and quantifies how much the data points, y_i, vary around their mean, $\bar{y}$:

$$SSE = \sum_{i=1}^{n} (y_i - \hat{y}_i)^2$$

Equation 54

$$SSTO = \sum_{i=1}^{n} (y_i - \bar{y})^2$$

Equation 55

To determine the best fit for the calculation, the Coefficient of Determination (r^2) was calculated from the Error Sum of Squares (SSE) and the Total Sum of Squares (SSTO):

$$r^2 = 1 - \frac{SSE}{SSTO}$$

Equation 56

6.3 Results

6.3.1 Batch Reactor Results

The batch reactor results for the three experiments are summarised in Table 16 below. The experiments were performed over about 14 days. Except for the last few days, samples were collected twice a day (morning and late afternoon). After every sampling, the pH was corrected. An interesting observation was that for the pH~3 experiment, the pH was always slightly above pH 3 (and had to be lowered with HCl) due to buffering of alumino-silicate minerals. For the pH ~5 and ~7 experiments, the pH was always slightly below the target pHs and had to be adjusted with NaOH.

The sulphate production was the lowest in the pH ~3 experiments and the highest in the pH ~7 experiment. This is because the oxidation of pyrite by oxygen is inversely proportional to the hydrogen activity, as discussed in Section 5.3.1. Given the sulphate production, the effective surface area of the pyrite could be calculated in the following section.

Table 18: Batch reactor results at pH ~3, pH ~5 and pH ~7.

Experiment 1 pH ~3			**Experiment 2 pH ~5**			**Experiment 3 pH ~7**		
Time (hour)	**pH**	**S as Sulphate (mg/l)**	**Time (hour)**	**pH**	**S as Sulphate (mg/l)**	**Time (hour)**	**pH**	**S as Sulphate (mg/l)**
0.0	3.050	21.154	**0.0**	4.743	21.010	**0.0**	6.793	24.575
5.5	3.094	19.443	**8.0**	4.743	21.667	**5.5**	6.678	26.231
7.5	3.054	22.403	**13.6**	4.886	20.601	**7.5**	6.869	27.092
16.5	3.079	22.108	**23.0**	4.892	22.567	**16.5**	6.641	29.913
23.0	3.054	21.814	**27.0**	4.945	24.293	**23.0**	7.044	32.648
28.0	3.054	24.828	**34.6**	4.953	24.607	**28.0**	7.265	32.857
32.0	3.040	25.652	**39.5**	4.949	25.658	**32.0**	6.954	33.972
40.0	3.060	21.995	**47.0**	4.949	27.228	**40.0**	6.838	34.617
45.5	3.025	25.409	**52.0**	4.949	28.041	**45.5**	6.916	36.773
55.0	3.059	26.468	**60.0**	4.959	28.855	**55.0**	6.979	38.906
59.0	3.005	26.667	**64.0**	5.050	30.502	**59.0**	7.015	37.353
66.5	3.015	26.591	**72.5**	4.969	32.293	**66.5**	6.964	39.239
71.5	3.039	26.899	**76.0**	4.984	32.466	**71.5**	6.959	41.569
79.0	3.000	26.893	**82.0**	4.939	33.271	**79.0**	7.080	44.200
84.0	3.015	26.440	**88.0**	4.940	34.000	**84.0**	6.904	48.417
92.0	3.005	26.750	**94.0**	4.968	34.425	**92.0**	6.838	50.913
96.0	3.035	26.485	**100.0**	4.975	36.990	**96.0**	6.964	48.902
104.5	3.030	25.621	**106.0**	4.980	38.004	**104.5**	6.929	49.774
108.0	3.020	28.629	**112.0**	4.983	35.076	**108.0**	6.853	54.213
120.0	3.010	28.966	**118.0**	4.973	34.244	**120.0**	6.913	55.623
132.0	3.019	30.948	**124.0**	5.029	38.944	**132.0**	6.948	56.266
144.0	3.015	27.125	**148.0**	4.959	39.628	**144.0**	7.014	55.899
156.0	3.024	29.848	**160.0**	4.975	43.330	**156.0**	6.913	58.590
168.0	3.010	32.777	**172.0**	4.975	48.273	**168.0**	6.966	62.606
Geomean	3.034	-	-	4.944	-	-	6.925	-

6.3.2 Modelling

Pyrite Surface Area of the pH 3 experiment

The ~pH 3 experiment results were used to back-calculate the effective surface area of the pyrite that would be required to produce the results. The calculation was performed according to the oxidation of pyrite below, where 2 moles of sulphate are produced from 1 mole of pyrite reacted:

$$FeS_2 + H_2O + 3.5O_2(aq) \rightarrow Fe^{2+} + 2SO_4^{2-} + 2H^+$$

The pyrite oxidation rate by oxygen from Williamson & Rimstidt (1994) was used (Section 5.3.1). Using the rate law, an inverse calculation was performed to calculate the surface area of the pyrite. The pH was fairly constant for each experiment, as discussed in the results above. The solution was also in equilibrium with the atmosphere, which was achieved by bubbling air through the solution. The only unknown, therefore, was the effective surface area of the pyrite. The experimental results were modelled for a range of hypothetical pyrite surface areas in 10 g/cm^2 intervals. The coefficient of determination (R^2) was calculated for each model. These were plotted, fitted, and the maxima calculated to determine the surface area that would best fit the data. The R^2 values against the model pyrite surface areas are plotted in Figure 46 below. The optimal surface area was determined at 1046.26 g/cm^2. The calculated sulphate concentration for the pH ~3 experiment, using a pyrite surface area of 1046.27 g/cm^2, was plotted against the measured concentrations in Figure 47 below.

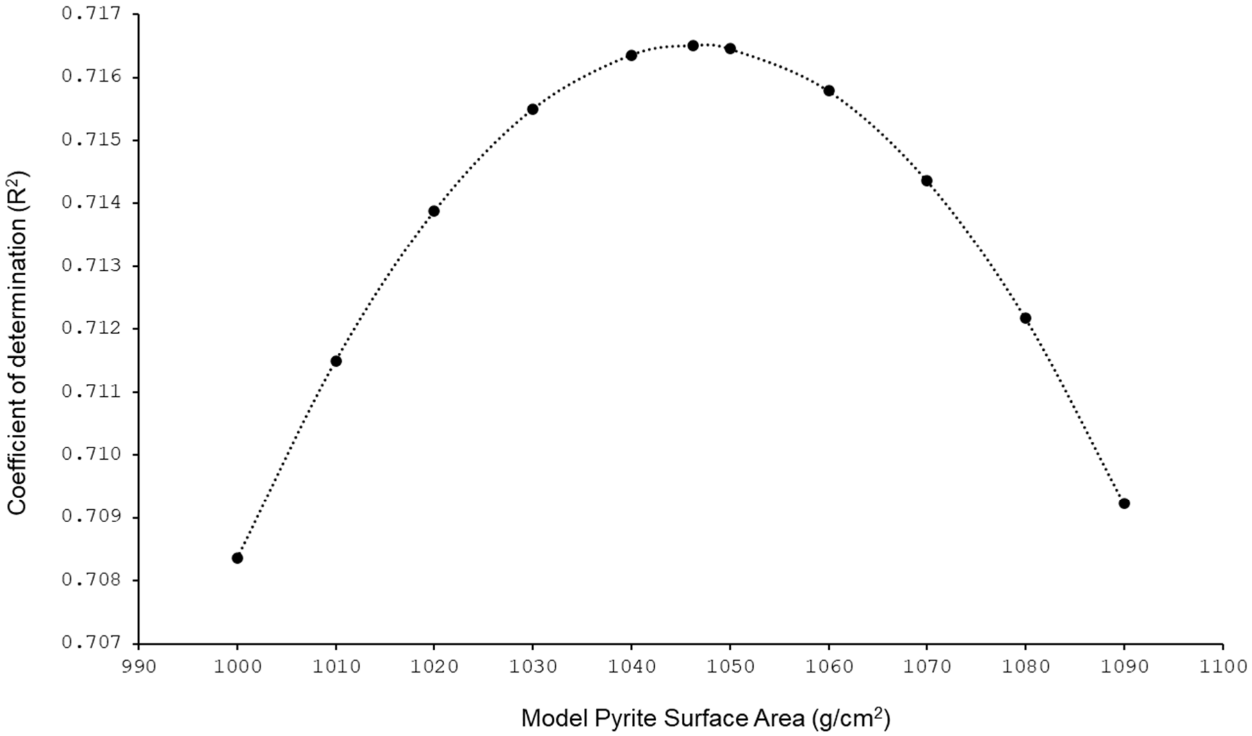

Figure 46: Coefficient of determination against model pyrite surface area.

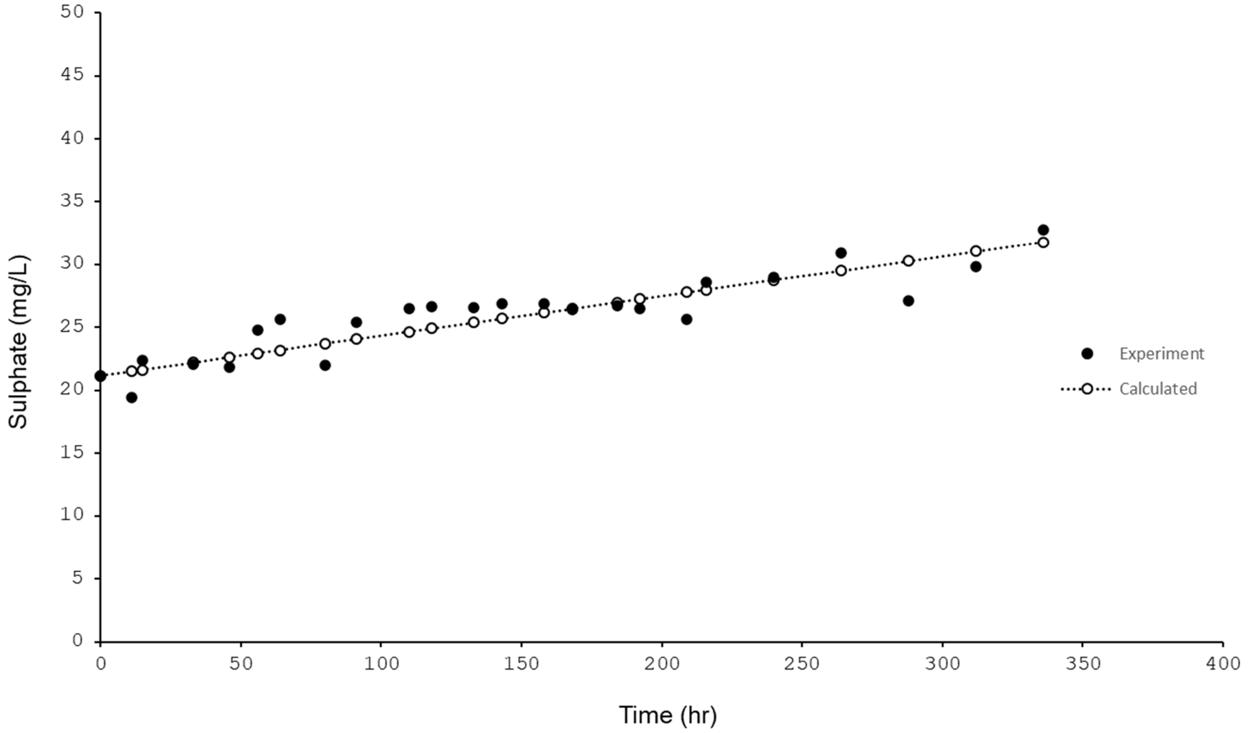

Figure 47: Measured and calculated sulphate concentration for the pH ~3 experiment. The calculation was performed with a pyrite surface area of 1046.27 g/cm^2.

Simulation of Batch Reactor Experiments

All three experiments were simulated using the pyrite surface area calculated for the pH ~3 experiment. Theoretically, all three experiments should have the same surface area. Using the rate from Williamson & Rimstidt (1994), and given that the aeration is the same, the pyrite reaction rate will only vary depending on the hydrogen activity. However, if the pyrite in the pH ~3 experiment is significantly oxidised by ferric iron, the rate will be significantly different from the pH ~5 and ~7 experiments.

The simulation results are shown in Figure 48 below. The modelled pyrite reaction rate fits the results for all three experiments very well. The correlation for the pH ~3, ~5, and ~7 have correlation coefficients of 0.9, 0.98 and 0.99, respectively. This also implies that the oxidation of pyrite is almost solely by oxygen and that the reaction rate will be valid over a wide pH range.

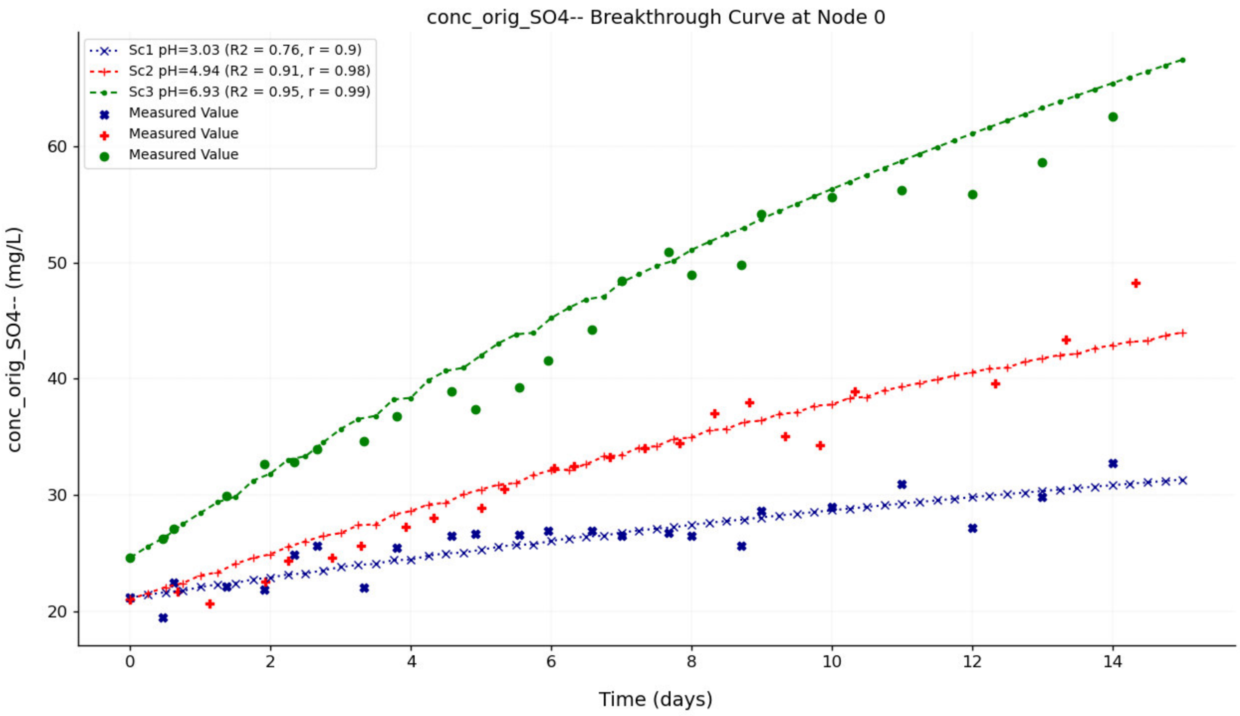

Figure 48: Measured and modelled sulphate for Experiments 1-3.

7 NUMERICAL GEOCHEMICAL MODEL

7.1 Introduction

Due to the complexity of the interaction between the solid, water, and gas phases in the tailings, numerical modelling was used to simulate the geochemical processes of the tailings dam. As with all models, the model presented here is a simplification of the complexity of the real world. It is very challenging to model all geochemical mechanisms involved and account for potential variability in geochemical parameters. The approach used was to include the major conceptual geochemical processes in the model and then to test the sensitivity of these by performing various scenarios with different settings for rainfall recharge, pyrite surface area and oxygen fugacity in the Anoxic Zone.

7.2 Objective

The primary objective of the modelling was to improve the understanding of the mechanisms that control the geochemical reactions and dispersion of chemicals. A secondary objective of the model was to match the observations 60 years after closure. However, as discussed in the Model Discussion (Section 7.7.3), the observational data was severely limited for most parameters. The specific objectives of the modelling were as follows:

- To model the major geochemical mechanisms that control the distribution of geochemical parameters in the tailings dam.
- To identify the sensitivity of the model in terms of variation in pyrite surface area, oxygen fugacity and flow rate.
- To identify which scenarios best match the observed data.
- To produce new insights into the conceptual understanding of the geochemical processes in the tailings dam.

The model was performed to roughly reflect the years after the closure of the tailings dam. The model, therefore, was not used to make any future predictions but rather to model some of the major geochemical processes that already took place. Because the tailings dam is already several decades old, it provides a rare opportunity to test how successful a geochemical can simulate the processes that already took place.

7.3 Model Code

The software used was discussed in Section 6.2.3. A subroutine was written in *Python 3.8* programming language, which used *ChemPlugin* to create the appropriate configuration of the unsaturated and saturated zone of the tailings. Nodes in the model are different *Chemplugin* instances which are the same as different *React* models, which are then connected by *Links*, each with the specified flow and between them.

The ability to specify different links between nodes was used to create both vertical and horizontal flow in the model configuration. The subroutine facilitated the modelling of various scenarios as well as the display of their results, something that will be particularly cumbersome with the commercial version.

7.4 Model Scenarios

The model scenarios are summarised in Table 19 below. For Model 1 – 3, a recharge of 4%, 8% and 12% (of annual precipitation of ±700 mm/a) was specified as the inflow for the model. Yibas et al. (2011) measured the deep infiltration in wits tailings dams to be at 15 - 17% of annual precipitation, as discussed in Section 2.6.2. As these were measured over a 4-month wet season period, a slightly lower recharge was chosen for Model 1 – 3. The seepage from tailing dams is lower than the deep infiltration (as discussed in Section 2.6.2), and the seepage from all models was specified at 3% of annual precipitation.

For each model, three scenarios were performed with pyrite surface areas of 295, 670, 1 045 cm^2 (Scenarios 1-3, 4-6 and 7-9, respectively). The lower surface area corresponds with the geometrical surface area calculated for pyrite in Section 7.5.2, with the higher value of the pyrite surface area calculated from the batch reactor experiment presented in Section 6. The intermediate value is the average of the lower and higher value.

For each scenario, three sub-scenarios were performed for the oxygen fugacity in the Anoxic Zone. The oxygen fugacity in the Oxic Zone could be calculated from the oxygen field measurements; however, the oxygen fugacity in the deeper Anoxic Zone was unknown and therefore varied to find the best match for the measured Eh conditions.

With the 3 models having 9 scenarios each, there is a total of 27 model scenarios in total.

Table 19: Geochemical Model Scenarios

Model	**Sub-scenarios of Model A-C**	**Pyrite Surface Area (cm^2)**	**O_2 Fugacity Anoxic Zone**
Model 1 Low Flow 4% MAP Recharge Model 2 Medium Flow 12% MAP Recharge Model 3 High Flow 8% MAP Recharge	Scenario 1	295	1 x 10^{-5}
	Scenario 2	295	1 x 10^{-6}
	Scenario 3	295	1 x 10^{-7}
	Scenario 4	670	1 x 10^{-5}
	Scenario 5	670	1 x 10^{-6}
	Scenario 6	670	1 x 10^{-7}
	Scenario 7	1 045	1 x 10^{-5}
	Scenario 8	1 045	1 x 10^{-6}
	Scenario 9	1 045	1 x 10^{-7}

7.5 Model Setup

7.5.1 Model Discretisation

The quasi-2D model configuration is depicted in Figure 49 below. The model is comprised of 20 nodes, numbered 0 – 19, with Node 0 at the top. The model was 1D with respect to its nodes' discretization; however, both vertical (Q_v) and (Q_h) flow was included in the model to generate a quasi-2D model.

The deep percolation (D_p) of rainwater will be equal to the infiltration rate (Q_i) in the unsaturated zone. In the saturated zone, the inflow for each node will split into vertical (Q_v) and horizontal flow (Q_h). The vertical flow from the final node will be the seepage water from the tailings dam. This seepage through the base will, in general, seep to the aquifer and underdrains ($Q_{SB + UD}$), whereas most of the horizontal flow end up as seepage to the toe and interception drains ($Q_{TS + ID}$), while the piezometric level in the tailings dam area is still fairly high above the base of the dam.

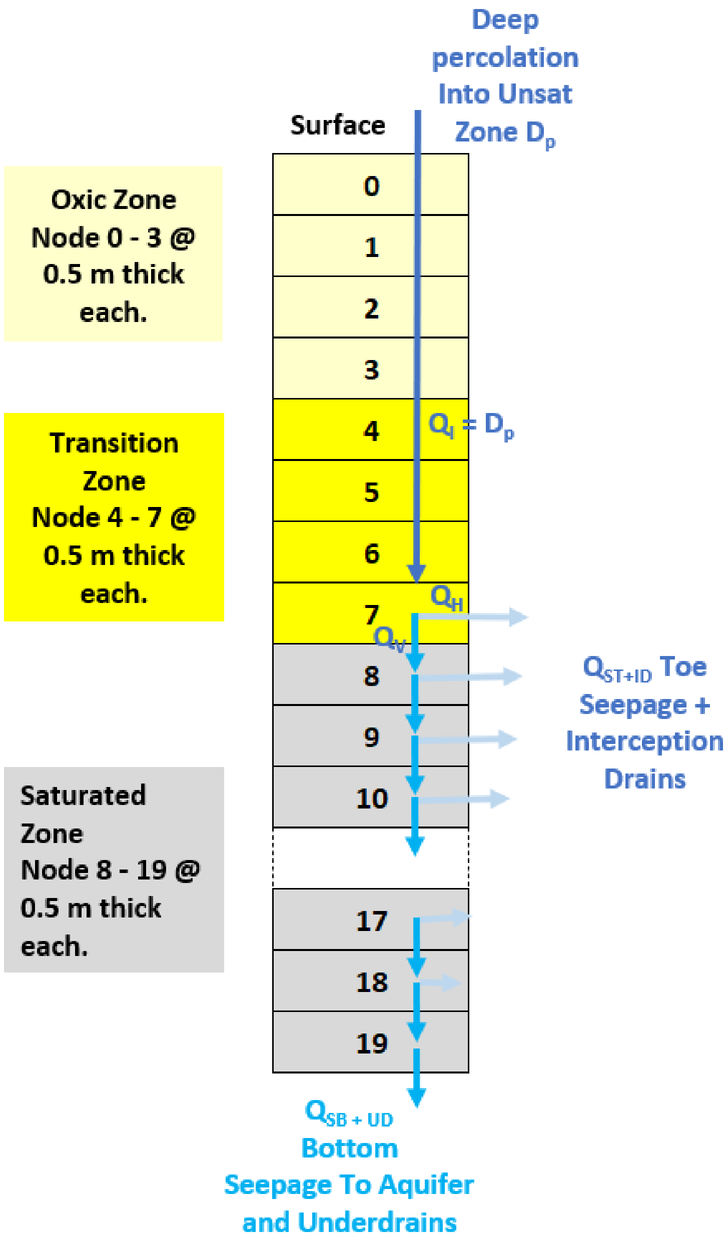

Figure 49: Node configuration for the quasi-2D geochemical model with the surface of the tailings dam at the top. Both vertical (Q_v) and (Q_h) flow was included in the model.

7.5.2 Model Input

Mineral Geometrical Surface Area

The geometrical surface area was used in the geochemical models to simulate the kinetic reaction of the minerals. Estimation of the reactive surface area is a key uncertainty in the geochemical modelling of mineral reaction rates. A mineral phase, however, has a range of grain sizes in tailings. In geochemical modelling, the “average effective surface area” is, however, often used. For now, there is no universally accepted method for evaluating the average reactive surface area; therefore, various estimation methods on surface areas, including geometric surface area (GSA), BET surface area (BET SA), and effective surface area (ESA), have been developed (Steefel et al., 2015b).

In this study, the geometrical surface area was used as the initial surface area in the models for all minerals except for pyrite, where three different surface areas were specified for the model scenarios, as discussed in Section 7.4.

The mineral per grain size distribution of an unoxidised tailings sample was presented before in Section 4.6.3 (for all silicates) and Section 6.2.2 (for pyrite and gypsum). The effective grain diameter (D_e) for each grain fraction was calculated from the following relationship given by Tester et al. (1994):

$$D_e = \frac{D_{max} - D_{min}}{ln\left(\frac{D_{max}}{D_{min}}\right)}$$

For quartz and pyrite, the effective diameter (m^2) and the mineral density, ρ (g/m^3), from the molar volume and molecular weight from the *thermo.dat* database, were used to calculate the geometric surface area A_{geo} (m^2/g) for each size fraction using the relationship given by Kimball et al. (2010), assuming the grains represents cubic particles:

$$A_{geo} = \frac{2\lambda\beta}{D_e\rho} = \frac{6}{D_e\rho} \; with \; \lambda = 1, \beta = 3$$

Where λ is the roughness factor, ρ (g/m^3) is the mineral density; β is a form factor where is equal to $\beta = 3$ for a cubic particle, $2 \leq \beta \leq 3$, for an elongated mineral, and $\beta > 3$ for a plate mineral. For phyllosilicates (muscovite and chlorite), an additional factor could be added where for each size fraction using the relationship given by the total geometrical surface area A_{tot} (m^2/g) could be estimated from the relationship given by Dubois et al. (2010) for the external and internal surface area:

$$A_{tot} = \frac{2\lambda\beta}{D_e\rho} + \frac{\alpha_{int}}{D_e\rho} + \frac{\alpha_{dist}}{D_e\rho}$$

Where α_{int} and α_{dist} represents the internal and mechanical disturbed (from the crushing of the ore) surface areas ($m^2.m^{-3}$). Dubois et al. (2010) calculated the following values for chlorite: $\lambda\beta = 90$ and $\alpha_{int} + \alpha_{dist} = 1 \times 10^6$ ($m^2.m^{-3}$) for grain sizes below 250 µm, and the $\lambda\beta = 260$ and $\alpha_{int} + \alpha_{dist} = 1 \times 10^5$ ($m^2.m^{-3}$) for grain sizes above 250 µm. These values were used in this study for phyllosilicates.

The calculated geometrical surface areas for the various minerals are summarised in Table 23 below.

Geochemical and Physical Model Input

A summary of geochemical and physical model constraints is given in Table 20 below. The model discretisation was discussed in Section 7.5.1. The average porosity and degree of saturation were obtained from field measurements (see Section 4.2.3). Inflow and interstitial water quality used in the modelling are summarised in Table 21. The inflowing water quality was taken to be fairly dilute, near-neutral water, and the interstitial water quality was taken for typical operational tailings water (e.g. Fourie, 2013). The oxygen fugacity used in the modelling for the Oxic Zone is summarised in Table 22. The oxygen fugacity specified for the oxic was calculated from the measured oxygen in the field (Section 4.2.3). The mineral properties used in the modelling are summarised in Table 23. The pyrite mineral volume was stoichiometrically calculated from the sulphide sulphur and gypsum from the sulphate sulphur (Section 4.4.3) from the unoxidized tailings (from the Anoxic Zone). The pyrite was modelled with a constant surface area and with a gradual decrease in its mass in the nodes where it was subjected to oxidation. The major silicate mineral volumes (quartz, muscovite, chlorite) were calculated from the XRD analyses (Section 4.6.3). Trace minerals (uraninite, arsenopyrite, chalcopyrite, galena, sphalerite) were stoichiometrically calculated from the elemental composition (of U, As, Cu, Pb, Zn) of unoxidized tailings (from the Anoxic Zone) (Section 4.4.3). The calculation of the mineral surface areas is described further above in this section.

Table 20: Summary of geochemical and physical model constraints

Parameters	**Model 1 - 3**
Model Discretisation	
Model type	1D (Quasi-2D)
Surface Area	1 m x 1 m
Oxic Unsaturated Zone	4 X 0.5 m nodes (0 m – 2 m)
Transition Unsaturated Zone	4 X 0.5 m nodes (2 m – 4 m)
Anoxic Saturated Zone	16 X 0.5 m nodes (4 m – 10 m)
Physical and Hydrogeological	
Porosity	45%
Degree of Saturation	100% in the saturated zone 60% in the unsaturated zone
Water Inflow Rate	4%, 12%, 8% of rainfall *
Geochemical	
Water Inflow Quality	Water quality as in Table 21.
Interstitial Water Initial Quality	Water quality as in Table 21.
Oxygen Anoxic Zone	1×10^{-4}, 1×10^{-5} and 1×10^{-6} **
Oxygen Oxic Zone	Oxygen Fugacity as in Table 22.
Mineralogy	Mineral properties as in Table 23.

* Model 1 – 3

** Three sub-scenarios for each model scenario

Table 21: Inflow and Interstitial Water Quality used in the modelling

Parameter (mg/L)	**Inflow Water Quality Year 0 - 60**	**Interstitial Initial Water Quality Year 0**
pH (value)	6.5	8.0
Calcium as Ca	20	400
Magnesium as Mg	15	300

Parameter (mg/L)	Inflow Water Quality Year 0 - 60	Interstitial Initial Water Quality Year 0
Sodium as Na	10	200
Potassium as K	1	50
Sulphate as SO_4	20	1 000
Chloride as Cl	Balance on Cl	Balance on Cl
All trace metals and elements (Al, Fe^{2+}, Fe^{3+}, As, U, Cu, Pb, Zn)	1×10^{-7}	1×10^{-7}
CO_2 (log fugacity)	-3.5	-3.5

Table 22: Oxygen fugacity used in the modelling for the Oxic Zone

Node	Oxic Zone Oxygen Fugacity
0	0.14000
1	0.06300
2	0.01807
3	0.00518
4	0.00148
5	0.00043
6	0.00012

Table 23: Mineral properties used in the modelling

Mineral	Volume%	Molar Weight (g/mol)	Density (g/cm^2)	Geometrical Surface Area, Ageo (cm^2/g)
Silicates				
Quartz	43.4%	60.0843	2.648	429
Muscovite	9.34%	398.3081	2.831	12 524
Chamosite	0.5030%	341.7689	3.218	11 016
Clinochlore	0.3026%	555.7973	2.628	13 490
Sulphides and sulphates				
Pyrite	0.4641%	119.967	5.011	295/670/1045*
Gypsum	0.6157%	172.1722	2.305	493
Arsenopyrite	0.0192%	162.8346	6.163	184

Mineral	Volume%	Molar Weight (g/mol)	Density (g/cm^2)	Geometrical Surface Area, Ageo (cm^2/g)
Chalcopyrite	0.0066%	183.525	4.285	265
Galena	0.0026%	239.266	7.598	150
Sphalerite	0.0082%	97.456	4.090	278
Other				
Uraninite	0.0018%	270.0277	10.968	104
Total	55%	-	-	-

* Scenario 1-3, 3-6, 7-9

7.6 Modelling Results

The model results and a brief description is provided here. The model results are further discussed in Section 7.7.3: Discussion of Model Results.

7.6.1 Model 1-3: pH change over depth

The pH change over the depth of the tailings after 60 years for Model 1 - 3 is depicted in Figure 50, Figure 51 and Figure 52, respectively. The pH is significantly lowered in the Oxic and Transition Zone because of sulphide oxidation and subsequent acid generation. The pH in the Oxic Zone matched the observed data well for Models 2 and 3 (12% and 8% recharge, respectively). However, the pH is a bit lowered in Model 1 (4% recharge) as less water is flowing into the model to leach the products of pyrite oxidation. The modelling considered both neutral and acidic possibilities for the Anoxic Zone. From the model results, it is, however, shown that only scenarios with a low oxygen fugacity (1×10^{-6}) in the Anoxic Zone do not show any acidification below pH 5.5.

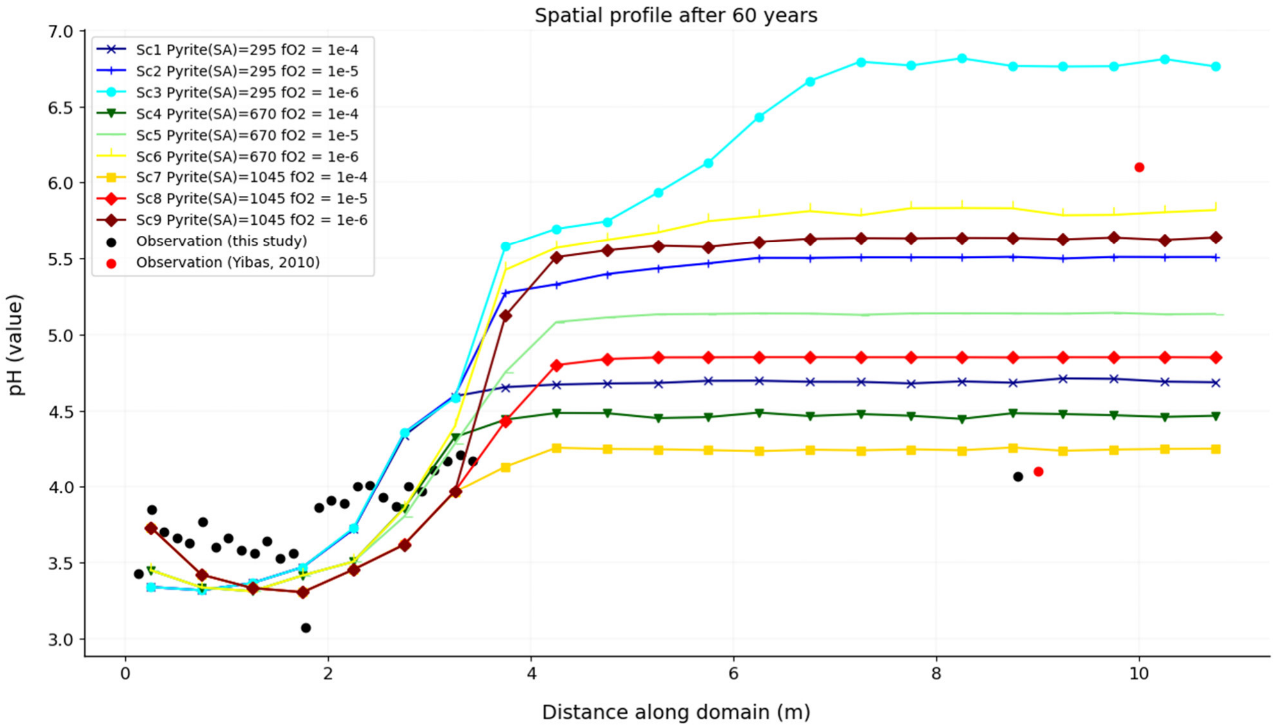

Figure 50: Model 1: Scenario 1 – 9: pH change over depth after 60 years

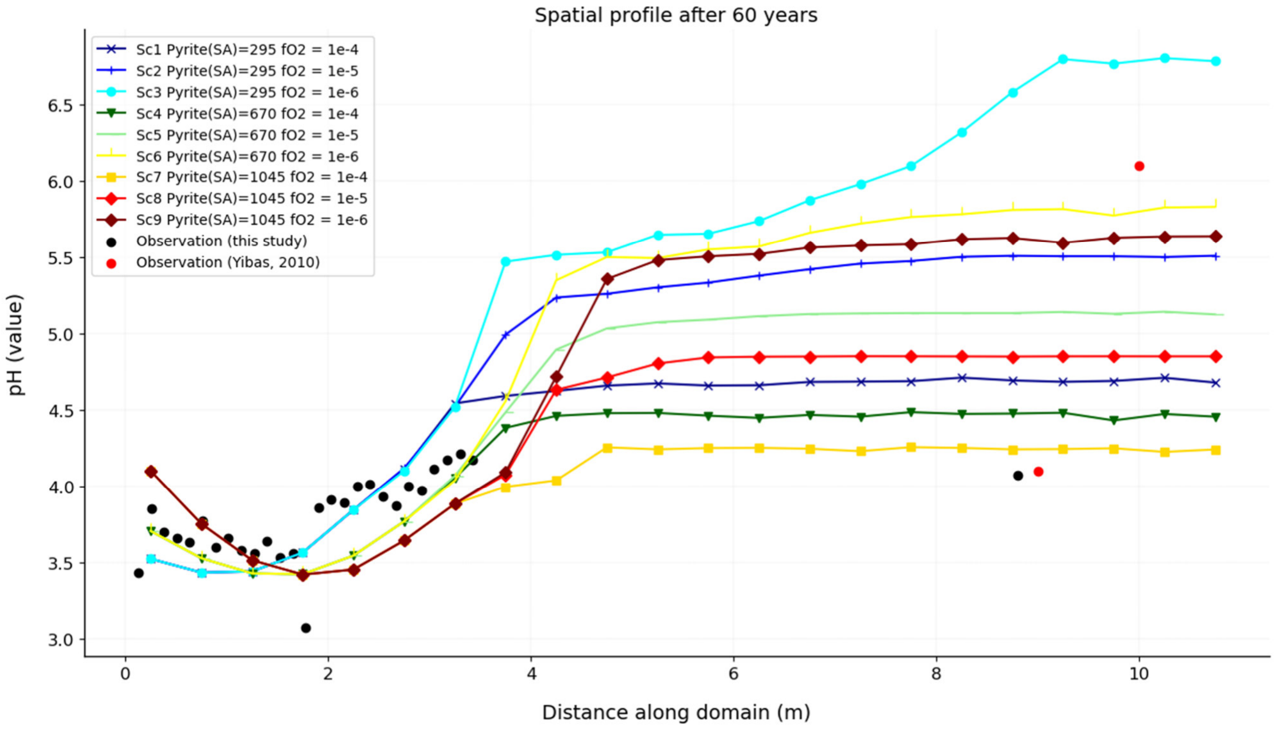

Figure 51: Model 2: Scenario 1 – 9: pH change over depth after 60 years

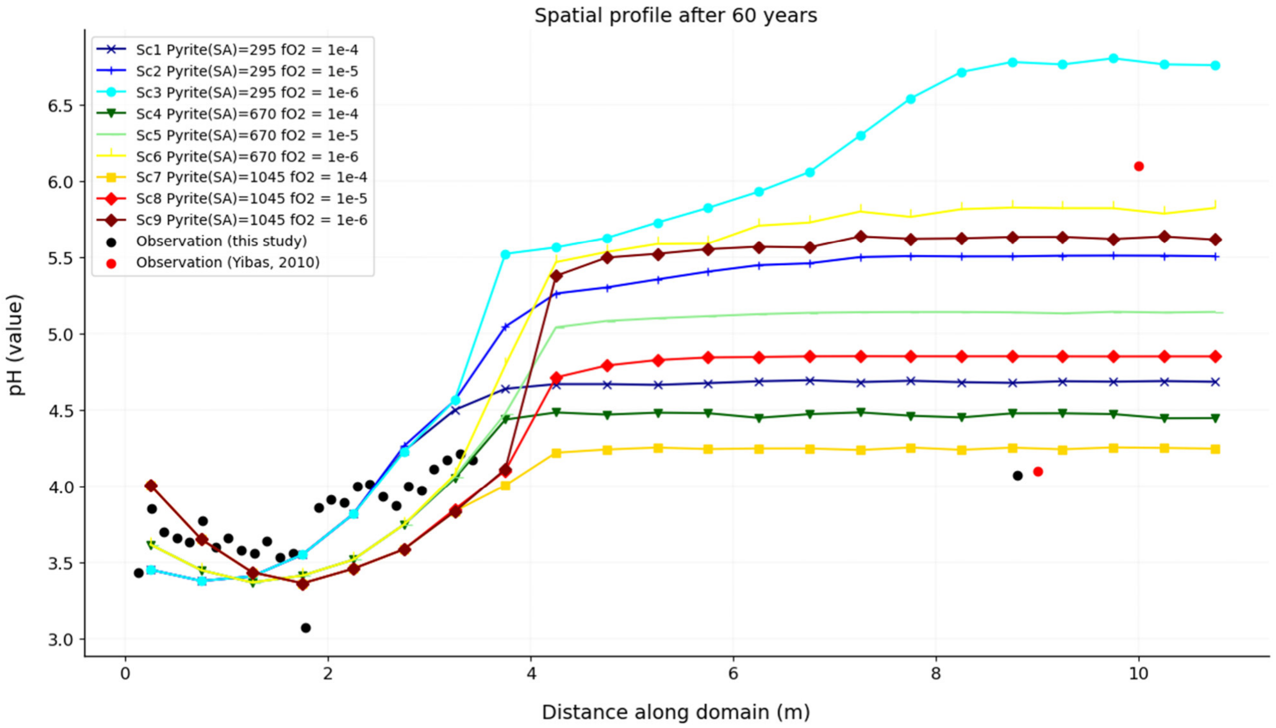

Figure 52: Model 3: Scenario 1 – 9: pH change over depth after 60 years

7.6.2 Model 1-3: Eh, Dissolved Iron and Iron-hydroxide

Ferrous and ferric iron are the dominant redox pair in the interstitial tailings water. The measured field Eh could therefore be the best matched with the Eh(Fe++/Fe+++).

Eh(Fe++/Fe+++)

The Eh(Fe++/Fe+++) change over the depth of the tailings after 60 years for Model 1 - 3 is depicted in respectively Figure 53, Figure 54 and Figure 55. The observed Eh in the Oxic Zone is fairly matched in most scenarios. However, the observed Eh in the Anoxic Zone is best matched by the low and medium oxygen fugacity scenarios (1 x 10^{-5} and 1 x 10^{-6}).

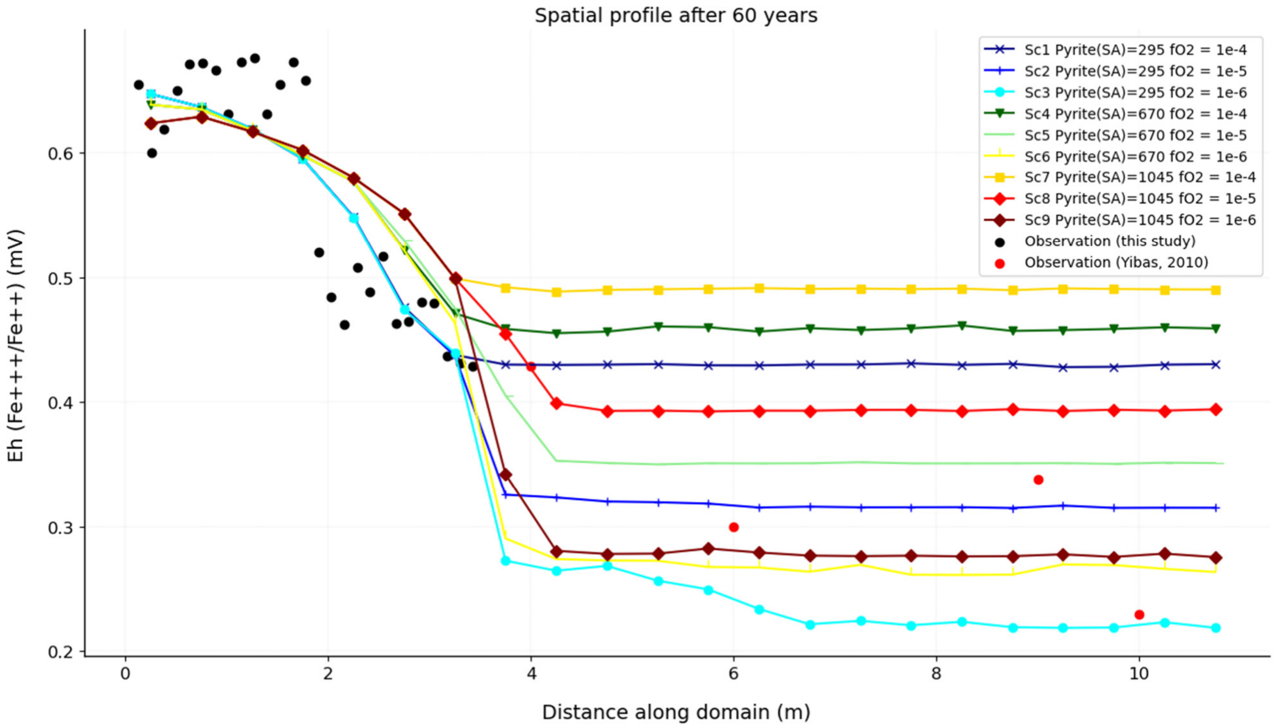

Figure 53: Model 1 Scenario 1 – 9: Eh change over depth after 60 years

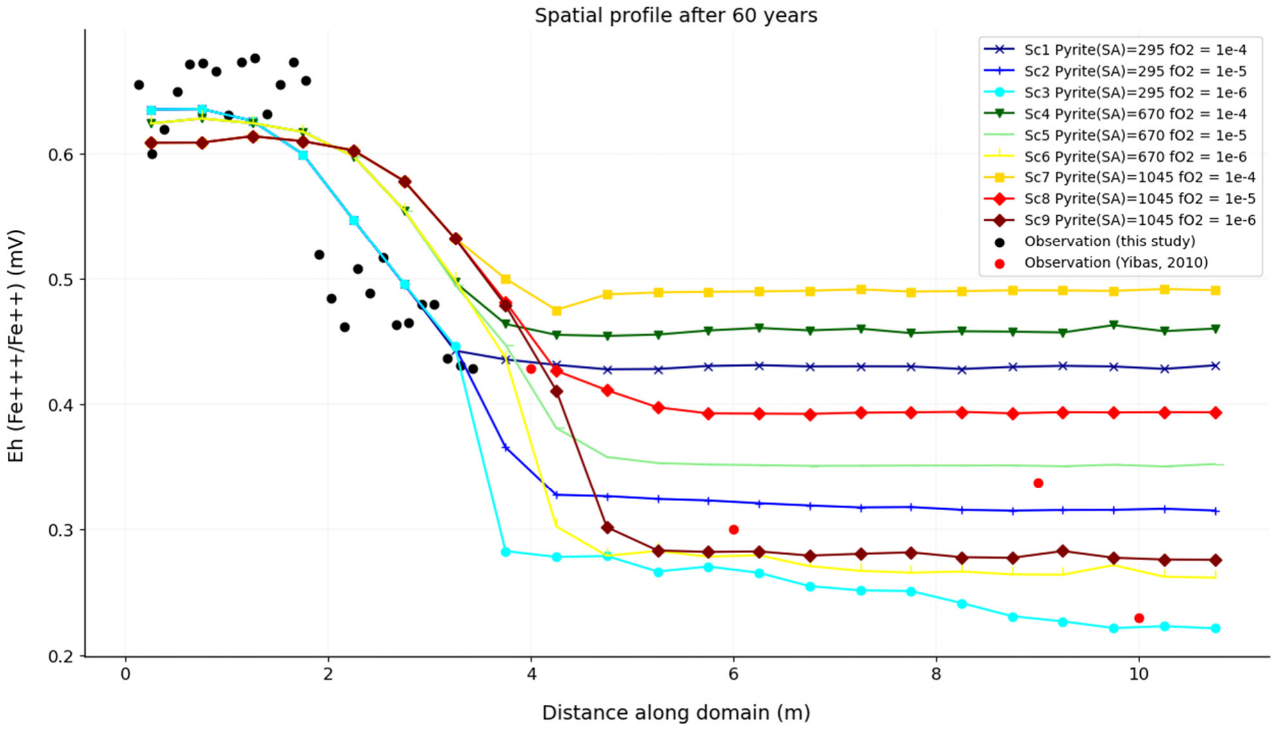

Figure 54: Model 2 Scenario 1 – 9: Eh change over depth after 60 years

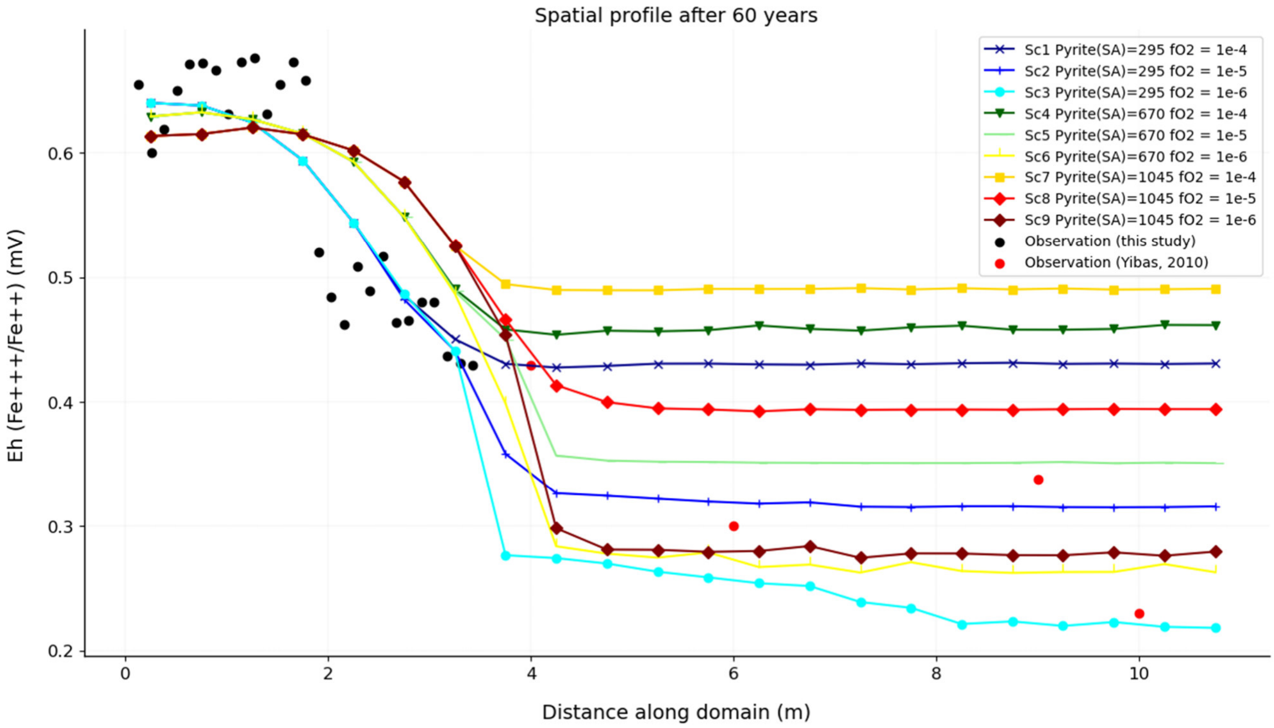

Figure 55: Model 3 Scenario 1 – 9: Eh change over depth after 60 years

Dissolved Ferrous and Ferric Iron

The ferrous iron change over the depth of the tailings after 60 years for Model 1 - 3 is depicted in respectively Figure 56, Figure 57 and Figure 58; similarly, ferric iron is depicted in Figure 59, Figure 60 and Figure 61. The iron reaches a maximum at about ~3 m in the Transition Zone and then decreases towards the Anoxic Zone, where it remains fairly stable. Both ferrous and ferric iron are at their respective highest concentrations in the Oxic Zone. In the Anoxic Zone, ferrous iron (100 - 1000 mg/L) is dominant over ferric iron (<10 mg/L).

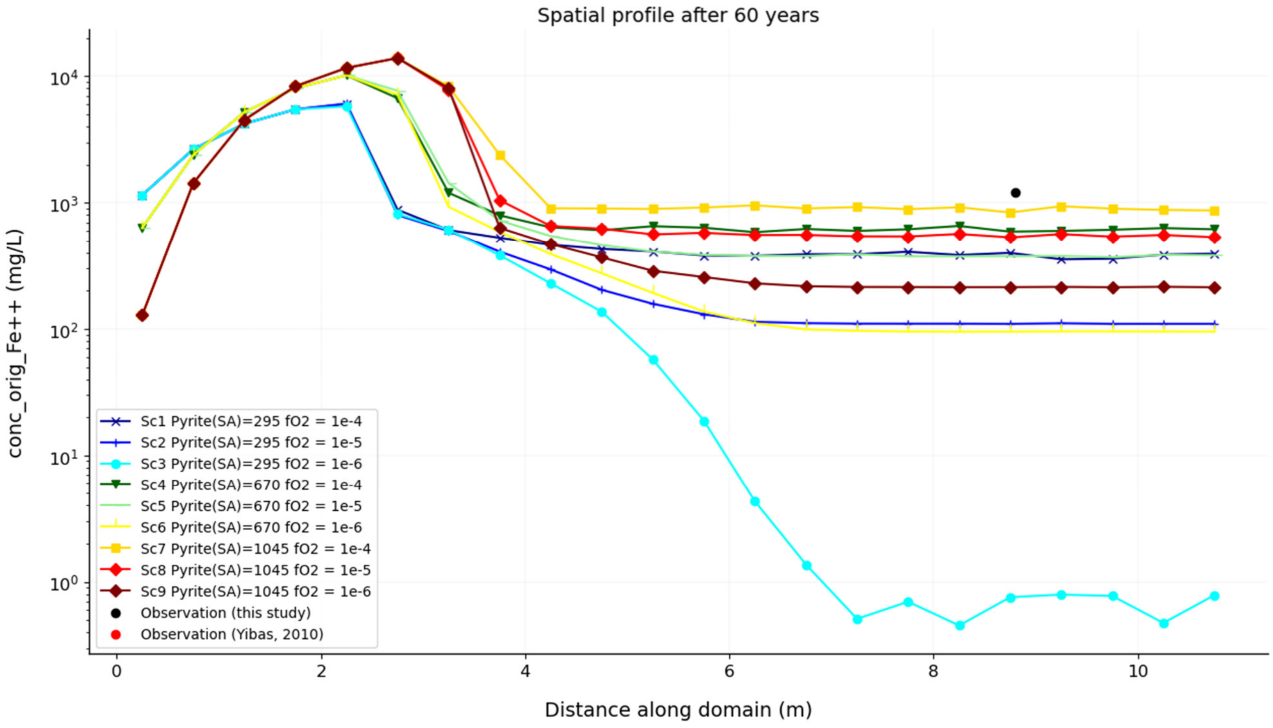

Figure 56: Model 1 Scenario 1 – 9: Dissolved ferrous iron change over depth after 60 years

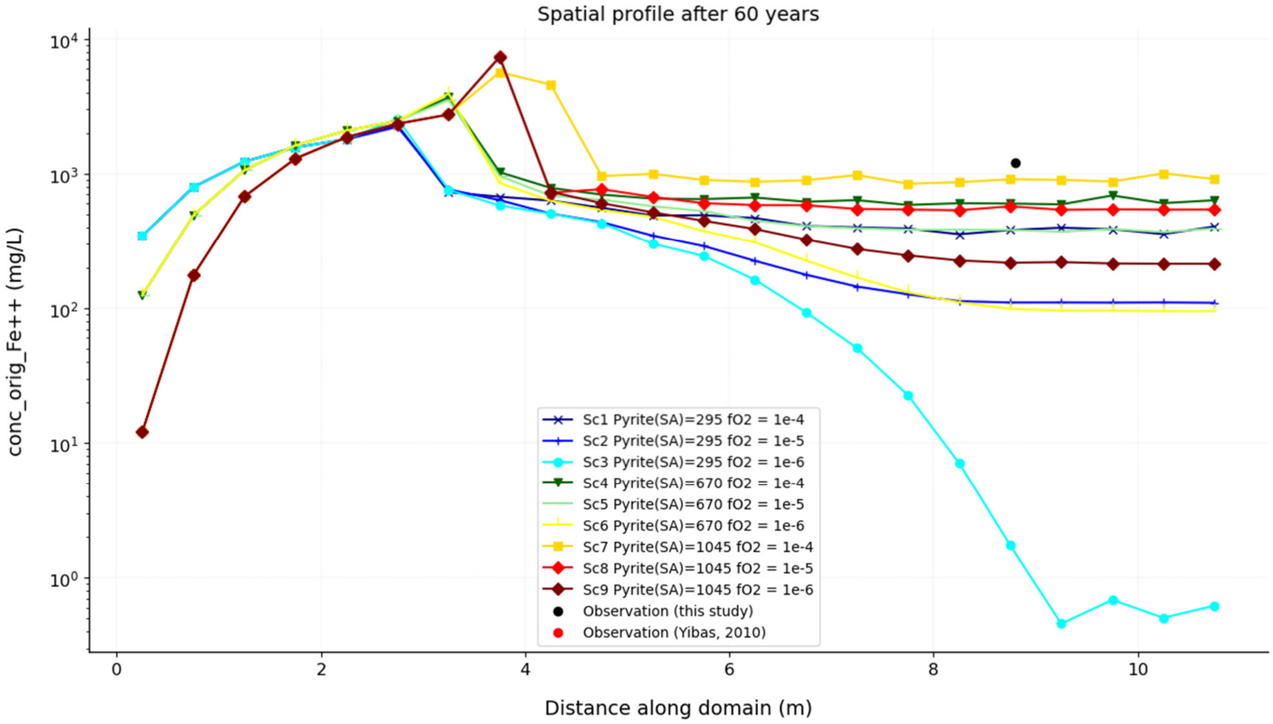

Figure 57: Model 2 Scenario 1 – 9: Dissolved ferrous iron change over depth after 60 years

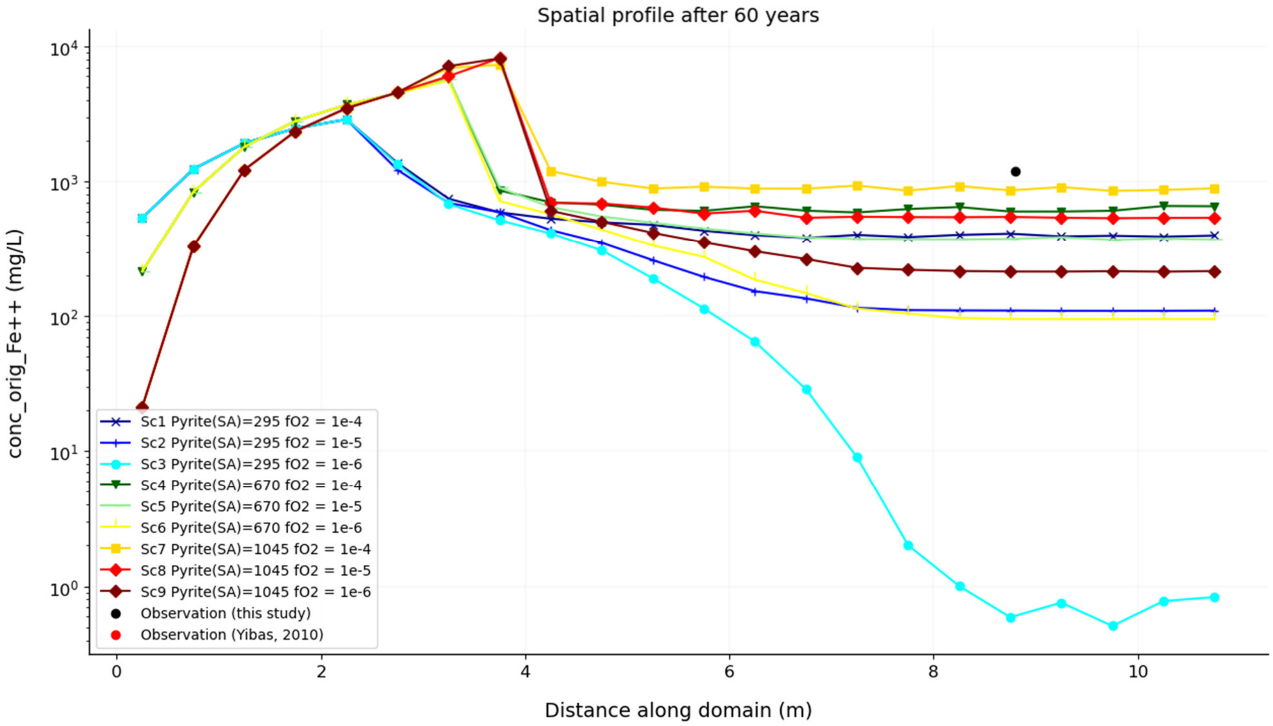

Figure 58: Model 3 Scenario 1 – 9: Dissolved ferrous iron change over depth after 60 years

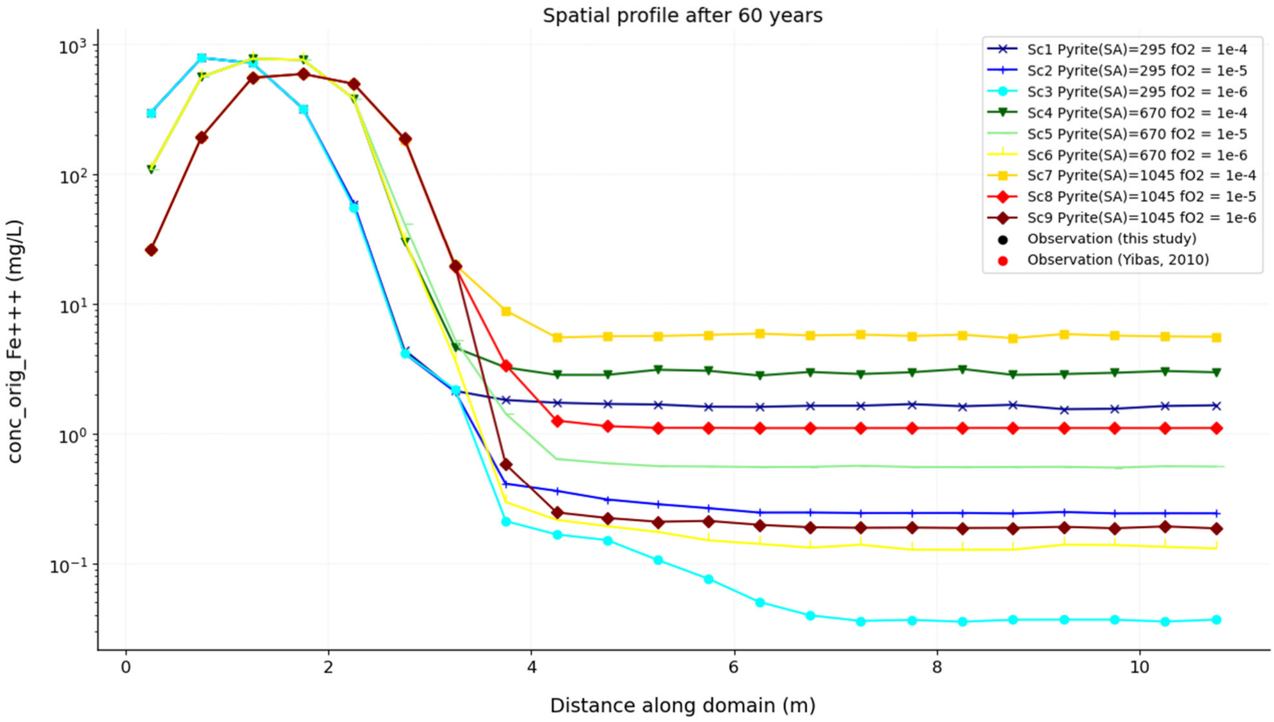

Figure 59: Model 1 Scenario 1 – 9: Dissolved ferric iron change over depth after 60 years

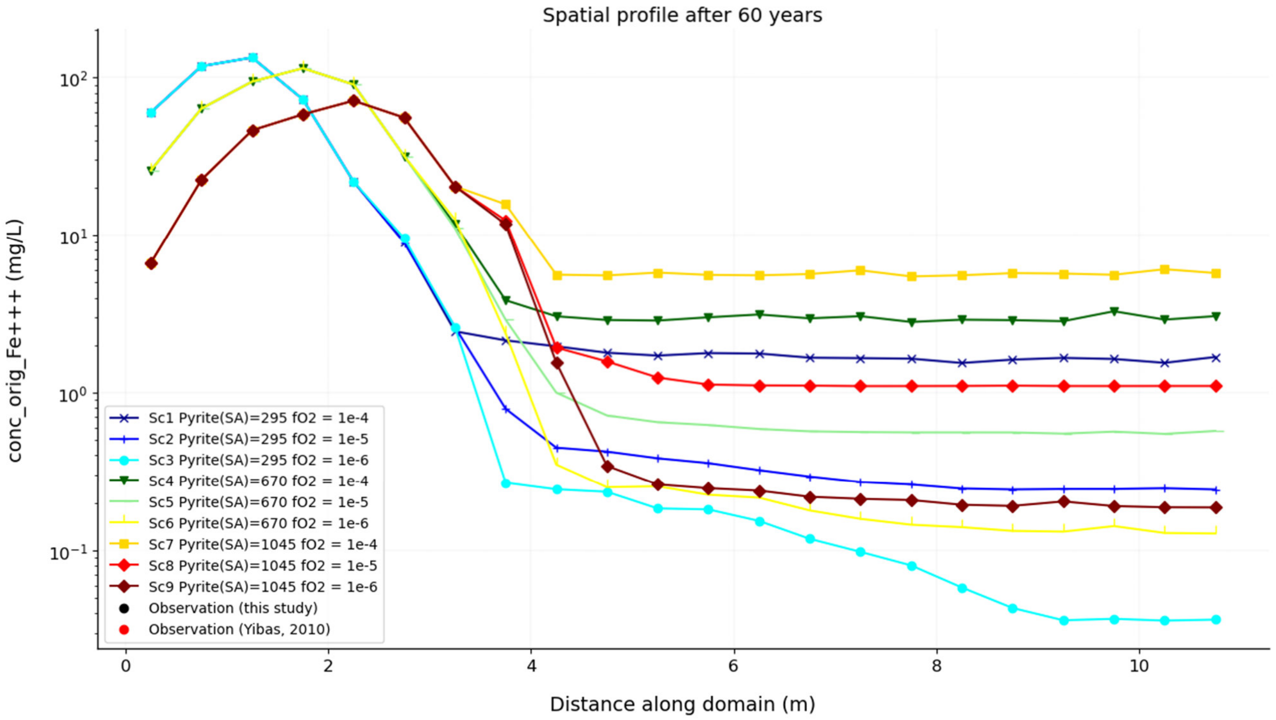

Figure 60: Model 2 Scenario 1 – 9: Dissolved ferric iron change over depth after 60 years

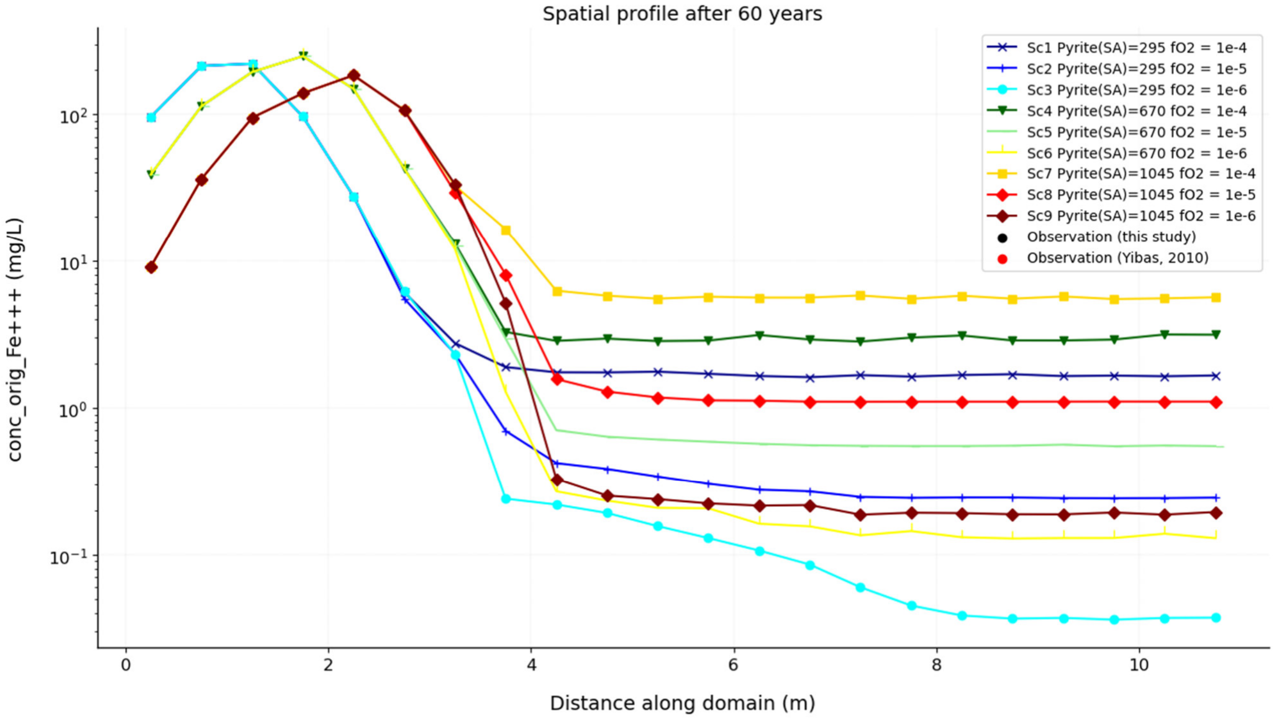

Figure 61: Model 3 Scenario 1 – 9: Dissolved ferric iron change over depth after 60 years

Precipitated Iron-hydroxide

The precipitated iron-hydroxide change over the depth of the tailings after 60 years for Model 1 - 3 is depicted in Figure 62, Figure 63 and Figure 64, respectively. Ferric iron significantly precipitates in the Oxic Zone, which results in that the total iron in the rock is not significantly leached from the tailings in the Oxic Zone as shown in the elemental composition of the tailings in Section 4.4.3.

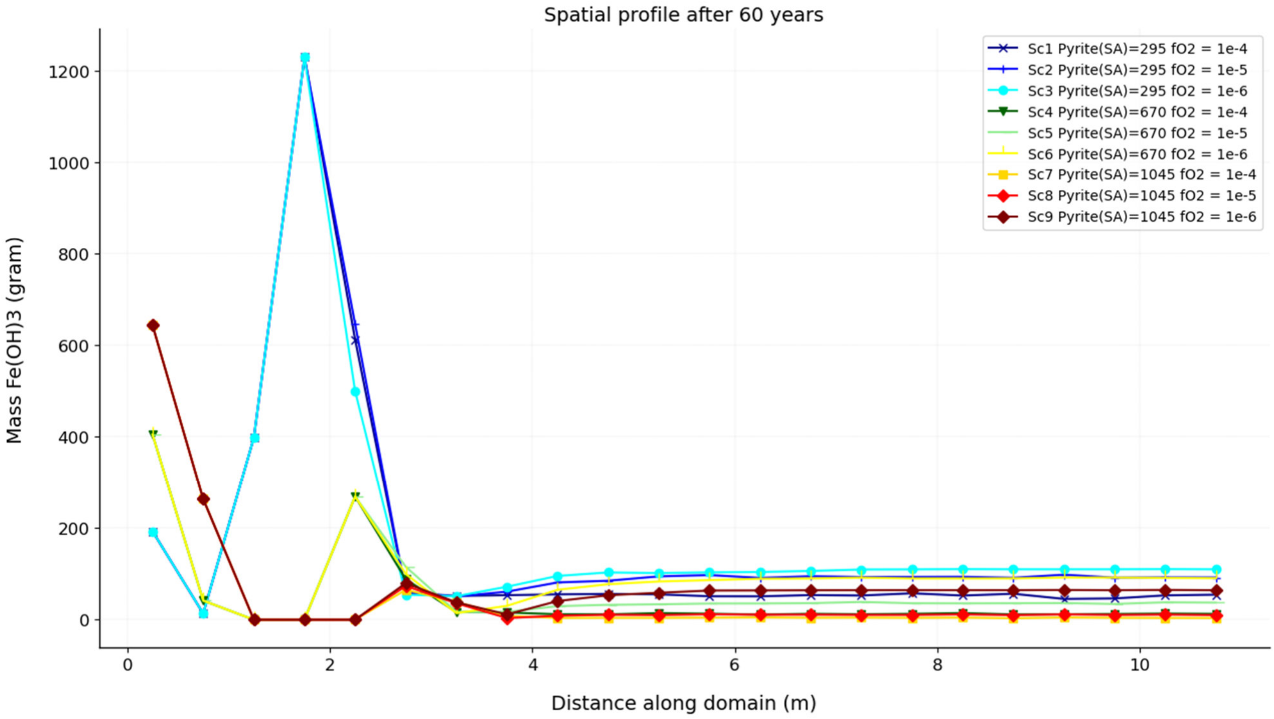

Figure 62: Model 1 Scenario 1 – 9: Precipitated $Fe(OH)_3$ change over depth after 60 years

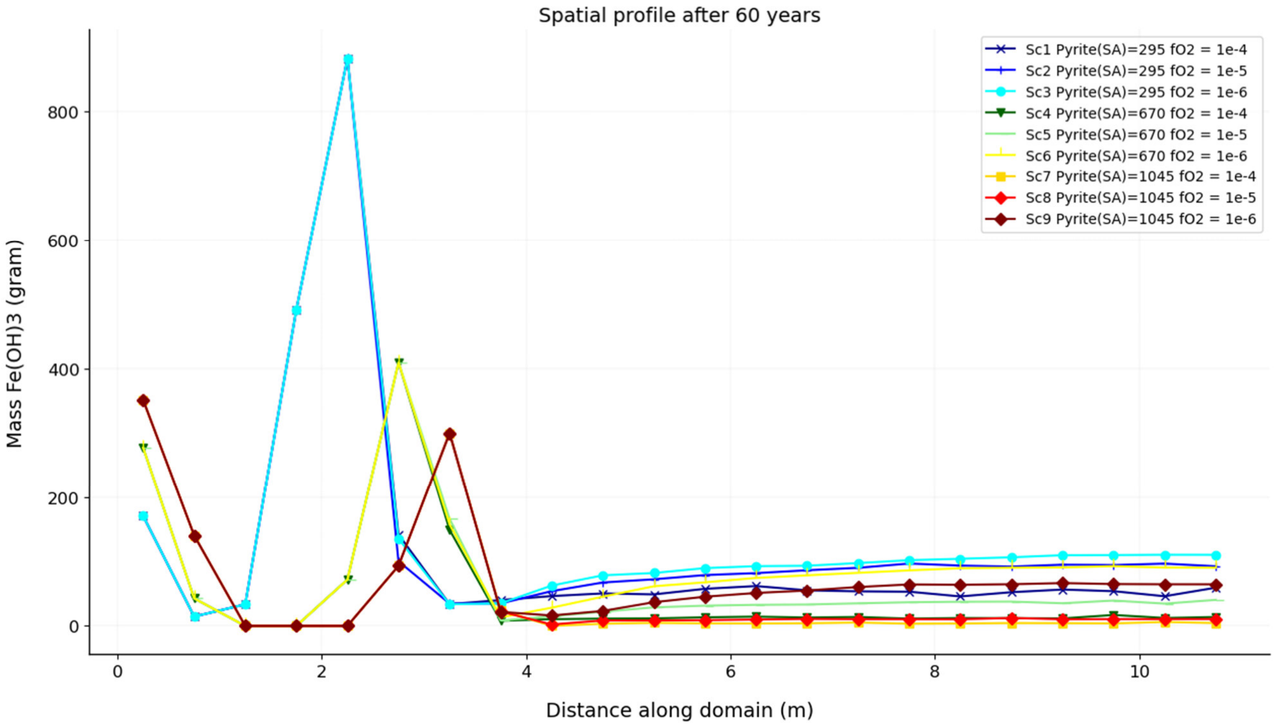

Figure 63: Model 2 Scenario 1 – 9: Precipitated $Fe(OH)_3$ change over depth after 60 years

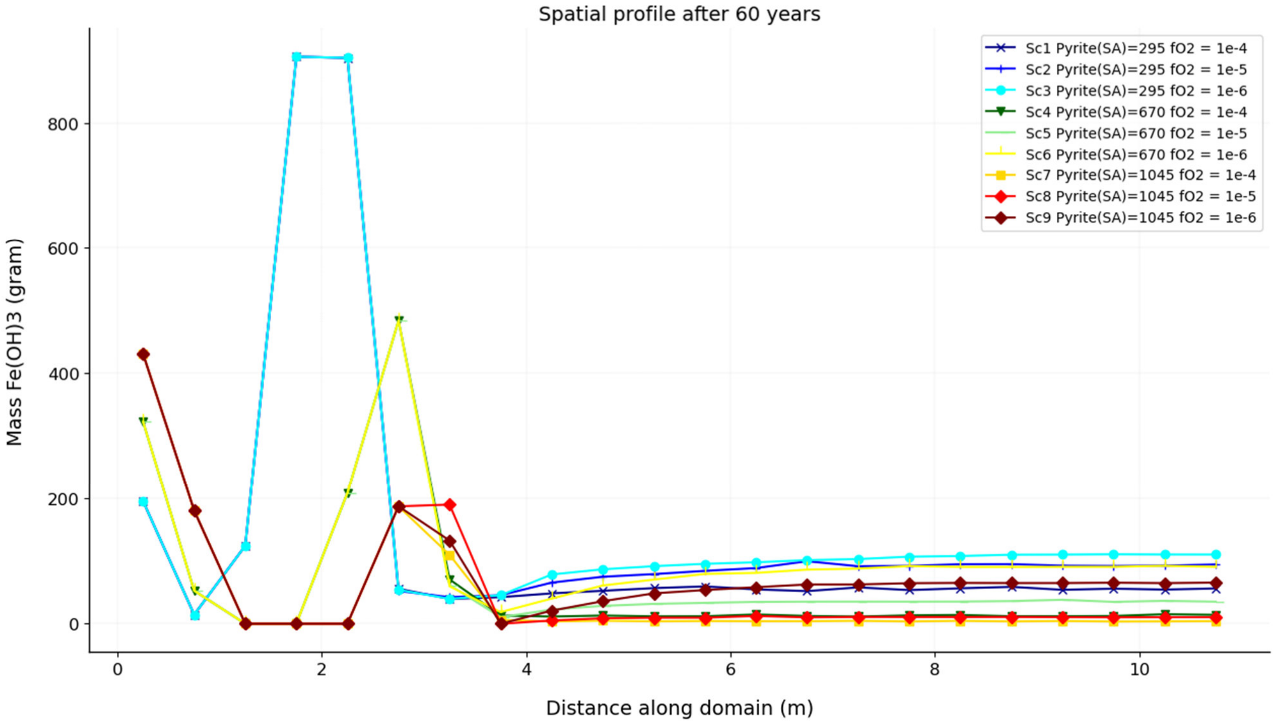

Figure 64: Model 3 Scenario 1 – 9: Precipitated $Fe(OH)_3$ change over depth after 60 years

7.6.3 Model 1-3: TDS and Dissolved Sulphate

The TDS change over the depth of the tailings after 60 years for Model 1 - 3 is depicted in Figure 65, Figure 66, and Figure 67, respectively; similarly, sulphate is depicted in Figure 68, Figure 69, Figure 70.

The TDS in the Oxic Zone is leached at the top, reaches a maximum at about ~3 m in the Transition Zone, and then decreases towards the Anoxic Zone, where it remains fairly constant. All model scenarios matched the TDS observations in the Anoxic Zone. In Model 1, the TDS is overestimated in the Oxic Zone for all model scenarios. In Model 2, the dissolved phase is leached by the high recharge at the top of the Oxic Zone, whereas for the high pyrite surface scenarios (Scenarios 7-9), the TDS is overestimated in the Transition Zone; the scenarios with the intermediate pyrite surface area (Scenario 4-6) fairly match the TDS in the Transition Zone. In Model 3, only the low pyrite surface areas scenarios (Scenarios 1-3) fairly matched the TDS in the Oxic Zone.

The sulphate observations are too limited in order to make a judgment on the model matching of the observations. However, since the sulphate is a major constituent of the TDS, it is expected that the sulphate should also be leached at the top, reaching a maximum at around ~3 m in the Transition Zone, and decreases towards the Anoxic Zone where it remains fairly constant at about 3 000 – 5 000 mg/L.

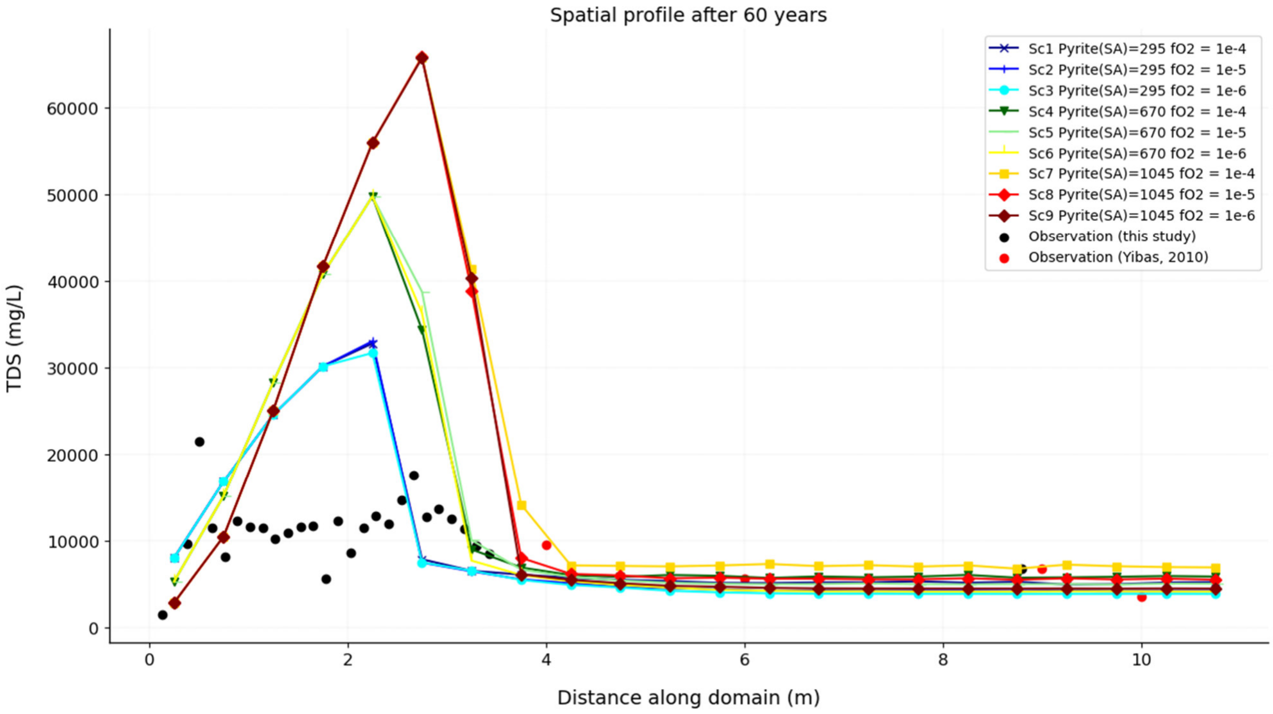

Figure 65: Model 1: Scenario 1 – 9: TDS change over depth after 60 years

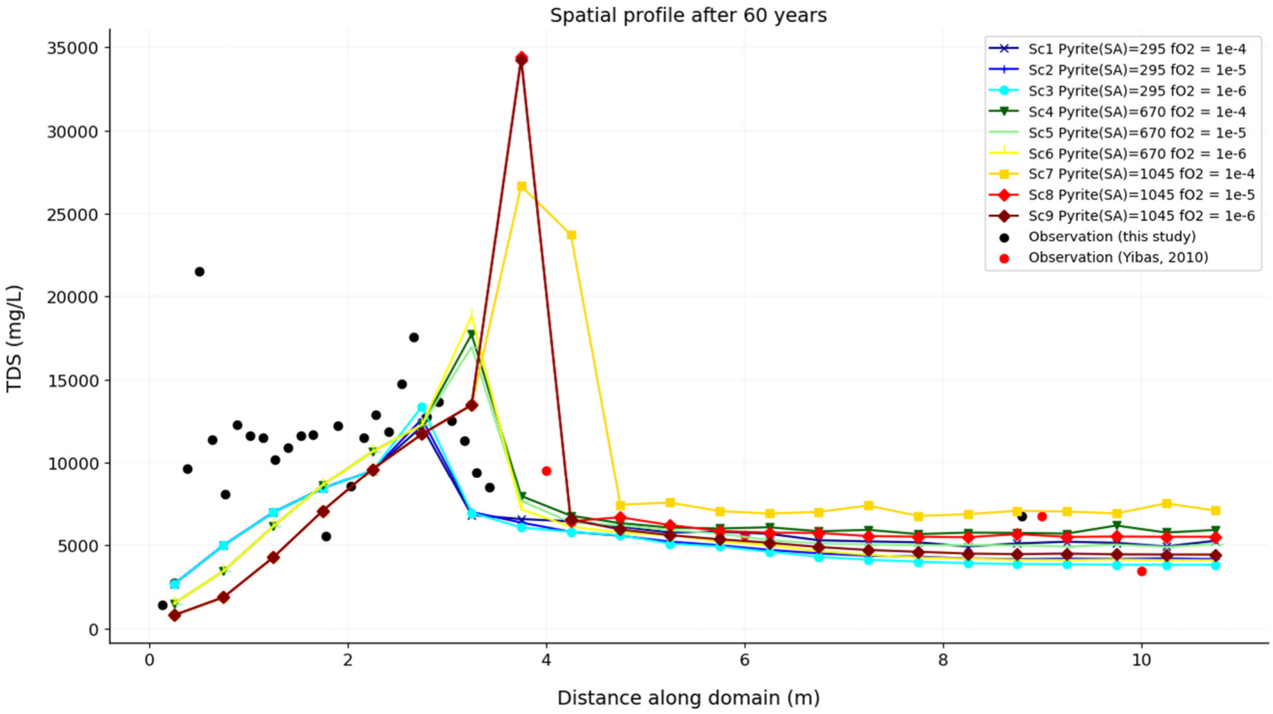

Figure 66: Model 2: Scenario 1 – 9: TDS change over depth after 60 years

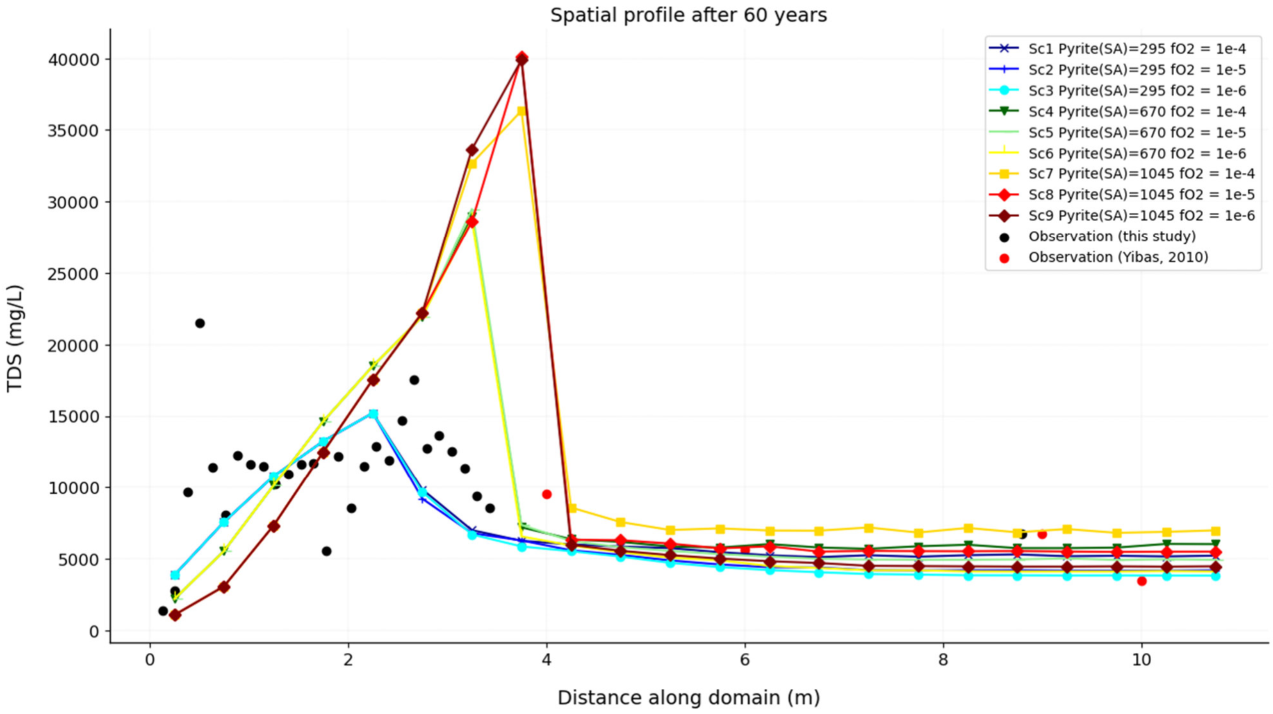

Figure 67: Model 3: Scenario 1 – 9: TDS change over depth after 60 years

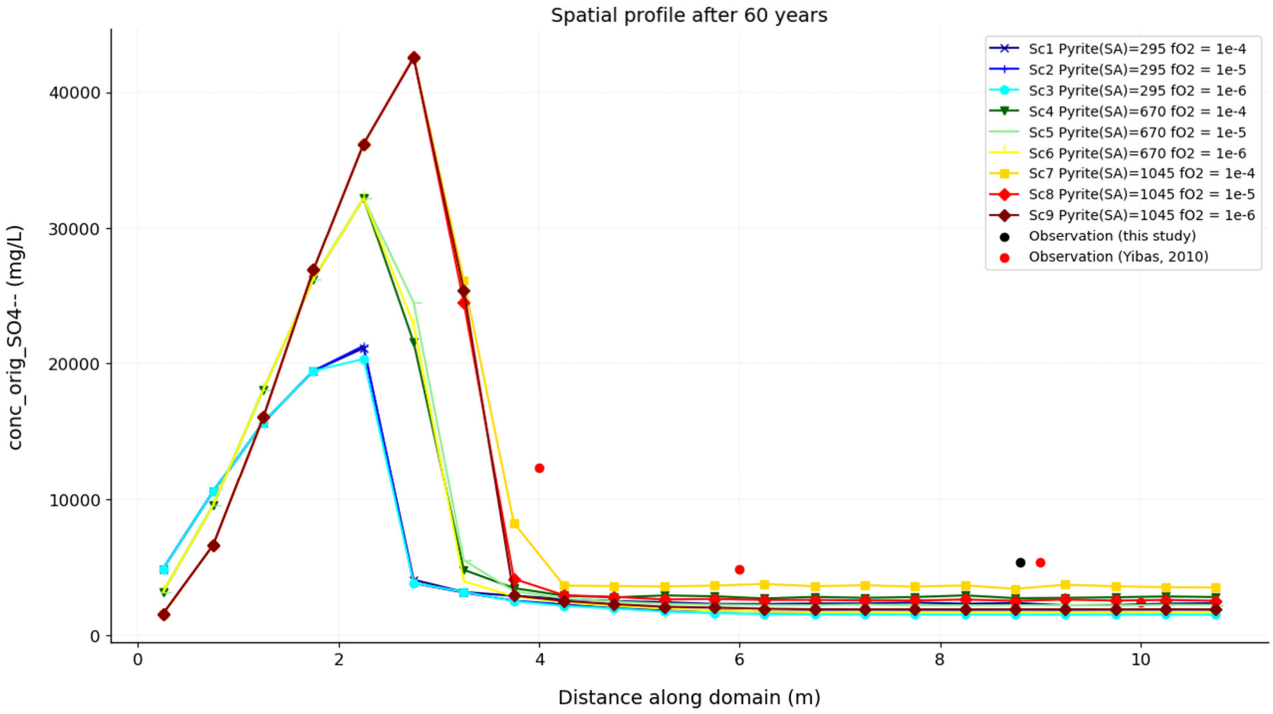

Figure 68: Model 1: Scenario 1 – 9: Dissolved sulphate change over depth after 60 years

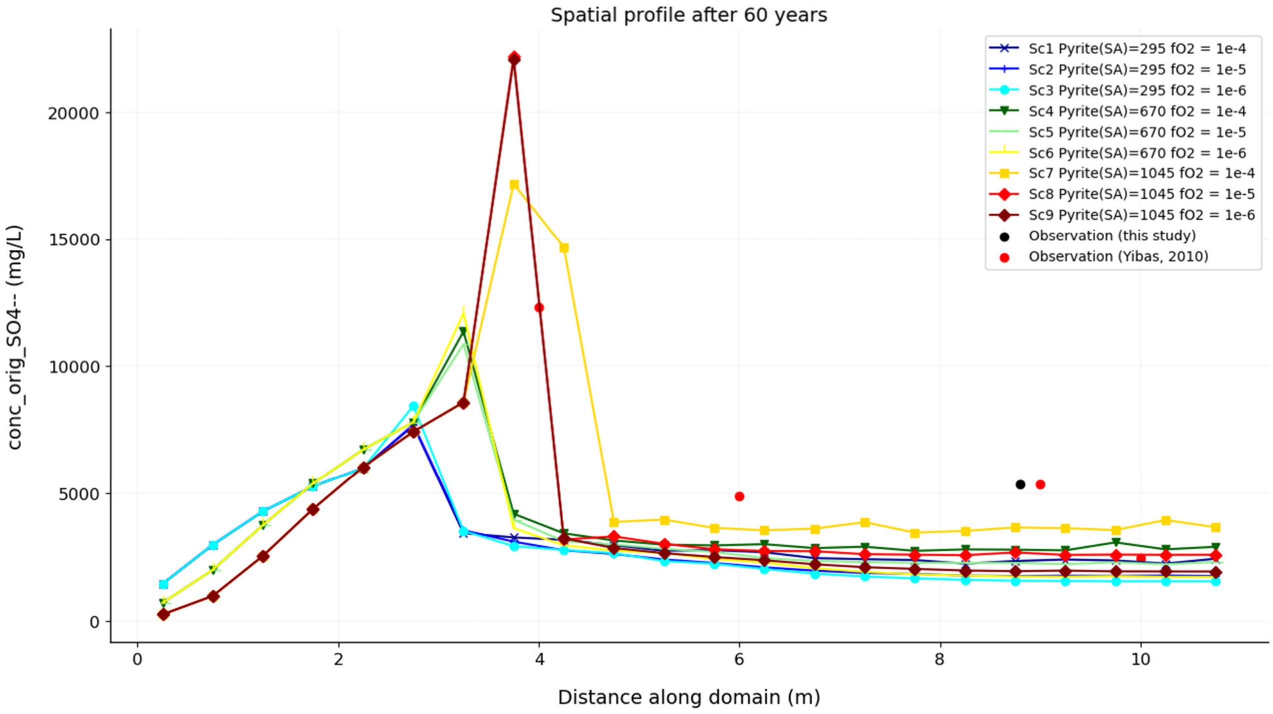

Figure 69: Model 2: Scenario 1 – 9: Dissolved sulphate change over depth after 60 years

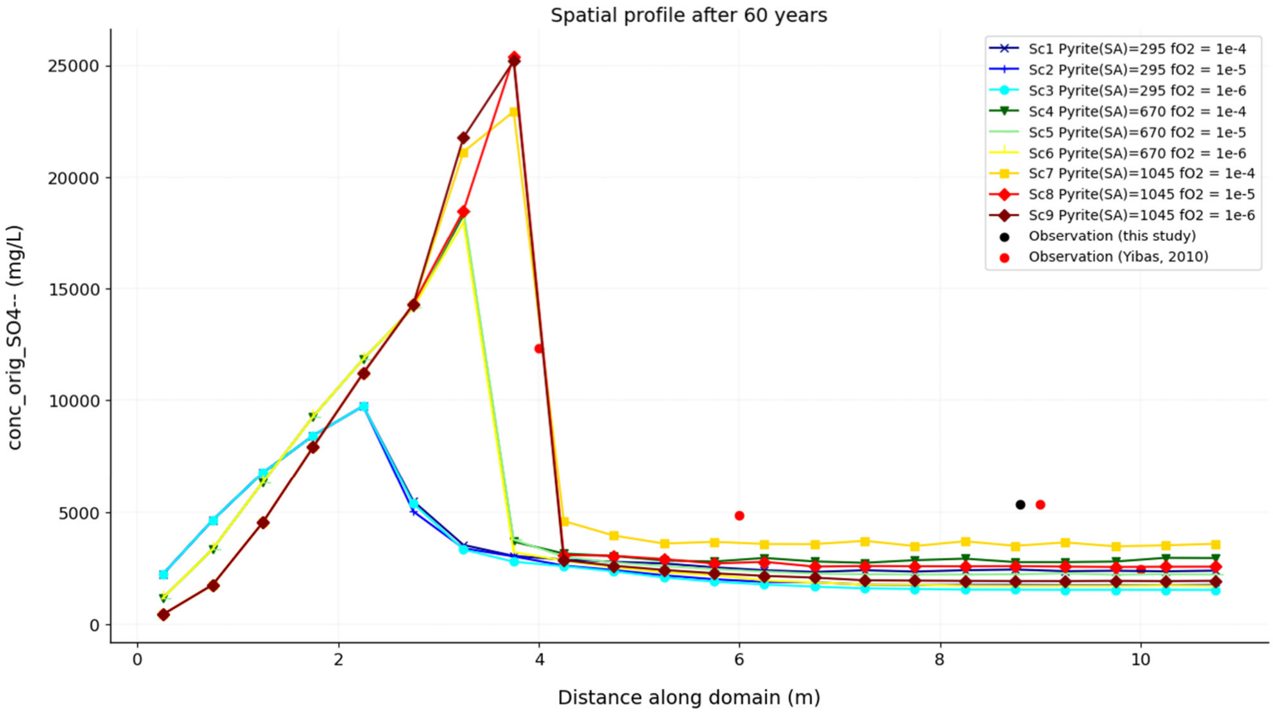

Figure 70: Model 3: Scenario 1 – 9: Dissolved sulphate change over depth after 60 years

7.6.4 Model 1-3: Dissolved Calcium and Precipitated Gypsum

The dissolved calcium change over the depth of the tailings after 60 years for Model 1 - 3, is depicted in Figure 71, Figure 72 and Figure 73, respectively; similarly, gypsum is depicted in Figure 74, Figure 75 and Figure 76. The calcium is very similar in the scenarios because it is controlled by gypsum saturation, except that it is leached a bit more in the Oxic Zone because of higher infiltration (Model 2) and because of higher acidity (Scenarios 7-9). Almost no gypsum precipitation is present in the Oxic Zone, with the most precipitation occurring in the Transition Zone.

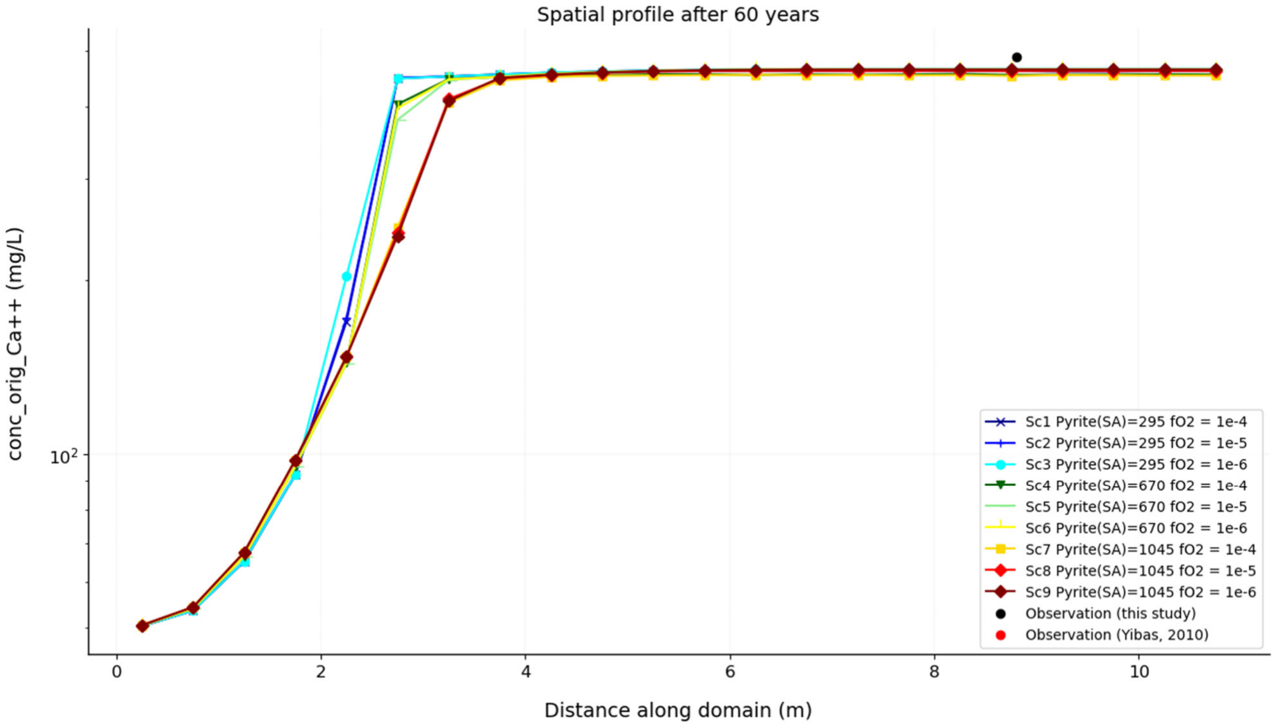

Figure 71: Model 1: Scenario 1 – 9: Dissolved calcium change over depth after 60 years

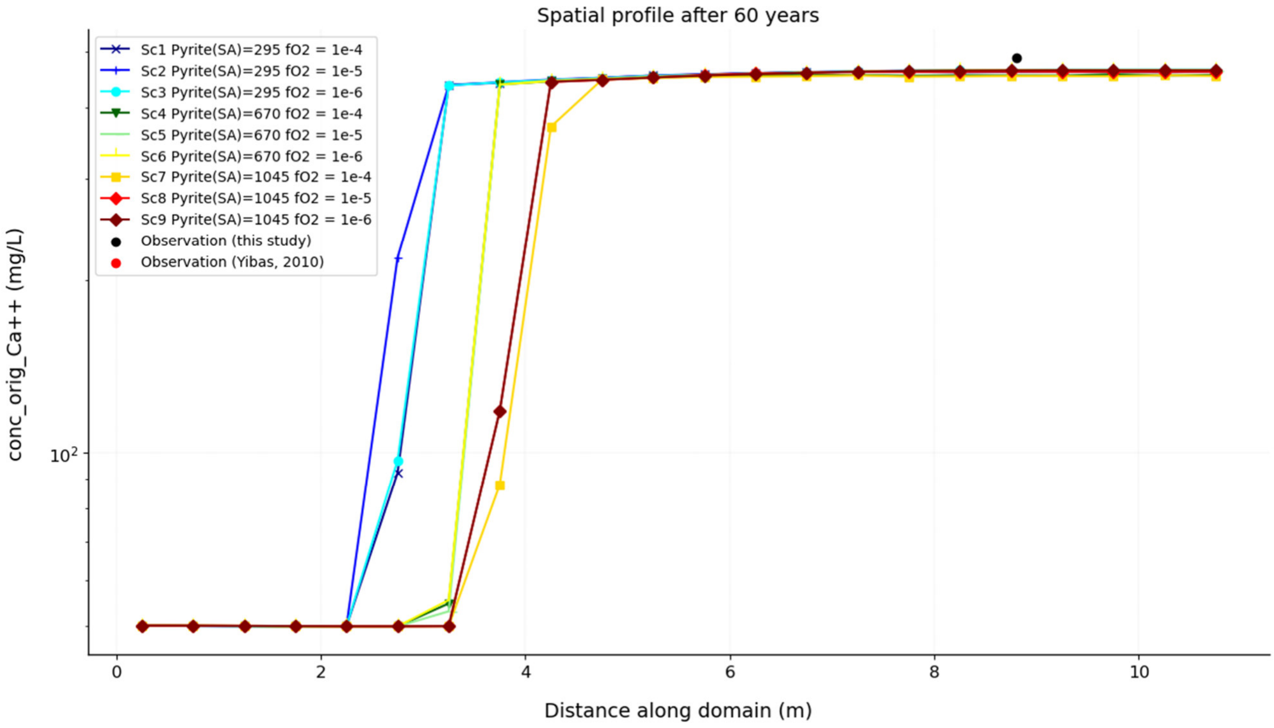

Figure 72: Model 2: Scenario 1 – 9: Dissolved calcium change over depth after 60 years

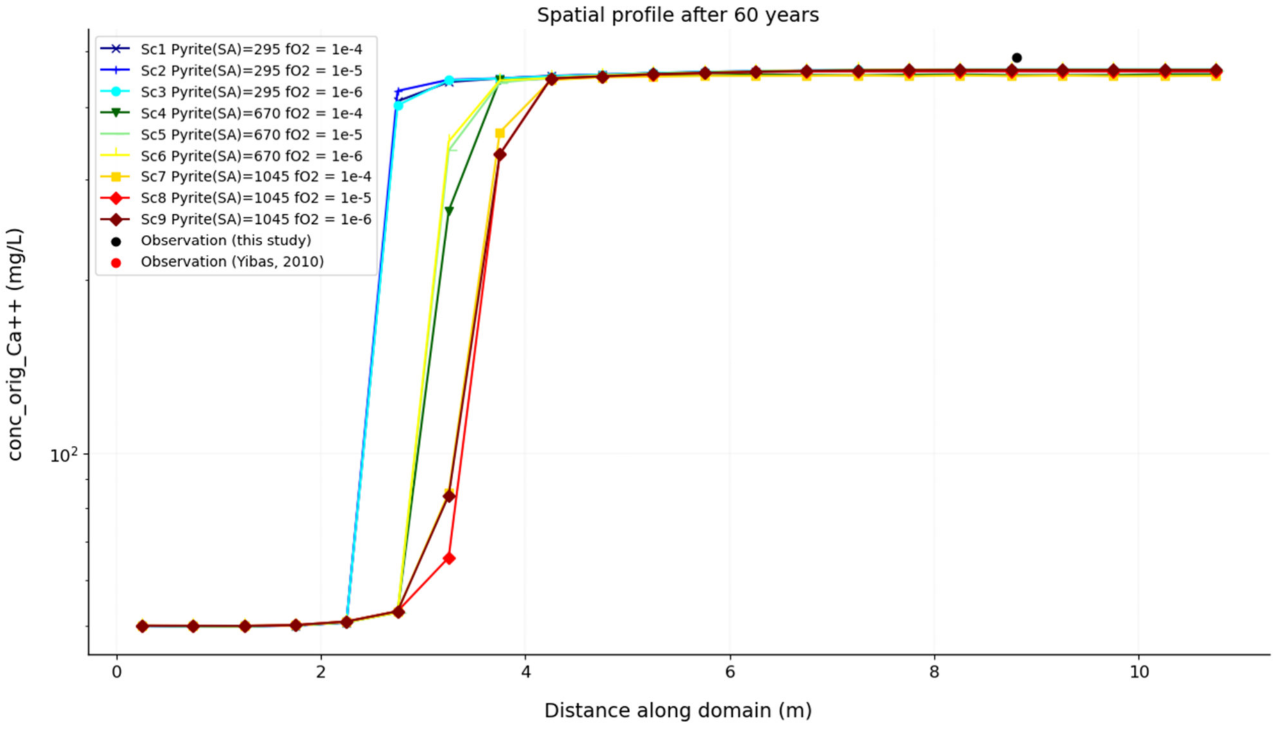

Figure 73: Model 3: Scenario 1 – 9: Dissolved calcium change over depth after 60 years

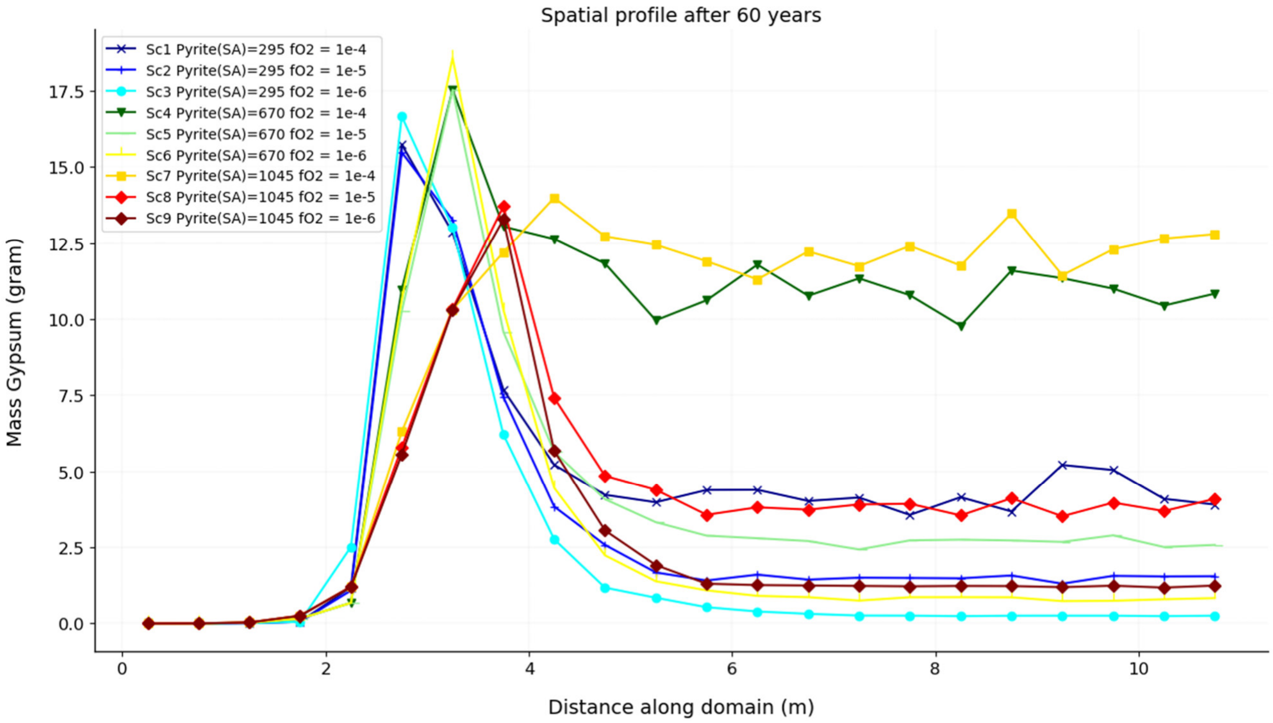

Figure 74: Model 1: Scenario 1 – 9: Gypsum change over depth after 60 years

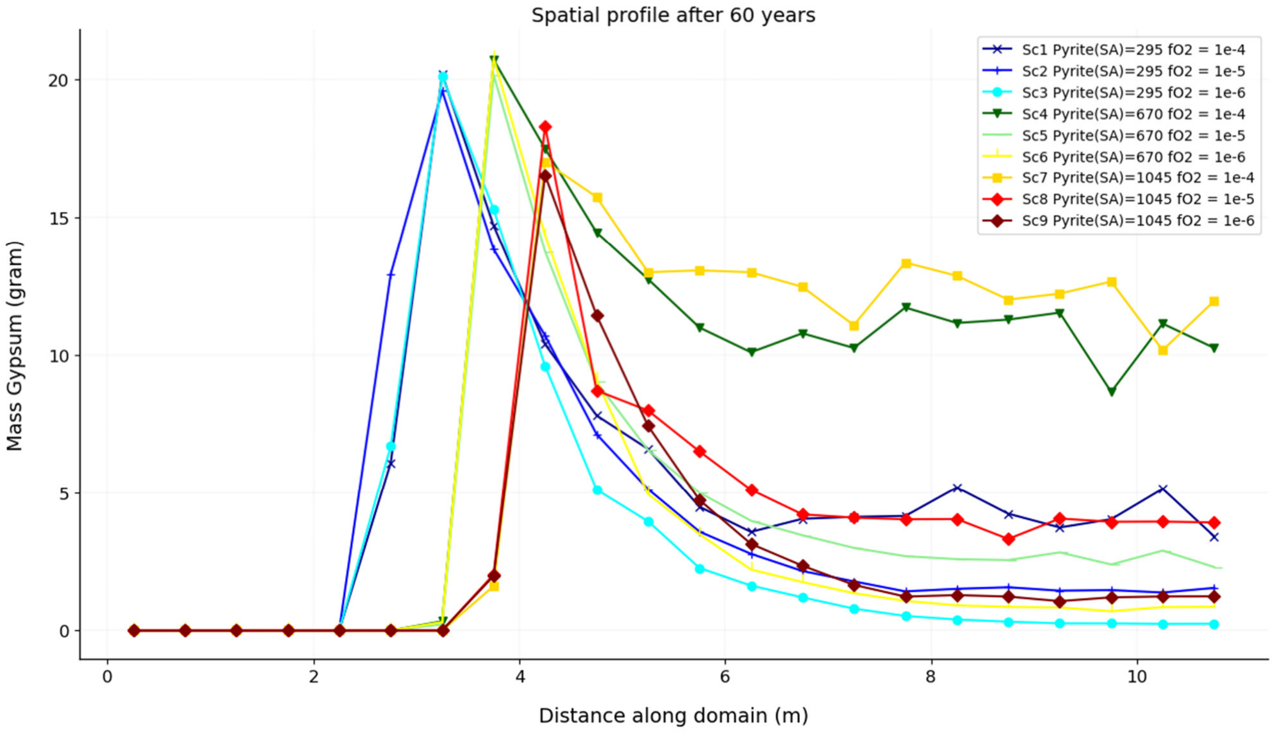

Figure 75: Model 2: Scenario 1 – 9: Gypsum change over depth after 60 years

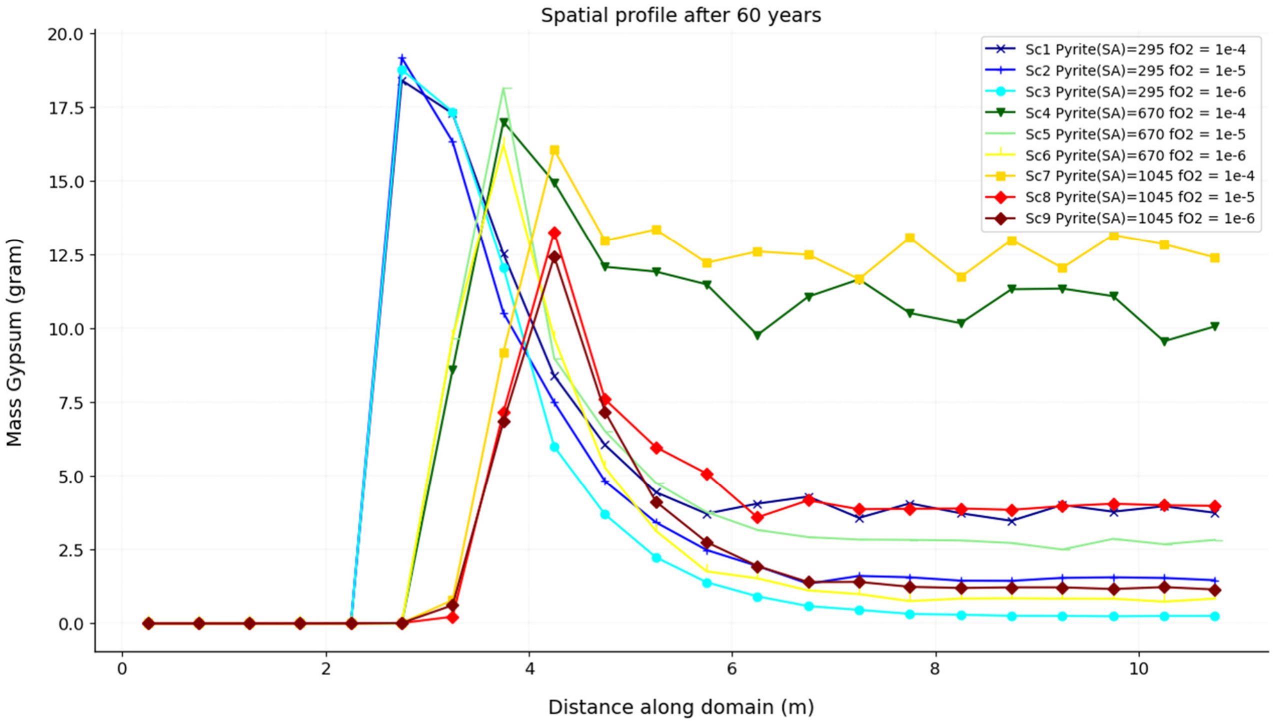

Figure 76: Model 3: Scenario 1 – 9: Gypsum change over depth after 60 years

7.6.5 Model 1-3: Dissolved Magnesium, Dissolved Aluminium and Chlorite

Dissolved Magnesium and Dissolved Aluminium

The dissolved magnesium change over the depth of the tailings after 60 years for Model 1 - 3 is depicted in Figure 77, Figure 78 and Figure 79respectively; similarly, dissolved aluminium is depicted in Figure 80, Figure 81 and Figure 82. The magnesium in the Oxic Zone is leached at the top, reaches a maximum at about ~3 m in the Transition Zone, and then decrease towards the Anoxic Zone. All model scenarios matched the magnesium in the Anoxic Zone which is at about ~500 mg/L.

The aluminium in the Oxic Zone is between 100-2 000 mg/L, reaches a maximum at about ~3 m in the Transition Zone, and then decreases towards the Anoxic Zone. All model scenarios have the aluminium at between 10 – 100 mg/L in the Anoxic Zone, which is lower than the observed value of about ~200 mg/L.

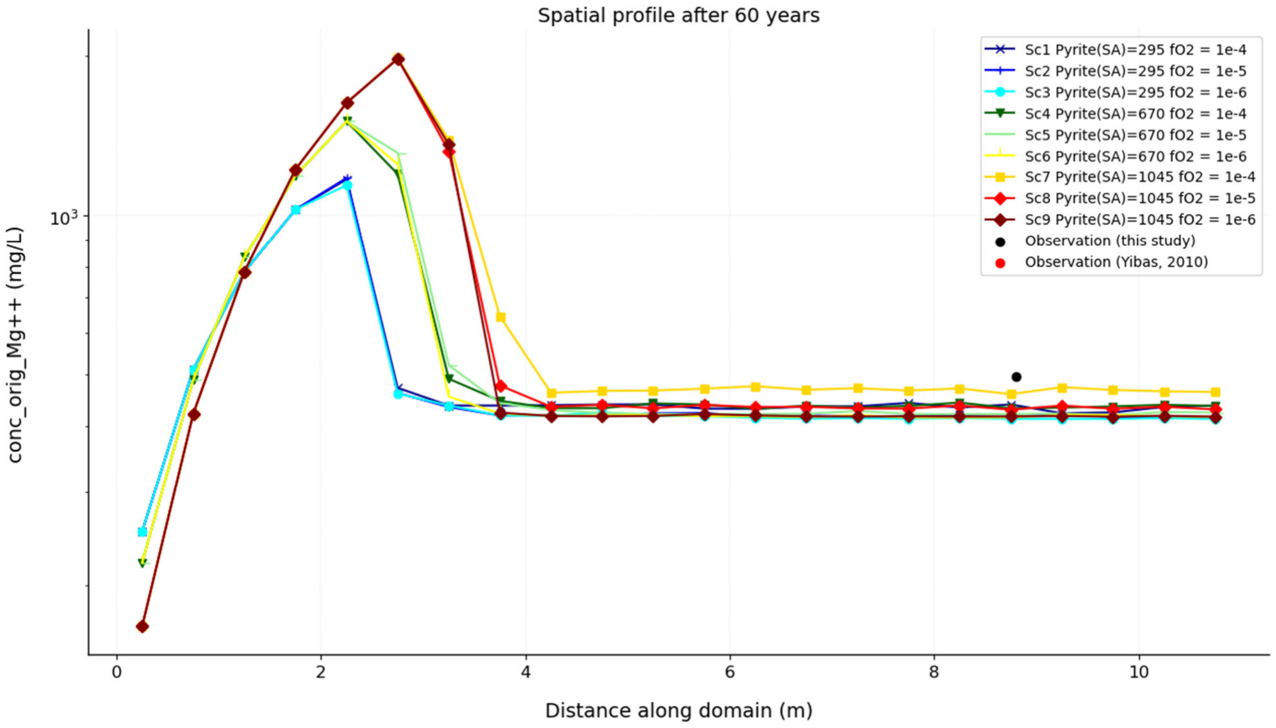

Figure 77: Model 1: Scenario 1 – 9: Dissolved magnesium change over depth after 60 years

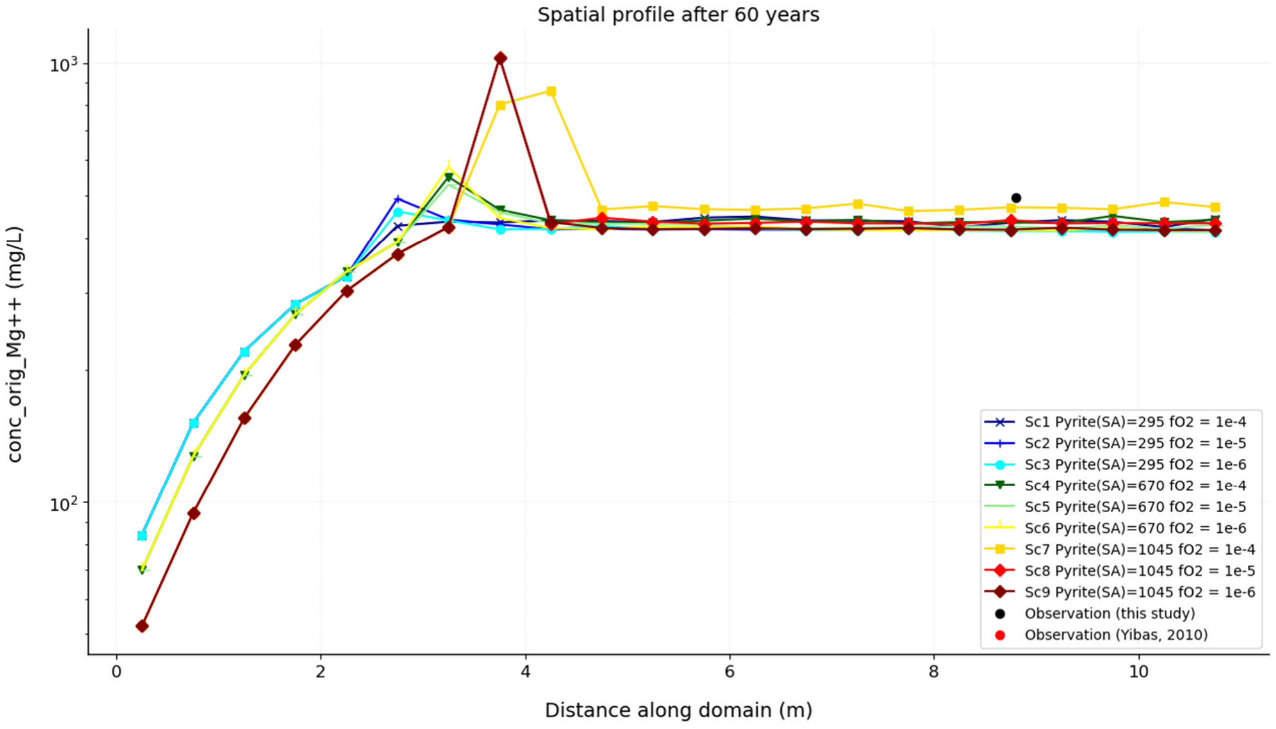

Figure 78: Model 2: Scenario 1 – 9: Dissolved magnesium change over depth after 60 years

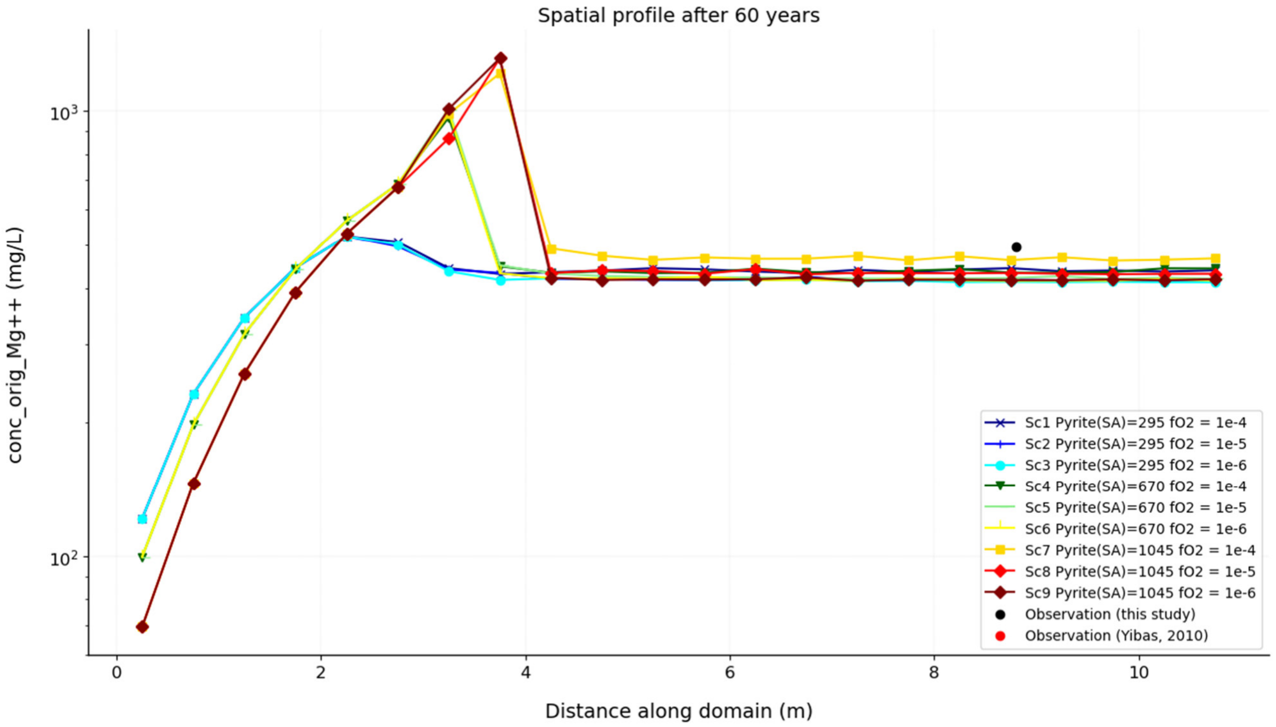

Figure 79: Model 3: Scenario 1 – 9: Dissolved magnesium change over depth after 60 years

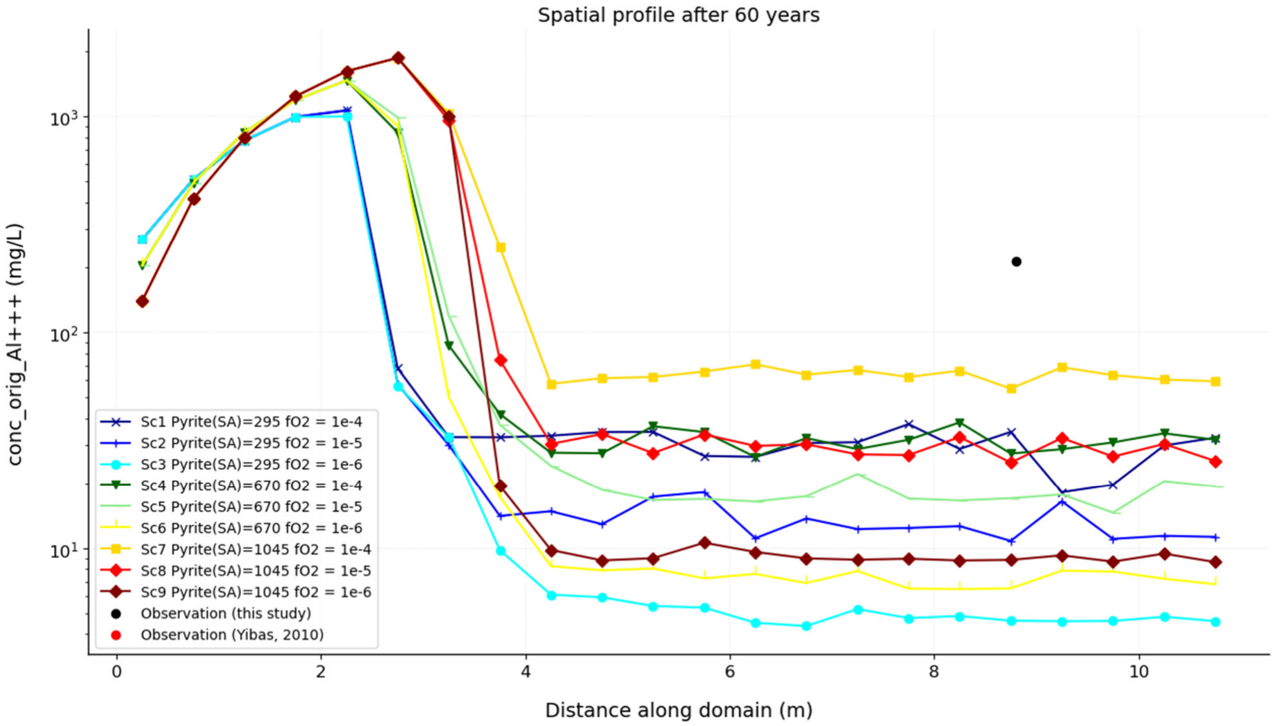

Figure 80: Model 1: Scenario 1 – 9: Dissolved aluminium change over depth after 60 years

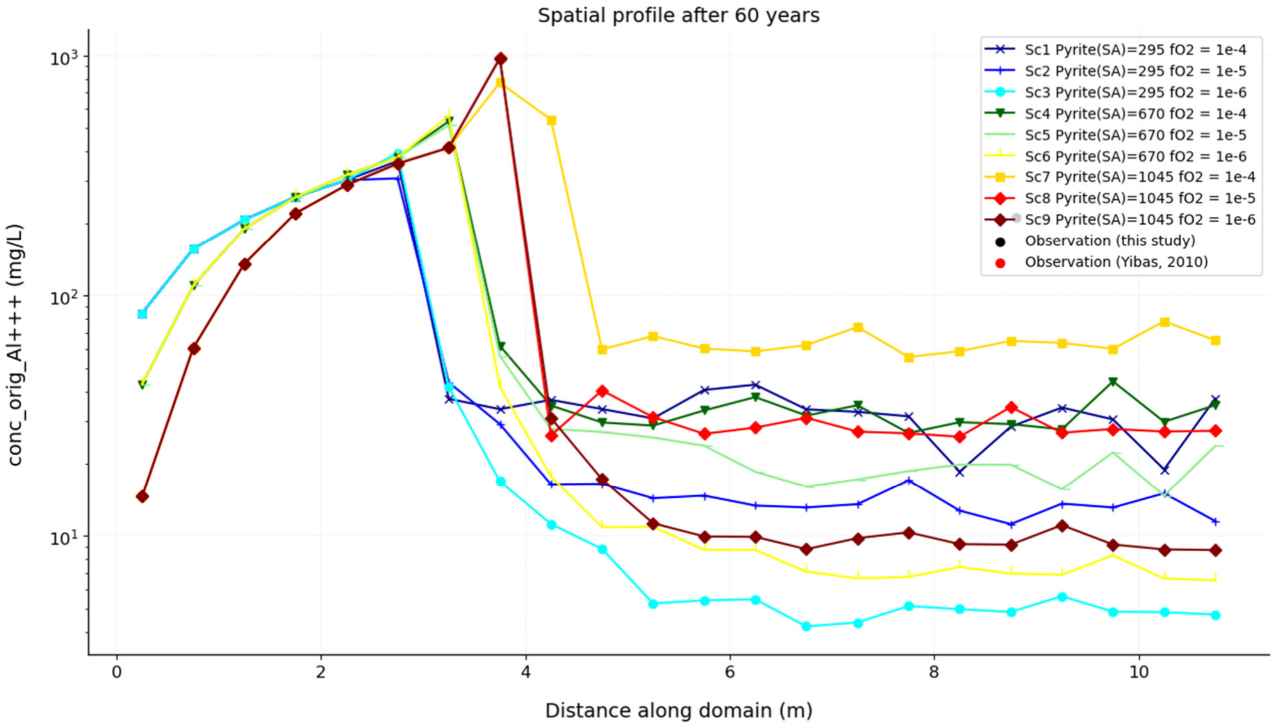

Figure 81: Model 2: Scenario 1 – 9: Dissolved aluminium change over depth after 60 years

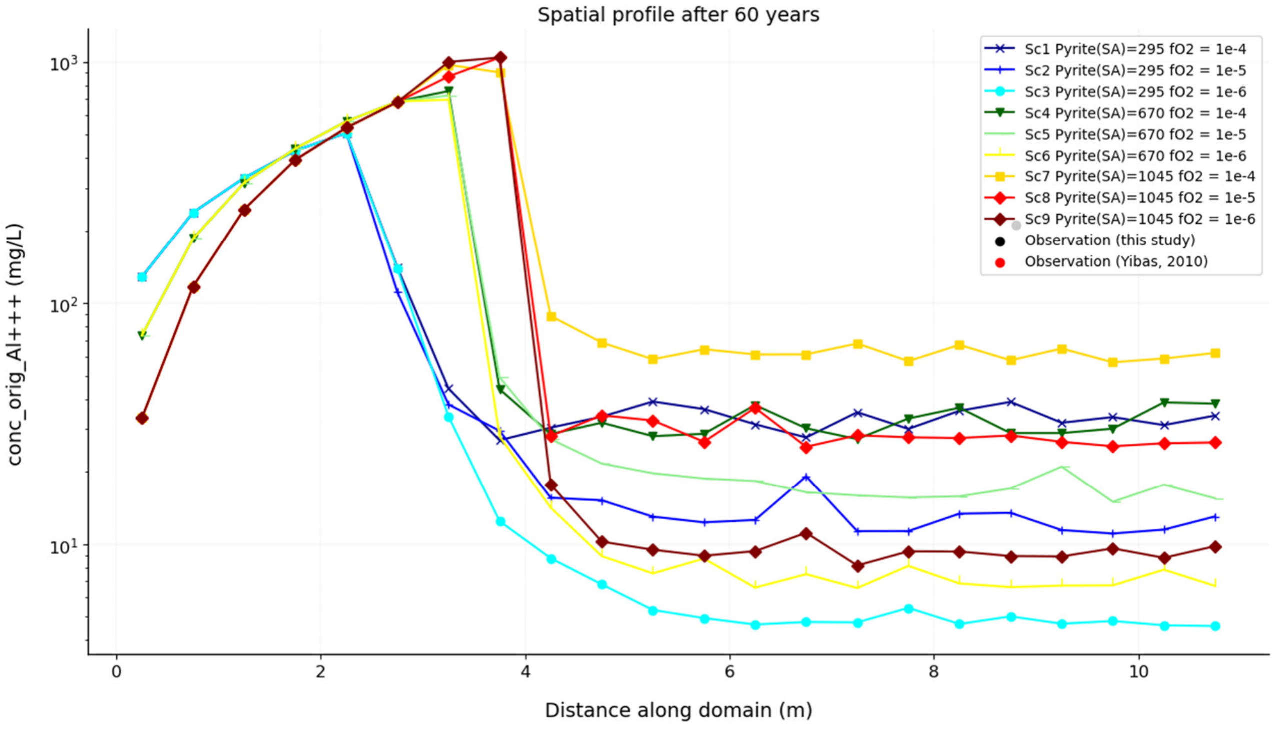

Figure 82: Model 3: Scenario 1 – 9: Dissolved aluminium change over depth after 60 years

Chlorite

The chlorite mineral, chamosite, change over the depth of the tailings after 60 years for Model 1 - 3 is depicted in Figure 83, Figure 84 and Figure 85, respectively. Only the chamosite is shown, but clinochlore shows a similar trend. The chlorite is significantly depleted in the Oxic Zone, which results in an increase in dissolved magnesium and aluminium in the Oxic and Transition Zones. Limited reaction of the chlorite took place in the Anoxic Zone.

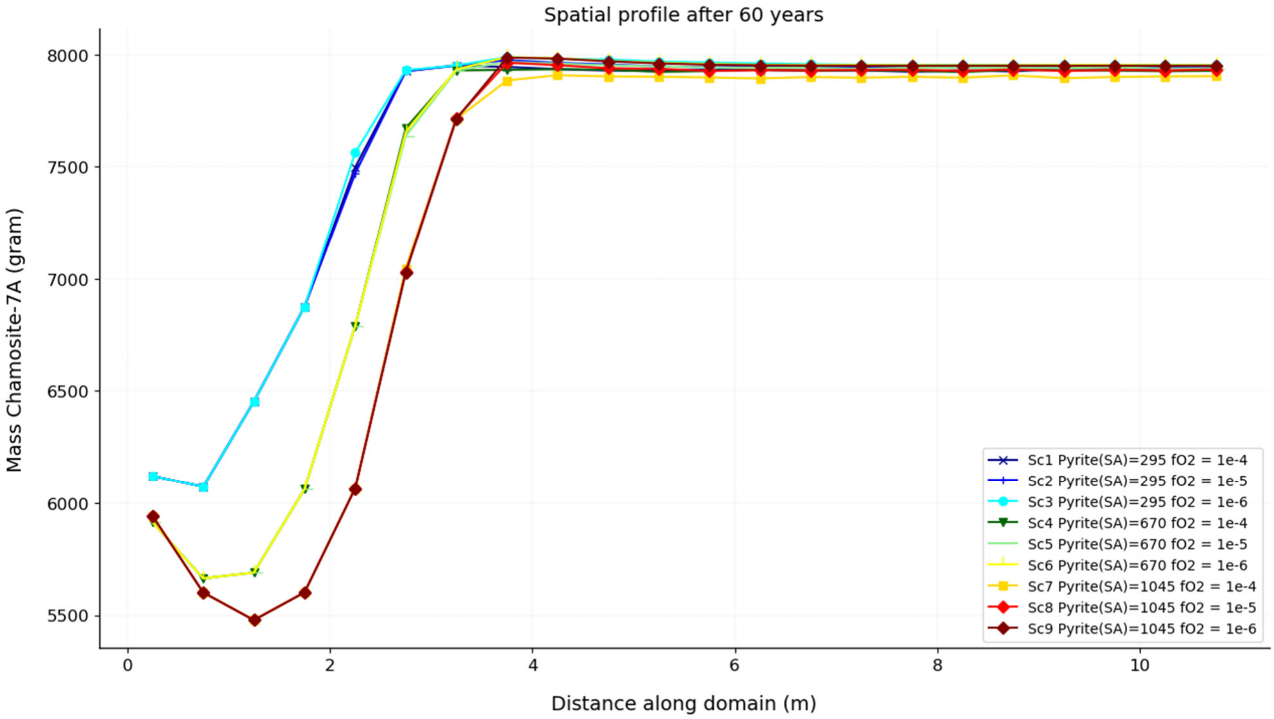

Figure 83: Model 1: Scenario 1 – 9: Chlorite change over depth after 60 years

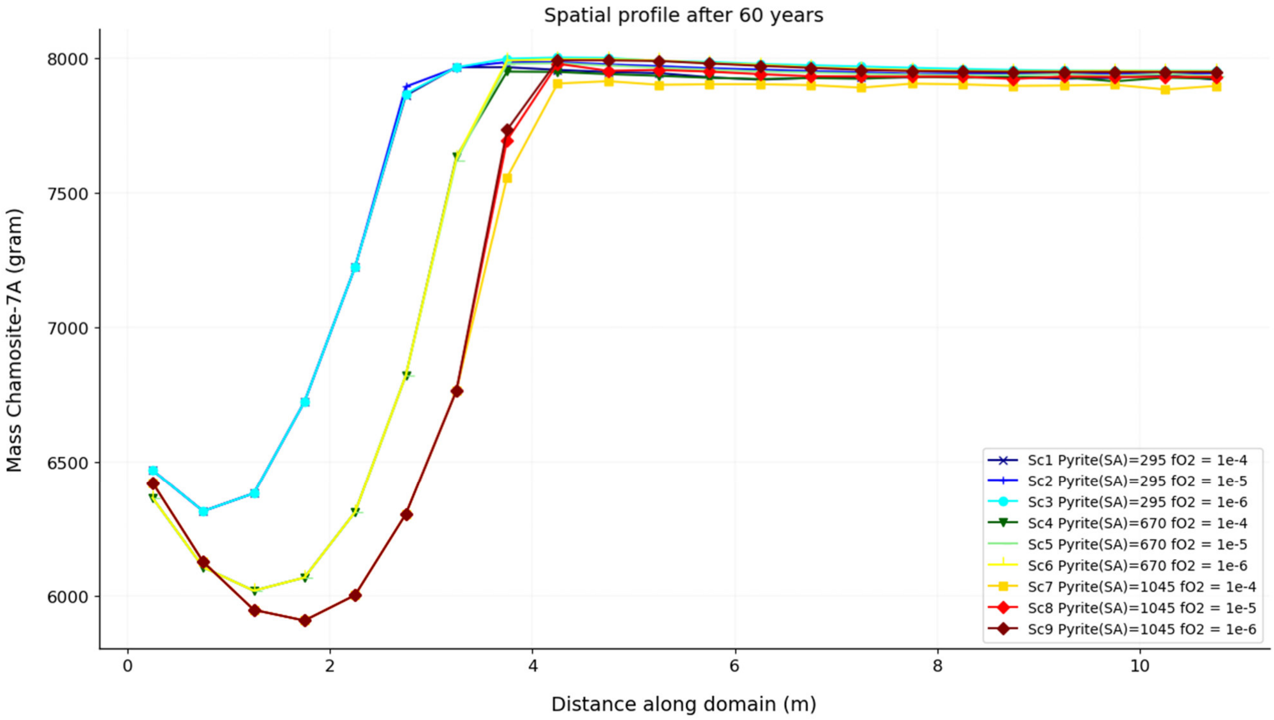

Figure 84: Model 2: Scenario 1 – 9: Chlorite change over depth after 60 years

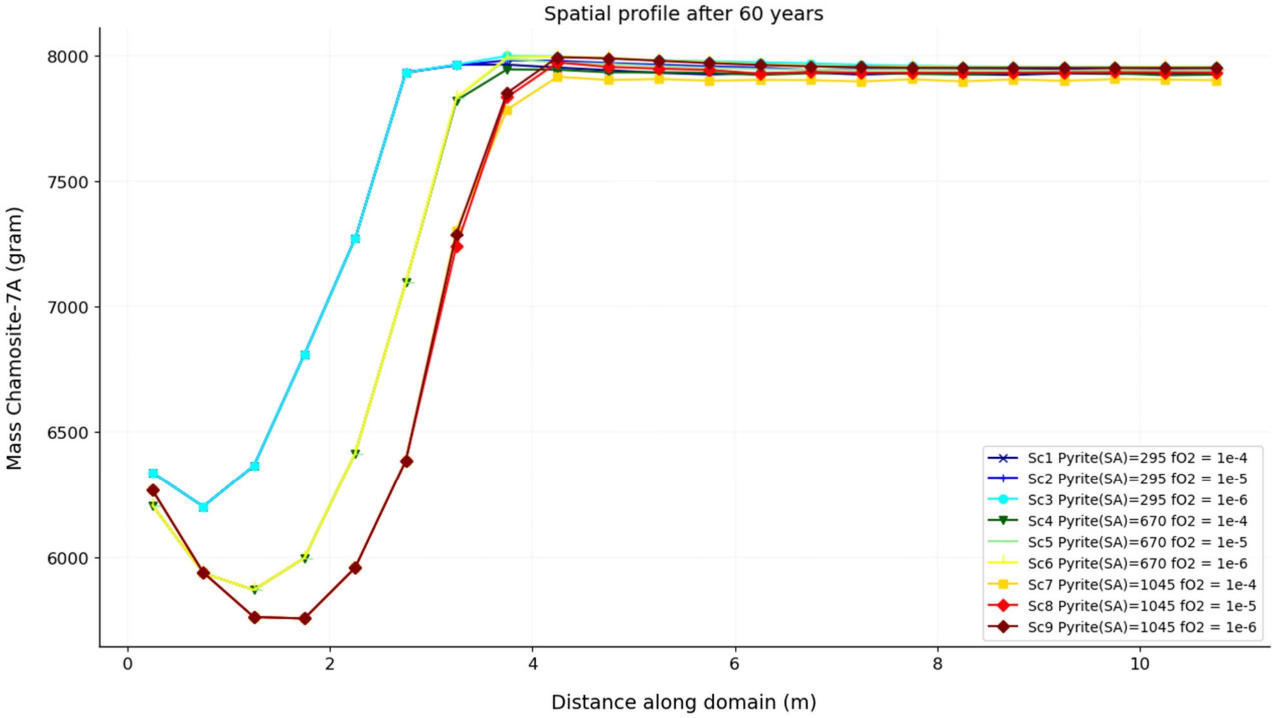

Figure 85: Model 3: Scenario 1 – 9: Chlorite change over depth after 60 years

7.6.6 Model 1-3: Dissolved Uranium and Associated Minerals

Dissolved Uranium

The dissolved uranium change over the depth of the tailings after 60 years for Model 1 - 3 is depicted in Figure 86, Figure 87 and Figure 88, respectively. The dissolved uranium shows an increase in the Oxic Zone and reaches a maximum at about ~3 m, and then decreases towards the Anoxic Zone, where it stays fairly constant. The uranium is sensitive to the oxygen fugacity settings in the Anoxic Zone, and the best match is observed for low oxygen fugacity (1 x 10^{-6}), similar to the iron and Eh(Fe++/Fe+++).

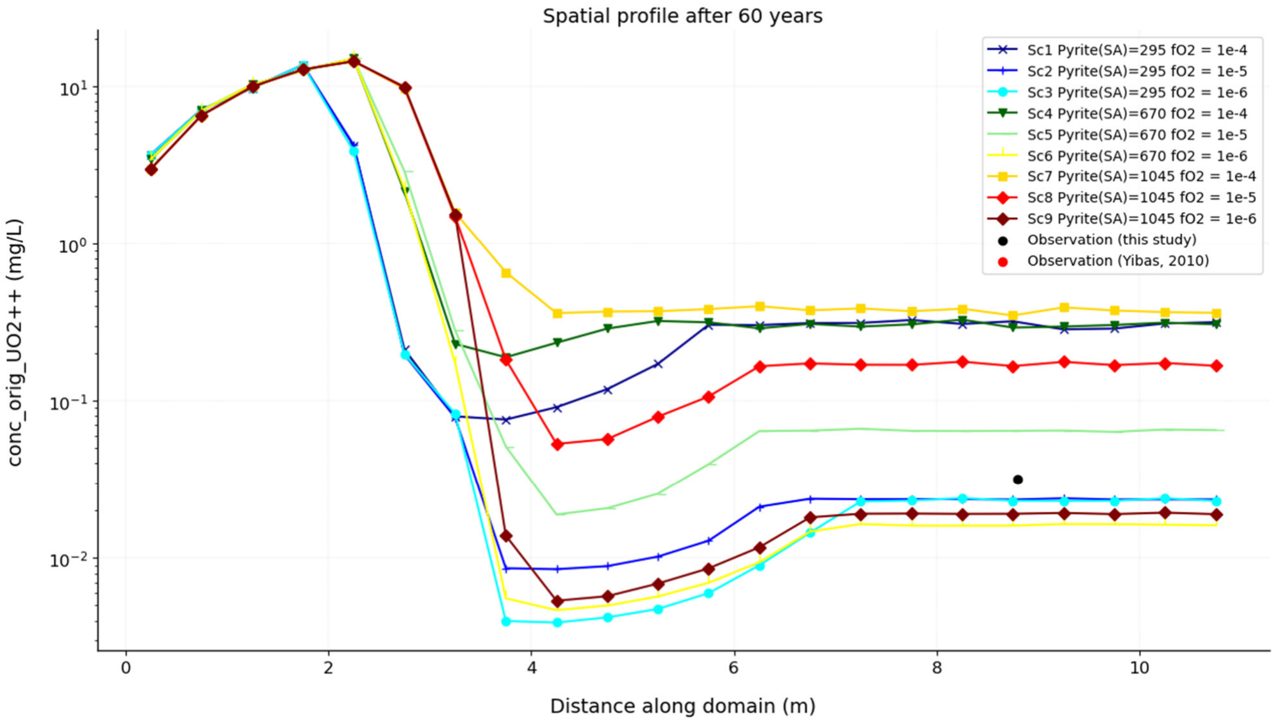

Figure 86: Model 1: Scenario 1 – 9: Dissolved uranium change over depth after 60 years

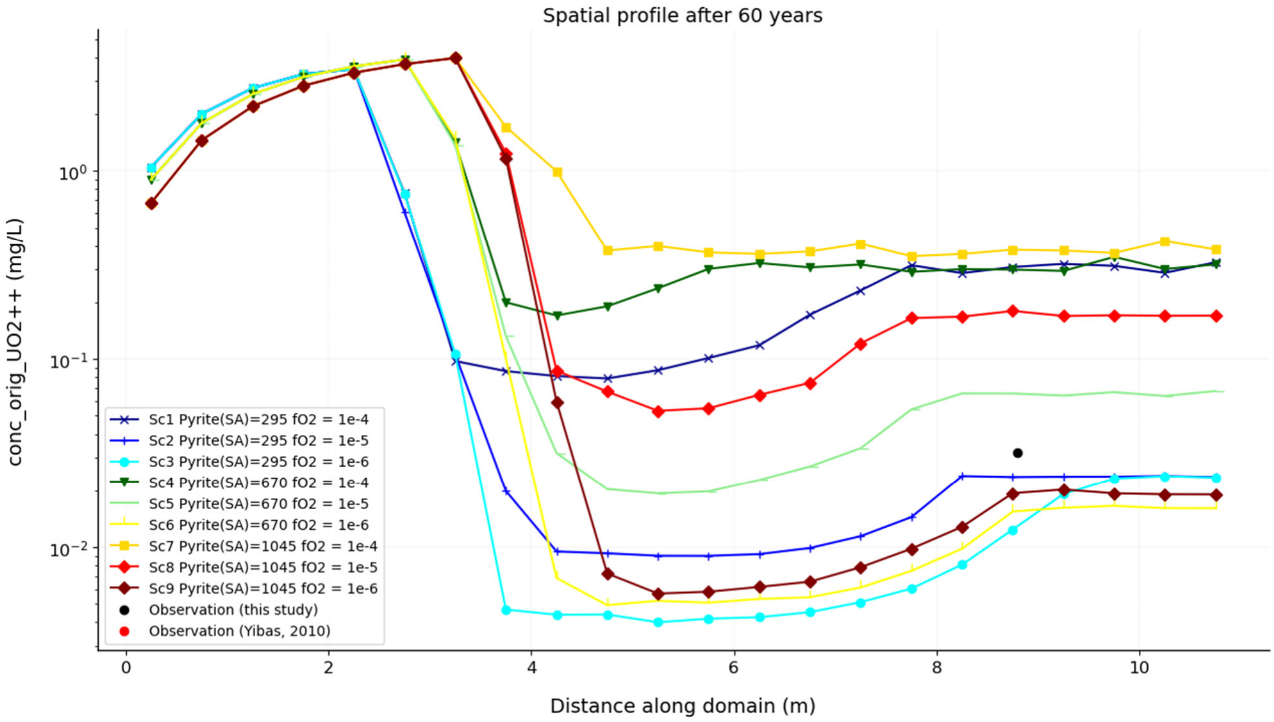

Figure 87: Model 2: Scenario 1 – 9: Dissolved uranium change over depth after 60 years

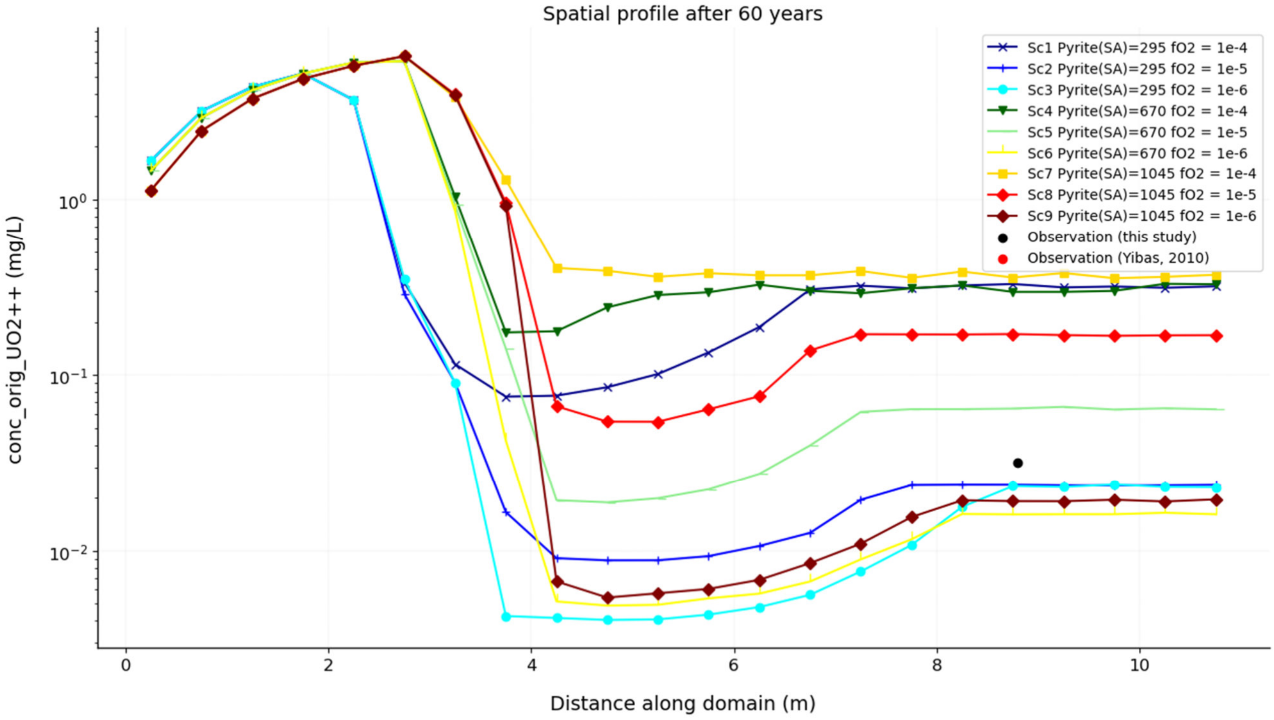

Figure 88: Model 3: Scenario 1 – 9: Dissolved uranium change over depth after 60 years

Uraninite and Secondary Uranyl Sulphate (Zippeite)

The uraninite mineral change over the depth of the tailings after 60 years for Model 1 - 3 is depicted in Figure 89, Figure 90 and Figure 91, respectively; similarly, Zippeite is depicted in Figure 92, Figure 93 and Figure 94. The uraninite in the Oxic Zone is significantly depleted at the top but unreacted in the Anoxic Zone. Uranium will mostly precipitate as zippeite-Zn (or zippeite-Mg not shown here) in the Transition Zone or at the top of the Anoxic Zone.

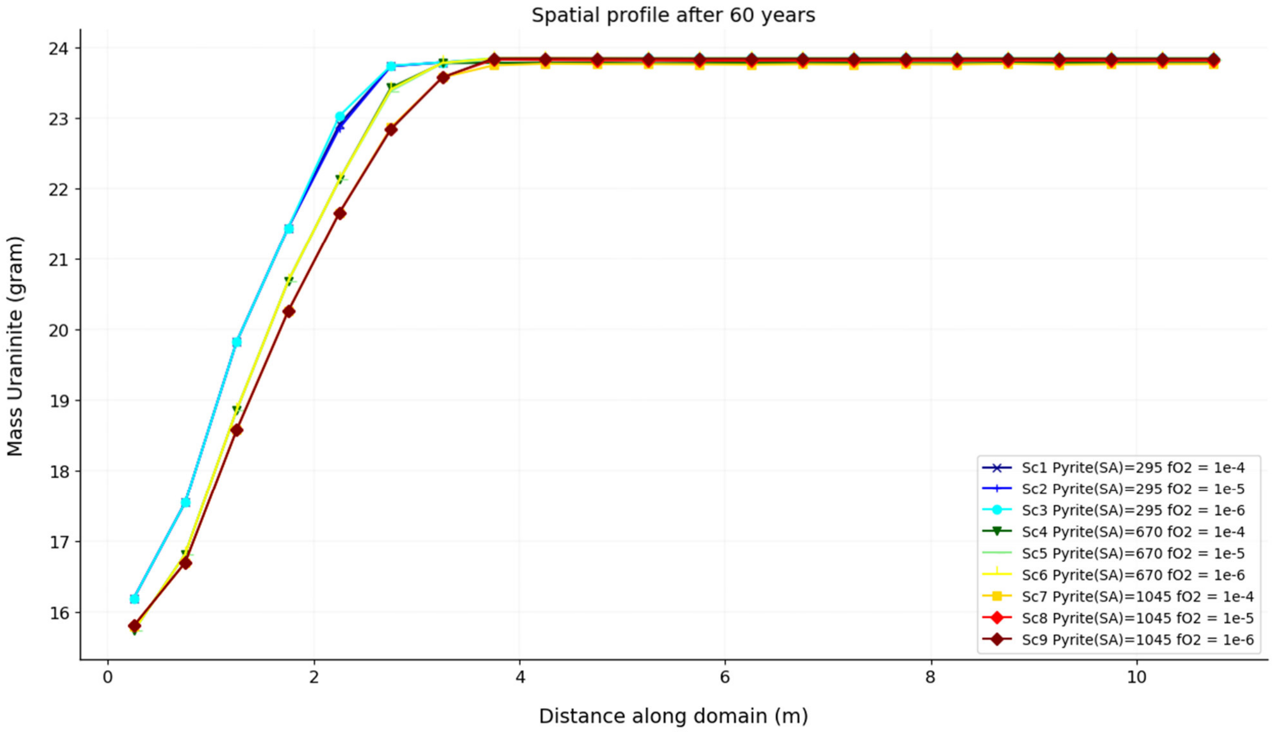

Figure 89: Model 1: Scenario 1 – 9: Uraninite change over depth after 60 years

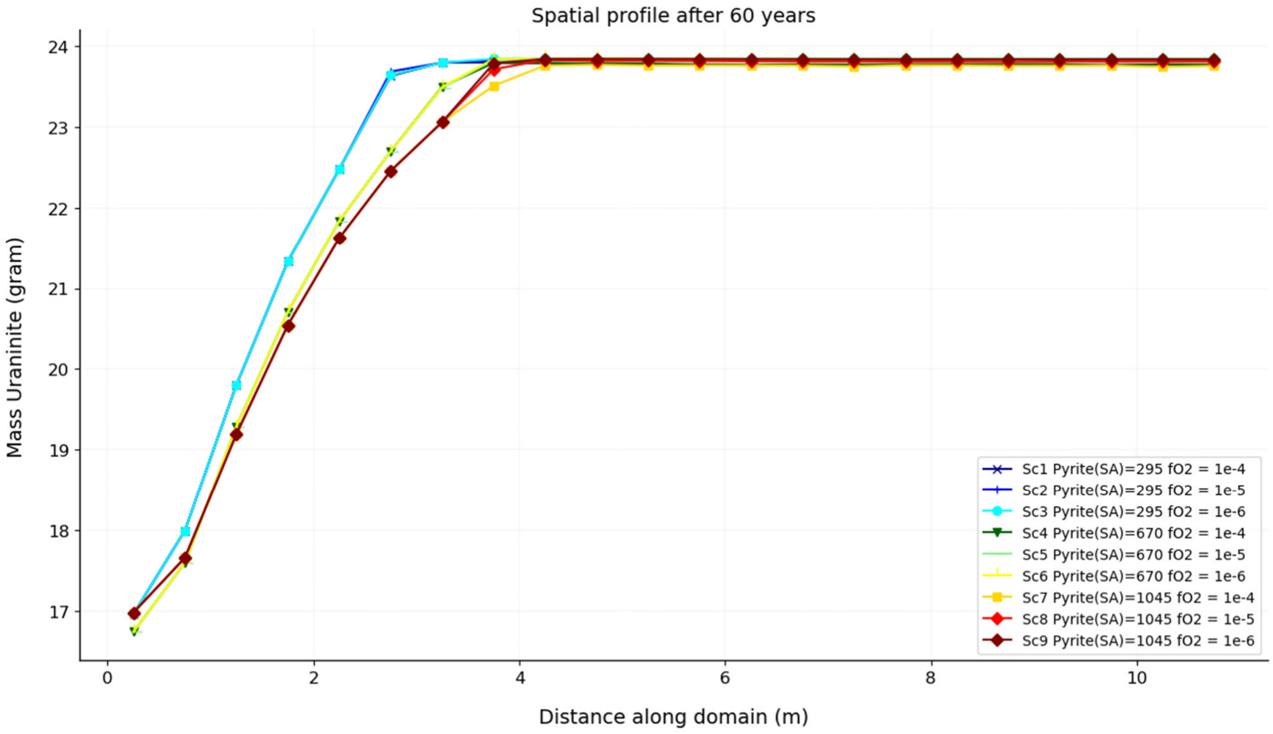

Figure 90: Model 2: Scenario 1 – 9: Uraninite change over depth after 60 years

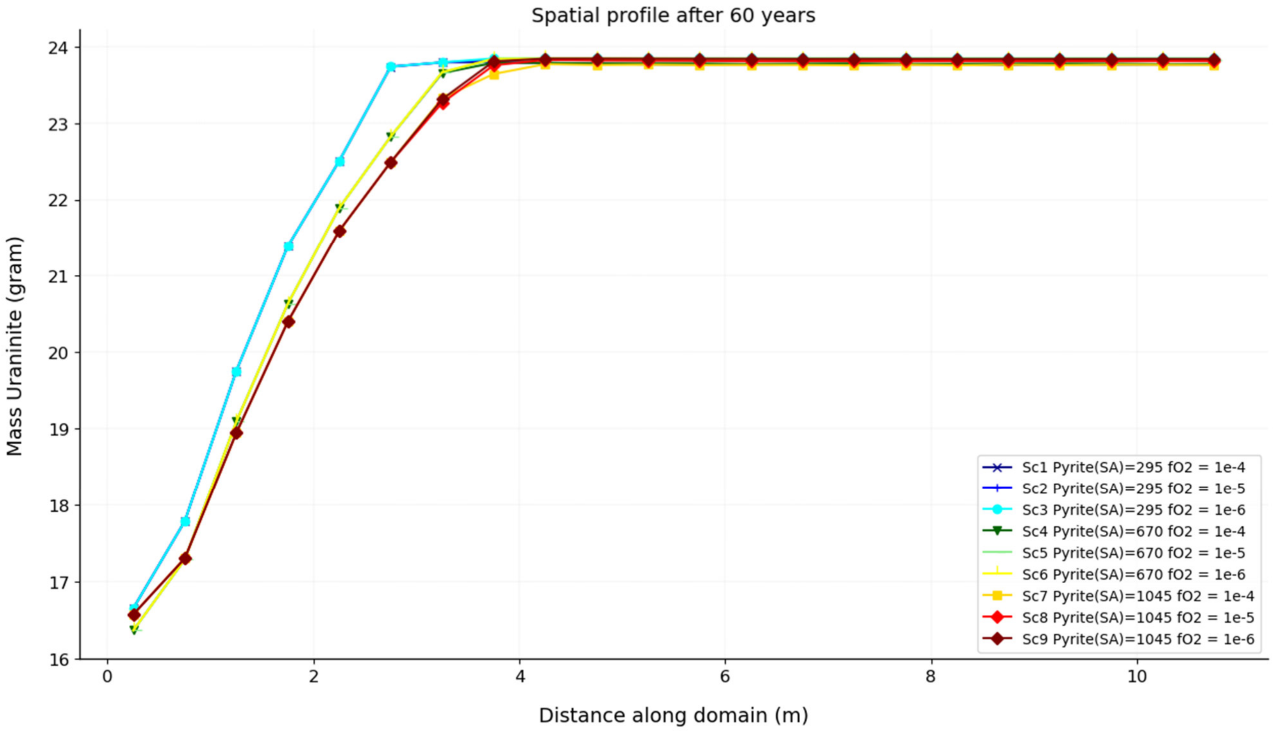

Figure 91: Model 3: Scenario 1 – 9: Uraninite change over depth after 60 years

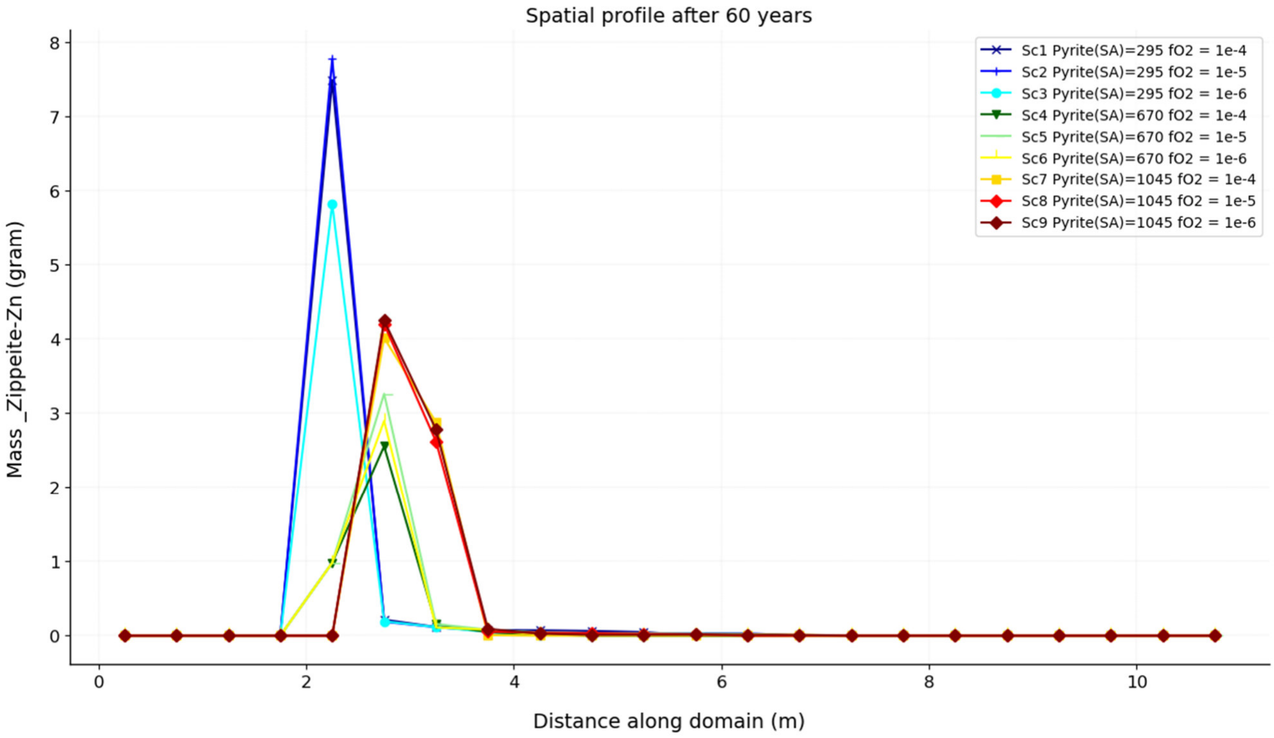

Figure 92: Model 1: Scenario 1 – 9: Zippeite-Zn change over depth after 60 years

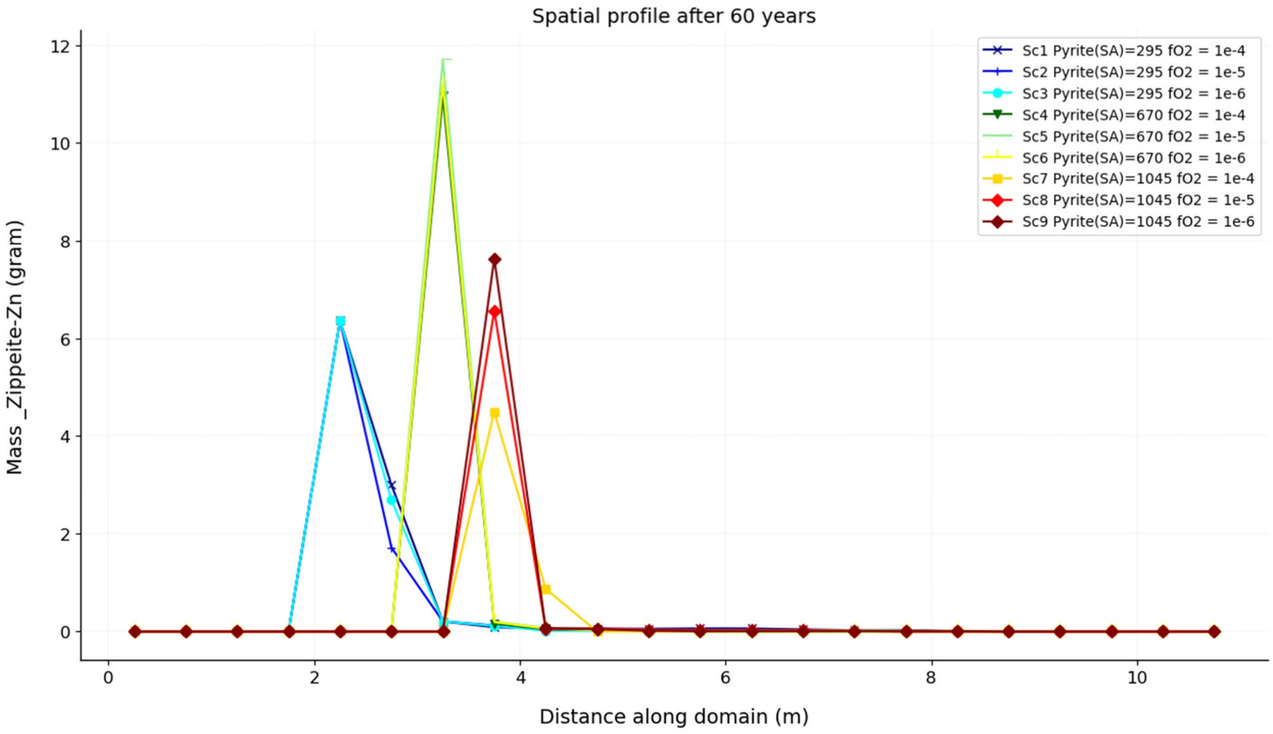

Figure 93: Model 2: Scenario 1 – 9: Zippeite-Zn change over depth after 60 years

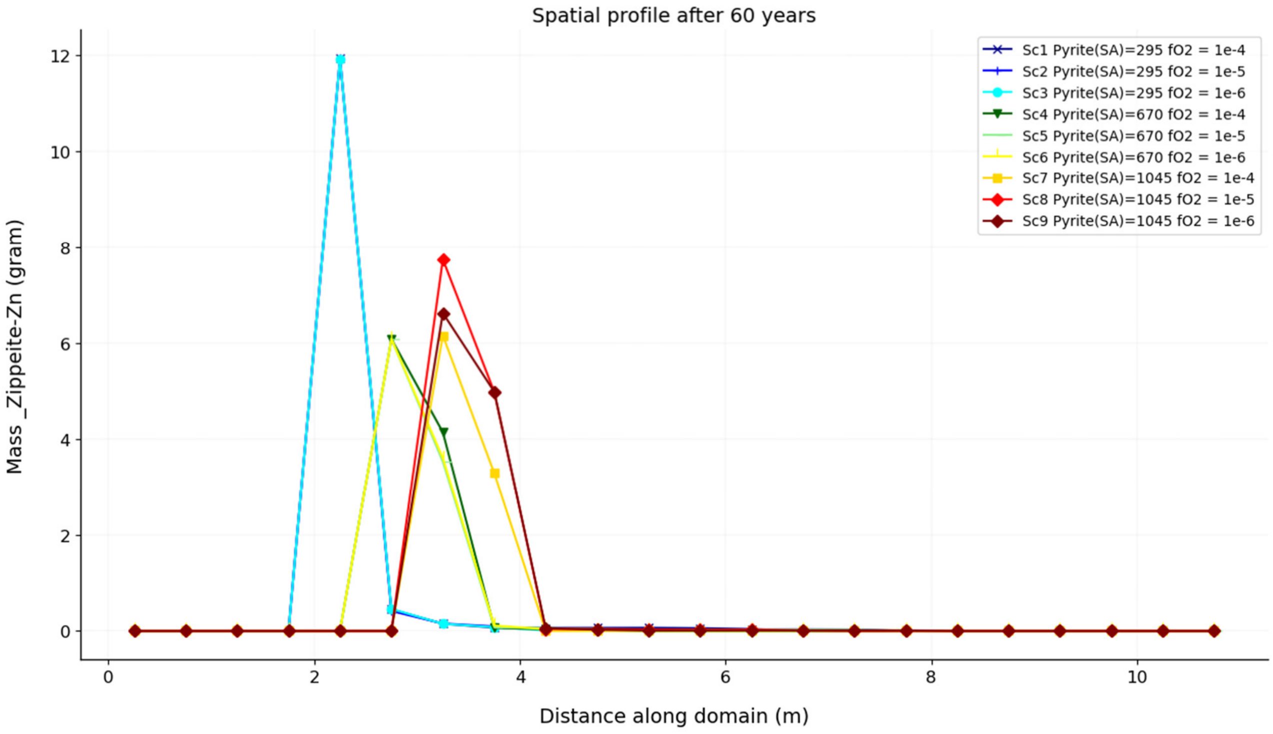

Figure 94: Model 3: Scenario 1 – 9: Zippeite-Zn change over depth after 60 years

7.6.7 Model 1-3: Dissolved Arsenic and Associated Minerals

Dissolved Arsenic

The dissolved arsenic change over the depth of the tailings after 60 years for Model 1 - 3 is depicted in Figure 95, Figure 96 and Figure 97respectively.

The dissolved arsenic is low in the Oxic Zone as most of it precipitated with iron. In the Anoxic Zone, it is fairly constant but (just like uranium and iron) very sensitive to the oxygen fugacity. Like iron and uranium, it could be best matched with the low oxygen fugacity conditions (1 x 10^{-6} and, to a lesser degree, 1 x 10^{-5}). As discussed in the conceptual model in Section 5.3.3, arsenic is more soluble under anoxic conditions.

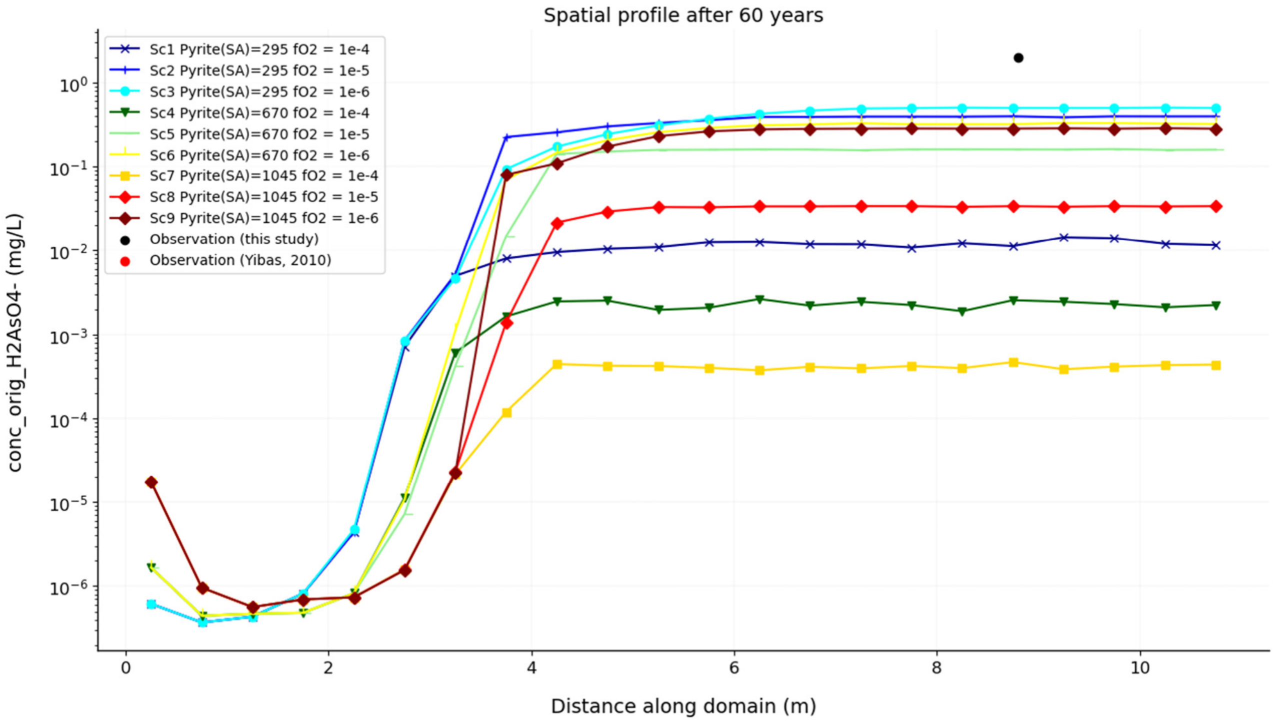

Figure 95: Model 1: Scenario 1 – 9: Dissolved arsenic change over depth after 60 years

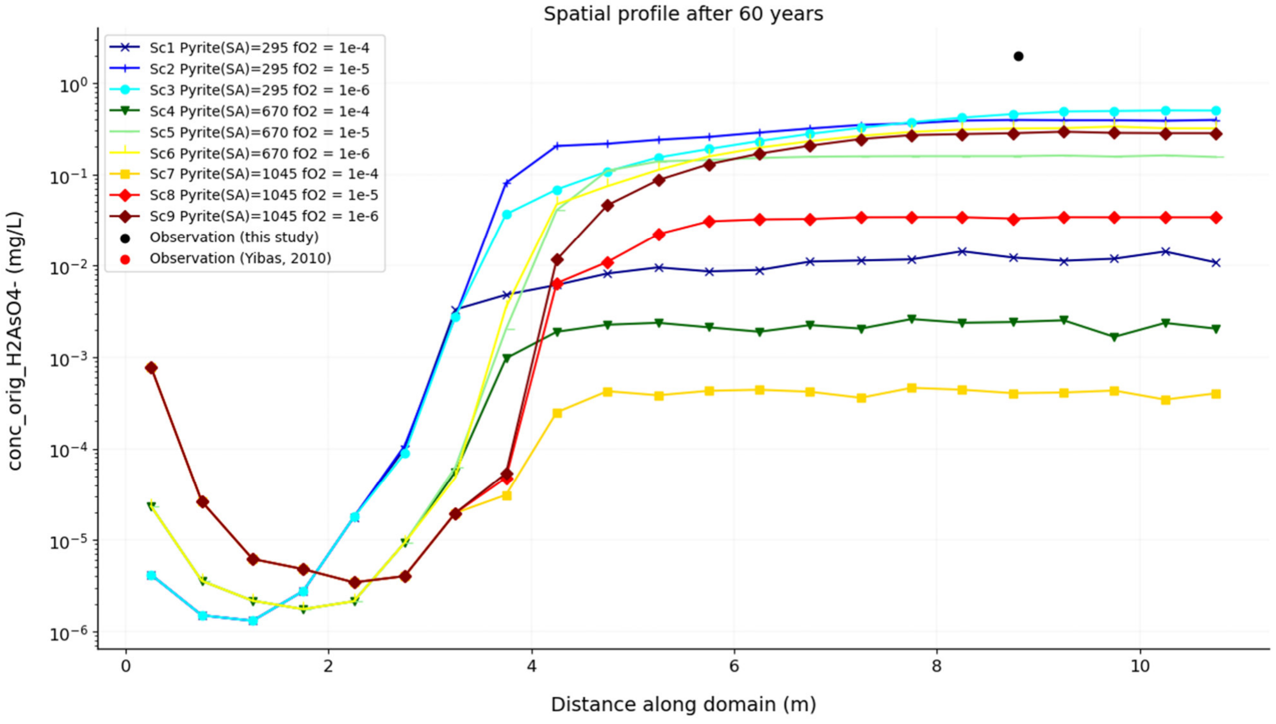

Figure 96: Model 2: Scenario 1 – 9: Dissolved arsenic change over depth after 60 years

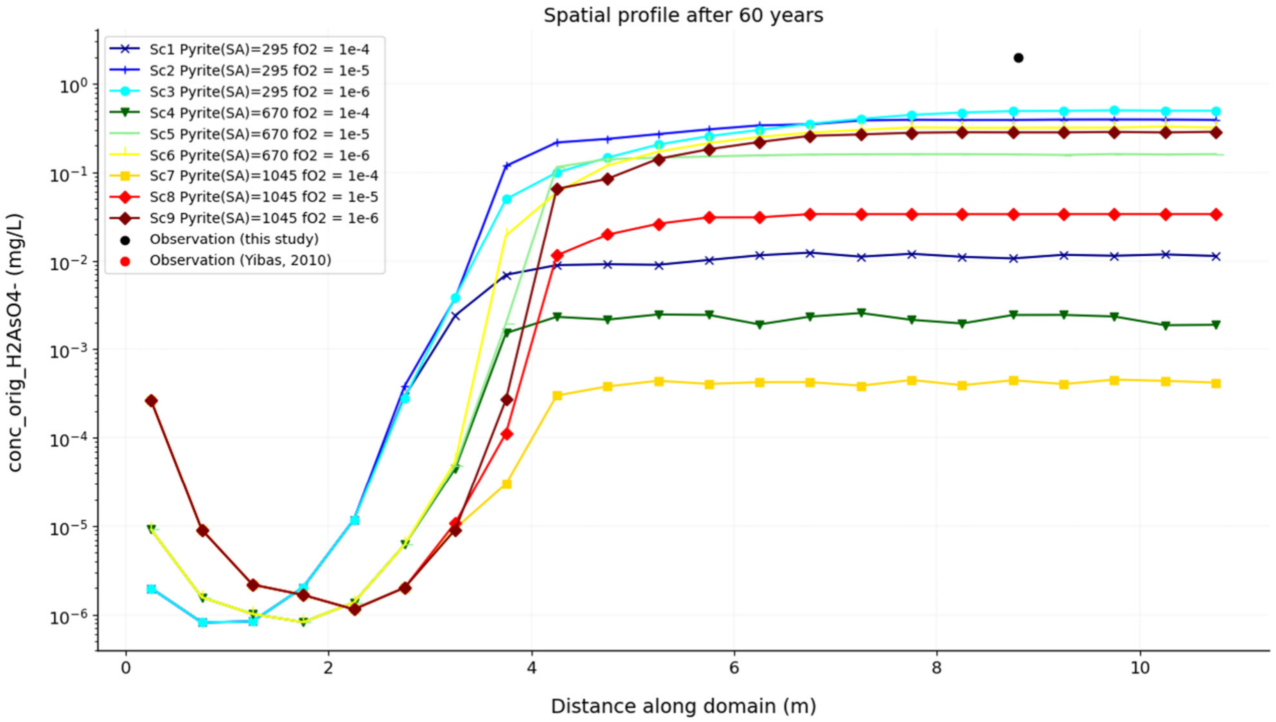

Figure 97: Model 3: Scenario 1 – 9: Dissolved arsenic change over depth after 60 years

Arsenopyrite and Secondary Arsenate Sulfate

The arsenopyrite change over the depth of the tailings after 60 years for Model 1 - 3 is depicted in Figure 98, Figure 99 and Figure 100, respectively; similarly, bukovskýite is depicted in Figure 101, Figure 102 and Figure 103. The arsenopyrite is significantly depleted in the Oxic Zone but fairly unreacted in the Anoxic Zone. Most of the released arsenic will precipitate with iron in the Oxic Zone, e.g. as secondary arsenate sulphate bukovskýite.

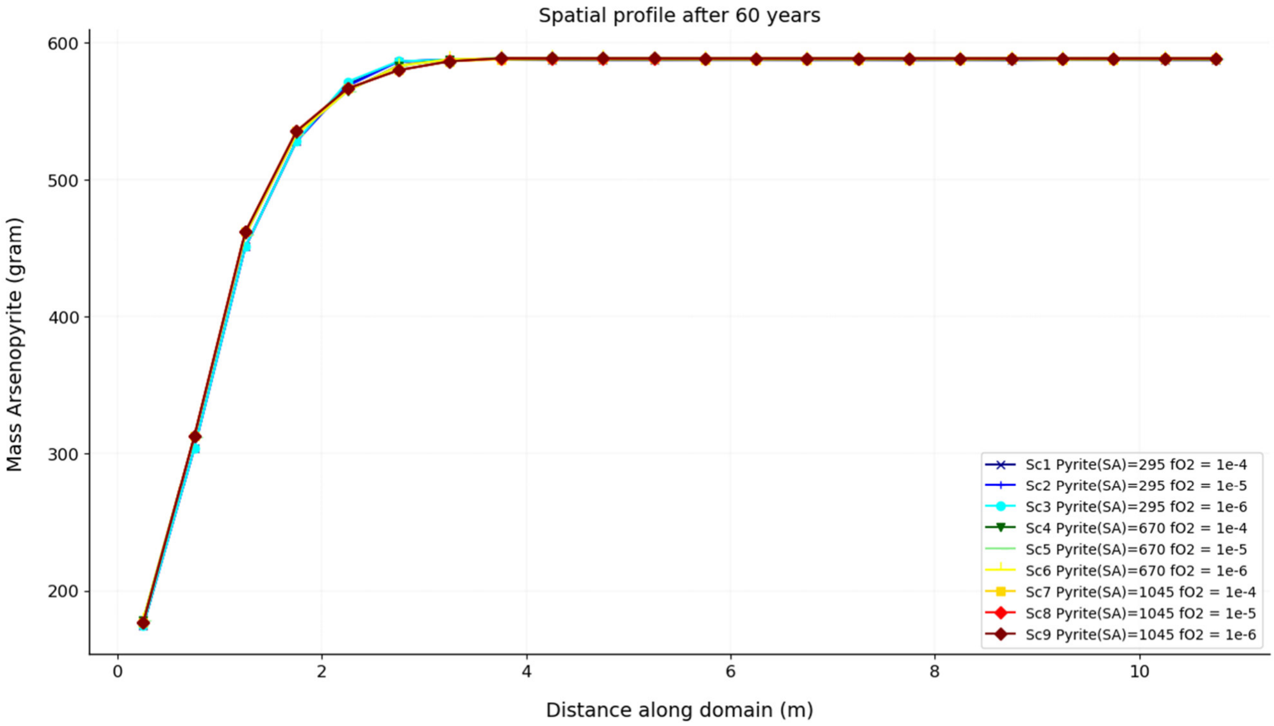

Figure 98: Model 1: Scenario 1 – 9: Arsenopyrite change over depth after 60 years

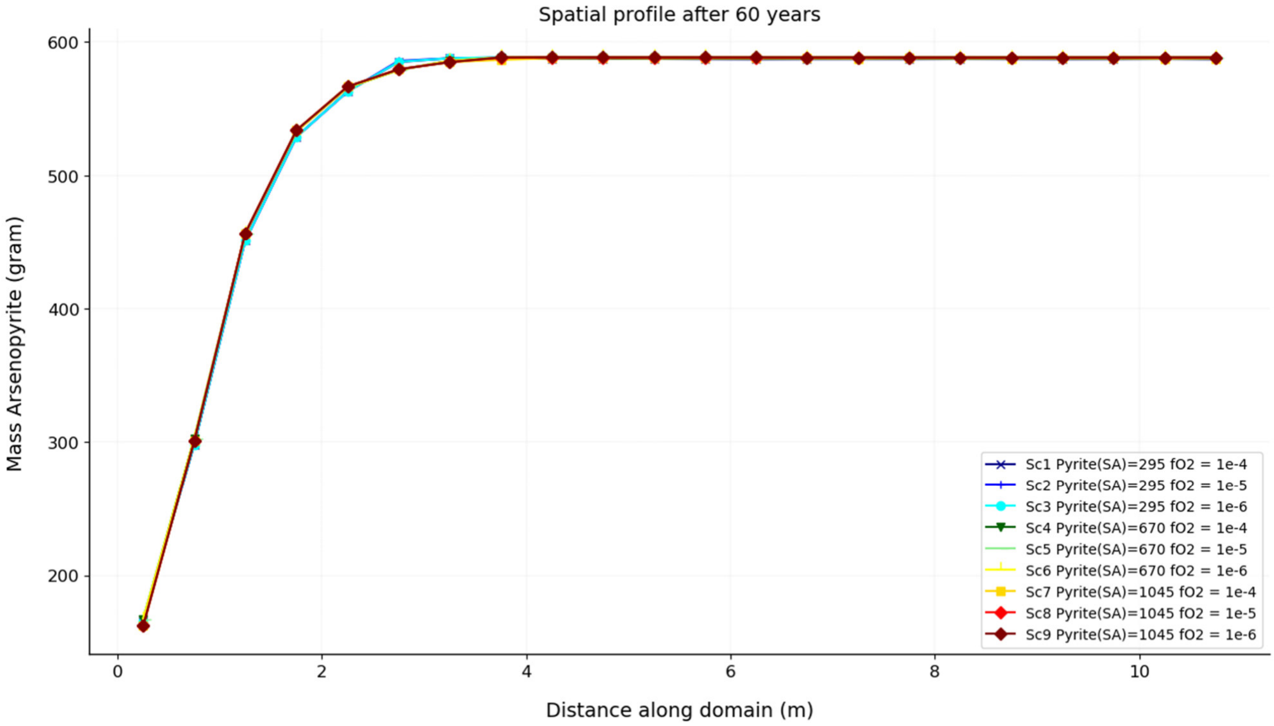

Figure 99: Model 2: Scenario 1 – 9: Arsenopyrite change over depth after 60 years

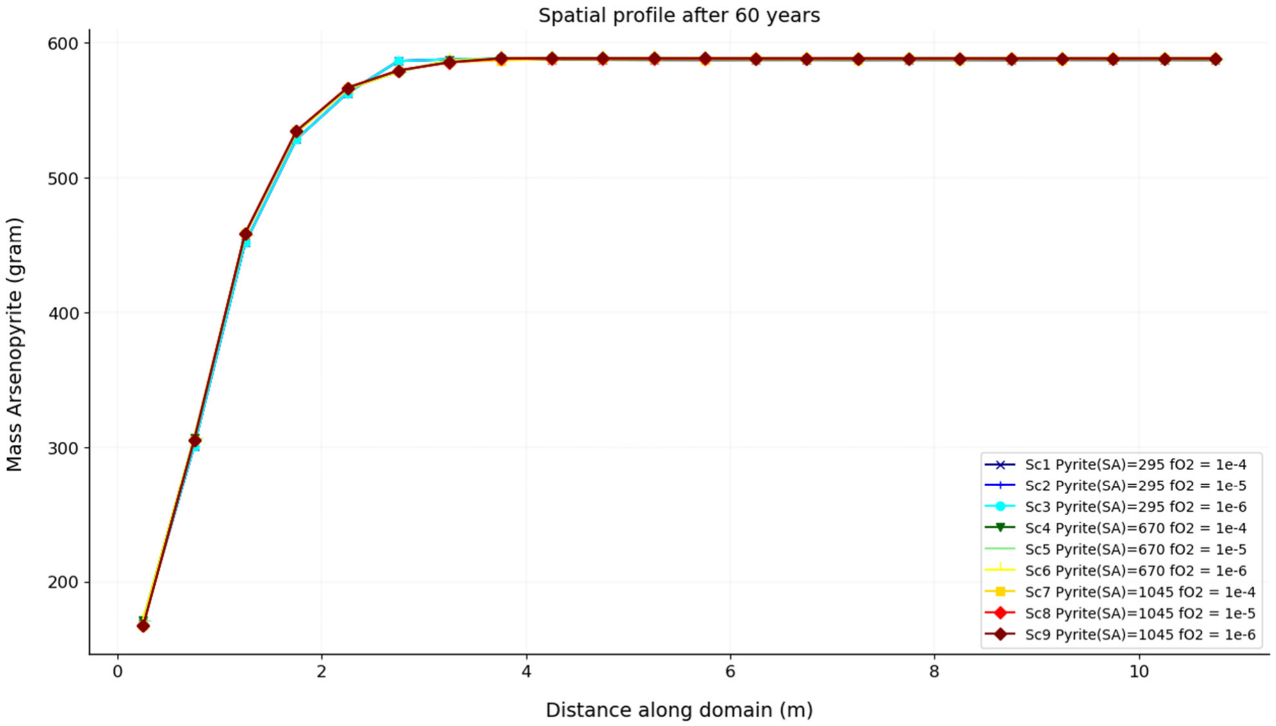

Figure 100: Model 3: Scenario 1 – 9: Arsenopyrite change over depth after 60 years

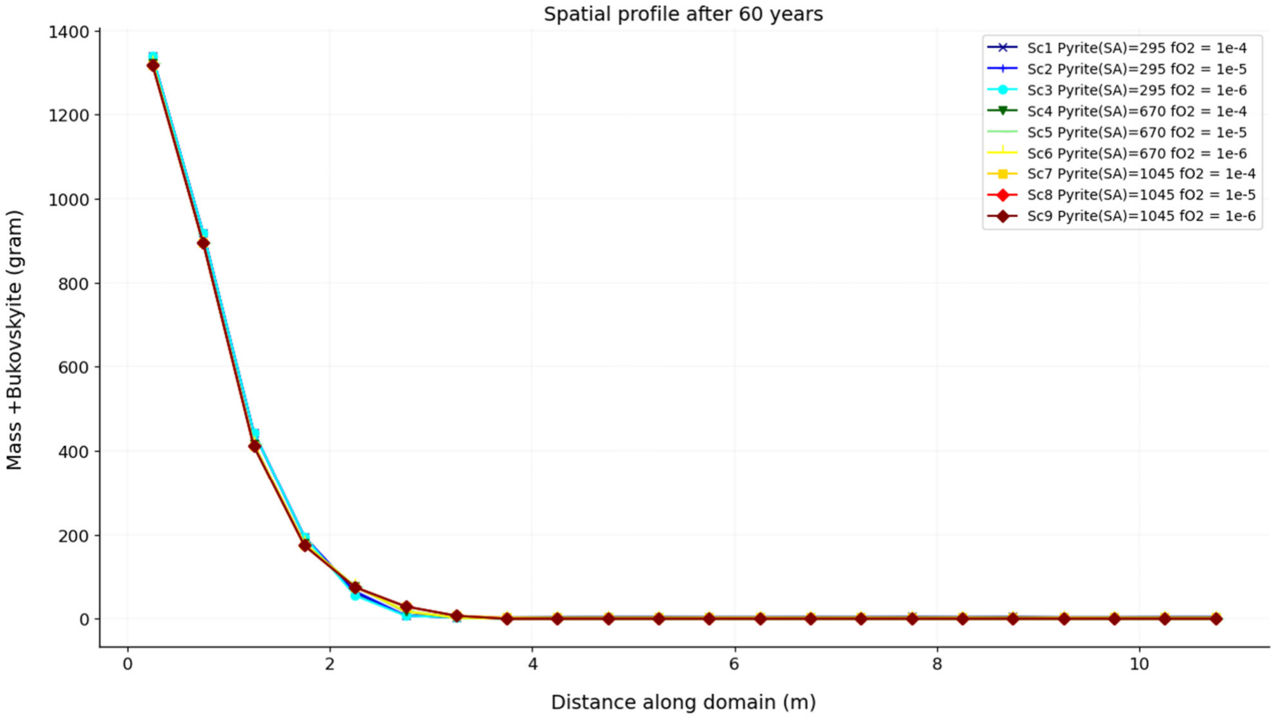

Figure 101: Model 1: Scenario 1 – 9: Bukovskýite change over depth after 60 years

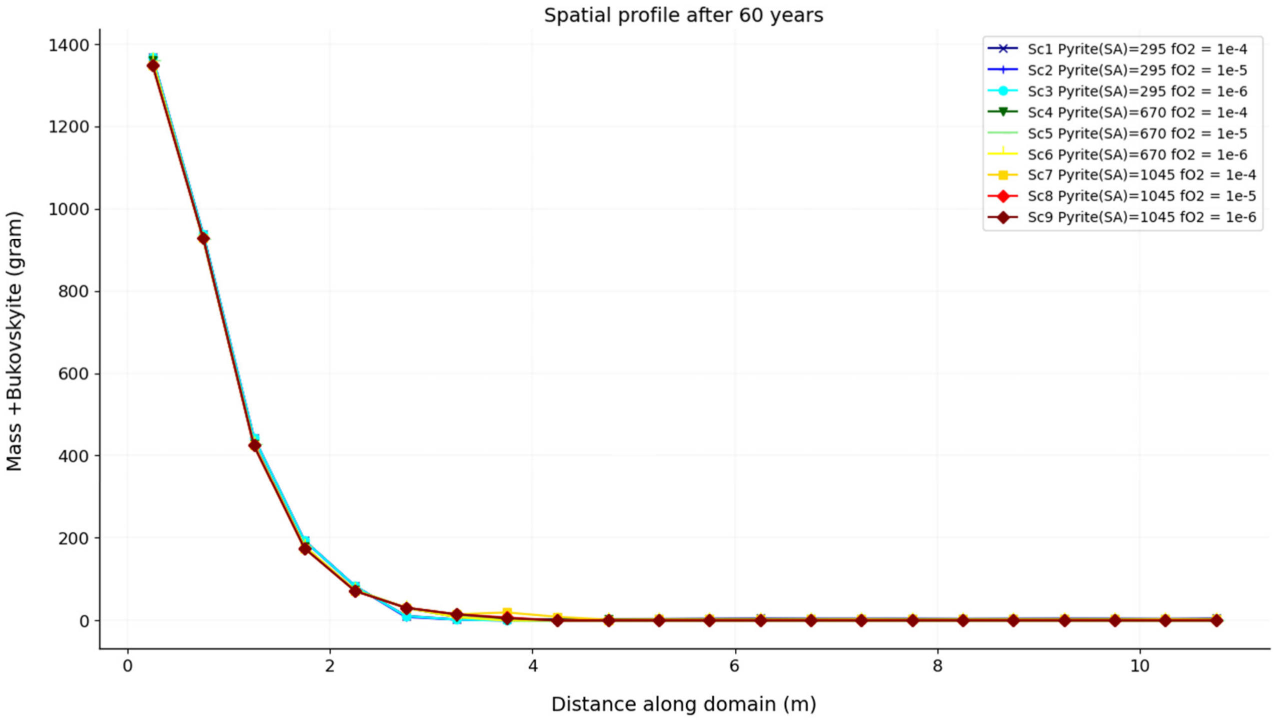

Figure 102: Model 2: Scenario 1 – 9: Bukovskýite change over depth after 60 years

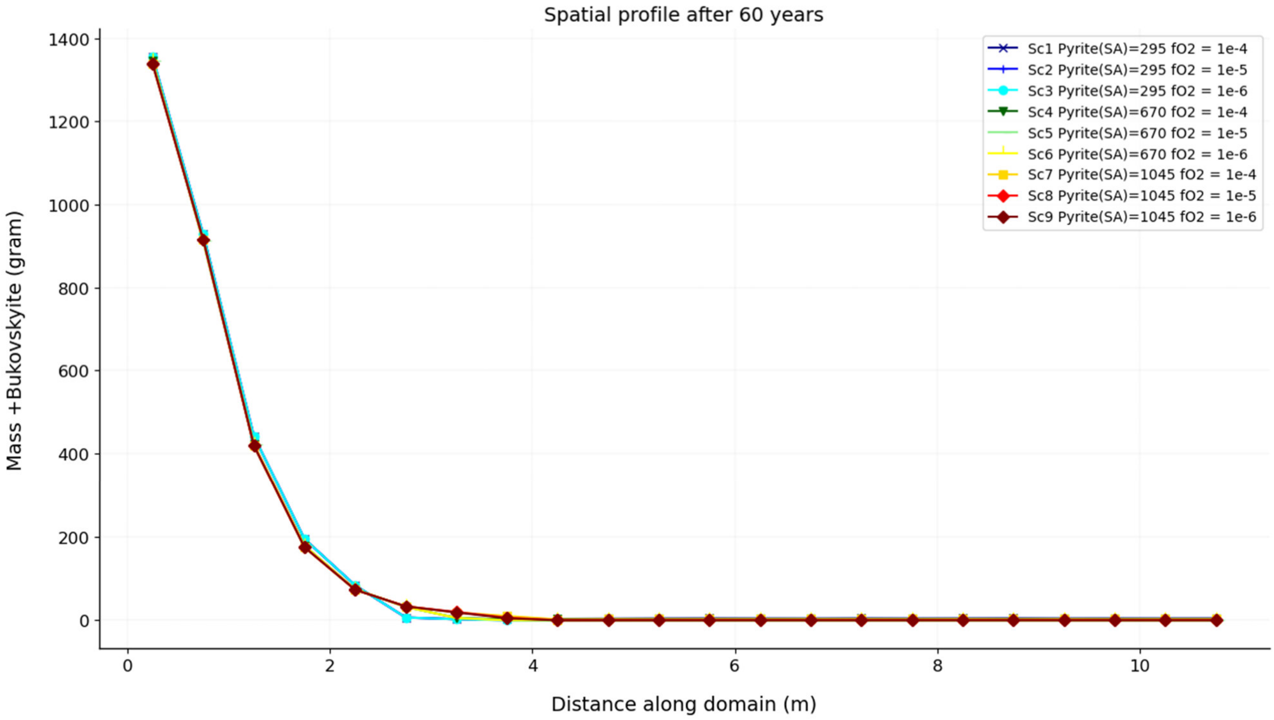

Figure 103: Model 3: Scenario 1 – 9: Bukovskýite change over depth after 60 years

7.6.8 Model 1-3: Dissolved Copper and Dissolved Zinc

The dissolved copper change over the depth of the tailings after 60 years for Model 1 - 3 is depicted in Figure 104, Figure 105 and Figure 106, respectively; similarly, dissolved zinc is depicted in Figure 107, Figure 108 and Figure 109. Both copper and zinc are released from the oxidation of chalcopyrite and sphalerite into solution in the Oxic Zone. These metals do not readily precipitate as secondary minerals under acidic conditions. Dissolved copper and zinc concentrations decrease in the Anoxic Zone as there is no oxidation of chalcopyrite and sphalerite.

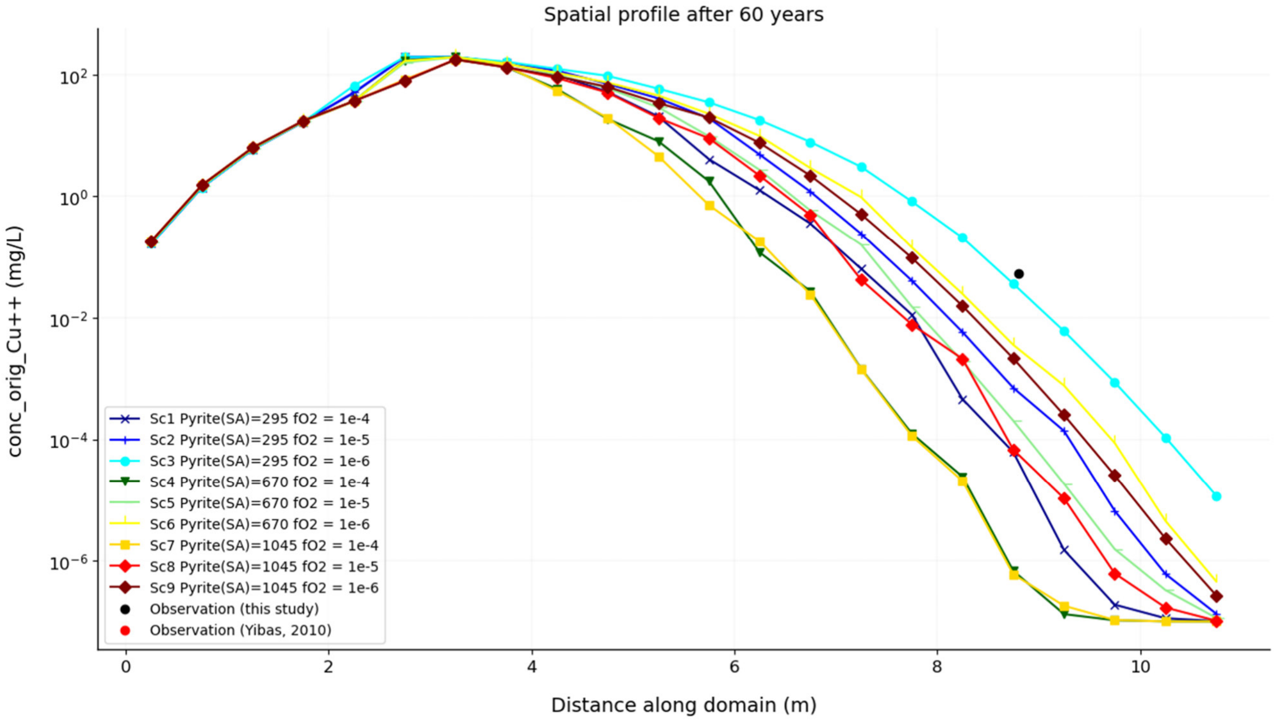

Figure 104: Model 1: Scenario 1 – 9: Dissolved copper change over depth after 60 years

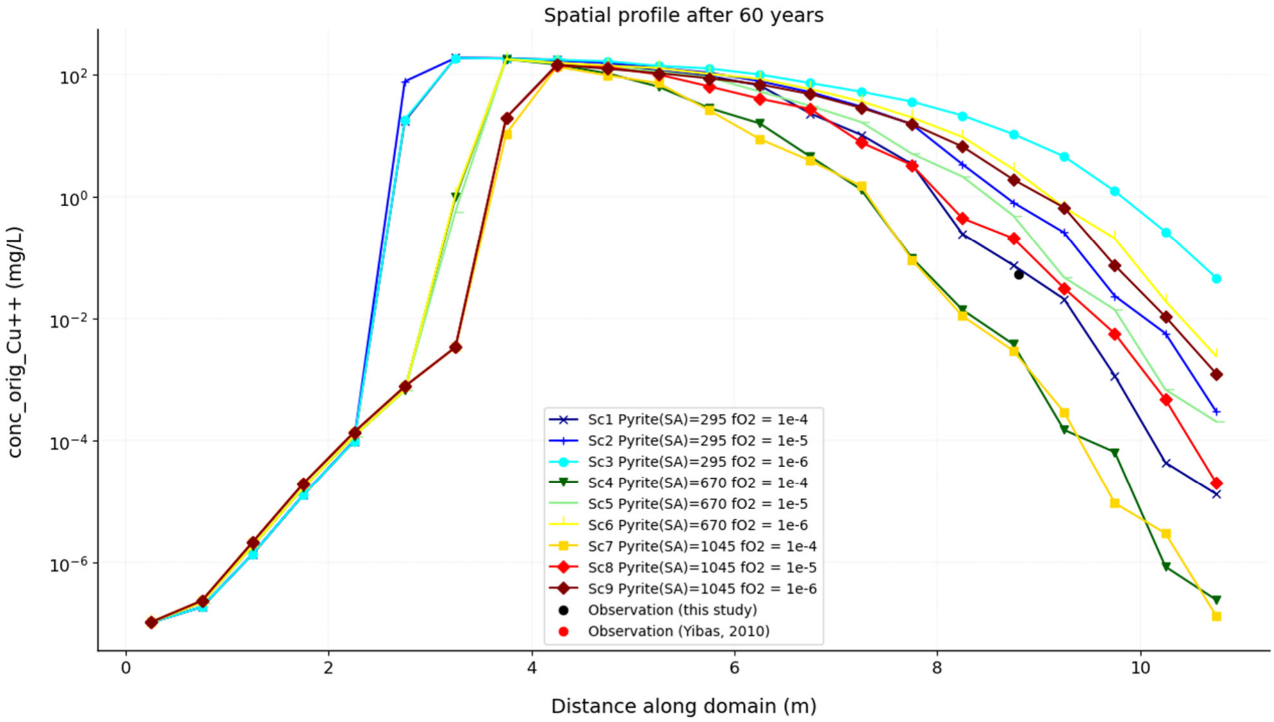

Figure 105: Model 2: Scenario 1 – 9: Dissolved copper change over depth after 60 years

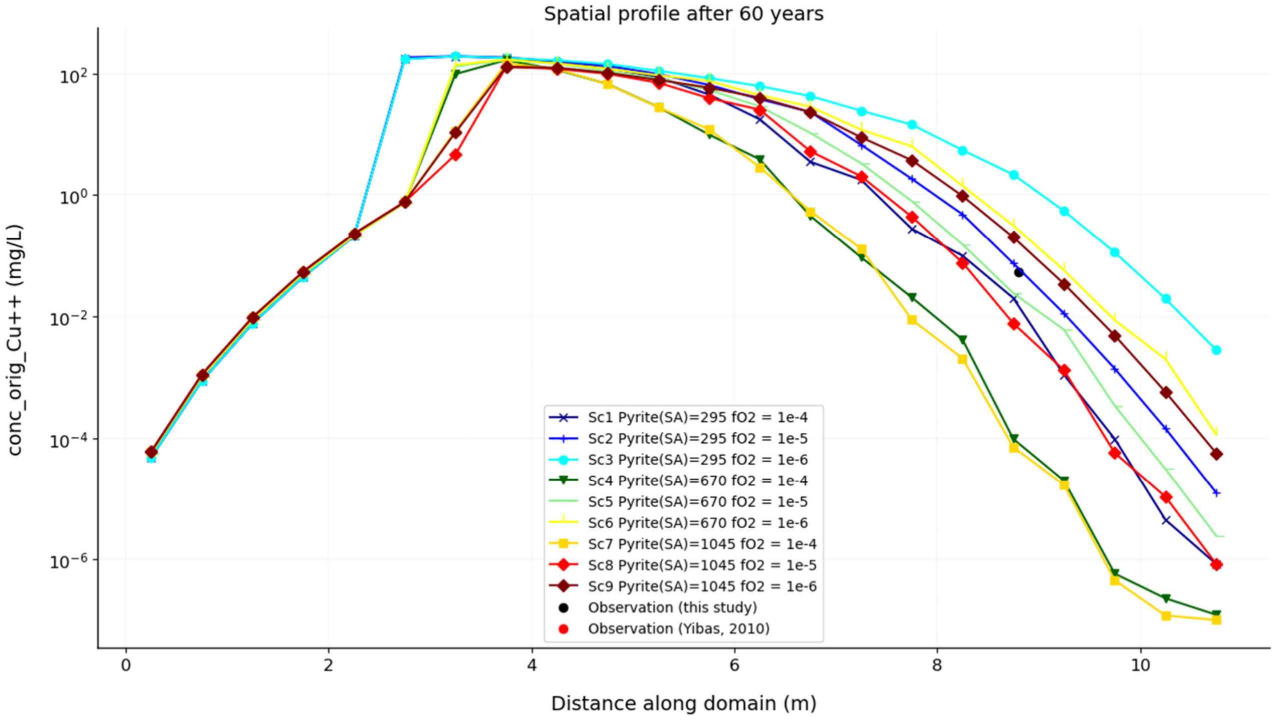

Figure 106: Model 3: Scenario 1 – 9: Dissolved copper change over depth after 60 years

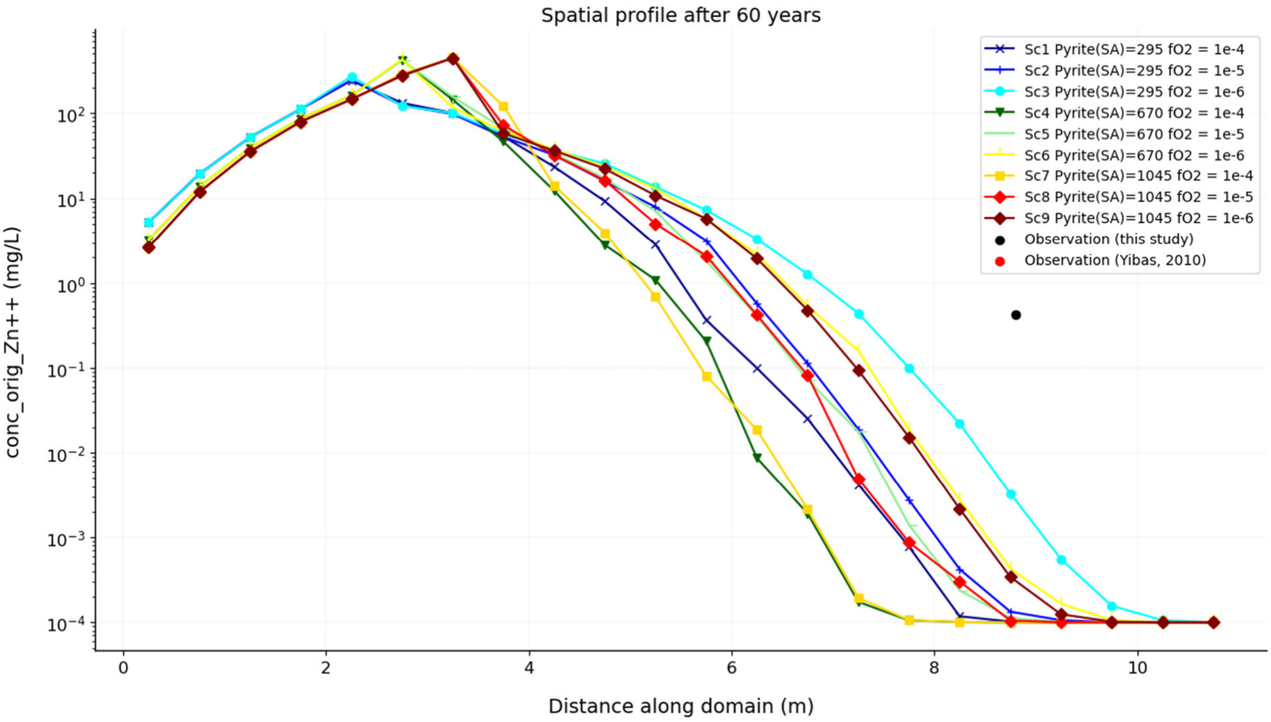

Figure 107: Model 1: Scenario 1 – 9: Dissolved zinc change over depth after 60 years

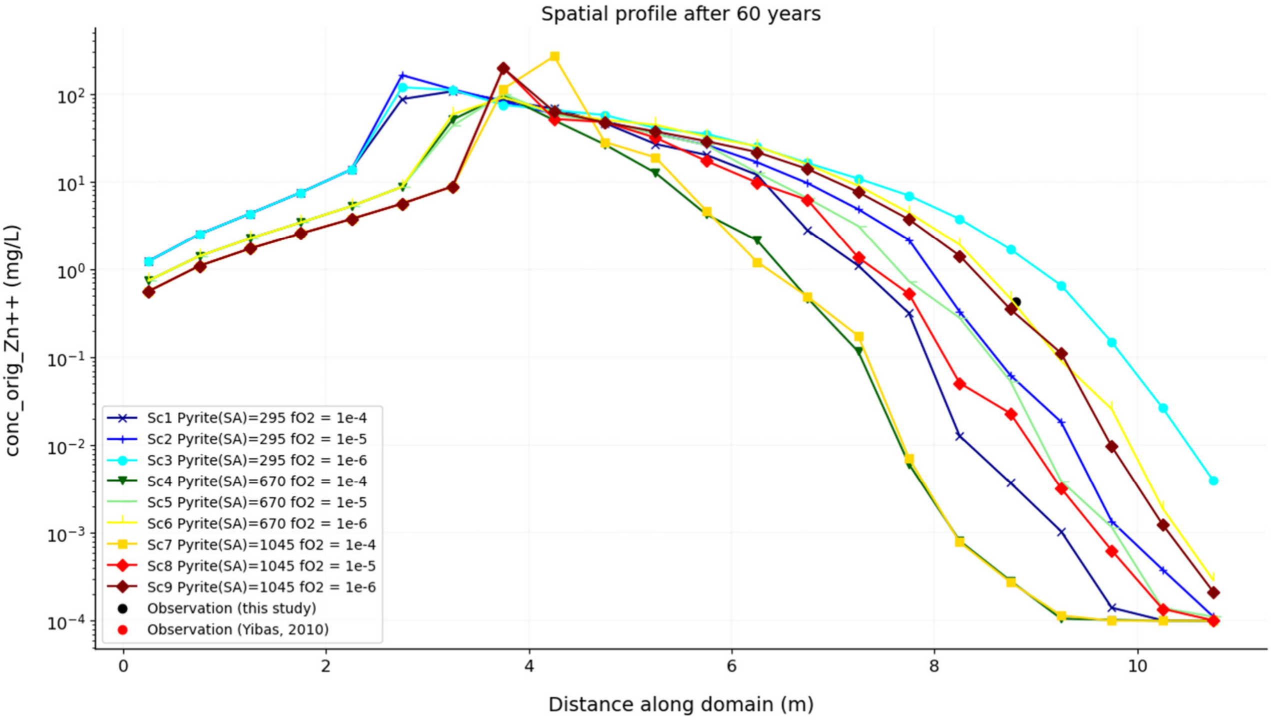

Figure 108: Model 2: Scenario 1 – 9: Dissolved zinc change over depth after 60 years

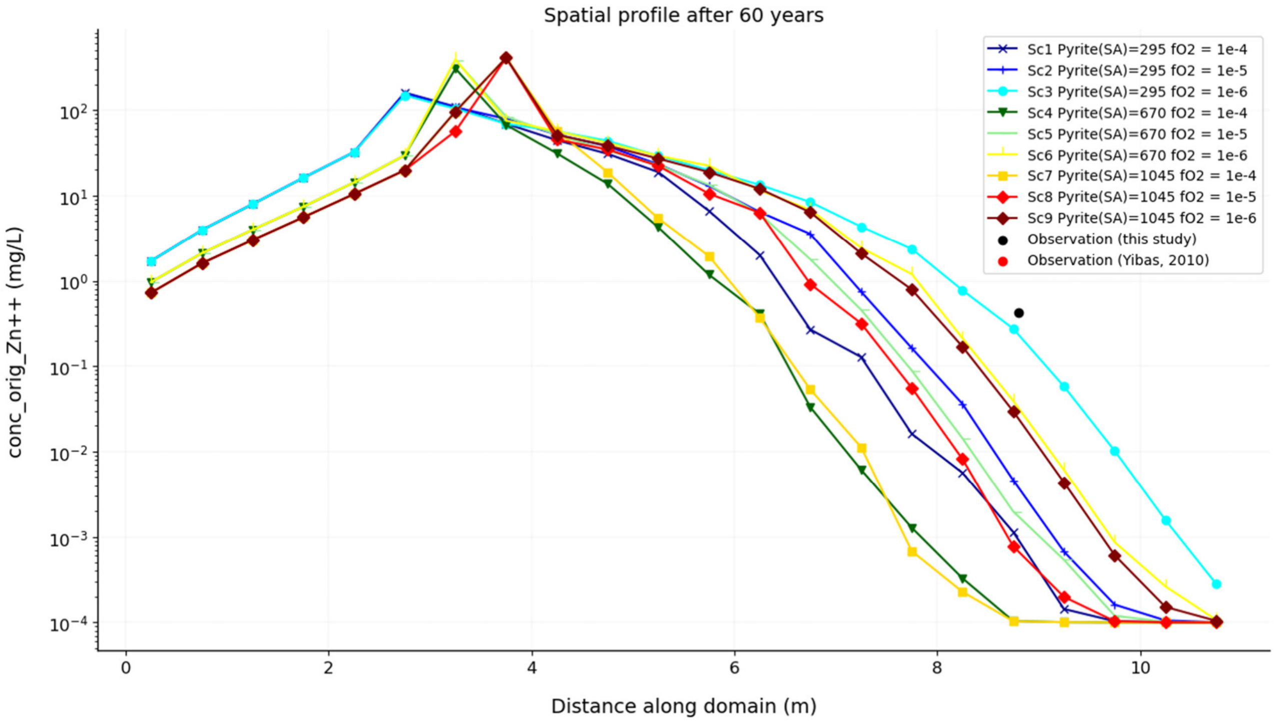

Figure 109: Model 3: Scenario 1 – 9: Dissolved zinc change over depth after 60 years

7.6.9 Model 1-3: Dissolved Lead and Secondary Lead Sulphate (Anglesite)

The change in the dissolved lead over the depth of the tailings after 60 years for Model 1 - 3 is depicted in Figure 110, Figure 111 and Figure 112, respectively; similarly, anglesite is depicted in Figure 113, Figure 114 and Figure 115. The dissolved lead in the Oxic Zone is just above 1 mg/L; in the Anoxic Zone, it is below this as there is no oxidation of galena that provides lead to the solution. The lead in the observed sample is at 0.354 mg/L, with the lower oxygen fugacity scenarios (1 x 10^{-6}) matching it the best. In the Oxic Zone, lead also significantly precipitates with sulphate to form anglesite $PbSO_4$.

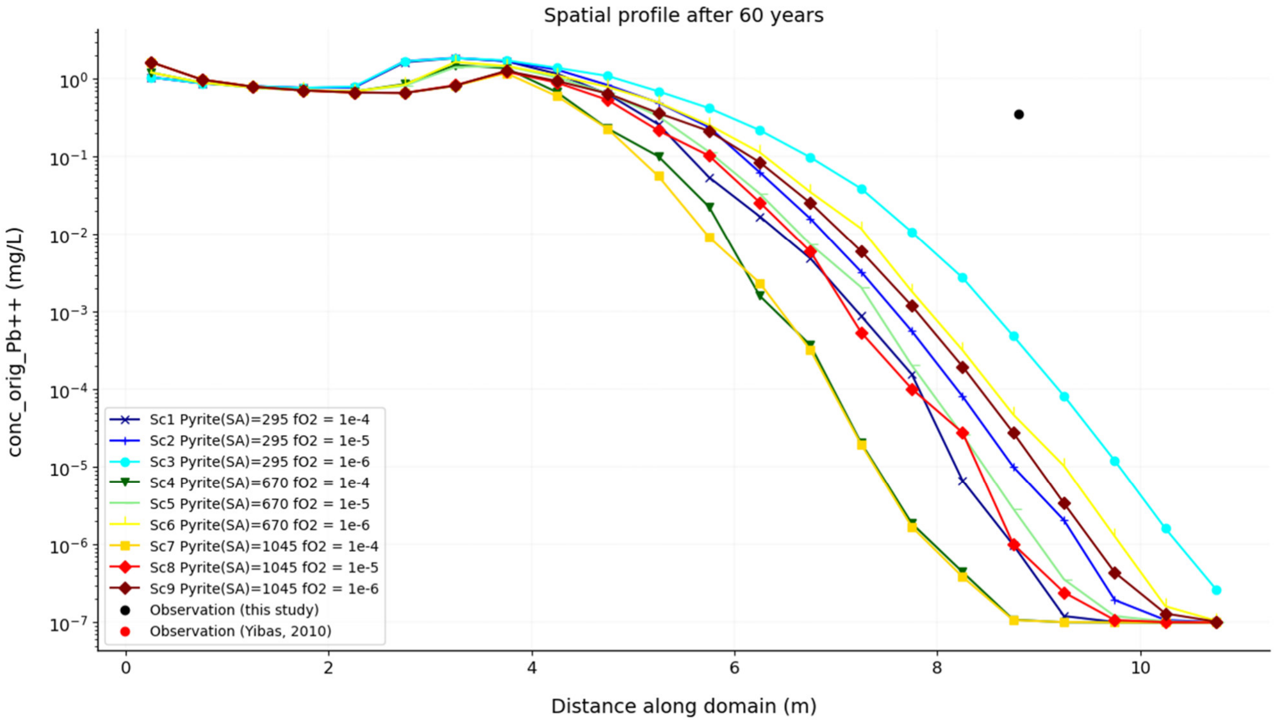

Figure 110: Model 1: Scenario 1 – 9: Lead change over depth after 60 years

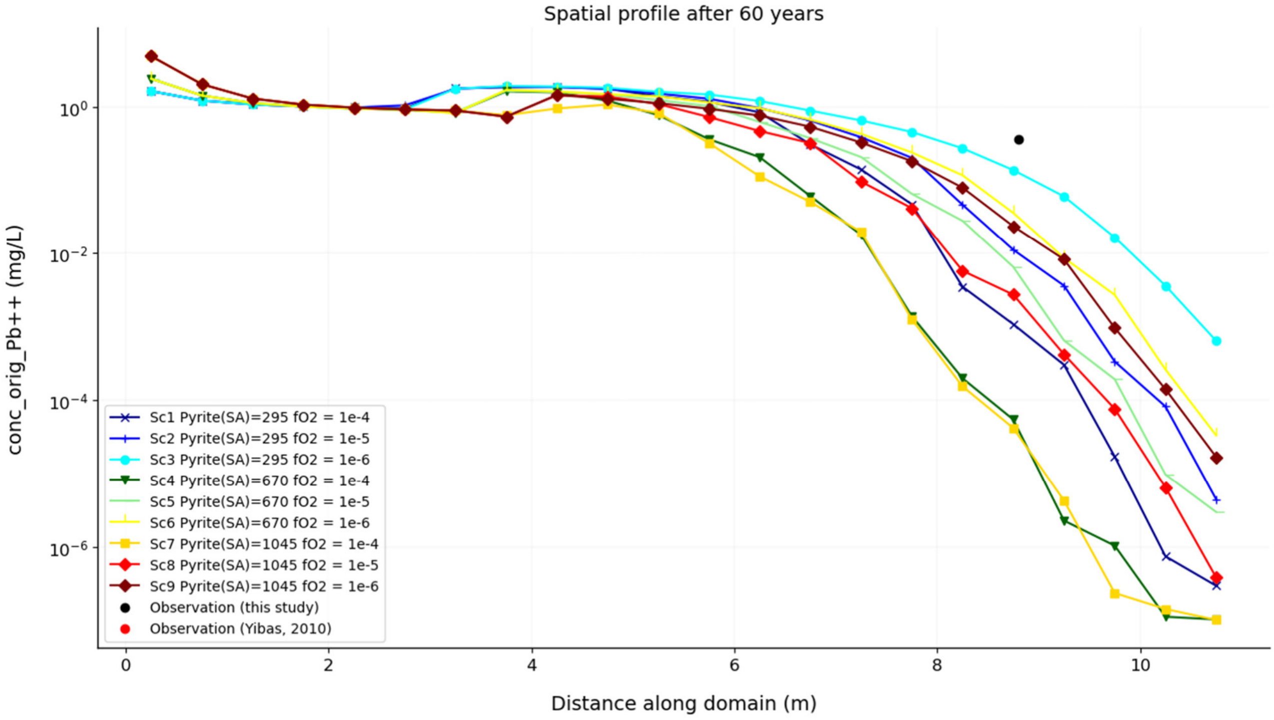

Figure 111: Model 2: Scenario 1 – 9: Lead change over depth after 60 years

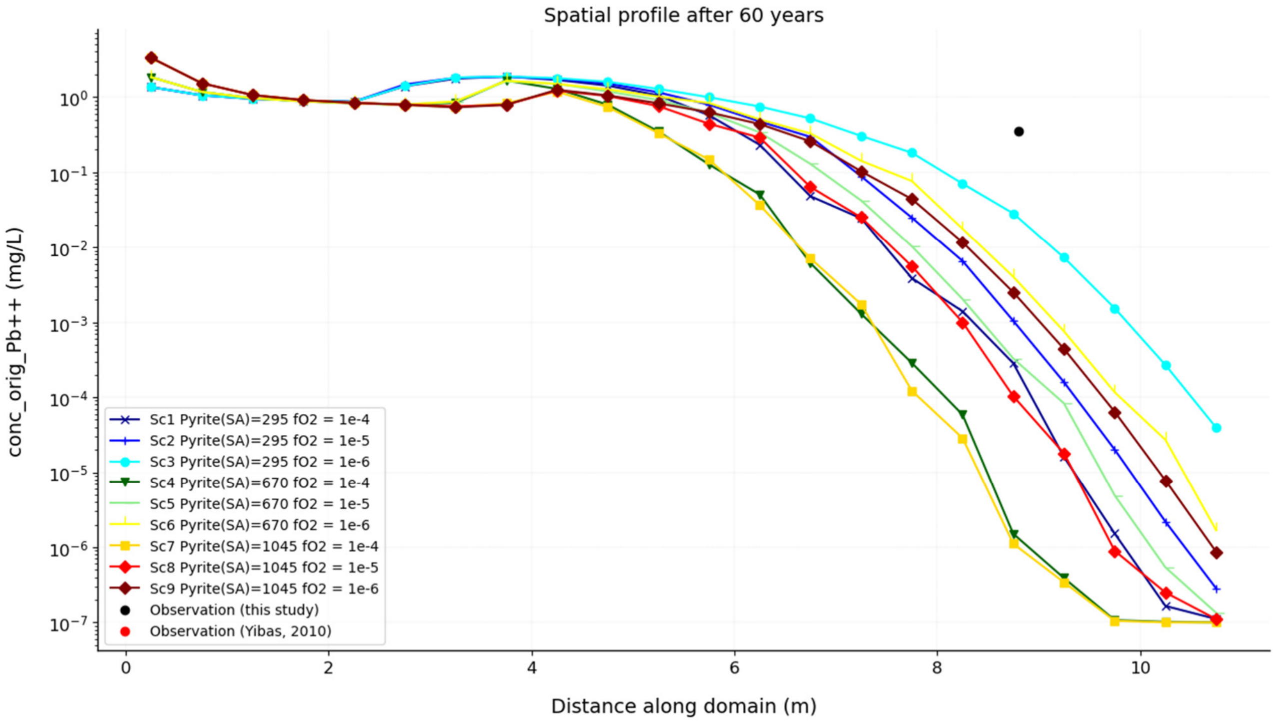

Figure 112: Model 3: Scenario 1 – 9: Lead change over depth after 60 years

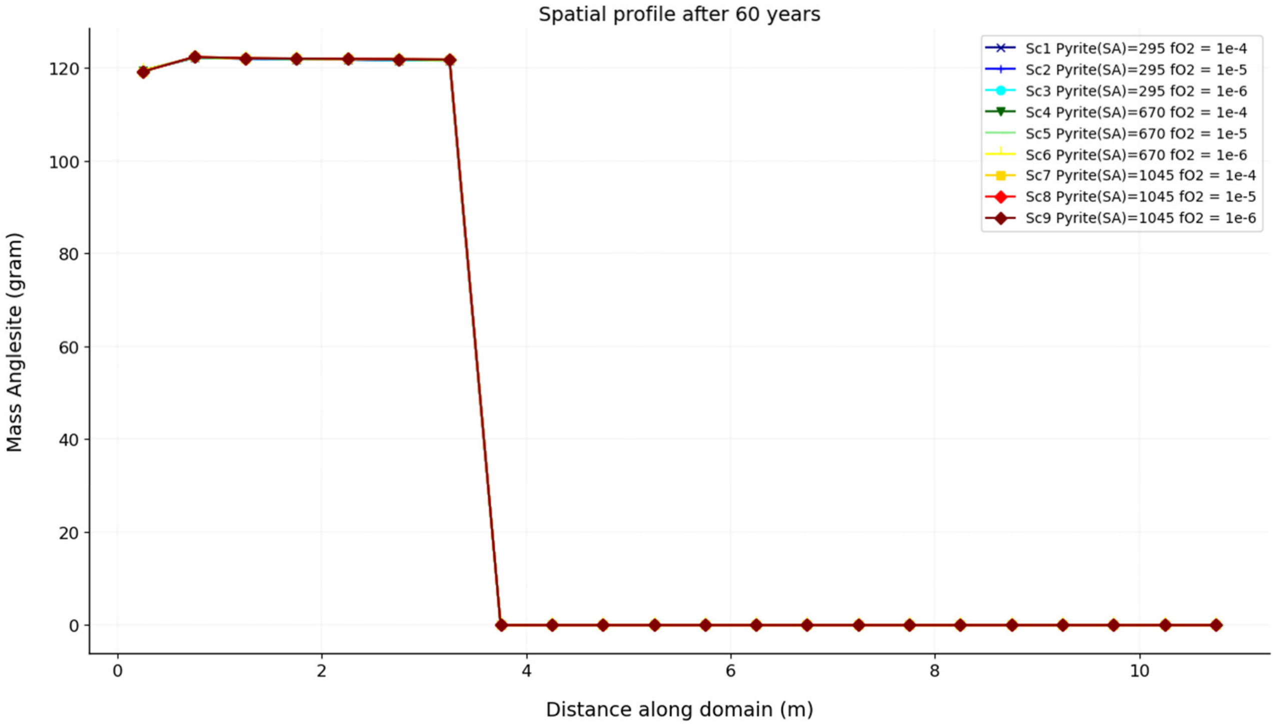

Figure 113: Model 1: Scenario 1 – 9: Anglesite change over depth after 60 years

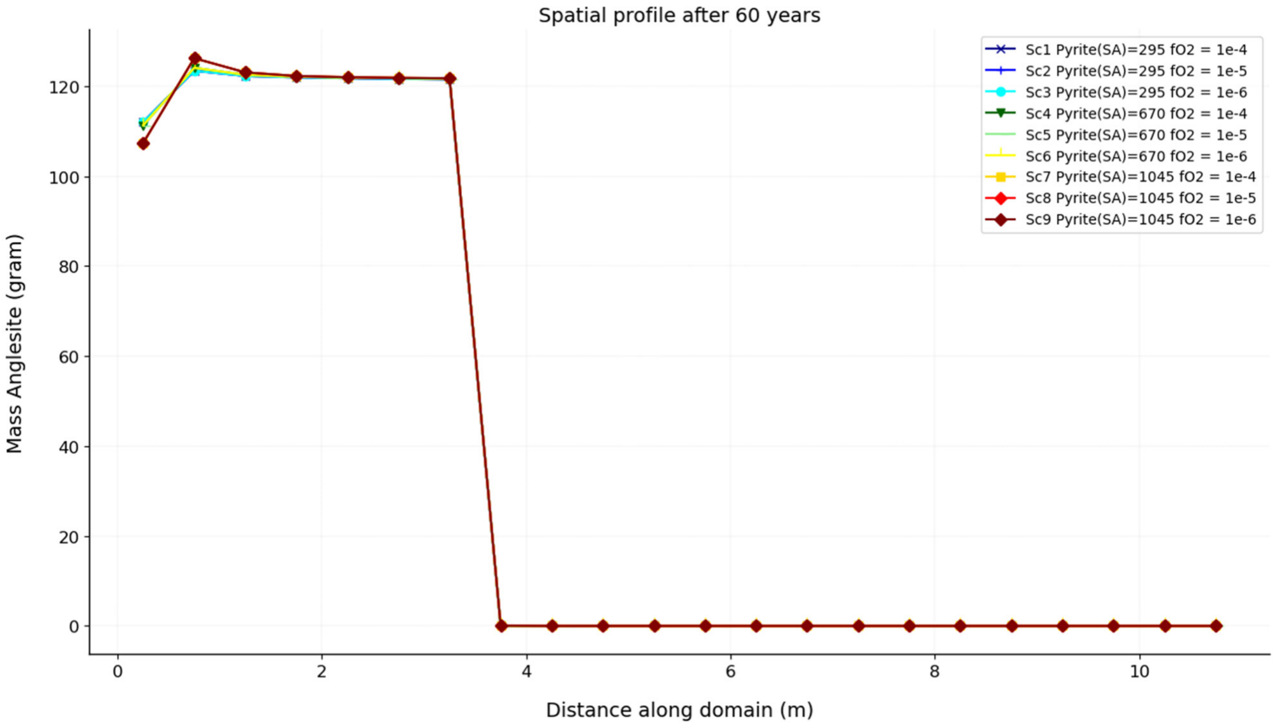

Figure 114: Model 2: Scenario 1 – 9: Anglesite change over depth after 60 years

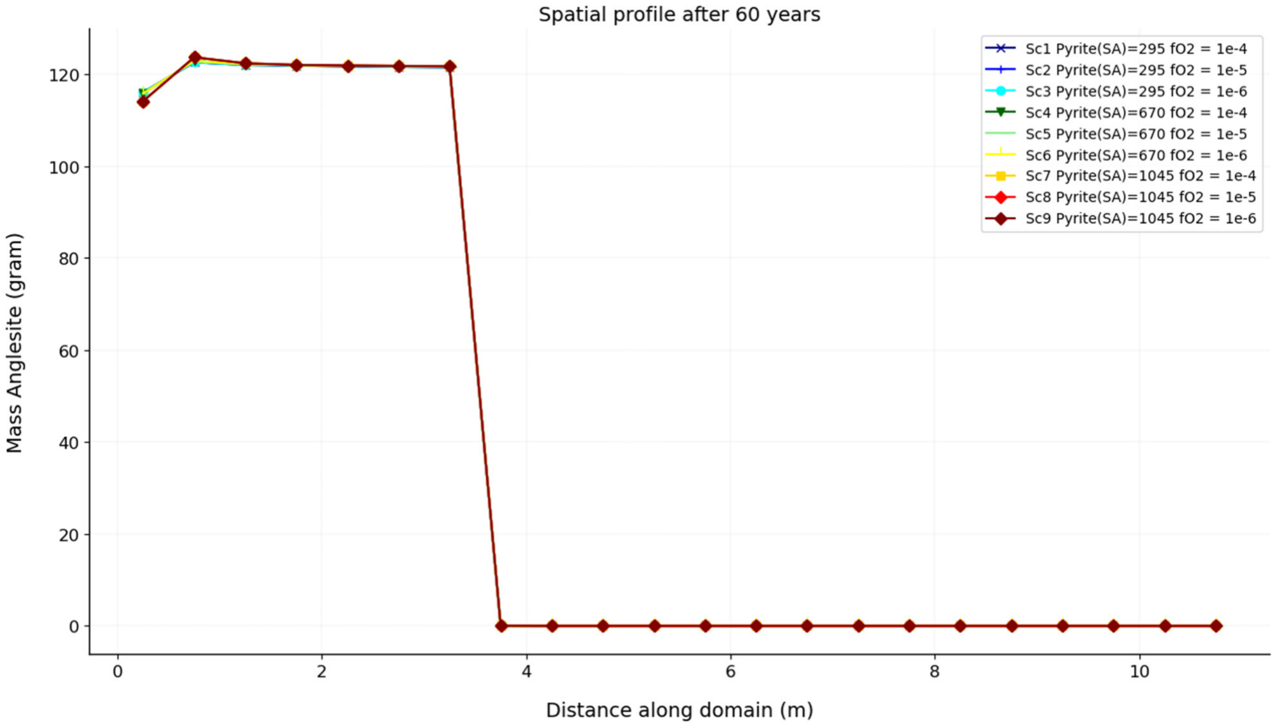

Figure 115: Model 3: Scenario 1 – 9: Anglesite change over depth after 60 years

7.7 Discussion

7.7.1 Revisit of the Primary Model Objective

As mentioned by Nordstrom (2012), we often use a reductionist way to approach problems in (environmental) science. That is, we try to reduce a very complex problem to very simple terms, e.g. a complex geochemical system is reduced to a simple numerical model. This obviously creates several problems. As stated by Nordstrom (2012):

"So part of the problem is to understand what we mean by 'model.' A model is a theoretical construct that begins with a concept (the conceptual model) and might be portrayed mathematically or diagrammatically or physically, or by analogy. It is always a simplification, an idealization, a picture of how we think about some aspect of physical phenomena. In one sense, it is always incorrect because it is never complete or exact."

To use the model purely to obtain quantitative results or to simulate observations without knowledge of the underlying mechanisms would be of very little value to our understanding. It was stated before that the primary objective of the model was to produce new insights into the conceptual understanding of the geochemical processes in the tailings dam. Bredehoeft (2003) has pointed out that the conceptual model is the starting point and the end point of any modelling exercise. This seems to be the most reasonable approach to performing the model to see how it could improve our conceptual understanding of the geochemical processes in the tailings dam.

7.7.2 Note on Matching Observed data and "Model Validation."

A secondary objective of the model was to match the observations 60 years after closure. However, the observational data was severely limited for most parameters. The challenges with the measured data were as follows:

- The model simulated the dissolved phases; however, the data on the actual interstitial water quality was limited to only a few samples.
- Only paste pH, EC and Eh data was available for the first few meters of the tailings.
- Two pH and Eh data points from the Anoxic Zone were retrieved from external sources (Yibas et al., 2010).
- A water sample was retrieved at 8.3 – 9.3 m before the drilled borehole collapsed. It is, however, uncertain whether the sample only presents interstitial water at this depth or more likely, a mix of water from different saturated horizons which had flowed into the borehole during drilling.
- The above water sample, however, had the most comprehensive data available, which included all dissolved parameters modelled. However, this presented only a single point for most parameters in the Anoxic Zone.

It is, therefore not possible to "validate the model" as the observations themselves is fairly limited. Several model scenarios were performed in an attempt to overcome this shortcoming; a total of 27 scenarios were performed to observe which best "matches" the measured data. A statistical approach for the fitting was not even considered (as with the batch reactor testing) because of the data shortcomings.

7.7.3 Discussion of Model Results

A detailed discussion of the model results with some consideration also of the measured field and laboratory test results is provided in Section 8.5. The results of the model and measured parameters are also summarized in Section 9.1.1.

8 FINAL DISCUSSION

8.1 Introduction

A detailed discussion of the model results with consideration also of the measured field and laboratory test results is provided in Section 8.5. Previous discussions of the results of the study are also summarized in this chapter.

The field and laboratory test results were discussed in Chapter 4. In Chapter 5, a conceptual model was generated to provide a framework for the numerical modelling. The conceptual model outlined the major mechanisms that influence the geochemical evolution of the dam. The results from the batch reactor experiment were discussed in Chapter 6. The experiment was performed to determine the pyrite's kinetic reaction rate and effective surface area in the tailings. A numerical geochemical model was generated with the results discussed in Chapter 7. The interaction between the air, water and mineral phases was modelled in a reactive transport model. Several scenarios were performed to evaluate the model's sensitivity in terms of variation in pyrite surface area, oxygen fugacity and flow rate.

The aim of the chapters with field and laboratory test results was to provide information on the geochemical properties of the tailings with the conceptual model outlining the understanding of the mechanisms that influence geochemical processes and the numerical geochemical model finally simulating these processes. A detailed discussion of the model results with consideration also of the field and laboratory test results is provided in Section 7.7.3.

8.2 Geochemical Characterisation

8.2.1 In-situ Oxygen Gas Measurements

Based on the oxygen abundance, the top of the tailings dam was subdivided into three geochemical environments: 1) the Oxic Zone (0-2 m), 2) the Transition Zone (2-4 m), and 3) Anoxic

Zone (>4 m). The Oxic Zone was also analogous to the observed depth of oxidation during the fieldwork. The criteria used for the spatial division were based on the presence or absence of oxygen. In the Oxic Zone, oxygen was present throughout the year. In the Transition Zone, oxygen was only present during the drier months, with the zone also showing a distinct decrease in its oxygen concentration relative to the overlying Oxic Zone. In the Anoxic Zone, oxygen was absent except just after drilling.

The volumetric water content was measured from the samples collected during drilling in the laboratory. The bounds of the Anoxic Zone correlate with the maximum volumetric water volume. Drilled-out samples from the Anoxic Zone were also water-saturated.

The oxygen measurements are comparable to previous oxygen measurements in Witwatersrand tailings dams performed by Yibas et al. (2010). However, a significant controlling factor on the oxygen infiltration for this tailings dam is the extent of water-saturated conditions that are still present in the 60 - 70-year-old dam. A comparison of the measured oxygen with the monthly temperature shows that the oxygen penetrates slightly deeper during the drier winter months than in the wetter summer months.

8.2.2 Field paste pH, EC and ORP measurements

- The field paste pH ranges between pH 3.5 – 4 in the Oxic and Transition Zone and is only slightly higher at 4 – 4.2 in the Anoxic Zone. The lower pH in the Oxic Zone could be attributed to the oxidation of pyrite and the absence of neutralisation minerals. The lower pH in the Oxic Zone could be attributed to the oxidation of pyrite and the absence of neutralisation minerals. The low pH in the Anoxic Zone may indicate that the tailings became acidic because of 1), the transport of acidic water from the Oxic Zone or 2), it became acidic just after deposition, which was also observed at an operational tailings dam in the East Rand by Fourie (2018) in Section 2.9.

- The Eh ranges between 600 – 675 mV, averaging at ~650 mV, in the Oxic Zone and between 430 – 520 mV, averaging at ~475 mV, in the underlying Transition Zone. As discussed in the conceptual model in Section 5.3.2, the Eh will be controlled by the ferric and ferrous redox coupled with the interstitial water containing both ferric and ferrous species in the Oxic Zone, but mostly ferric iron in the Anoxic Zone.

The EC is the lowest (<5 mS/cm) at the top (0-25 cm), where the tailings are leached by infiltrating water. The EC reaches a maximum of ~35 mS/cm at 0.5 m in the Oxic Zone. It gradually increases in the Transition Zone where it reaches a maximum of ~28 mS/cm before decreasing towards the bottom of the Transition Zone to ~13 mS/cm. The spike of the EC in the Transition Zone is most likely related to the spike of sulphate, also observed as discussed in the section below.

8.2.3 Whole Rock Elemental Composition

The sulphur speciation shows a good correlation with the depth of oxygen ingress. The sulphide sulphur is significantly lowered in the first two meters, where oxygen ingress occurs throughout the year, and the sulphide minerals have been converted through oxidation reactions. The sulphate and sulphide sulphur are slightly elevated in the Transition Zone at 2 – 4 m, where oxygen is only present during drier months (which is a result of sulphate mineral precipitation as indicated by the modelling in Section 7.6.4). Uranium abundance in the tailings is lower in both the Oxic and Transition Zone, indicating the uranium's high mobility under acidic, oxidising conditions. The uranium abundance is higher at the top of the Anoxic Zone due to secondary uranium precipitation, as shown in the model in Section 7.6.6.

The major oxides, namely SiO_2, Al_2O_3, Fe_2O_3, CaO, K_2O, MgO and Na_2O, do not show detectable enrichment or depletion throughout the profile. Although some are typically more resistant to weathering (e.g. SiO_2, Al_2O_3, Fe_2O_3 that can be present in resistant minerals like quartz, gibbsite, hematite etc., as discussed by Perkins, 2021), the oxic zone is probably not weathered enough (not "mature" enough) for the more resistant oxides to get enriched. More mobile trace elements like Cu, Ni, and Zn show lower abundance in the Oxic Zone, whereas the less mobile elements like Cr, Pb and Th show no relative decrease in the Oxic Zone. Arsenic shows a minimal decrease in the Oxic Zone as it can form relatively stable secondary minerals in their higher oxidation state.

8.2.4 Identified Minerals

Quartz was present as a dominant mineral at between 75 – 87 wt% over the profile, which corresponds to the SiO_2 in the whole rock elemental composition. The CRG is mostly arenaceous with quartz-pebble conglomerate reefs, as discussed in Section 2.3.2. Muscovite is a minor to intermediate mineral between 11 – 21 wt%. Muscovite is a metamorphic mineral formed after clays (e.g. illite and smectite), as discussed in Section 2.3.2. Chlorite is present as a trace to a minor mineral at between 1 – 4 wt%. Chlorite is a metamorphic mineral that formed after previously formed chlorite and/or biotite as well as clays (e.g., smectite), as discussed in Section 2.3.2. Pyrophyllite is present as a trace mineral at below 2 wt%. Pyrophyllite is a metamorphic mineral formed after previously formed chlorite and clays (e.g., kaolinite, smectite), as discussed in Section 2.3.2. Other trace minerals identified include plagioclase, pyrite, pyrrhotite, chromite, rutile and zircon. These minerals, except chromite, were also identified in the SEM analyses in Section 4.7. However, chromite and chrome spinel are common trace minerals in the Witwatersrand (e.g. Marakushev et al., 2012).

The majority of the sample (66 wt%) falls within the 50 – 125 um size fraction, which would classify it as *unsorted fine sand with coarse silt*. The proportion of minerals seems to be evenly distributed between the grain fractions which is a result of the milling process. However, quartz reaches its maximum proportion in the 75 – 125 um fraction, whereas the sheet silicates reach their maximum in the 50 – 63 um fraction.

Almost all sulphate sulphur is associated with the sample's coarser (>180 um; medium to coarse sand) fraction. This is because gypsum was not subjected to the milling process (as the other minerals) but precipitated in the tailings dam, as observed in the SEM analyses. Sulphide sulphur is fairly distributed over the grain fractions, as with most of the other minerals. However, the highest proportion of sulphide sulphur was present in the finest -50 um and the coarsest +425 um fractions. However, some of the pyrite in the coarse fraction could be particles on quartz or replacements in the phyllosilicates, as observed in the SEM analyses.

8.2.5 Scanning Electron Microscopy

One sample from the Transition Zone and two from the Anoxic Zones were investigated by SEM to inspect the interrelation between minerals and to identify the major sulphide and secondary minerals present. The SEM identified a dominant quartz and muscovite matrix. Chlorite is present as a minor mineral in the matrix, often intergrown with TiO_2 because of the chloritization of biotite.

Pyrite was the dominant sulphide mineral identified in the SEM. Some detrital pyrite was identified, which was intergrown with quartz and/or also had some sulphide mineral inclusions. A syn-sedimentary pyrite and quartz aggregate were also identified.

Sulphide mineral inclusions in the detrital pyrite observed included galena and pentlandite. Authigenic pentlandite, pyrrhotite and chalcopyrite were also observed, which was often associated with quartz or chlorite. Sulphurarsenides (i.e. cobaltite-arsenopyrite-gersdorffite association) had non-ideal composition, with the cobaltite having a significant lead content and the gersdorfite containing some iron.

Large gypsum crystals (>200 um) have been identified that precipitated after tailings deposition. Most gypsum encloses matrix minerals, including quartz and pyrite grains. Where exposed, some of the gypsum has also been rounded due to weathering. Sulphate sulphur (mostly gypsum) was also identified to be the highest in the coarser fraction of the tailings, as discussed in Section 6.2.2.

8.2.6 Water Quality

Tailings Interstitial Water

A slurry sample was collected 8.3 – 9.3 m deep from the borehole before the borehole collapsed. It is uncertain whether the sample only presents interstitial water at this depth or more likely, a mix of water from different saturated horizons which had flowed into the borehole during drilling. The pH of the sample is 4.03, which is in a similar range to the paste pH measurements of the tailings below the Transition Zone described in Section 4.2.3. The Total Sulphur (as SO_4) is at 5 347 mg/l. The calcium, magnesium, sodium and potassium concentrations are at 487, 495, 18.3 and 75.3 mg/l, respectively. The only calcium minerals identified in the SEM analyses in Section 4.7 were gypsum and apatite. The sample is close to gypsum saturation, as indicated in Table 16. As discussed in Section 4.7.5, gypsum precipitated in the tailings dam after deposition. The potassium originates mostly from muscovite weathering, and the magnesium from the chlorite weathering.

Ammonium as N is at 5.49 mg/l. The ammonium may originate from the weathering of the muscovite in the tailings dam. Ammonium in the Witwatersrand muscovite has been described before, and it was suggested that it originates from the hydrothermal fluid that circulated through the deposit where ammonium replaced the potassium in muscovite (Meyer & Ridgway, 1991).

Toe Seepage Drain

Overall, the toe seepage sample is very similar in composition to the interstitial water, apart from the following exceptions: the sample had a slightly lower pH (pH 3.63) and substantially lower dissolved iron (2.94 mg/L) than the interstitial water (pH 4.03 and dissolved iron 1 197 mg/L). This is because of ferrous iron oxidation (e.g. $Fe^{2+} + 2.5H_2O + 0.25O_2 \rightarrow Fe(OH)_3 + 2H^+$) that occurs as the seepage daylight and are exposed to atmospheric conditions.

The sample does not have the high sodium and chloride of the drains from the tailing's reclamation. The sample has a lower Ca, Mg and K than the interstitial water (potentially because of precipitation of secondary minerals, e.g. gypsum, jarosite), but slightly higher trace metals like Co, Cu, Ni, and Zn (because of the lower pH).

8.3 Conceptual Model

8.3.1 Water and Oxygen Flow

See the detailed discussion on the conceptual water and oxygen flow in 5.3.1. Water flow in the unsaturated zone will be vertical, whereas in the saturated zone, there will be both a horizontal and vertical flow component. As discussed in Section 2.6.2, the deep infiltration into the tailings dam is higher than the seepage through the base because of horizontal flow and subsequent losses at the toe. In this study, a 1D model was developed with vertical flow in the model nodes situated in the unsaturated zone but with both vertical and horizontal flow in the saturated zone nodes.

According to GARDGuide (2021), the oxidation front within a tailings dam frequently "stalls" at a relatively shallow depth, approaching steady-state conditions. This means that at some point in time, the diffusive oxygen flux will approach the pyrite consumption rate, with the storage of oxygen in the porous medium becoming smaller. Pseudo-steady-state conditions are often reached more rapidly in tailings with significant pyrite (GARDGuide, 2021) and water content (this study). In this study, it was found that the Anoxic Zone was at only ~4 m deep in the 60–70-year-old TSF. The Anoxic Zone also correlates with the maximum volumetric water content. Because the stalled Oxic Zone is so shallow, the depth of the Oxic Zone was taken to be constant over the life of the tailings dam in the geochemical model.

8.3.2 Mineral Reactions

Pyrite

See the detailed discussion on pyrite mineral reaction in Section 5.3.1. In the geochemical model, only oxidation of pyrite by oxygen was considered as the pH was above pH 3.5 in the interstitial water, and for this reason, bacterial catalysis was not considered. In the batch reactor test (Section 6), it was found that the oxidation rate of pyrite by oxygen from Williamson & Rimstidt (1994) was applicable to kinetic tests on the tailings performed at different pHs.

Secondary Iron and Sulphate Minerals

See the detailed discussion on secondary iron and sulphate minerals in Section 5.3.2. The pH and Eh of the samples from the Oxic and Transition Zones for the tailings dam investigated were plotted on two Fe-S-H_2O Eh-pH stability diagrams at relatively lower and higher iron activities. It was concluded that interstitial water would contain both ferric and ferrous species in the Oxic Zone but mostly ferric iron in the Anoxic Zone. There are no other major redox couples in the tailings, and ferric and ferrous iron is therefore expected to control the system Eh.

Arsenic Minerals and Stability

Arsenopyrite, cobaltite and gersdorfite have been identified as the dominant arsenic-bearing minerals in the tailings dam investigated. The oxidation of these minerals will be important to understand the distribution of arsenic in the tailings dam. Plotting the field results on the stability diagrams, it was shown that ferric-arsenate minerals are stable in the Oxic Zone, and to a lesser degree, also in the Anoxic Zone. This explains why, although arsenopyrite may be oxidised in the Oxic Zone, arsenate is not very mobile as it can precipitate as several (especially Fe- as well as some Ca-) minerals. Under low Eh conditions, arsenate (and some arsenite) will be more mobile in solution. As discussed in the conceptual model, bukovskýite will often form in mine waste under acidic (pH 3-4) moist conditions where higher dissolved sulphate concentrations are present.

Base Metal Sulphides and Stability

Base metal sulphides and their stability are discussed in detail in Section 5.3.4. Together with arsenopyrite discussed above, these sulphides will, upon oxidation, exert a major control on the distribution of trace metal(loid)s (e.g. As, Co, Cu, Ni, Pb, and Zn) in the tailings.

Nickel, copper and zinc do not precipitate as secondary minerals at pH 3 - 5 and will be quite mobile in the interstitial water. This will result in that these metals will be easily leached from the Oxic Zone, as was also observed in the whole rock elemental composition of the tailings, as shown in Section 4.4. In contrast, lead is less mobile, and lead released from the oxidation of galena, will also be prone to precipitate with sulphate as anglesite. The cerussite stability field is large, and above pH 4, the lead will precipitate with carbonate as cerussite.

These metals may also adsorb to some degree to iron-(hydr)oxides in the tailings dam. In the review of metal adsorption on mineral surfaces by Smith (1997), she notes that the sorption selection on most metal-oxide minerals follows the sequence Cr > Pb > Cu > Co > Zn, Ni > Cd. However, under the pH conditions of the Oxic Zone (pH 3 – 4), only lead will be prone to adsorption, and copper will only adsorb at a pH of about 4 – 5, with zinc and nickel only at pH values above this. Sorption was therefore not considered under the acidic conditions, with lead mobility expected to be dominated by precipitation rather than adsorption.

Uranium Minerals and Stability

Uranium minerals and stability are discussed in detail in Section 5.3.5. Uraninite will oxidise in the Oxic Zone to produce uranyl (UO_2^{2+}) which will mostly form soluble carbonate and sulphate complexes, as shown in stability diagrams in Section 5.3.5. Uranyl (UO_2^{2+}) will be fairly mobile in the Oxic Zone. Uranyl will precipitate above pH 4 in the Anoxic Zone as hydrous uranyl sulphate (e.g. zippeite-Mg, $Mg_2(UO_2)_6(SO_4)_3(OH)_{10}$:$4H_2O$ or other Ca-, Mg-, Na- and K-uranyl sulphates), as illustrated in stability diagrams in Section 5.3.5.

Alumino-Silicate Minerals

Uranium minerals and their stability are discussed in detail in Section 5.3.5. Aluminium is present at about ~200 mg/l in the tailings water samples (See Section 4.8.3), which indicates significant weathering of alumino-silicates. Despite having no acid neutralisation potential, the tailings can still maintain a pH in the 3.5 – 4.2 range due to the reaction of alumino-silicates, i.e., muscovite and chlorite.

Muscovite is present as a minor to intermediate mineral at between 11 – 21 wt%. There is a fair amount of potassium present in water samples which could mostly be attributed to the dissolution of muscovite. As discussed in Section 4.8.3, the ammonium present in all water samples may also originate from the weathering of the muscovite in the tailings dam.

Chlorite is present as a trace to a minor mineral at between 1 – 4 wt% in the tailings. Magnesium is present in the tailings water, which could be attributed to the weathering of chlorite, although the chlorite is expected to be Fe-Mg-chlorites (e.g. Smits, 1990).

Carbonate Minerals

Carbonate minerals are discussed in more detail in Section 5.3.5. Carbonate minerals would not endure the acidic conditions under which the Witwatersrand sediments were deposited (Smits, 1990). Smits (1990) also notes that carbonates would anyway be destroyed under post-burial conditions. Samples from the tailings dam investigated in this study had a paste pH of ~3.5 - 4 in the Oxic and Transition Zone. There are not ample samples from the Anoxic Zone; however, the water sample collected at 8.3 – 9.3 m deep (anoxic zone) had a pH of 4.03.

8.4 Batch Reactor Testing

The objective of the batch reactor testing was to calculate the effective surface area of the pyrite in the tailings based on its reaction rate in a batch reactor. The experiment was performed at pH ~3, ~5, and ~7. After every aliquot sampling, the pH was corrected. An interesting observation was that for the pH~3 experiment, the pH was always slightly above pH 3 (and had to be lowered with HCl) due to buffering of alumino-silicate minerals. For the pH ~5 and ~7 experiments, the pH was always slightly below the target pH and had to be adjusted with NaOH. The sulphate production was the lowest in the pH ~3 experiment and the highest in the pH ~7 experiment. This is because the oxidation of pyrite by oxygen is inversely proportional to the hydrogen activity, as discussed in Section 5.3.1.

The ~pH 3 experiment results were used to back-calculate the effective surface area of the pyrite that would be required to produce the results. The pyrite oxidation rate by oxygen from Williamson & Rimstidt (1994) was used (Section 5.3.1). Using the rate law, an inverse calculation was performed to calculate the surface area of the pyrite. The calculated sulphate concentration for the pH ~3 experiment, using a pyrite surface area of 1046.27 g/cm^2, was plotted against the measured concentrations. All three experiments were simulated using the pyrite surface area calculated for the pH ~3 experiment. Theoretically, all three experiments should have the same surface area. The modelled pyrite reaction rate fits the results for all three experiments very well. The correlation for the pH ~3, ~5, and ~7 have correlation coefficients of 0.9, 0.98 and 0.99, respectively. This also implies that the oxidation of pyrite is almost solely by oxygen and that the reaction rate will be valid over a wide pH range.

8.5 Discussion of the Model Results

The model results indicated that the pH is significantly lowered in the Oxic and Transition Zone because of sulphide oxidation and the subsequent acid generation that took place over the years. The pH is slightly more elevated at the top of the Oxic Zone because of infiltrating circum-neutral water. The pH in the Oxic Zone matched the observed data well for Models 2 and 3 (12% and 8% recharge). As discussed previously with the acid-base test results (Section 4.5.3), the tailings have no potential to buffer significant acid generation. Iron-hydroxides do, however, provide some buffering at pH 3 and gibbsite from aluminosilicate weathering at around pH 4 (GARDGuide, 2021). This buffering was also observed for the pH~3 batch reactor experiment, where the pH was always slightly above pH 3 when samples were taken (and had to be lowered with HCl) (See Section 6.3.1).

The modelling considered both neutral and acidic interstitial water scenarios for the Anoxic Zone. The water sample taken at a depth of 8.3 – 9.3 m has a pH of 4.03, which is similar to the pH (pH = 4) reported for tailings water 1:10 extractions by Nengovhela et al. (2006) at the same depth for the same tailings dam. Yibas et al. (2010), however, report a paste pH of 6.4 for the same depth at the dam (most likely the same samples as Nengovhela et al., 2006). The modelling considered both neutral and acidic possibilities for the Anoxic Zone of the tailings dam. From the model results, it is, however, shown that only scenarios with a low oxygen fugacity (fO_2 $<1 \times 10^{-6}$) in the Anoxic Zone do not show any acidification below pH 5.5.

Ferrous and ferric iron are the dominant redox pair in the interstitial tailings water. The measured field Eh could therefore be the best matched with the Eh(Fe++/Fe+++). The observed Eh in the Oxic Zone is fairly matched in most scenarios. However, the observed Eh in the Anoxic Zone is best matched by the low and medium oxygen fugacity scenarios (1×10^{-5} and 1×10^{-6}). This is because the pH influences the Eh; the Eh in the Anoxic Zone is, therefore, best matched in slightly acidic to circum-neutral conditions. However, these Eh values in the Anoxic Zone (from Nengovhela et al., 2006), were reported as part of the water extraction tests, and it is not sure whether it was actually measured in the field or in the lab as part of the extractions. It was also assumed that these are measured ORP (Oxidation-reduction Potential) values from Nengovhela et al. (2006), and it was converted to Eh in this study.

The Total Iron reaches a maximum at about ~3 m in the Transition Zone and then decreases towards the Anoxic Zone, where it remains fairly stable at concentrations of 100 – 1000 mg/L for the various model scenarios. The observed iron data is limited, and only the water sample from the Anoxic Zone is available, which has a Total Iron of 1 197 mg/L[8]. The Eh is on the boundary of Fe++/Fe+++ stability in the Oxic Zone (see Section 5.3.2). Therefore, both ferric and ferrous iron could be expected in the Oxic Zone. From the model results, it is shown that ferrous and ferric iron are at their respective highest concentrations in the Oxic Zone. The Eh is more in the Fe++ stability field in the Transition Zone (see Section 5.3.2). Therefore, more ferrous iron is expected in the Anoxic Zone. In the Anoxic Zone, ferrous iron (100 - 1000 mg/L) is dominant over ferric iron (<10 mg/L). Significant precipitation of ferric iron could, however, be expected in the Oxic Zone. This results in that the total iron in the rock is not significantly leached from the tailings in the Oxic Zone, as shown in the elemental composition of the tailings in Section 4.4.3. Iron-hydroxide is the most stable secondary mineral; however, in reality, several precursor minerals like schwertmannite may also precipitate.

---

[8] It is uncertain whether the sample only present interstitial water at this depth, or more likely, a mix of water from different saturated horizons which had flowed into the borehole during drilling.

The TDS and sulphate in the Oxic Zone are leached at the top, reach a maximum at about ~3 m in the Transition Zone, and then decrease towards the Anoxic Zone where it remains fairly constant (with the sulphate at about 3 000 – 5 000 mg/L). The low and high recharge scenarios over or underestimate the TDS, with the medium recharge (Model 3; 8% of annual rainfall) providing the best match. All model scenarios show this trend, but as with the TDS, it seems that for Model 3, the scenarios with the intermediate pyrite surface area (670 cm^2/g) (Scenario 4-6) best match the sulphate in the Transition Zone.

The calcium is very similar in the scenarios because it is controlled by gypsum saturation, except that it is leached a bit more in the Oxic Zone because of higher infiltration (Model 2) and because of higher acidity (Scenarios 7-9). Almost no gypsum precipitation is present in the Oxic Zone, with the most precipitation occurring in the Transition Zone. This correlates with the increase in the sulphate sulphur in the Transition Zone observed from the elemental composition of the tailings (see Section 6.2.2).

Chlorite is the only magnesium mineral identified in this study and will exert a major influence on the magnesium concentration in interstitial water. The chlorite is significantly depleted in the Oxic Zone, which results in an increase in dissolved magnesium and aluminium in the Oxic and Transition Zones. Limited reaction of the chlorite took place in the Anoxic Zone. The magnesium and aluminium in the Oxic Zone are leached at the top, reach a maximum at about ~3 m in the Transition Zone, and then decrease towards the Anoxic Zone. The modelled magnesium and aluminium in the Anoxic Zone are respectively at about ~500 mg/L and between 10 – 100 mg/L in the Anoxic Zone.

The uraninite in the Oxic Zone is significantly depleted at the top but unreacted in the Anoxic Zone. This corresponds with the low uranium content in the elemental composition of the tailings of the Oxic and Transition Zone (see Section 4.4.3). Uranium will mostly precipitate as zippeite-Zn (or zippeite-Mg not shown here) in the Transition Zone or at the top of the Anoxic Zone. The zippeite is a hydrous uranyl sulphate (e.g. zippeite-Zn, $Zn_2(UO_2)_6(SO_4)_3(OH)_{10}:4H_2O$), and the depth it precipitates could be related to the peak of the dissolved sulphate as discussed in Section 7.6.3. The dissolved uranium shows an increase in the Oxic Zone and reaches a maximum at about ~3 m, and then decreases towards the Anoxic Zone, where it stays fairly constant. The uranium is sensitive to the oxygen fugacity settings in the Anoxic Zone, and the best match is observed for low oxygen fugacity (1×10^{-6}), similar to the iron and Eh(Fe++/Fe+++).

The arsenopyrite is significantly depleted in the Oxic Zone but fairly unreacted in the Anoxic Zone. Despite the oxidation of arsenopyrite in the Oxic Zone and the significant release of arsenic, arsenic is not depleted in the tailings samples, as shown in Section 4.4.3. This is because most of the released arsenic will precipitate with iron in the Oxic Zone, e.g. as secondary arsenate sulphate bukovskýite. As discussed in the conceptual model, bukovskýite will often form in mine waste under acidic (pH 3-4) moist conditions where higher dissolved sulphate concentrations are present.

Both copper and zinc are released from the oxidation of chalcopyrite and sphalerite into solution in the Oxic Zone. The conceptual model in Section 5.3.4 indicated that these metals do not readily precipitate as secondary minerals under acidic conditions. It was, however, shown that some Zn will precipitate with uranium in the Transition Zone or on top of the Anoxic Zone in Section 7.6.6. The most significant leaching of the copper and zinc occurs in the higher recharge model (Model 2). The leaching of copper and zinc from the tailings in the Oxic Zone is shown in the elemental analyses of the tailings in Section 4.4.3. Dissolved copper and zinc concentrations decrease in the Anoxic Zone as there is no oxidation of chalcopyrite and sphalerite.

The dissolved lead in the Oxic Zone is just above 1 mg/L in the Anoxic Zone, it is below this as there is no oxidation of galena that provides lead to the solution. The lead in the observed sample is at 0.354 mg/L, with the lower oxygen fugacity scenarios ($fO_2 = 1 \times 10^{-6}$) matching it the best. In the Oxic Zone, lead also significantly precipitates with sulphate to form anglesite $PbSO_4$, with the result that the total lead in the solid phase is not depleted (like copper and zinc) as shown in the elemental composition of the tailings in Section 4.4.3.

9 CONCLUSIONS

9.1 Project Conclusions

The aims of the research were: 1) to geochemically characterise the tailings, 2) to quantify oxygen infiltration into the tailings dam, and 3) to develop a numerical geochemical model to simulate the geochemical evolution that took place within the dam over the past 60 years.

9.1.1 Conclusions on the Measured and Modelled Parameters

The field paste pH ranged between pH 3.5 – 4 in the Oxic and Transition Zone and is only slightly higher at 4 – 4.2 in the Anoxic Zone. The Eh ranged between 600 – 675 mV, averaging at ~650 mV, in the Oxic Zone and between 430 – 520 mV, averaging at ~475 mV, in the underlying Transition Zone. The EC reaches a maximum of ~35 mS/cm at 0.5 m in the Oxic Zone, whereafter it decreases close to 13 mS/cm. It gradually increases in the Transition Zone, where it reaches a maximum of ~28 mS/cm before decreasing towards the bottom of the Transition Zone to ~13 mS/cm.

The acid-base test results indicated that the tailings have no potential to buffer significant acid generation. Iron-hydroxides do, however, provide some buffering at pH 3 and gibbsite from aluminosilicate weathering at around pH 4. This buffering was also observed for the pH ~3 batch reactor experiment, where the pH was always slightly above pH 3 when samples were taken (and had to be corrected with HCl).

From the numerical model results, it was shown that the pH is significantly lowered in the Oxic and Transition Zone because of sulphide oxidation and the subsequent acid generation that took place over the years. The pH is a bit more elevated at the top of the Oxic Zone because of infiltrating circum-neutral water. The pH in the Oxic Zone matched the observed data well for the model with high and medium recharge (12% and 8% of annual precipitation).

The sulphide sulphur is significantly lower in the first two meters of the tailings, where oxygen ingress occurs throughout the year, and the sulphide minerals have been converted through oxidation reactions. The sulphate and sulphide sulphur are slightly elevated in the Transition Zone at 2 – 4 m, where oxygen is only present during drier months. This corresponds to the model results that indicated precipitation of gypsum in the Transition Zone.

Uranium abundance in the tailings is lower in both the oxic and Transition Zone, indicating the uranium's high mobility under acidic, oxidising conditions. This corresponds to the modelling results that indicated that uraninite would oxidise in the Oxic Zone with some precipitation of hydrous uranyl sulphates in the Transition Zone and upper Anoxic Zone.

The major oxides do not show detectable enrichment or depletion throughout the profile. Although some are typically more resistant to weathering (e.g. SiO_2, Al_2O_3, Fe_2O_3 that can be present in resistant minerals like quartz, gibbsite, hematite etc.), the Oxic Zone is probably not weathered ("mature") enough for the more resistant oxides to be enriched. CaO and Na_2O were relatively low in abundance in comparison to K_2O and MgO. The latter are major constituents of muscovite and chlorite. Muscovite was found not to be very reactive in the model, whereas chlorite was faster reacting and was the major contributor of Mg in the interstitial water.

More mobile trace elements like Cu, Ni, and Zn show lower abundance in the Oxic Zone, whereas the less mobile elements like Cr, Mn, Pb, Th, and Ti show no relative decrease in the Oxic Zone. Arsenic shows a minimal decrease in the Oxic Zone as it can form relatively stable secondary minerals in their higher oxidation state. This corresponds to the model results that indicated that Cu and Zn would leach from the Oxic Zone. Although not included in the model, Ni will show similar behaviour. This is because these metals are fairly mobile under acidic conditions and will not precipitate as secondary minerals. Pb and As precipitates as anglesite and secondary arsenate sulphate, bukovskýite, respectively. Although not included in the model, Cr, Mn, Th, and Ti will form fairly inert oxides, which will not be significantly leached from the Oxic Zone.

9.1.2 Conclusions on the Study Methodology

Direct measurement of oxygen in the tailings is very effective to indicate the depth range of the Oxic, Transition and Anoxic Zones. The oxygen is expected to vary slightly over dry and wet seasons due to differences in the soil moisture content at the top of the tailings dam.

Field pH, EC and ORP measurements, whole-rock elemental composition, mineralogy through X-ray diffraction, Scanning Electron Microscopy, and water quality measurement have been performed. Most testing was only performed in the top few meters of the dam, and an improvement would be to perform the testing on deeper samples also. The X-ray diffraction is only semi-quantitative, and the Scanning Electron Microscopy was very useful for improved understanding of the mineralogy. The X-ray fluorescence was also useful in understanding the distribution of chemicals in the different geochemical zones. However, X-ray fluorescence is also semi-quantitative, and acid digestion with an ICP-MS finish would have improved the test results significantly. The water quality measurements were very useful as they can be used to quantify the presence of all parameters of interest. In this study, water quality measurements were, however, limited, with only one sample taken at 8.3 – 9.3 m from a drilled borehole. An improved approach would be to analyse several interstitial water samples over the whole vertical profile.

The batch reactor test was used instead of a kinetic column. The test results could be used very successfully to determine the effective pyrite surface area. However, the test did not give a lot of information on other chemical reactions. This is because water is added after sampling, which makes it very difficult to identify any trends for trace elements like arsenic.

The software programming object used for the geochemical modelling made it possible to introduce both vertical and lateral flow in the model. This is not possible with the commercial version of the software. The subroutine facilitated the modelling of various scenarios as well as the display of their results, something that will be particularly cumbersome with the commercial version.

9.2 Recommendations

The following recommendations relate to the measurement of oxygen in the tailings dam:

- The oxygen directly after drilling overestimates the oxygen depth. Oxygen should be measured in follow-up measurements at least two months after drilling, as was performed in this study.
- The measured oxygen showed some seasonal effects. Measurements could be improved by monthly (manual) measurements or by using permanently installed oxygen probes at different depths. The latter will, however, be significantly more expensive and could, however easily be vandalised.
- Monthly oxygen measurements should be accompanied by a measurement of water saturation in the tailings dam. This could be achieved by monthly drilling or by installing water content probes (like Watermark) at different depths.

The following recommendations relate to the geochemical characterization of the tailings:

- Ideally, characterisation of the tailings should be performed over the whole vertical profile of the tailings dam. The sampling frequency of 15 cm was adequate for the Oxic and Transition Zone. A smaller frequency (e.g. 0.5 m) might be adequate for the Anoxic Zone.
- More samples from the Oxic and Anoxic Zone should be tested by Scanning Electron Microscopy. This could be very useful to determine the mineralisation in the tailings, especially the sulphides present. Most sulphides are not detected by X-

ray Diffraction. It could also be useful to determine the composition of major minerals, although Laser Ablation might be more useful in this regard.

- X-ray Fluorescence is only semi-quantitative but could be useful to determine the major oxides. To more accurately determine the whole-rock elemental composition for trace elements, acid digestion with an ICP-MS finish would improve the test results significantly.
- Interstitial water sampling could be performed by directly sampling the wet tailings after drilling and extracting the pore water through a vacuum.
- The methodology for the batch reactor testing should be refined so that the reaction of more minerals can be determined. This test could also be performed along with kinetic column leach leaching.

The following recommendations relate to the geochemical numerical modelling:

- The modelling of geochemical scenarios with multiple variables is a challenge, especially when trying to manually match the simulation results with observed data. For this purpose, automatic parameter estimation software like PEST could be used in further modelling. PEST automates calibration by estimating or adjusting model parameters within certain ranges by running it many times (PEST, 2022).

10 REFERENCES

Acero, P., Cama, J., & Ayora, C. (2007). Rate law for galena dissolution in acidic environment. *Chemical Geology*, *3–4*(245), 219–229. https://doi.org/10.1016/j.chemgeo.2007.08.003

Acero, P., Cama, J., & Ayora, C. (2013). Sphalerite dissolution kinetics in acidic environment. *Applied Geochemistry*, 1872–1883. https://doi.org/10.1016/j.apgeochem.2007.03.051

Acero, P., Cama, J., Ayora, C., & Asta, M. P. (2009). Chalcopyrite dissolution rate law from pH 1 to 3. *Geologica Acta*, 9.

Adler, R. A., Claassen, M., Godfrey, L., & Turton, A. R. (2007). Water, mining, and waste: An historical and economic perspective on conflict management in South Africa. *The Economics of Peace and Security Journal*, *2*(2). https://doi.org/10.15355/epsj.2.2.33

Ambani, A.-E., & Annegarn, H. (2015). A reduction in mining and industrial effluents in the Blesbokspruit Ramsar Wetland, South Africa: Has the quality of the surface water in the wetland improved? *Water SA*, *41*, 648. https://doi.org/10.4314/wsa.v41i5.08

Appelo, C. A. J., & Postma, D. (2005). *Geochemistry, Groundwater and Pollution*. Routledge & CRC Press.

Asta, M., Cama, J., Ayora, C., Acero, P., & Giudici, G. (2010). *Arsenopyrite dissolution rates in O2-bearing solutions*. https://doi.org/10.1016/J.CHEMGEO.2010.03.002

Barnicoat, A. C., Henderson, I. H. C., Knipe, R. J., Yardley, B. W. D., Napier, R. W., Fox, N. P. C., Kenyon, A. K., Muntingh, D. J., Strydom, D., Winkler, K. S., Lawrence, S. R., & Cornford, C. (1997). Hydrothermal gold mineralization in the Witwatersrand basin. *Nature*, *386*(6627), 6627. https://doi.org/10.1038/386820a0

Berner, R. A. (1980). *Early Diagenesis: A Theoretical Approach (Princeton Series in Geochemistry)*. https://www.abebooks.com/9780691082585/Early-Diagenesis-Theoretical-Approach-Princeton-0691082588/plp

Bethke, C. M. (2007). *Geochemical and Biogeochemical Reaction Modeling* (2nd ed.). Cambridge University Press. https://doi.org/10.1017/CBO9780511619670

Bezuidenhout, N., & Rousseau, P. D. S. (2005). An investigation into the depth and rate of weathering on gold tailings dam surfaces as key information for long-term AMD risk assessments. *Water Research Commission*, 113.

Bigham, J. M., & Nordstrom, D. K. (2000). Iron and Aluminum Hydroxysulfates from Acid Sulfate Waters. *Reviews in Mineralogy and Geochemistry*, *40*(1), 351–403. https://doi.org/10.2138/rmg.2000.40.7

Bredehoeft, J. D. (2003). From models to performance assessment: The conceptualization problem. *Ground Water*, *41*(5), 571–577. https://doi.org/10.1111/j.1745-6584.2003.tb02395.x

Cama, J., Acero, P., Asta, M. P., Torrento, C., Ayora, C., & Soler, J. (2006). The effect of dissolved oxygen on the dissolution kinetics of sulfides. *XXVI REUNiÓN (SEM) / XX REUNiÓN (SEA)*, 1.

Campbell, K. M., & Nordstrom, D. K. (2014). Arsenic Speciation and Sorption in Natural Environments. *Reviews in Mineralogy and Geochemistry*, *79*(1), 185–216. https://doi.org/10.2138/rmg.2014.79.3

da Costa, G., Hofmann, A., & Agangi, A. (2020). A revised classification scheme of pyrite in the Witwatersrand Basin and application to placer gold deposits. *Earth-Science Reviews*, *201*, 103064. https://doi.org/10.1016/j.earscirev.2019.103064

Davis, G. B., & Ritchie, A. I. M. (1986). A model of oxidation in pyritic mine wastes: Part 1 equations and approximate solution. *Applied Mathematical Modelling*, *10*(5), 314–322. https://doi.org/10.1016/0307-904X(86)90090-9

Dingman, S. L. (2015). *Physical Hydrology: Third Edition*. Waveland Press.

Dubois, I. E., Holgersson, S., Allard, S., & Malmström, M. (2010). *Correlation between particle size and surface area for chlorite and K-feldspar*. 717–720. http://urn.kb.se/resolve?urn=urn:nbn:se:kth:diva-41536

Elberling, B., & Nicholson, R. V. (1996). Field determination of sulphide oxidation rates in mine tailings. *Water Resources Research*, *32*(6), 1773–1784. https://doi.org/10.1029/96WR00487

Els, B. G. (1998). The question of alluvial fans in the auriferous Archaean and Proterozoic successions of South Africa. *South African Journal of Geology*, *101*(1), 17–25.

Ergo. (2021). *Ergo Website*. https://www.drdgold.com/our-business/ergo

Feather, C. E., & Koen, G. M. (1975). *The mineralogy of the Witwatersrand reefs*. National Institute for Metallurgy.

Fourie, P. J. (2013). *Environmental Geochemical Assessment of the Kareerand Tailings Storage Facility. Anglo Gold Ashanti. June 2013. Report No. 1306001. Report Status: Final Report.*

Fourie, P. J. (2018). *Environmental Geochemical Report: Geochemical Assessment of the Modder-east Gold Mine. Gold One Resources. August 2018. Report No. 1611003.*

Frimmel, H. E. (2019). The Witwatersrand Basin and Its Gold Deposits. In A. Kröner & A. Hofmann (Eds.), *The Archaean Geology of the Kaapvaal Craton, Southern Africa* (pp. 255–275). Springer International Publishing. https://doi.org/10.1007/978-3-319-78652-0_10

GARDGuide. (2021). http://www.gardguide.com/index.php?title=Main_Page

GWB. (2020). *The Geochemist's Workbench® Release 14*. https://www.gwb.com/software_overview.php

Haffert, L., Craw, D., & Pope, J. (2010). Climatic and compositional controls on secondary arsenic mineral formation in high-arsenic mine wastes, South Island, New Zealand. *New Zealand*

Journal of Geology and Geophysics, *53*(2–3), 91–101. https://doi.org/10.1080/00288306.2010.498403

Hallbauer, D. K. (1986). The mineralogy and geochemistry of Witwatersrand pyrite, gold, uranium, and carbonaceous matter. *Mineral Deposits of Southern Africa. V. 1-2*. http://inis.iaea.org/Search/search.aspx?orig_q=RN:18013040

Hallbauer, D. K., & Gehlen, K. von. (1983). The Witwatersrand pyrites and metamorphism. *Mineralogical Magazine*, *47*(345), 473–479. https://doi.org/10.1180/minmag.1983.047.345.08

Hansen, R. N. (2015). Contaminant leaching from gold mining tailings dams in the Witwatersrand Basin, South Africa: A new geochemical modelling approach. *Applied Geochemistry*, *61*, 217–223. https://doi.org/10.1016/j.apgeochem.2015.06.001

Hansen, R. N. (2018). Inter-comparison geochemical modelling approaches and implications for environmental risk assessments: A Witwatersrand gold tailings source term characterisation study. *Applied Geochemistry*, *95*, 71–84. https://doi.org/10.1016/j.apgeochem.2018.05.017

Harck, T. (2016). *Sulphate source terms for the Brakpan TSF, September 2016. Solution[H=] report.*

Jaynes, D. B., Rogowski, A. S., & Pionke, H. B. (1984). Acid Mine Drainage From Reclaimed Coal Strip Mines 1. Model Description. *Water Resources Research*, *20*(2), 233–242. https://doi.org/10.1029/WR020i002p00233

Kimball, B. E., Rimstidt, J. D., & Brantley, S. L. (2010). Chalcopyrite dissolution rate laws. *Applied Geochemistry*, *25*(7), 972–983. https://doi.org/10.1016/j.apgeochem.2010.03.010

Kirk Nordstrom, D. (2012). Models, validation, and applied geochemistry: Issues in science, communication, and philosophy. *Applied Geochemistry*, *27*(10), 1899–1919. https://doi.org/10.1016/j.apgeochem.2012.07.007

Koglin, N., Frimmel, H. E., Lawrie Minter, W. E., & Brätz, H. (2010). Trace-element characteristics of different pyrite types in Mesoarchaean to Palaeoproterozoic placer deposits. *Mineralium Deposita*, *45*(3), 259–280. https://doi.org/10.1007/s00126-009-0272-0

Krieger, R. A., Hatchett, J. L., & Poole, J. L. (1957). Preliminary survey of the saline-water resources of the United States. In *Preliminary survey of the saline-water resources of the United States* (USGS Numbered Series No. 1374; Water Supply Paper, Vol. 1374, p. 174). U.S. Government Printing Office. https://doi.org/10.3133/wsp1374

Krupp, R., Oberthuer, T., & Hirdes, W. (1994). The early Precambrian atmosphere and hydrosphere; thermodynamic constraints from mineral deposits. *Economic Geology*, *89*(7), 1581–1598. https://doi.org/10.2113/gsecongeo.89.7.1581

Ledin, M., & Pedersen, K. (1996). The environmental impact of mine wastes—Roles of microorganisms and their significance in treatment of mine wastes. *Earth-Science Reviews*, *41*(1), 67–108. https://doi.org/10.1016/0012-8252(96)00016-5

Lowson, R., Comarmond, M., Rajaratnam, G., & Brown, P. (2005). *The kinetics of the dissolution of chlorite as a function of pH and at 25°C*. https://doi.org/10.1016/J.GCA.2004.09.028

Marakushev, A., Glazovskaya, L., Paneyakh, N., & Marakushev, S. (2012). The problem of the origin of the Witwatersrand uranium-gold deposit. *Moscow University Geology Bulletin*, *67*. https://doi.org/10.3103/S0145875212030052

Marsden, J., & House, I. (2006). *The chemistry of gold extraction. SME.*

Mbonimpa, M., Aubertin, M., Aachib, M., & Bussière, B. (2003). Diffusion and consumption of oxygen in unsaturated cover materials. *Canadian Geotechnical Journal*. https://doi.org/10.1139/t03-040

McCarthy, T. S. (2011). The impact of acid mine drainage in South Africa. *South African Journal of Science*, *107*(5/6), 5/6. https://doi.org/10.4102/sajs.v107i5/6.712

McCarthy, T. S., Johnson, M. R., Anhausser, C. R., & Thomas, R. J. (2006). *The Witwatersrand Supergroup. The Geology of South Africa.* (pp. 155–186).

McKibben, M. A., Tallant, B. A., & del Angel, J. K. (2008). Kinetics of inorganic arsenopyrite oxidation in acidic aqueous solutions. *Applied Geochemistry*, *23*(2), 121–135. https://doi.org/10.1016/j.apgeochem.2007.10.009

McMahon, P. B., & Chapelle, F. H. (2008). Redox Processes and Water Quality of Selected Principal Aquifer Systems. *Groundwater*, *46*(2), 259–271. https://doi.org/10.1111/j.1745-6584.2007.00385.x

McPhail, G. I., & Wagner, J. G. (1987). Chapter 11 Disposal of Residues. In *The Extractive Metallurgy of gold in South Africa (Edited by G.G. Stanley). SAIMM Monograph Series M7.: Vol. Volume 2*.

Mellor, E. T. (1916). *The conglomerates of the Witwatersrand. 25*, 226–291.

Meyer, F. M., & Ridgway, J. (1991). Ammonium in Witwatersrand reefs: A possible indicator of metamorphic fluid flow. *South African Journal of Geology*, *94*(5–6), 343–347.

Miller, S., Robertson, A., & Donahue, T. (1997). *Advances in acid drainage prediction using the net acid generating (NAG) test*. https://www.osti.gov/etdeweb/biblio/620895

Molson, J., Fala, O., Aubertin, M., & Bussière, B. (2005). Numerical simulations of pyrite oxidation and acid mine drainage in unsaturated waste rock piles. *Journal of Contaminant Hydrology*, *78*, 343–371. https://doi.org/10.1016/j.jconhyd.2005.06.005

Munson, R. A. (1968). The synthesis of iridium disulfide and nickel diarsenide having the pyrite structure. *Inorganic Chemistry*, *7*(2), 389–390. https://doi.org/10.1021/ic50060a047

Nagy, K. L. (1995). *Dissolution and precipitation kinetics of sheet silicates. In Chemical Weathering Rates of Silicate Minerals (AF White and SL Brantley, eds.), Mineralogical Society of America, vol. 31, Washington, D.C., 173-233.*

Naudé, A. A. J. (2016). *A methodology to quantify the groundwater impacts of mega-tailings dams for the gold mining industry, South Africa* [Thesis, North-West University (South Africa), Potchefstroom Campus]. https://repository.nwu.ac.za/handle/10394/26031

Nengovhela, A. C., Yibas, B., & Ogola, J. S. (2006). Characterisation of gold tailings dams of the Witwatersrand Basin with reference to their acid mine drainage potential,Johannesburg, South Africa. *Water SA*, *32*(4), 4. https://doi.org/10.4314/wsa.v32i4.5290

Nengovhela, A., Yibas, B., & Ogola, J. (2009). An investigation into the availability and role of oxygen gas in gold tailings dams of the Witwatersrand basin with reference to their acid mine drainage potential. *Water SA*, *33*(2). https://doi.org/10.4314/wsa.v33i2.49088

Nicholson, R. V. (1994). Iron-sulfide oxidation mechanisms: Laboratory studies. *Environmental Geochemistry of Sulphide Mine-Wastes*, *22*, 163–183.

Nordstrom, D. K., Majzlan, J., & Königsberger, E. (2014). Thermodynamic Properties for Arsenic Minerals and Aqueous Species. *Reviews in Mineralogy and Geochemistry*, *79*(1), 217–255. https://doi.org/10.2138/rmg.2014.79.4

Nordstrom, D. K., & Munoz, J. L. (1994). *Geochemical thermodynamics*. Blackwell Scientific Publ.

Ondruš, P., Skála, R., Viti, C., Veselovský, F., Novák, F., & Jansa, J. (1999). *Parascorodite, FeAsO4·2H2O—a new mineral from Kaňk near Kutná Hora, Czech Republic*. https://doi.org/10.2138/am-1999-0923

Penman, A. D. M. (1994). *Tailings dams, some aspects of their design and construction, in K.R. Saxena (ed.), Geotechnical Engineering: Emerging Trends in Design and Practice, 247- 277.*

Perkins, D. (2021, December 30). *7: Sedimentary Minerals and Sedimentary Rocks*. Geosciences LibreTexts. https://geo.libretexts.org/Bookshelves/Geology/Mineralogy_(Perkins_et_al.)/07%3A_Sedimentary_Minerals_and_Sedimentary_Rocks

PEST. (2022). *PEST: Model-Independent Parameter Estimation and Uncertainty Analysis*. https://pesthomepage.org/

Prasad, M., Mensah-Biney, R., & Pizarro, R. (1991). Modern trends in gold processing—Overview. *Minerals Engineering*, *4*(12), 1257–1277.

Pretorius, D. A. (1974). *The nature of the Witwatersrand gold-uranium deposits. Economic geology research unit, Univ. Of the Witwatersrand. Information Circular No. 86, May 1974.*

Reardon, E. J., & Moddle, P. M. (1985). Gas diffusion coefficient measurements on uranium mill tailings: Implications to cover layer design. *Uranium (Amsterdam)*, *2*(2), 111–131.

Ritchie, A. I. M. (1994). The waste-rock environment. *Environmental Geochemistry of Sulfide Mine-Waste. Mineralogical Association of Canada*, *22*, 201–244.

Robb, L. J., & Meyer, F. M. (1990). The nature of the Witwatersrand hinterland; conjectures on the source area problem. *Economic Geology*, *85*(3), 511–536. https://doi.org/10.2113/gsecongeo.85.3.511

Robb, L. J., & Meyer, F. M. (1995). The Witwatersrand Basin, South Africa: Geological framework and mineralization processes. *Ore Geology Reviews*, *10*(2), 67–94. https://doi.org/10.1016/0169-1368(95)00011-9

Rösner, T. (1999). *The environmental impact of seepage from gold mine tailings dams near Johannesburg, South Africa. Unpublished Ph.D. Thesis, University of Pretoria.*

Rösner, T., & van Schalkwyk, A. (2000). The environmental impact of gold mine tailings footprints in the Johannesburg region, South Africa. *Bulletin of Engineering Geology and the Environment*, *59*, 137–148. https://doi.org/10.1007/s100640000037

Ruhmer, W. T. (1974). *Slimes-dam construction in the gold mines of the Anglo American Group. SAIMM, February 1974.*

SA Weather. (2021). *Climate data for Jan Smuts weather station #04763989 provided by SA Weather via email (18/10/2021)* [Personal communication].

Smith, K. S. (1997). *Metal Sorption on Mineral Surfaces: An Overview with Examples Relating to Mineral Deposits*. https://doi.org/10.5382/Rev.06.07

Smits, G. (1990). *The geochemical history of the sedimentary rocks of the Witwatersrand as reflected in the mineralogy of the heavy-mineral assemblage of the uranium-bearing reefs of the Central Rand Group. Doctor of Science Unpublished Thesis, Potchefstroom University.*

Stumm, W., & Morgan, J. J. (1995). *Aquatic Chemistry: Chemical Equilibria and Rates in Natural Waters, 3rd Edition | Wiley*. Wiley.Com.

Tester, J. W., Worley, W. G., Robinson, B. A., Grigsby, C. O., & Feerer, J. L. (1994). Correlating quartz dissolution kinetics in pure water from 25 to 625°C. *Geochimica et Cosmochimica Acta*, *58*(11), 2407–2420. https://doi.org/10.1016/0016-7037(94)90020-5

Todd, D. K., & Mays, L. W. (2004). *Groundwater Hydrology, 3rd Edition | Wiley*. Wiley.Com. https://www.wiley.com/en-us/Groundwater+Hydrology%2C+3rd+Edition-p-9780471059370

Torrero, M. E., Baraj, E., De Pablo, J., Gimenez, J., & Casas, I. (1997). *Kinetics of corrosion and dissolution of uranium dioxide as a function of pH.Kinetics of corrosion and dissolution of uranium dioxide as a function of pH. International Journal of Chemical Kinetics, 29/4, p. 261-267,*.

Turton, A. R. (2017). *Personnel communication via email with Anthony Turton.* [Personal communication].

USDA. (2021). *SSM - Ch. 3. Examination and Description of Soil Profiles | NRCS Soils*. https://www.nrcs.usda.gov/wps/portal/nrcs/detail/soils/ref/?cid=nrcs142p2_054253

USEPA. (2017). *Field Measurement of Oxidation-Reduction Potential (ORP)*. 22.

Vermeulen, N. J. (2001). *The composition and state of gold tailings. Unpublished PhD Thesis, University of Pretoria.*

Vick, S. G. (1990). *Planning, Design, and Analysis of Tailings Dams*. https://doi.org/10.14288/1.0394902

Ward, A. D., & Trimble, S. W. (2003). *Environmental Hydrology, Second Edition*. Taylor & Francis. https://books.google.com.au/books?id=yANwmTjf588C

Wels, C., Lefebvre, R., & Robertson, A. M. (2003). *An Overview of Prediction and Control of Air Flow in Acid-Generating Waste Rock Dumps. 6th ICARD Conference, Cairns, Australia.*

Williamson, M. A., & Rimstidt, J. D. (1994). The kinetics and electrochemical rate-determining step of aqueous pyrite oxidation. *Geochimica et Cosmochimica Acta*, *58*(24), 5443–5454. https://doi.org/10.1016/0016-7037(94)90241-0

Yibas, B., Pulles, W., Lorentz, S., & Maiyana, B. (2011). *Development of water balances for operational and post-closure situations for gold mine residue deposits to be used as input to pollution prediction studies for such facilities: Report to the Water Research Commission*.

Yibas, B., Pulles, W., Nengovhela, A. C., South Africa, & Water Research Commission. (2010). *Kinetic development of oxidation zones in tailings dams with specific reference to the Witwatersrand gold mine tailings dams: Report to the Water Research Commission*. Water Research Commission.

Zhang, C., Li, X., Almeev, R. R., Horn, I., Behrens, H., & Holtz, F. (2020). Ti-in-quartz thermobarometry and TiO2 solubility in rhyolitic melts: New experiments and parametrization. *Earth and Planetary Science Letters*, *538*, 116213. https://doi.org/10.1016/j.epsl.2020.116213